



City Research Online

City, University of London Institutional Repository

Citation: De Moor, E.K. (1989). Modelling of deep tunnel behaviour in clay. (Unpublished Doctoral thesis, City University London)

This is the accepted version of the paper.

This version of the publication may differ from the final published version.

Permanent repository link: <https://openaccess.city.ac.uk/id/eprint/7396/>

Link to published version:

Copyright: City Research Online aims to make research outputs of City, University of London available to a wider audience. Copyright and Moral Rights remain with the author(s) and/or copyright holders. URLs from City Research Online may be freely distributed and linked to.

Reuse: Copies of full items can be used for personal research or study, educational, or not-for-profit purposes without prior permission or charge. Provided that the authors, title and full bibliographic details are credited, a hyperlink and/or URL is given for the original metadata page and the content is not changed in any way.

MODELLING OF DEEP TUNNEL BEHAVIOUR IN CLAY

by

Eileen Karen De Moor

A Dissertation submitted for the Degree of
Doctor of Philosophy

THE CITY UNIVERSITY
Civil Engineering Department

February 1989

CONTENTS

List of Tables	6
List of Figures	7
Acknowledgements	19
Declaration	21
Abstract	22
List of Symbols	23
CHAPTER 1 INTRODUCTION	26
1.1 Background to the dissertation	26
1.1.1 Research at Mol	28
1.1.2 Small scale model tests related to the Mol experiment	31
1.2 Behaviour of tunnels in clay	32
1.2.1 Undrained behaviour	33
1.2.2 Time dependent behaviour	38
1.3 Modelling of Tunnel Behaviour	42
1.3.1 Physical modelling	42
1.3.2 Simplified analytical modelling	44
1.3.3 Finite element modelling	47
1.4 Objectives of the research	48
CHAPTER 2 SMALL SCALE MODEL TESTING OF DEEP TUNNELS	49
2.1 Introduction	49
2.1.1 Outline of model test series	49
2.2 Small scale modelling techniques	50
2.2.1 Similarity	53
2.2.2 Scaling laws for different diameter tunnels	54
2.3 Apparatus	57
2.3.1 Introduction	57
2.3.2 Triaxial apparatus	58
2.3.3 Model tunnels	59

2.4	Instrumentation	61
2.4.1	Pore pressure transducers	61
2.4.2	Total stress transducers	62
2.4.3	Cell and back pressure transducers	62
2.4.4	Differential pressure transducers	62
2.4.5	Displacement transducers	63
2.5	Experimental Procedure	64
2.5.1	Sample preparation	64
2.5.2	Model preparation	65
2.5.3	Testing procedure	67
CHAPTER 3	RESULTS FROM SMALL SCALE MODEL TESTS	70
3.1	Introduction	70
3.1.1	Preliminary tests	71
3.2	Selection of initial stress conditions	75
3.2.1	Series I	75
3.2.2	Series II	76
3.2.3	Position of tunnel face	77
3.3	Deformation of the tunnel face	78
3.3.1	Series I	78
3.3.2	Series II	81
3.4	Pore pressure response	84
3.4.1	Series I	84
3.4.2	Series II	93
3.5	Water contents	97
3.6	Conclusions	100
CHAPTER 4	MATERIAL BEHAVIOUR	103
4.1	Introduction	103
4.1.1	Choice of material	104
4.2	Mathematical models	105
4.2.1	Critical state soil mechanics	105
4.2.2	Cam-clay and modified Cam-clay	109
4.2.3	Elastic-perfectly plastic model	111

4.3	Soil parameters for the finite element analyses	112
4.3.1	Modified Cam-clay model	112
4.3.2	Elastic-perfectly plastic model	118
4.4	Undrained shear strength of kaolin	118
CHAPTER 5	ANALYSIS OF SMALL SCALE MODEL TESTS	123
5.1	Introduction	123
5.2	Simplified analytical solutions	124
5.2.1	Thick cylinder analogue	124
5.2.2	Thick sphere analogue	126
5.2.3	Comparison of experimental data with the thick cylinder and thick sphere predictions	127
5.2.4	Influence of soil model on closed form solutions	131
5.2.5	Influence of experimental procedure	132
5.2.6	N_{crit} and load factor	134
5.3	Non-dimensional groups	135
5.3.1	Scaling laws for tunnels of different diameters (Series I)	137
5.3.2	Scaling laws for tunnels of different diameters (Series II)	140
5.4	Time dependent pore pressure response	145
5.4.1	Dissipation phase A	146
5.4.2	Dissipation phase B	148
5.5	Conclusions	150
CHAPTER 6	FINITE ELEMENT ANALYSES - THICK CYLINDER	153
6.1	Introduction	153
6.2	Details of the analyses	155
6.2.1	Development of thick cylinder finite element meshes	155
6.2.2	Development of analysis procedure	156
6.2.3	Selection of soil model	157
6.3	Undrained analyses of a thick cylinder	158

6.4	Consolidation analyses of a thick cylinder	162
6.4.1	Introduction	162
6.4.2	Undrained response	163
6.4.3	Consolidation behaviour	166
6.4.4	Comparison with experimental data	172
6.5	Conclusions	173
CHAPTER 7	FINITE ELEMENT ANALYSES - MODEL TUNNEL TESTS	177
7.1	Introduction	177
7.2	Details of the analyses	177
7.2.1	Development of the model tunnel test meshes	177
7.2.2	Development of analysis procedure	179
7.2.3	Selection of soil model	181
7.3	Analyses of the model tunnel tests	181
7.3.1	Series I Stage 1 analyses	182
7.3.2	Influence of pore pressure	190
7.3.3	Influence of load factor	193
7.3.4	Influence of kappa	196
7.3.5	Influence of analysis procedures	199
7.4	Comparison with experimental data	203
7.5	Conclusions	207
CHAPTER 8	CONCLUSIONS	212
8.1	Deformations and pore pressure behaviour around an unsupported tunnel face in clay	212
8.2	Recommendations for further research	217
APPENDICES		219
Appendix A	Expressions for thick cylinder solution	219
Appendix B	Expressions for thick sphere solution	225
References		229
Tables		
Figures		

LIST OF TABLES

Table 3.1(a)	Summary of initial stress states for Series I tests
Table 3.1(b)	Summary of initial stress states for Series I tests and tests performed in sample no. 13
Table 3.2	Summary of initial stress states for all Series II tests
Table 3.3	Summary of events during tests nos. 1 and 2
Table 3.4	Values of p' (in kPa) required for given load factors and initial pore pressures
Table 3.5	Summary of model tunnel test data from representative tests in Series I
Table 3.6	Summary of model tunnel test details from representative tests in Series II
Table 4.1	Modified Cam-clay parameters describing the behaviour of Speswhite kaolin
Table 4.2	Seepage parameters for Speswhite kaolin used in the finite element analyses
Table 4.3	Parameters used in the undrained thick cylinder finite element analyses
Table 6.1	Initial stress states and final displacements for the undrained thick cylinder analyses
Table 6.2	Initial stress states and displacements at the end of removal of face support and final time factors for the thick cylinder consolidation analyses
Table 7.1	Details of finite element analyses of the model tunnel tests

LIST OF FIGURES

Figure 1.1	The Underground Research Laboratory at Mol (after Manfroy et al, 1987)
Figure 1.2	Concept of tunnelled repository in a deep clay formation (after Bonne and Neerdael, 1986)
Figure 1.3	The test drift at Mol (after Beaufays et al, 1987)
Figure 1.4	Idealized representation of heading during tunnel construction (after Mair, 1979)
Figure 1.5	Variation of N_{crit} with tunnel geometry (after Mair, 1979)
Figure 1.6	Variation of volume loss with load factor (after Mair, 1979)
Figure 1.7	Deformation around shallow and deep tunnels
Figure 1.8	Deformation data from the experimental drift (after Neerdael et al, 1987)
Figure 1.9	Components of deformation caused by tunnel construction (after Lo et al, 1984)
Figure 1.10	Thick cylinder analogue for in situ tunnel deformations
Figure 1.11	Lower bound stress fields for the circular tunnel heading (after Davis et al, 1980)
Figure 2.1	The triaxial apparatus
Figure 2.2	Strain-gauged model tunnel
Figure 2.3	Tunnel face support
Figure 2.4	Arrangement of tunnel face support apparatus prior to a tunnel test
Figure 2.5	Section through a miniature pore pressure transducer
Figure 2.6	Consolidometer used in sample preparation
Figure 2.7	Transfer of sample to triaxial apparatus
Figure 2.8	Insertion of pore pressure transducers
Figure 2.9(a)	Assembly of triaxial apparatus
Figure 2.9(b)	Assembly of triaxial apparatus

Figure 2.10	Summary of model test procedure
Figure 2.11	Sample reconsolidation prior to testing
Figure 2.12	Section through sample after testing
Figure 3.1(a)	Pore pressure response during stage 3 of test no. 2
Figure 3.1(b)	Pore pressure response during stage 3 of test no. 2
Figure 3.2(a)	Change of volume (squeeze) of sample during stage 1 of test no. 1
Figure 3.2(b)	Change of volume (squeeze) of sample during stage 2 of test no. 1
Figure 3.3(a)	Water contents of clay augered out of tunnel during stages 1 and 2 of test no. 1
Figure 3.3(b)	Water contents of clay augered out of tunnel during stages 2 and 3 of test no. 2
Figure 3.4	Definition of overall pressure gradient (OPG) and values used in the model tunnel tests of Series I
Figure 3.5(a)	Locations of the model tunnel face for the various stages of the Series I tests and the tests in sample no. 13
Figure 3.5(b)	Locations of the model tunnel face for tests from Series 2
Figure 3.6	Deformation and pore pressure response Test 14/1 (12.7mm) $p' = 770\text{kPa}$ $u = 199\text{kPa}$
Figure 3.7	Deformation and pore pressure response Test 12/1A (12.7mm) $p' = 767\text{kPa}$ $u = 198\text{kPa}$
Figure 3.8	Deformation and pore pressure response Test 11/1 (25.4mm) $p' = 771\text{kPa}$ $u = 193\text{kPa}$
Figure 3.9	Deformation and pore pressure response Test 10/1 (50.8mm) $p' = 766\text{kPa}$ $u = 195\text{kPa}$
Figure 3.10	Deformation and pore pressure response Test 12/2A (12.7mm) $p' = 799\text{kPa}$ $u = 80\text{kPa}$
Figure 3.11	Deformation and pore pressure response Test 14/2 (12.7mm) $p' = 779\text{kPa}$ $u = 80\text{kPa}$
Figure 3.12	Deformation and pore pressure response Test 14/3A (12.7mm) $p' = 784\text{kPa}$ $u = 78\text{kPa}$
Figure 3.13	Deformation and pore pressure response Test 14/3 (12.7mm) $p' = 782\text{kPa}$ $u = 87\text{kPa}$
Figure 3.14	Deformation and pore pressure response Test 11/2 (25.4mm) $p' = 809\text{kPa}$ $u = 74\text{kPa}$

Figure 3.15	Deformation and pore pressure response Test 10/2 (50.8mm) $p' = 815\text{kPa}$ $u = 76\text{kPa}$
Figure 3.16	Deformation and pore pressure response Test 11/3 (25.4mm) $p' = 783\text{kPa}$ $u = 78\text{kPa}$
Figure 3.17	Deformation and pore pressure response Test 10/3 (50.8mm) $p' = 784\text{kPa}$ $u = 80\text{kPa}$
Figure 3.18	Deformation and pore pressure response Test 16/2 (25.4mm) $p' = 759\text{kPa}$ $u = 56\text{kPa}$
Figure 3.19	Deformation and pore pressure response Test 16/1 (25.4mm) $p' = 556\text{kPa}$ $u = 200\text{kPa}$
Figure 3.20	Deformation and pore pressure response Test 16/3 (25.4mm) $p' = 266\text{kPa}$ $u = 350\text{kPa}$
Figure 3.21	Deformation and pore pressure response Test 19/1A (12.7mm) $p' = 438\text{kPa}$ $u = 401\text{kPa}$
Figure 3.22	Deformation and pore pressure response Test 17/1 (25.4mm) $p' = 550\text{kPa}$ $u = 350\text{kPa}$
Figure 3.23	Deformation and pore pressure response Test 17/2 (25.4mm) $p' = 771\text{kPa}$ $u = 352\text{kPa}$
Figure 3.24	Deformation and pore pressure response Test 18/1A (12.7mm) $p' = 454\text{kPa}$ $u = 203\text{kPa}$
Figure 3.25	Deformation and pore pressure response Test 18/3 (25.4mm) $p' = 435\text{kPa}$ $u = 398\text{kPa}$
Figure 3.26	Deformation and pore pressure response Test 19/3A (12.7mm) $p' = 804\text{kPa}$ $u = 820\text{kPa}$
Figure 3.27	Deformation and pore pressure response Test 19/3 (25.4mm) $p' = 800\text{kPa}$ $u = 820\text{kPa}$
Figure 3.28	Variation in the g and h components of the distance r from the pore pressure transducer to the centre of the tunnel face
Figure 3.29(a)	Comparison of the experimental pore pressure response at r/r_o of 1.8 (along the central axis) to the removal of the face support
Figure 3.29(b)	Comparison of the experimental pore pressure response at r/r_o of 2.6 (perpendicular to the central axis) to the removal of the face support
Figure 3.30(a)	Pore pressure response recorded by transducers at the top and base of the sample
Figure 3.30(b)	Pore pressure response recorded by transducers at top and base of sample

Figure 3.30(c)	Pore pressure response recorded by transducers at top of sample
Figure 3.31	Measured water contents of samples of clay removed from the model at the end of a test demonstrating the influence of time
Figure 3.32	Measured water contents of samples of clay removed from the model at the end of a test demonstrating the influence of time
Figure 3.33	Measured water contents of samples of clay removed from the model at the end of a test demonstrating the influence of initial pore pressure
Figure 3.34	Measured water contents of samples of clay removed from the model at the end of a test demonstrating the influence of tunnel diameter
Figure 3.35	Measured water contents of samples of clay removed from the model at the end of a test demonstrating the influence of tunnel diameter
Figure 3.36	Measured water contents of samples of clay removed from the model at the end of tests performed at high load factor
Figure 4.1	Critical states (after Schofield and Wroth, 1968)
Figure 4.2	State boundary surface (after Atkinson and Bransby, 1978)
Figure 4.3	Projection of yield curves onto the $q = 0$ plane in $v : \ln p'$ space
Figure 4.4	Projections of the Cam-clay and modified Cam-clay yield curves
Figure 4.5(a)	Typical undrained stress paths to failure for the Cam-clay soil model
Figure 4.5(b)	Typical stress paths to failure for an elastic-perfectly plastic model (Tresca criterion)
Figure 4.6	Variation of undrained shear strength with overconsolidation ratio in triaxial compression tests
Figure 4.7	Influence of reducing confining stress to zero on the undrained shear strength of kaolin (samples consolidated isotropically to confining stress) (after Mair, 1979)
Figure 5.1(a)	Comparison of model test conditions with the thick cylinder
Figure 5.1(b)	Comparison of model test conditions with the thick sphere

Figure 5.2	Idealized stress distribution for a thick cylinder
Figure 5.3	Total and effective stress paths for the Tresca yield criterion
Figure 5.4	Idealized pore pressure distribution for a thick cylinder
Figure 5.5	Zones of approximately cylindrical or spherical conditions
Figure 5.6(a)	Experimental pore pressure response from zone A compared with the theoretical distributions based on the thick cylinder solution using N^*
Figure 5.6(b)	Experimental pore pressure responses in zone A plotted non-dimensionally using the modified stability ratio N^*
Figure 5.7(a)	Experimental pore pressure response from zone B compared with the theoretical distributions based on the thick sphere solution
Figure 5.7(b)	Experimental pore pressure responses in zone B plotted with the non-dimensional idealized spherical pore pressure distribution
Figure 5.8(a)	Response of a pore pressure transducer ahead of the tunnel face to the removal of the face support in test 14/3
Figure 5.8(b)	Response of pore pressure transducers some radial distance from the central axis to the removal of the face support in test 16/2
Figure 5.8(c)	Response of pore pressure transducers some radial distance from the central axis to the removal of the face support in test 11/2
Figure 5.9	Comparison of Series I stage 1 face deformation data plotted in non-dimensional groups to demonstrate the influence of tunnel diameter
Figure 5.10	Comparison of Series I stage 2 and 3 face deformation data plotted in non-dimensional groups to demonstrate the influence of tunnel diameter
Figure 5.11	Influence of the inclusion of initial pore pressure in the non-dimensional time factor on Series I data (all stages)
Figure 5.12	The influence of the inclusion of load factor in a non-dimensional group on the deformation data from Series I tests
Figure 5.13	The influence of the inclusion of load factor in a non-dimensional group on the deformation data from Series II tests

Figure 5.14	Experimental deformations at a constant t/D^2 and various pore pressures
Figure 5.15	Experimental deformation data at a constant t/D^2 plotted in logarithmic space to determine variation with load factor
Figure 5.16	Experimental deformation data at a constant $ktu_o/(D^2\gamma_w)$ plotted in logarithmic space to determine variation with load factor
Figure 5.17	Deformation data from tests in sample no. 17 with a load factor range of 0.45 to 0.74 plotted in non-dimensional groups
Figure 5.18	Deformation data from tests in sample no. 18 with a load factor range of 0.35 to 0.67 plotted in non-dimensional groups
Figure 5.19	Deformation data from tests in sample no. 19 with a load factor range of 0.44 to 0.91 plotted in non-dimensional groups
Figure 5.20	Comparison of deformation data from Series I and II excluding tests using the 50.8mm diameter tunnel
Figure 5.21	Comparison of deformation data (uncorrected for loss of strength) from tests in sample no. 13 with Series I tests
Figure 5.22	Comparison of tests in sample no. 13 with equivalent Series I tests using the 12.7mm diameter tunnel
Figure 5.23	Comparison of data from the 19.1mm diameter tests with a number of the Series I and II tests
Figure 5.24	Two phases of pore pressure behaviour during the model tunnel tests
Figure 5.25	Pore pressure data from Series I Stage 1 tests plotted against the non-dimensional time factor developed in the analysis of the tunnel face deformations
Figure 5.26(a)	Pore pressure data at different r/r_o values in test 11/1
Figure 5.26(b)	Pore pressure data at different r/r_o values in tests 11/2
Figure 5.26(c)	Pore pressure data from tests 14/3
Figure 5.27(a)	Seepage flow net for conditions of axisymmetry (after Taylor, 1948)

Figure 5.27(b)	Comparison of pore pressures predicted for radial seepage and the phase B pore pressure measured in test 11/2
Figure 5.27(c)	Comparison of pore pressures predicted for radial seepage and the phase B pore pressure measured in test 16/1
Figure 5.27(d)	Comparison of pore pressures predicted for radial seepage and the phase B pore pressure measured in test 16/2
Figure 6.1(a)	Finite element mesh for the thick cylinder analyses
Figure 6.1(b)	Detail of node and elements referred to in text close to the inner boundary of the thick cylinder
Figure 6.2(a)	Deformed mesh at the end of analysis TCU1
Figure 6.2(b)	Deformed mesh at the end of analysis TCU2
Figure 6.2(c)	Deformed mesh at the end of analysis TCU3
Figure 6.3(a)	Predicted pore pressure changes at the end of the undrained removal of support pressure at the inner radius of the thick cylinder from analyses using K_w of about 100K'
Figure 6.3(b)	Predicted pore pressure changes at the end of the undrained removal of support pressure at the inner radius of the thick cylinder from analyses using K_w of about 10K'
Figure 6.4	Initial deformation of the inner boundary at the end of the removal of support pressure as function of load factor
Figure 6.5	Comparison of predicted pore pressure changes at the end of the removal of support pressure at the inner radius in the thick cylinder consolidation analyses
Figure 6.6(a)	Pore pressure distribution at the end of removal of face support pressure $t=0.3$ seconds
Figure 6.6(b)	Changes in specific volume at the end of removal of face support pressure $t=0.3$ seconds
Figure 6.7(a)	Pore pressure distribution at the end of removal of face support pressure $t=0.3$ seconds
Figure 6.7(b)	Changes in specific volume at the end of removal of face support pressure $t=0.3$ seconds
Figure 6.8	Predicted deformation at node 4 on the inner boundary from thick cylinder consolidation analysis TCC1

Figure 6.9	Total and effective stress paths predicted for element 17 in thick cylinder consolidation analysis TCC1
Figure 6.10	Predicted specific volume change for element 17 from thick cylinder consolidation analysis TCC1
Figure 6.11(a)	Deformation at inner boundary (node 4) during thick cylinder consolidation analyses
Figure 6.11(b)	Deformation at node 4 on the inner boundary plotted in non-dimensional groups
Figure 6.12	Predicted pore pressure response at node 4 on the inner radius of the thick cylinder from analyses with different initial OCR values
Figure 6.13	Predicted pore pressure response at element 17 from analyses with different initial OCR values
Figure 6.14	Comparison of specific volume changes at element 17 from analyses with different initial OCR values
Figure 6.15(a)	Total and effective stress paths predicted at element 17 in analysis TCC2
Figure 6.15(b)	Total and effective stress paths predicted at element 17 in analysis TCC5
Figure 6.16	Predicted pore pressure response at node 4 on the inner radius of the thick cylinder from analyses with different initial OCR values
Figure 6.17	Predicted pore pressure response at element 17 from analyses with different initial OCR values
Figure 6.18(a)	Total and effective stress paths predicted for element 17 in analysis TCC3
Figure 6.18(b)	Total and effective stress paths predicted for element 17 in analysis TCC4
Figure 6.19	Specific volume changes at element 34 in analysis TCC3 showing dry of critical behaviour
Figure 6.20(a)	Pore pressure distribution at $t \approx 10$ seconds
Figure 6.20(b)	Changes in specific volume at $t \approx 10$ seconds
Figure 6.20(c)	Pore pressure distribution at $t \approx 100$ seconds
Figure 6.20(d)	Changes in specific volume at $t \approx 100$ seconds
Figure 7.1(a)	Mesh used in 50mm diameter tunnel analyses
Figure 7.1(b)	Detail of element layout close to tunnel face
Figure 7.2(a)	Mesh used in preliminary model tunnel test analyses

Figure 7.2(b)	Deformation predicted at tunnel face from analyses using preliminary mesh
Figure 7.3	Meshes used in 25mm and 12.5mm diameter tunnel analyses, incorporating a reduced scale 50mm diameter tunnel mesh
Figure 7.4	Elements affected by numerical difficulties in the modified Cam-clay analyses
Figure 7.5	Deformed meshes showing non-uniform distortions in analyses SI25 and SI13
Figure 7.6(a)	Deformed meshes near the end of analyses investigating the influence of tunnel diameter $ktu_o/(D^2\gamma_w) = 4.4 \times 10^{-6}$
Figure 7.6(b)	Deformed meshes near the end of analyses investigating the influence of tunnel diameter $ktu_o/(D^2\gamma_w) = 4.4 \times 10^{-6}$
Figure 7.6(c)	Deformed meshes and element states near the end of analyses investigating the influence of tunnel diameter $ktu_o/(D^2\gamma_w) = 4.4 \times 10^{-6}$
Figure 7.6(d)	Deformed meshes and element states near the end of analyses investigating the influence of tunnel diameter $ktu_o/(D^2\gamma_w) = 4.4 \times 10^{-6}$
Figure 7.7	Deformation at the tunnel face from analyses of different tunnel diameters with identical initial stress states
Figure 7.8	Influence of load factor on predicted tunnel face deformation for different tunnel diameters
Figure 7.9	Predicted pore pressure behaviour at node 52 in analysis SI50
Figure 7.10	Pore pressure response with time ahead of the tunnel face in finite element analysis SI50
Figure 7.11	Total and effective stress paths predicted for element 25 in analysis SI50
Figure 7.12	Comparison of specific volume changes predicted for element 25 from analyses of different tunnel diameters
Figure 7.13	Predicted specific volume changes for elements 25 and 33 in analysis SI50
Figure 7.14	Total and effective stress paths predicted for element 33 in analysis SI50
Figure 7.15	Pore pressure response with time from finite element analysis SI50

Figure 7.16(a)	Pore pressure distribution at the end of removal of face support pressure in SI50
Figure 7.16(b)	Pore pressure distribution during SI50 $ktu_o/(D^2\gamma_w) = 2.4 \times 10^{-6}$
Figure 7.17(a)	Total stress distribution in the analysis SI50 investigating the influence of diameter
Figure 7.17(b)	Total stress distribution in the analysis SI25 investigating the influence of diameter
Figure 7.17(c)	Total stress distribution in the analysis SI13 investigating the influence of diameter
Figure 7.18(a)	Deformed mesh during KAP05 $ktu_o/(D^2\gamma_w) = 4.4 \times 10^{-6}$
Figure 7.18(b)	Deformed mesh at the end of KAP05 $ktu_o/(D^2\gamma_w) = 15.1 \times 10^{-6}$
Figure 7.18(c)	Element states during KAP05 $ktu_o/(D^2\gamma_w) = 4.4 \times 10^{-6}$
Figure 7.19	Comparison of tunnel face deformation using non-dimensional groups developed from experimental observations
Figure 7.20	Pore pressure reductions ahead of the tunnel face plotted in non-dimensional groups
Figure 7.21	Comparison of pore pressure predictions for element 25 in finite element analyses SI50 and KAP05
Figure 7.22	Comparison of pore pressure predictions for node 52 at the tunnel face in analyses SI50 and KAP05
Figure 7.23	Comparison of specific volume changes predicted for elements 25 and 33 in analysis KAP05
Figure 7.24	Total and effective stress paths predicted for element 25 in analysis KAP05
Figure 7.25(a)	Deformed mesh from analysis LF5 $ktu_o/(D^2\gamma_w) = 4.4 \times 10^{-6}$
Figure 7.25(b)	Element states during analysis LF5 $ktu_o/(D^2\gamma_w) = 4.4 \times 10^{-6}$
Figure 7.26	Comparison of predicted pore pressure behaviour for elements 25 and 33 in analyses LF5 and SI50
Figure 7.27	Total and effective stress paths predicted for element 25 in analysis LF5
Figure 7.28	Comparison of specific volume changes at elements 25 and 33 in analysis LF5

Figure 7.29(a)	Deformed mesh from analysis KAP02 $ktu_0/(D^2\gamma_w) = 4.4 \times 10^{-6}$
Figure 7.29(b)	Element states during analysis KAP02 $ktu_0/(D^2\gamma_w) = 4.4 \times 10^{-6}$
Figure 7.30	Comparison of pore pressure predictions for node 52 at the tunnel face in analyses KAP05 and KAP02
Figure 7.31	Comparison of predicted pore pressure changes with variation in κ in analyses KAP05 and KAP02
Figure 7.32	Comparison of predicted specific volume changes for variation in κ in analyses KAP05 and KAP02
Figure 7.33	Influence of κ on the specific volume of element 25 in analyses KAP05 and KAP02
Figure 7.34	Total and effective stress paths for different κ values in finite element analyses
Figure 7.35	Comparison of pore pressure changes to illustrate the influence of the stiff elastic elements
Figure 7.36	Comparison of specific volume changes to illustrate the influence of the stiff elastic elements
Figure 7.37	Comparison of effective stress paths to illustrate the influence of the stiff elastic elements
Figure 7.38(a)	Comparison of predicted pore pressure behaviour at element 65 in front of a typical transducer (element 66)
Figure 7.38(b)	Comparison of predicted pore pressure behaviour at element 47 in front of a typical transducer location (element 66)
Figure 7.39	Comparison of specific volume changes at elements in front of a typical transducer location (element 66)
Figure 7.40	Comparison of the total and effective stress paths predicted at element 65
Figure 7.41	Comparison of pore pressures predicted for node 52 at the tunnel face with and without a stiff ring
Figure 7.42	Comparison of pore pressure response to illustrate the effect of modelling pore pressure transducers as a stiff ring
Figure 7.43	Comparison of predicted and experimental pore pressure behaviour close to the tunnel face
Figure 7.44	Comparison of predicted and experimental pore pressure responses at r/r_0 of about 1.6 and 2.2 perpendicular to the central axis

- Figure 7.45 Comparison of predicted and experimental pore pressure responses ahead of the tunnel face
- Figure 7.46 Experimental and predicted deformation of the tunnel face in terms of dimensionless groups
- Figure 7.47 Experimental and predicted deformation of the tunnel face in terms of dimensionless groups

ACKNOWLEDGEMENTS

My time as a member of the Geotechnical Engineering Research Centre has been both interesting and enjoyable, and I am indebted to Professor J.H. Atkinson for the opportunity to join the Centre. I would like to thank my supervisor, Dr. R. Neil Taylor for being an unfailing source of advice and encouragement; I have benefitted greatly from the many interesting discussions. His generosity in giving so freely of his time, during both the experimental and written stages of this project, is highly valued. Dr. R.J. Mair has given very valuable advice and comments and his continued interest in the project is greatly appreciated. The helpful comments made by Sir A.M. Muir Wood are also appreciated. Many thanks are due to Dr. A.M. Britto for his advice and assistance with use of the finite element program, CRISP. My thanks also go to Dr. M.R. Coop and Miss S.E. Stallebrass for their interest and friendship, and in particular to the latter for her comments on the manuscript.

Physical model testing is inevitably a time consuming and repetitive process. I am particularly grateful to the technical staff of the research centre, Mr. K. Osborne and his assistants Messrs. G. Nash, L. Martyka, J. Wathen and A. Harland, who skillfully manufactured numerous pieces of equipment, and who always assisted patiently and cheerfully in the more laborious and backbreaking tasks of model testing. I am also grateful to Miss R.A. Pearce for typing the draft manuscript.

I am grateful to the Cambridge Soil Mechanics Group for the loan of the apparatus used in the model tunnel tests. During my studentship I was financially supported by the Science and Engineering Research Council.

I would like to thank Jill and Sue for their generosity in providing a quiet space, and Dr. W. Powrie for his friendship and interest in the project. My special thanks are due to Carol for her continual support and friendship, and to my sister and father for their patience and encouragement.

DECLARATION

I grant powers of discretion to the University Librarian to allow this dissertation to be copied in whole or in part without further reference to me. This permission covers only single copies made for study purposes, subject to normal conditions of acknowledgement.

ABSTRACT

Several aspects of the ground response to tunnel excavation in deep clay formations have been studied. Such strata may be only lightly overconsolidated and an unsupported tunnel could have a high stability ratio. Consequently, at large depths there may be construction difficulties similar to those encountered in soft ground at shallow depths. Problems which may be encountered are squeezing ground, i.e. a continually increasing volume loss with time, and possible collapse after a 'stand-up' time.

A range of parameters likely to influence the time dependent deformation behaviour at an unsupported tunnel face was investigated in a number of small scale model tunnel tests. The tests were performed in large cylindrical samples of kaolin clay under axisymmetric conditions, with measurement of tunnel face displacement and pore pressure changes in the clay.

After removal of the tunnel face support, soil intruded into the tunnel at a rate which gradually increased with time until a constant rate was reached. The steadily increasing deformation was frequently associated with increasing pore pressures close to the tunnel face as water flow occurred towards the tunnel face due to the changed boundary conditions. Two parameters, the initial pore pressure in the soil and the initial load factor, were shown to have a major influence on the time dependent behaviour, and were incorporated into a new deformation time factor.

Initial undrained pore pressure changes caused by the removal of tunnel face support have been compared with simplified closed form solutions for the thick cylinder and thick sphere analogue. As a result two zones were identified at the tunnel face, in which either approximately cylindrical or spherical behaviour was observed.

The small scale tests were modelled numerically using the finite element program CRISP. Elasto-plastic soil behaviour and consolidation were included in the analyses. Although the predictions were affected by the complex geometry and boundary conditions of the model tests, the mechanics of the time dependent deformations were demonstrated. Deformations at the tunnel face were poorly predicted and pore pressure changes were confined to smaller zones than in the model tests. However, comparisons of the finite element predictions and the closed form solutions for the plastic zone were more favourable. Longer term pore pressure predictions showed only limited agreement with the experimental behaviour.

For both the model tunnel and thick cylinder, CRISP predicted localized zones of softened soil close to the unsupported boundary which developed over a very short time period. The rapid local drainage implies that time dependent movements will be observed which are governed by changes in pore pressure and water flow.

LIST OF SYMBOLS

a	current radius of tunnel
b	radius of model sample
c	radius of plastic zone
c_u	undrained shear strength
c_v	coefficient of consolidation
d	distance behind or ahead tunnel face for water content samples
e	void ratio
g	vertical distance from tunnel face to centre of porous stone in pore pressure transducer
h	horizontal distance from tunnel central axis to centre of porous stone in pore pressure transducer
Δh	head of water driving seepage flow
i	hydraulic gradient
k	coefficient of permeability
l	distance
m_v	coefficient of volumetric compressibility
n	scaling factor
n_f	scaling factor in finite element analyses
p	mean normal total stress $[(\sigma_1 + \sigma_2 + \sigma_3)/3]$
p'	mean normal effective stress $[(\sigma'_1 + \sigma'_2 + \sigma'_3)/3]$
p'_C	value of p' at intersection of Cam-clay yield locus with critical state line
p'_p	preconsolidation pressure
q	deviator stress $(\sigma_1 - \sigma_3)$
r	distance from central point of tunnel face
r_0	tunnel radius
t	time
u	pore pressure

u_0	initial pore pressure
\dot{u}	change in pore pressure at removal of tunnel face support pressure
v	apparent velocity of water flow
v	specific volume
C	cover or distance between radius of sample and outer radius of tunnel
D	tunnel diameter
E'	Young's modulus in terms of effective stresses
K_0	coefficient of lateral earth pressure at rest
K'	bulk modulus in terms of effective stresses
K_w	bulk modulus of water
LF	load factor (N/N_{crit})
N	stability ratio
N_{crit}	stability ratio at which plastic radius, c , equals radius of sample, b
OCR	overconsolidation ratio in terms of mean normal effective stress
OPG	overall pressure gradient (between tunnel face and drainage plates)
P	length of tunnel heading
T_v	time factor in pore pressure dissipation
T_δ	deformation time factor
c	saturated bulk unit weight of soil
γ_w	unit weight of water
$-\kappa$	gradient of swelling line in $v : \ln p'$ space
$-\lambda$	gradient of compression line in $v : \ln p'$ space
ν'	Poisson's ratio in terms of effective stresses
$\sigma'_1, \sigma'_2, \sigma'_3$	principal effective stresses
$\sigma'_r, \sigma'_\theta$	radial and circumferential effective stresses in a thick cylinder
σ'_v	normal effective stress in vertical direction

ϕ'	effective angle of friction
ϕ'_{cs}	effective angle of friction at critical state
Γ	value of specific volume at $p' = 1\text{kPa}$
M	critical state frictional constant

CHAPTER 1. INTRODUCTION

1.1 Background to the dissertation

Tunnel construction is increasingly used as a possible solution to a number of problems being addressed by the civil engineering profession. For example in developed countries tunnels are frequently used to provide for public services. Regional development and economic growth has increased the pressure on the existing transport network and utilities, often resulting in the need to expand services with the adoption of the tunnelling solution to avoid further land take and to minimise surface disruption in urban areas. As a consequence, significant research has been conducted in recent years to study some of the difficulties of tunnelling at shallow depths in soft ground and to develop a better understanding of the mechanics involved.

A less common possible use for tunnels has arisen from the need to develop an acceptable means for long term storage and disposal of toxic and radioactive wastes. Although tunnel construction is a proven solution for a transportation problem, its applicability to the problem of radioactive waste storage has not yet been established. Such a development might involve a tunnelled repository in deep clay or rock formations. The principal aim of any storage facility is to isolate the high level radioactive material from the biosphere for about 10,000 years, a length of time two orders of magnitude greater than the design life of most civil engineering projects, Bohlke and Monsees (1988). Clay is thought to be a suitable host medium for the

storage of radioactive materials since it has some desirable properties such as a very low permeability which reduces the risk of contamination of the human environment by water flow from the storage area. It has also been found to provide an effective barrier against the migration of radionuclides due to sorption on argillaceous particles, Hudson and Boden (1982).

In the U.S.A. and Canada research is directed towards the construction of repositories in rock, with the development of a multiple barrier system which includes a clay based buffer and backfill to ensure isolation of the radioactive material, Lopez et al (1984). These repositories or vaults are likely to be at depths of 500m - 1000m and may extend for areas of 1400-4000 acres. Developments of this type are envisaged at these considerable depths since the waste material will then be removed from the human environment, and contained in a host medium of competent plutonic rock such as granite or sedimentary rock, for example salt or shale. Other factors including transportation, population and hydrology also need to be taken into consideration in the selection of the most suitable site. In Canada it is envisaged that a major repository is likely to be needed early in the 21st century, based on the present growth in demand for electricity.

Research into the difficulties associated with the design and construction of repositories in deep clay formations has been actively pursued by Studie Centrum voor Kernenergie (SCK)/Centre d'étude de l'Energie Nucléaire (CEN) at Mol in Belgium since 1974. In contrast with the hard rock options, there has been very little experience with excavation in deep clay. The research therefore has taken the form of

a full scale experimental laboratory constructed at a depth of 220m in the Boom Clay below the nuclear energy research establishment, with a view to developing the site for radioactive waste storage in the future, Manfroy et al (1987). Various factors such as the volume of waste to be stored (Belgium produces about 60% of its electricity from nuclear reactors), difficulties in finding another suitable location at or below surface and the advantages of developing the site at Mol without the need for a public inquiry have led to the continued development of this project. In the U.K. formations which might be suitable for repository construction are the Gault Clay and Oxford Clay at depths of about 400m, Hudson and Boden (1982).

1.1.1 Research at Mol

At Mol the Boom Clay lies between 188m and 280m below ground level, and is overlain by saturated sand and gravel. The experimental facility has been constructed in a number of stages, and a section through the facility is shown in Fig. 1.1. Construction commenced in October 1980 with the 227m deep, 4.3m diameter access shaft, Funcken et al (1983). Ground freezing techniques were used to advance the shaft through the sand and gravel, and remained in use when the shaft progressed into the clay since the difficulties likely to be experienced in excavations in clay at such depth were unclear at that stage. Problems were encountered when the shaft had been extended some 20m into the clay. The lowest metre of the concrete lining cracked in compression several days after the shuttering was removed. Convergence measurements showed that the excavation was closing in at a rate of the order of several centimetres per day and the lining stresses measured were in excess of the overburden pressure. The

shaft was eventually completed early in 1982 after some modifications to the design had been carried out. Although it was recognised that the difficulties with the large movements and high pressures acting on the shaft lining were the result of the ground freezing, the connecting chamber and the underground research laboratory were also excavated in frozen ground, with more stringent techniques being adopted, since a high creep rate was anticipated from the unfrozen clay. The underground research laboratory, 36m long and 4.5m excavated diameter, was constructed during 1983. Data from the instrumentation installed prior to the excavation are of limited value in the assessment of any difficulties that may occur on construction of a tunnelled repository in unfrozen ground. Construction of a repository of the scale indicated in Fig. 1.2 in frozen ground would not be feasible on an economic basis.

After completion of the underground research laboratory a preliminary investigation was carried out to assess the behaviour of unfrozen clay during and after excavation. This involved sinking a smaller diameter vertical experimental shaft (2.1m external diameter) from the end of the gallery, as shown in Fig. 1.1, for a distance of 23m, the first 8m to 10m of which passed through the zone directly affected by ground freezing. A small experimental drift of the same diameter and about 7m long was subsequently excavated from the base of this shaft. The shaft and drift were hand dug and lined with small concrete segments separated by wooden plates. The face of the small drift was left unsupported and has shown 200mm axial movement since its completion in 1984. It has also been noted that blocks of clay have fallen in from the face and "fissures" are clearly visible, which may be the result of high shear stresses at the face on excavation. Boom clay has shown

some slightly brittle characteristics at failure in triaxial compression tests. Data from the small diameter excavations are very limited but some displacement measurements were made close to the excavation and are discussed later in Section 1.2.1.

In 1987 a 4.7m diameter 52m long test drift was constructed in unfrozen clay, Beaufays et al (1987), at the same depth as the gallery, but in the diametrically opposite direction, as shown in Fig 1.3. The test drift has been used to assess the performance of two different types of lining. For the first 40m the excavation was lined with 0.60m thick concrete segments, whereas sliding steel ribs were used for a further 12m. The face (or front) of the excavation has been protected by a 150mm thick layer of shotcrete but is otherwise unsupported. A number of the lining rings were instrumented with convergence bolts, load cells and Gloetzel pressure cells. Piezometers were also installed to measure the pore pressure response to the excavation. An extensometer was installed shortly after excavation to monitor subsequent movements, and displacement of the shotcreted face has also been recorded.

Results from the lining instrumentation indicated that the lining loads had increased to between 30% and 50% of the overburden pressure, and were rising very slowly some months after construction. The piezometers recorded very substantial pore pressure reductions during excavation, which rose steadily towards new equilibrium values after the lining had been placed. Data from the extensometer showed that the movement around the excavation varied with the reciprocal of the radial distance from the tunnel axis. Movements of the order of 5mm were measured at the face over a period of about two weeks.

1.1.2 Small scale model tests related to the Mol experiment

At the time of the main shaft excavation at Mol a research contract funded by the Department of the Environment was initiated, as part of the U.K.'s research programme for radioactive waste storage, to investigate the principal phenomena observed in deep tunnel construction. The intention was to develop an understanding of the behaviour which would allow the data from the experimental work at Mol to be extrapolated to sites in the U.K. The research proposed involved a series of small scale lg model tunnel tests to investigate the parameters controlling the behaviour during and after the construction of a tunnel in deep clay formations; these model tests are the subject of this dissertation.

At shallower depths, problems with tunnel construction are sometimes related to the time dependent movements of soil at an unsupported tunnel heading. Such behaviour is sometimes referred to as "squeezing ground" or "tunnel squeeze", and as at Mol, is often attributed to viscous properties of the soil. However the mechanics controlling such behaviour are not well understood, and it was thought that similar problems might occur at greater depths, thereby indicating a need for clarification of this phenomenon.

The small scale model tests were developed specifically to investigate the parameters controlling the time dependent behaviour of an unsupported tunnel face at stress levels equivalent to those in deep clay deposits, and to gain a better understanding of the mechanics involved. Some research has already been completed in the investigation of shallow tunnel behaviour by means of small scale

model testing either at 1g or on a centrifuge. The findings of the earlier research relevant to this investigation are discussed and reviewed later, together with a brief description of appropriate methods of numerical modelling.

After this introductory chapter, some general model testing principles are outlined and the experimental work is described in Chapter 2, with details of some modifications to the apparatus and model testing techniques. Typical test data are presented and discussed in Chapter 3. Models of soil behaviour relevant to the phenomena observed in the small scale tests, and the parameters required to allow analyses to be performed are considered in Chapter 4. Some aspects of the model tunnel tests have been analysed using simplified theories in Chapter 5, and have been modelled numerically using the finite element method in Chapters 6 and 7. It will be concluded that the time dependent behaviour of an unsupported tunnel face has been shown, by both physical and numerical modelling, to be a function of the initial stress state, stress level and factor of safety, and the subsequent changes in effective stress with time. Initial pore pressures have a major influence on the rate at which the effective stress reduces or the clay softens and hence on the rate at which deformation of the tunnel face develops.

1.2 Behaviour of tunnels in clay

The class of behaviour observed during and after tunnel construction is principally due to the stress state and stress history of the clay through which the tunnel is driven. Other factors such as the tunnelling method employed and the standard of workmanship are also

significant. Various references will be made to research in soft ground tunnelling and therefore it is necessary to define the meaning of the term soft ground as it has been used in the references. The conditions implied by this term are such that a tunnel face or heading must be supported during construction since otherwise it would become unstable. These conditions are likely to prevail where the clay is normally consolidated or lightly overconsolidated. At a later stage the permanent lining is erected to support the ground. For more heavily overconsolidated or stiff clays, where the undrained shear strength of the clay is greater than that of the normally consolidated soil under comparable effective stresses, the excavation remains stable for a sufficient length of time to allow the permanent lining to be erected. Such soil conditions have been referred to as firm ground, Peck (1969).

1.2.1 Undrained behaviour

A substantial amount of research over the last few years has been devoted to the investigation of the mechanics of shallow tunnel behaviour, particularly in soft ground conditions. Although the results obtained from that research are not directly applicable to the subject of this dissertation, a brief description of the research is included since it provides a useful framework within which tunnelling terminology may be defined and comparisons between shallow and deep tunnels can be made.

Small scale model tunnel tests on a centrifuge were performed by Mair (1979) to study the mechanics of tunnel construction in clay under undrained conditions. Undrained in this context implies that the rate

of construction is rapid relative to the rate of pore pressure dissipation and that no changes in water content or undrained strength occur during this time. An analysis of the problem in terms of total stresses would also be possible under these conditions.

The tests performed by Mair demonstrated the influence of tunnel geometry on stability and ground movements in terms of C/D and P/D, where C is the cover or distance from ground surface to the tunnel crown, D is the tunnel diameter and P is the length of heading given temporary support; these parameters are illustrated in Fig. 1.4. The value of P/D influences the nature of the deformations around the heading. If P/D is large then a large proportion of the movements occurring are radial and perpendicular to the tunnel axis, whereas if $P/D \approx 0$ the movements are three dimensional and a considerable percentage of the movements occur axially at the face. A basic parameter used in assessing the undrained stability of a tunnel heading is the stability ratio N, first defined by Broms and Bennermark (1967) and given by Mair as

$$N = \frac{(C + D/2)\gamma - \sigma_T}{c_u} \quad 1.1$$

which may be rewritten

$$N = \frac{\sigma'_{ax} + u_{ax} - \sigma_T}{c_u} \quad 1.2$$

where C = cover
D = tunnel diameter
 γ = bulk density

- σ_T = tunnel support pressure
- c_u = undrained shear strength
- σ'_{ax} = vertical effective stress at tunnel axis
- u_{ax} = pore pressure at tunnel axis

Deformations increase in magnitude with increasing stability ratio until a failure point is reached. In his model tests Mair decreased the tunnel support pressure until the heading collapsed. This allowed the critical stability ratio (N_{crit}) at which collapse occurred to be determined, which was shown to be strongly dependent on the values of C/D and P/D. The maximum value of C/D in these tests was three, for which N_{crit} was nine for P/D of zero. These findings are summarized in Fig. 1.5.

Although N may give an indication of the stability of the heading in terms of the possible magnitude of ground movements to be anticipated, the load factor is a measure of the closeness to collapse of the heading. Load factor was defined by Atkinson and Potts (1977) as

$$LF = \frac{1 - \sigma_T/\gamma z}{1 - \sigma_{Tf}/\gamma z} \quad 1.3$$

where σ_T = tunnel support pressure

σ_{Tf} = tunnel support pressure at which undrained collapse would occur

z = $C + D/2$

In terms of stability ratio, load factor is given by

$$LF = \frac{N}{N_{crit}} \quad 1.4$$

where N = actual stability ratio

N_{crit} = stability ratio at undrained collapse

Load factor may be considered to be the reciprocal of a factor of safety and is a more appropriate parameter to use when comparing the behaviour of two tunnels at different depths, each with the same N value. If the two values of N_{crit} are not the same then one tunnel will be closer to collapse than the other. As the load factor tends towards unity the excavation approaches undrained collapse. A clear indication of the increase in volume loss with increasing load factor under undrained conditions is shown in Fig. 1.6 for tunnels of relatively low C/D ratios. A positive volume loss is defined as the volume of excavated material greater than the volume of the tunnel divided by the volume of the tunnel.

As the tunnel support pressure was lowered in Mair's model tests the collapse mechanisms associated with particular geometries also became apparent, and were subsequently analysed using upper and lower bound solutions from plasticity theory. It was noted that for the deeper model tunnels, i.e. $C/D \geq 3$, the development of a fully plastic zone from the crown to the upper surface of the sample could not be assumed and that an approximately axisymmetric plastic zone developed around the tunnel. This led to the lower bound solution also being on the unsafe side. These statements about shallow tunnel behaviour may also

be applied to deep tunnels although a number of modifications need to be taken into account.

The influence of the proximity of the ground surface on deformation patterns for shallow and deep tunnels was given by Mair in discussion at the British Geotechnical Society (De Moor, 1987), and is shown in Fig. 1.7. A 'block' movement occurs for the small C/D values and the magnitude of the movement is not reduced with distance from the tunnel, whereas the displacement varies with the reciprocal of radius from the tunnel axis for the deeper case. Although the 'block' type of collapse mechanism is not possible for the deep tunnel, collapse of the tunnel face may occur locally. The more axisymmetric behaviour around deeper tunnels ($C/D \geq 3$) has been demonstrated by extensometer data from the experimental drift at Mol, where C/D was in excess of 40. The data in Fig. 1.8 show that displacements above the crown of the tunnel varied inversely with radius from the tunnel axis, which is as expected under constant volume axisymmetric conditions. Such movements occur irrespective of elastic or plastic soil behaviour.

The definition of collapse for deep tunnels is unclear and leads to difficulties in determining an appropriate value for N_{crit} . A simplified analysis, which is discussed in Chapter 5, allows a value for N_{crit} in the model tests to be estimated. No clearly defined collapse mechanism or point of failure is observed, since the tunnel heading steadily becomes filled with plastically deforming soil, which in itself provides some support and stabilizes the tunnel face to some extent.

Stability ratio for deep tunnels is defined in the same manner as for the shallow case. It should also be noted that whereas the stress levels vary significantly between crown and invert in a shallow tunnel, the variation may be assumed to be negligible for the deep situation. Comparison of the in situ stress states for shallow and deep tunnels indicates that there may be other similarities in behaviour. At great depth the overconsolidation ratio due to the erosion of overburden is likely to be low. Based on geological evidence the Boom clay formation in the vicinity of Mol, Schittekat et al (1983), would appear to be only lightly overconsolidated with a correspondingly high stability ratio. Consequently deep tunnels may be expected to encounter undrained stability difficulties similar to those of shallow tunnels in soft clays.

Undrained movements have been shown to be inevitable as a function of the undrained shear strength, an undrained stiffness modulus and of the changes in total stress at the time of excavation, De Beer and Buttiens (1966). Other movements occur simultaneously as a result of the tunnelling procedure and the quality of workmanship, although in squeezing ground it is difficult to distinguish between the two causes, except in cases where a clearly inappropriate method of excavation has been adopted.

1.2.2 Time dependent behaviour

Deformations occurring with time (squeezing ground) at an unsupported excavation may be considered to be due to either of two different classes of behaviour. Dissipation of excess pore pressures caused by excavation or any loading increment (primary consolidation) is

followed by creep or secondary consolidation, in which the deformation increases linearly with the logarithm of time at a constant effective stress level. Creep in this case is a phenomenon associated with much longer time periods than primary consolidation. Keedwell (1984) attributes the creep behaviour of soils to the viscous nature of the interparticle contact zones as a result of the very high stresses at these points. For viscous materials the strain rate is dependent on the shear stress level. In non-linear viscosity strains may be related to the stress level by a power law, an exponential function or a hyperbolic sine function, and to time by either a power law or a logarithmic law.

Alternatively the movements have been considered to be entirely due to the viscous properties of clay. The description of soil behaviour as a viscous material may include the assumption that soil is a one phase medium, Gioda (1982), and leads to the development of a range of stress-strain-time functions which are not based on any fundamental soil parameters.

A series of model tests were performed by Myer et al (1977) to study the relationship between tunnel diameter, rate of advance and 'stand-up' time. It was anticipated that the time dependent movements were due to a viscous characteristic of soil. Consequently a material consisting of sand and wax was used to model the squeezing ground phenomenon, and the observed behaviour was necessarily described by a visco-plastic constitutive equation.

Model tunnel tests in clay have also been used to investigate the time dependent movements resulting from an excavation event. Seneviratne

(1979) investigated the deformations around a shallow tunnel and at the ground surface as the support pressure was reduced though not sufficiently to induce undrained collapse. Yielding of the normally consolidated clay caused excess pore pressures to be generated, which dissipated with drainage towards the surface of the model. An impermeable tunnel lining was modelled in these tests. Surface settlement increased appreciably during the consolidation period. Seneviratne's consolidation tests results are not appropriate to this investigation since the pore pressure conditions were not controlled and seepage flow towards the tunnel was not modelled.

Taylor (1984) conducted model tests on a centrifuge to study the time dependent deformations of a structurally unsupported shallow tunnel. Situations where the tunnel heading collapses after being unsupported for a time are described as 'stand-up' problems. 'Stand-up' time refers to the period of time for which the tunnel section remains stable after excavation. Assessment of the 'stand-up' time is particularly difficult since the soft ground deforms continuously without having a clear failure point. Taylor identified the influence of changes in effective stress, due to dissipation of pore suctions caused by excavation, on the 'stand-up' phenomenon. No clear statements were made concerning the importance of specific soil parameters to the observations. The mechanics of squeezing ground may, in principle, be applied to the deep tunnel case, with further research required to assess the influence of the relevant soil parameters and the magnitude of the pore pressure gradients close to the tunnel face.

Field observations of the 'stand-up' phenomenon are scarce since tunnel headings in soft ground are not commonly left unsupported. Rebull (1972) reported a case of an unsupported tunnel face in which the deformations varied linearly with the logarithm of time as also observed by Taylor (1984). Rebull considered the tunnel heading in terms of spherical consolidation and found that the observed rate of movement coincided with the theoretical curve initially, but then deviated from the section of the theoretical curve which predicted a reducing rate of settlement. The field observations showed a continued steady rate of deformation, as expected from the difference in boundary conditions applicable to the theoretical and field situations.

Terzaghi (1936) reported variations in the water content of the soil surrounding a tunnel excavation. Close to the tunnel boundary the water content had increased significantly above the in situ value. The softened zone was surrounded by soil of reduced water content, i.e. less than in situ, indicating the region from which the water had migrated.

For lined tunnels the lining load has been shown to increase linearly with the logarithm of time, a similar form of relationship to that for displacement considered earlier, Peck (1969) and Farmer (1978). Unfortunately the relationship is often interpreted as being similar to creep or secondary consolidation. Farmer, however, considered that such behaviour was due to the consolidation of the surrounding soil. Clough and Schmidt (1981) also related the increase in lining loads with the process of pore pressure dissipation, assuming the lining to be watertight.

1.3 Modelling of Tunnel Behaviour

1.3.1 Physical modelling

Model testing techniques for tunnels either on a centrifuge or in a laboratory have become well established through years of development. Tests on the centrifuge were particularly appropriate for the shallow tunnel investigations where a linearly increasing stress distribution with depth was required to achieve similarity between model and prototype. Appropriate modelling of the stress distribution allows the soil in the model to be subjected to the correct effective stress paths so that the most representative response is observed. For deep tunnels the stress distribution may be assumed to be uniform for some small distance from the tunnel boundary, i.e. not significantly affected by the presence of the ground surface, in which case the problem can most readily be modelled at 1g in the laboratory by application of uniform boundary stresses to the model.

Small scale model tests may be conducted for a variety of purposes, Taylor (1987). Investigations where interest is directed towards the mechanics of soil behaviour and geotechnical structures are known as mechanistic studies. These may indicate new modes of failure without the risk or expense involved in carrying out field studies. Parametric studies allow the importance of various parameters over a suitable range of values for a particular geotechnical structure to be assessed. The most significant parameters are often combined in non-dimensional groups for design purposes. The model tunnel tests performed by Mair (1979) are an example of such a study.

Widespread availability and use of computers in geotechnical engineering has led to the development of more advanced computer programs to model geotechnical problems. A frequently used means of numerically modelling a geotechnical structure is the finite element method, which allows problems which are complex both in terms of soil behaviour and geometry to be analysed. Such programs must be tested against reliable experimental or field data to determine the accuracy of their predictions. Model tests are performed on samples under carefully controlled conditions with known stress states and stress histories, and therefore provide high quality data for checking numerical predictions. Tests carried out for this purpose are known as numerical validation studies.

Small scale testing for any of the studies discussed above has a number of benefits, such as being much less costly than undertaking full scale trials, the ability to take the model to failure and the much shorter time period required to produce results. Events which might take months or years to occur at prototype scale may be observed in a few minutes in the model test. Details of the scaling laws for model testing which allow comparisons between model and prototype to be made are discussed in Section 2.2.2.

The small scale tests described in this dissertation were designed to investigate the mechanics of squeezing ground as well as being a parametric study to investigate how the response changed with a variation of significant parameters. Time dependent effective stress changes caused by the dissipation of excess pore pressures, and the effect of these on the deformation observed at the tunnel face are of primary importance in modelling tunnel behaviour for this research.

1.3.2 Simplified analytical modelling

Numerical modelling and predictions of tunnel behaviour for design purposes and post construction analyses are often based on empirical relationships or assumed and much simplified conditions. Deformation (both at surface and subsurface) associated with tunnel excavation is usually the parameter of foremost concern, whereas the influence of the pore pressure is generally not given the same attention. The magnitude of deformation is a function of the soil strength and its stress-strain response, as well as the in situ stress levels and the tunnelling procedure.

A common method of tunnelling involves excavation with a tunnel boring machine and shield, in which the lining is also erected. An overcutting bead, fixed to the outer surface of the machine or shield to facilitate steerage, results in some radial deformation. Another source of radial deformation may be due to the void which exists between the excavated diameter and that of the lining, particularly where expanded linings are not used, as shown in Fig. 1.9. The void is subsequently grouted, and the component of radial deformation developed is a function of the standard of workmanship.

Ground movement ahead of the face may have both radial and axial components, also illustrated in Fig. 1.9, which may be minimized by the use of an appropriate tunnelling method. For shallow tunnels estimates of the surface settlement are based on the assumption that the surface settlement trough is of a Gaussian distribution form. The volume of the settlement trough is empirically related to the volume of soil excavated, which includes the effect of workmanship.

Predictions based on analytical solutions necessarily cannot incorporate the effects of construction methods and are based on the stress relief anticipated.

In heavily overconsolidated clays radial displacement at the crown of deeper tunnels, or at any radius, can be calculated from the solution for a circular opening in an elastic infinite medium for the imposed stress changes, Lo et al (1984). For normally consolidated or lightly overconsolidated soils a plastic zone is developed around the tunnel due to the excavation. Plastic deformations are obtained by idealizing the in situ conditions to be axially symmetric and plane strain, Fig. 1.10. The tunnel may be represented by a cylindrical cavity in an infinite isotropic medium, allowing only radial components of deformation to be calculated. The behaviour of the material is assumed to be undrained and elastic-perfectly plastic to allow a closed form solution to be obtained.

This simplified approach is analogous to the thick cylinder analysis or cavity expansion where an internal pressure change is applied, and has been adopted by Lo et al (1984) and De Beer and Buttiens (1966) to determine displacements and critical stresses at the tunnel boundary in an infinite medium. The model tunnel tests undertaken, and described in Chapter 2, represented a simplified excavation process involving radial and axial deformation only at the tunnel face. Axial symmetry was imposed by the cylindrical sample and an isotropic stress state applied without the condition of plane strain. The thick cylinder closed form solution provides a distribution of radial and circumferential stresses as well as displacements, throughout the plastic zone. For an undrained elastic-perfectly plastic material

pore pressure changes at the removal of the face support can be predicted directly from the total stress reductions. Calculation of the undrained displacements is not appropriate for the model tests, since cylindrical radial movements were not measured.

Two parameters, stability ratio and undrained shear strength, have a major influence on the total stress changes, and careful consideration is required in determining suitable values for them. Davis et al (1980) considered two lower bound stress fields around a tunnel heading, as illustrated in Fig. 1.11(a). For the first of these the volume of soil ahead of the cylindrical cavity is treated as an extension of the excavation in terms of the total axial (minor principal) stress, and is equal to the tunnel support pressure, σ_T . Radially, in planes perpendicular to the tunnel axis the major principal stress is equal to $\sigma_T + 2c_u$. The tunnel heading is secondly considered with a hemispherical cap at the tunnel face, as shown in Fig. 1.11(b). An isotropic stress field σ_T exists within the hemisphere.

The spherical representation can be formulated in a thick sphere solution similar to that of the thick cylinder, and may be more appropriate to the problem of the model tunnel face where conditions of plane strain cannot develop. It is assumed that the flat circular surface of the face is adequately represented by a hemisphere, and that the stress distribution is radial in all directions from the centre of the sphere. The thick sphere analogue is not commonly used in tunnel analyses. However, it does have applications in metal forming processes, such as the extrusion of cylindrical rods through a

conical die. Inward radial plastic flow takes place in both the metal forming process and in the model tunnel tests.

1.3.3 Finite element modelling

The finite element method is a technique frequently used to analyse complex problems involving three dimensional stress changes, which in geotechnical applications often include a time dependency. The boundary conditions and the geometry of the problem can also be more realistically modelled. Use of this method involves the discretization of the structure and the displacements and stresses to which it is subjected, which may influence the accuracy of the analysis to some extent. The principal limitations are a function of the mathematical models describing soil behaviour incorporated in the programs, and on the parameters specified to characterise the soil. Both the mathematical models and parameters are based on observations from laboratory tests with clearly defined boundary conditions and much simpler loading paths, for example the stress path tests on triaxial samples.

A finite element program, CRISP, was developed at Cambridge, (Britto and Gunn, 1987) which allows elasto-plastic analyses within the framework of critical state soil mechanics to be performed. Consolidation analyses are also possible based on Biot's coupled consolidation theory, a feature not available in many other finite element programs. Such analyses are appropriate to the investigation of time dependent movements at an unsupported tunnel face in lightly overconsolidated clay.

1.4 Objectives of the Research

From the previous discussion, it is apparent that there are a number of shortfalls particularly in terms of observations relating the mechanics of time dependent behaviour to parameters controlling that behaviour. Consequently the research objectives were identified as:

- i) to develop existing apparatus and model testing procedures to provide data on the behaviour of unsupported deep tunnel faces in normally consolidated and lightly overconsolidated clay by means of small scale model tests;
- ii) to demonstrate the importance of time dependent stress changes to the observed movements at the tunnel face;
- iii) to establish scaling relationships between the model tests to allow extrapolation to other small scale models where different conditions exist (e.g. different soil) or possibly to prototype scales;
- iv) to determine factors controlling the time dependent behaviour;
- v) to perform numerical analyses of the tests to compare the results with the test data and to assess the suitability of the numerical methods used for modelling this type of problem.

2.1 Introduction

The main apparatus in which the model tunnel tests were conducted was designed and built at Cambridge University, and is in principle similar to a hydraulic triaxial cell. Initially it had been intended to obtain indications of changes in lining loads with time by means of strain gauges bonded to the inside of the model tunnel lining. However, after two preliminary tests it was concluded that it would not be possible to produce data of any reliable quality, particularly with the strain gauge arrangement adopted. Consequently the strain-gauged model tunnel was replaced by simple model tunnels and the research then focused on an investigation of transient changes in pore pressure, associated deformations at an unsupported tunnel face and the factors controlling such behaviour.

2.1.1 Outline of model tests series

Two preliminary tests were performed to assess difficulties and to allow an appropriate testing procedure to be developed. These are described in more detail in Section 3.1.1. After the preliminary tests two series of tests were conducted and all experiments involved the tunnel face being unsupported for a period of time.

The Series I testing programme was devised as a result of observations from the preliminary tests and investigated the influence of the end drainage plates and position of the tunnel in the sample on the rate

of deformation. Series II tests were designed to clarify the dependency of rate of deformation on the initial pore pressure in the sample and the load factor, based on results from Series I. The factors to be considered in designing a series of model tests, including scaling aspects, are discussed later in this chapter. Detailed descriptions of apparatus used and experimental procedures are also provided.

2.2 Small scale modelling techniques

Scaling relationships and an understanding of their use are essential in relating model test data and events to the corresponding prototype or to other model tests. Although scaling relationships do not provide solutions or demonstrate failure mechanisms they allow data to be interpreted for extrapolation to and correlation with other situations. Similarity between the model and prototype as described by relevant scaling laws may be determined by dimensional analysis, which is discussed in more detail in Chapter 5.

If a prototype is to be modelled it is probable that not all the features of the prototype can be included in the small scale model. It becomes necessary to simplify the model, but this should only be done when it can be demonstrated that the particular feature or aspect of the model does not have a disproportionate influence on the behaviour observed. It should also be shown that the modelling technique itself does not cause significant differences in behaviour, known as scale effects, simply as a result of the scale of the test.

The development of appropriate scaling relationships requires firstly that the phenomena observed in the model tests are properly understood. This understanding may already exist or may come about as a result of the tests themselves. When the parameters influencing the behaviour have been correctly related, the parameters needed to relate models at different scales can be identified.

In considering the scale and similarity of geotechnical models an additional difficulty, arising from the dependence of soil behaviour on stress state and stress history, needs to be taken into account. The total vertical stress distribution at any point in a soil mass is dependent on the self weight of the soil and its variation will, in general, be linear with depth, assuming that there are no inclusions in the ground, for example, a tunnel. The effective stress distribution which controls the soil response and soil strength is dependent on the pore pressure as well as the total stress (both dependent on self weight), and the stress history. It is therefore necessary to create a similar stress state in the model to ensure that the stress-strain behaviour observed adequately replicates that of the prototype.

A shallow tunnel heading is an example of where correct modelling of the stress state is important. The self weight of the soil above the tunnel axis has the potential to cause an undrained collapse of the heading, and the undrained shear strength provides a resistance to such a collapse. These two factors are combined in the dimensionless parameter known as the stability ratio, N , which is used as a measure of stability. If the stress states and soil strengths were

incorrectly modelled, the value of N would also be incorrect, so that model and prototype would not correspond.

One method of modelling the correct N value in the laboratory is to apply only the self weight stresses of the model to the soil with an appropriately low strength. Such a technique could result in considerable difficulties with model preparation. Alternatively the application of surface loading to the model would result in a uniform stress distribution and an appropriate N value at the tunnel axis, provided the soil is initially in equilibrium with the boundary stresses. However, in cases where the variation with depth is important, the response observed throughout the model could not be said to correspond to the prototype due to the lack of overall similarity in stress states. A method used to model an effective stress distribution increasing linearly with depth involves a technique known as downward hydraulic gradient modelling. An increasing effective stress with depth is produced by allowing steady seepage to occur between constant high pore pressure at the surface of the model and low pore pressure at the base. A uniform total stress greater than the maximum pore pressure is applied to the model. This method is clearly not suitable where the pore pressure distributions are of interest or where the high pore pressures may dissipate horizontally towards an excavation.

All of the methods and difficulties previously discussed have been for 1g models in the laboratory. In many cases the only means available to realistically model the in situ stress states would be on a centrifuge where a model of dimensional scale factor n is subjected to an acceleration of n times earth's gravity. The stress distribution

in the model will then correspond to that of the n times larger prototype. The scaling laws then become dependent on the acceleration as well as the dimensions used.

There are some instances where centrifuge model testing would be very difficult. An example of one such case is the deep tunnel problem. Certain features of the problem make it more amenable to laboratory testing at 1g. The problem may be simplified and approximated by the assumption that the variation in stress level between the crown and invert of the tunnel is insignificant in comparison with the in situ stress level. Consequently the problem may be represented by a model in which there is a uniform stress distribution produced by a constant pressure at the model boundaries, which is equivalent to the total stress required at the tunnel axis. Uniform stress levels above and below the tunnel axis are considered to be adequate first approximations, given that the stress level at the axis is correct. It is essential in model testing that the consequences of necessary assumptions and simplifications should be fully appreciated to allow the best possible correlation between model and prototype to be made.

2.2.1 Similarity

Similarity was mentioned in the previous section as an essential requirement to allow extrapolation from model scale to prototype scale. Complete similarity can rarely be attained in a model test; however an understanding of the scaling laws will ensure that adequate similarity exists.

Geometrical similarity between the model and prototype is a fundamental requirement. Points which correspond to each other in the model and prototype are known as homologous points. Kinematic similarity may also be necessary where movements within two particular cases are being studied. Such movements can be described as being similar if similar particles are found at homologous points at homologous times. The model and prototype may then be described as being homologous systems in which two neighbouring points and times in one system can be related uniquely to two neighbouring points and times in the other system.

2.2.2 Scaling laws for different diameter tunnels

One of the objectives of this research project was to attempt to establish the scaling laws applicable to the model tests with a view possibly to permit extrapolations to prototype scales at a later stage. In order to do this a technique known as 'modelling of models' was adopted. Modelling of models refers to a procedure used to verify scaling laws determined from a series of tests which have been conducted as a mechanistic study or a parametric study. For instance, in centrifuge model testing different model dimensions and accelerations would be used such that each model would correspond to the same prototype, and even if no such prototype exists they would provide a check on the modelling technique used and the scaling laws adopted.

Under 1g conditions the modelling of models technique is more difficult to use successfully. An apparatus used for one particular scale of model test cannot be used to model another scale exactly.

Hence a different apparatus must be used, ideally one which is a scaled replica of the first apparatus. For this investigation such a replica was unavailable though a standard 100mm triaxial cell was modified to model some of the early model tunnel tests. Full details of these tests are given by Baker (1987) and a number of the results are presented in Section 5.3.2.

If it is considered that the scaling laws are functions of the dimensions involved, an alternative form of 'modelling of models' may be to use the same apparatus but with at least three different model tunnel diameters, provided the sample diameter does not affect the response. The influence (if any) of the various sample diameter/tunnel diameter ratios should then be identified and data for three different scales obtained. This method was adopted for the main test series.

The scaling law between linear dimensions is simply

$$l_m = l_p/n \quad 2.1$$

where n = the scale factor

l_m = model dimension

l_p = prototype dimension

The subscripts m and p will be used to denote model and prototype.

If the model and prototype are similar then the stress levels at homologous points should be identical. In cases where the flow of water through the sample is an important feature, the influence of the

geometrical scale factor on the rate of flow must be established. The apparent velocity of water, v , permeating the given soil is related to the permeability, k , and hydraulic gradient, i , in Darcy's law given by

$$v = ki \quad 2.2$$

Since the pore pressures or heads of water are the same at geometrically similar points, the hydraulic gradient will be n times greater in the model than in the prototype, hydraulic gradient being defined as the loss of head over unit distance. Returning to Darcy's law, it can be shown that

$$v_m = \frac{n k_m v_p}{k_p} \quad 2.3$$

and hence the apparent velocity of water in the model is n times greater than in the prototype, assuming that the permeabilities of the model and prototype soils are the same. The water travels between two geometrically similar points such that

$$l_m = v_m t_m \quad \text{and} \quad l_p = n l_m = \frac{v_m t_p}{n} \quad 2.4$$

from which it can be shown that

$$t_m = \frac{t_p}{n^2} \quad 2.5$$

i.e. the scale factor for steady seepage is n^2 .

In situations where a time dependency exists such as in pore pressure dissipation, homologous dissipation times for model and prototype are related by the dimensionless time factor, T_v , defined as

$$T_v = \frac{c_v t}{l^2} \quad 2.6$$

where c_v = coefficient of consolidation

t = time

l = length of drainage path (scaled)

Hence

$$\frac{c_{vm} t_m}{l_m^2} = \frac{c_{vp} t_p}{l_p^2} \quad 2.7$$

and

$$t_m = \frac{1}{n^2} \frac{c_{vp}}{c_{vm}} t_p \quad 2.8$$

If it is assumed that c_{vp} and c_{vm} are the same, then for a linear scale factor, n equal to 100, it can be shown that a model time of one minute is equivalent to a prototype time of 6.9 days. Knowledge of the scaling laws is necessary for use at a later stage in the dimensional analysis of the data to establish appropriate non-dimensional groups.

2.3 Apparatus

2.3.1 Introduction

Model testing for a parametric or mechanistic study allows a range of stress states to be chosen for convenience and therefore it was not considered necessary to model stress levels equivalent to those at a depth of 220m at Mol. It was anticipated that dimensionless

parameters would be established which may allow data to be extrapolated. The triaxial apparatus available for performing the model tests was therefore quite adequate in that it allowed a total stress of 2MPa to be applied, which is equivalent to an overburden depth of about 100m. A further simplification was introduced by the application of isotropic stresses to the samples. However isotropic conditions are likely to be a close approximation to the in situ stress states since K_0 is approximately unity for an OCR of about 2.5. Although the geological evidence referred to in Chapter 1 indicated that the Boom clay at Mol was only lightly overconsolidated, it was suggested by Horseman et al (1987) that the clay has an apparent OCR of about 2.5. Therefore the simplified isotropic stress state, imposed on the model tests as a function of the apparatus, may be a reasonable representation of that existing in the ground (for clays of this age and depth).

2.3.2 Triaxial apparatus

The model tests were carried out in a large diameter apparatus which is illustrated in Fig. 2.1. It can contain a 250mm diameter, 600mm long sample, which is stressed by a pressure applied to the cell fluid (water). Radial and axial stresses are applied to the sample by the pressurised cell fluid in the cylinder and the base piston, the pressure being controlled by a regulated compressed nitrogen supply via the cell pressure burette. A latex rubber membrane is clamped inside the aluminium alloy cylinder, separating the cell pressure fluid from the sample. The aluminium alloy piston moves inside a nickel plated steel housing in which a central guide rod acts as an end stop, as well as preventing the piston from rocking and binding

inside the housing. A Bellofram rolling rubber diaphragm has been used in the piston for the pressure seal to minimise friction losses. Drainage from the sample to a second burette is possible through porous plastic plates at the base and top of the sample. These also allow a back pressure to be applied to the pore water when necessary, using a compressed air or nitrogen supply via the pore water pressure burette. Two connections have been provided to each of the drainage plates to allow them to be de-aired. Water draining from the sample is channelled to the appropriate outlets via grooves machined in the top plate and piston.

A guide tube located centrally in the aluminium alloy top plate allows the tunnel to be driven vertically into the sample by a hydraulic piston. Water is prevented from leaking past the tunnel during a test by a U-ring in the guide tube. During initial reconsolidation of the sample (after transfer from the consolidometer) the guide tube is blanked off with a dural plug.

Four holes were drilled in the top plate which allowed the pore pressure transducer cables to be passed out of the cell. The holes were sealed off by fittings developed specifically to allow three cables to pass through each hole in the top plate. Other holes in the top plate allowed single transducer cables to be passed out of the cell.

2.3.3 Model tunnels

The first model tunnel used, as shown in Fig. 2.2, consisted of an open-ended outer stainless steel tube, 50.8mm in diameter, which had

been strain-gauged to allow longitudinal and circumferential stresses in the lining to be calculated. An inner stainless steel tube, 38mm in diameter, was screwed onto a tapered face piece. Data from the existing arrangement of strain gauges during the two preliminary tests were erratic and unexpected, and attempts to calibrate the tunnel proved unsuccessful. The flow of clay into the tunnel was restricted by the inner lining and the tunnel was cumbersome to use. After the preliminary tests it was decided to replace the strain-gauged tunnel by simple tunnels of three different diameters. These tunnels consisted of cylindrical open-ended brass tubes with tapered cutting edges and had outside diameters of 12.7mm, 25.4mm and 50.8mm and wall thicknesses of 0.4mm, 0.8mm and 1.6mm respectively.

The tunnels were driven into the samples through a guide tube in the top plate to the required position. The triaxial cell was based on a reaction frame with a hydraulic jack which provided the driving force to advance the tunnel into the sample at a controlled rate. A microswitch, placed at various levels on the reaction frame, was connected to a solenoid valve in the hydraulic system and controlled the depth to which the tunnels were driven.

Tunnel face support was provided by a thick brass disc fixed to the end of a length of brass tube, as shown in Fig. 2.3. A hole was drilled along the central axis of the disc and threaded for part of its length so that an inner plug at the end of a brass rod could be screwed into it. An 'o' ring below the threaded section of the inner plug and an 'o' ring on the face support disc allowed the tunnel face to be sealed off. The inner plug was necessary to allow the face support to be placed in and removed from the tunnel without causing

large positive pressures or suctions. Reaction for the face support, as illustrated in Fig. 2.4, was applied by a frame consisting of a length of box section and lengths of studding bolted through the top plate of the cell.

2.4 Instrumentation

2.4.1 Pore pressure transducers

Miniature pore pressure transducers manufactured by Druck Ltd. were used in all the tests. The overall dimensions of the transducers are 6.35mm in diameter and 13mm in length, as shown in Fig. 2.5. Strain gauges are diffused directly onto the pressure sensing silicon diaphragm. The diaphragm is bonded onto a glass support ring which isolates it from the outer stainless steel shell.

A porous stone is placed at the front of the transducer, thereby allowing only the water pressure to be applied to the diaphragm. The gap of 0.05mm between the porous stone and the diaphragm should be saturated with water to ensure a rapid response; this was achieved by placing the transducers in de-aired water in a cylinder which was virtually evacuated by means of a vacuum pump. The effectiveness of the de-airing process was checked by suddenly releasing the vacuum whilst the transducers' responses were monitored. A limitation of the transducers is the measurement of large pore suctions, which is restricted by the size of the gap between the stone and the diaphragm which causes cavitation at suctions of the order of 100kPa to 150kPa. Some problems were experienced with sudden changes in the zero values of the calibration constants, although calibration gradients remained

stable. A further problem noted occasionally was the less rapid response to pressure changes once the transducers had been placed in the sample. This may have been due to lack of saturation in the sample or the stone as a result of the installation process. During the early tests the transducers had a high failure rate (the reasons for this remain unknown) but this was much reduced in the later tests where the transducers performed more reliably.

2.4.2 Total stress transducers

Pressure transducers (P302) manufactured by Maywood Instruments Ltd. were used in several tests in an attempt to record the total stresses within the sample as well as at the boundaries. Use of these transducers proved quite unsuccessful since it was not possible to calibrate them reliably, and they eventually became totally defective.

2.4.3 Cell and back pressure transducers

The cell pressure transducer was made by Bell and Howell Ltd. Pressure is sensed by a stainless steel diaphragm which is strain-gauged. The back pressure transducer for measurement of the pressure applied to the pore fluid was manufactured by Druck Ltd., and had strain gauges diffused directly onto its pressure sensing silicon diaphragm.

2.4.4. Differential pressure transducers

Attempts were made to measure cell fluid flow to and from the cell using differential pressure transducers manufactured by Druck Ltd.

One side of the transducer was connected to the base of the burette, the other to the nitrogen gas or compressed air supply. The measured difference in pressure corresponded to the height, and therefore the volume, of water in the burette. Changes in the volume of water in the cell burette gave an indication of the sample deformations. These volume changes were initially compared with the volume of clay removed from the tunnel, but it was found that correspondence between the measurements was poor. Later the transducers also developed problems with changing calibration constants and their use for measuring sample deformations became too unreliable.

2.4.5 Displacement transducers

Linear variable differential transformers (LVDTs), produced by Sangamo Weston Ltd., were used for monitoring the deformation of the tunnel face and also for recording the position of the tunnel within the sample. The electrical output from an LVDT varies with the position of a ferrite core within the transducer body. In order to measure the deformation of the tunnel face, the LVDT was clamped above the tunnel and a lightweight extension probe attached to the spindle. A thin 15mm diameter disc was fixed at the end of the extension probe to reduce the bearing pressure at the tunnel face, due to the weight of the core and spindle. A smaller diameter disc was used for the 12.7mm diameter tunnel tests.

2.5 Experimental procedure

2.5.1 Sample preparation

Speswhite kaolin in powder form was mixed with de-aired distilled water at a water content of 120% (approximately twice its liquid limit) to produce a reasonably thin slurry. The clay was mixed in an industrial catering mixer for two to four hours. Originally the mixing time was two hours, but it was found that increasing the time to four hours reduced the number and size of visible air bubbles and produced an apparently more homogeneous slurry.

The slurry was placed into a consolidometer, 1200mm in height and 250mm in diameter, which had been cleaned and coated with Duckhams 'Keenomax' L3 lithium base water pump grease. Mair (1979) had found this grease to be more successful than others in reducing the friction losses on the consolidometer walls. Even so, about 20% of the vertical stress was still lost for a sample initially 800mm high.

The consolidometer consisted of two cylinders about 600mm long, Fig. 2.6, the lower half being filled with slurry first before the upper half was lifted into position and bolted to the lower one. Porous plastic plates were placed at the base and top of the sample for drainage. A surface pressure was applied by a hydraulic jack bolted to the assembled consolidometer, as shown in Fig. 2.6. Load increments to consolidate the sample one dimensionally were applied at intervals of about three days to allow 90% dissipation of excess pore pressures to occur based on a c_v of $1.0\text{mm}^2/\text{s}$ for Speswhite kaolin.

The final increment to reach a maximum vertical effective stress of 800kPa was applied for a minimum of three days to ensure full consolidation, after which the sample was gradually swelled back to 60kPa in decrements of vertical stress of not more than 100kPa to avoid cavitation problems on transfer to the triaxial apparatus. The cause and effects of cavitation are discussed later in Section 4.4.

2.5.2 Model preparation

Surplus water was removed from the surface of the sample and the base drainage tap of the consolidometer closed before the sample was unloaded completely, after which the hydraulic jack and the upper half of the consolidometer were unbolted and removed. The height of sample was generally several centimetres greater than required and was therefore trimmed to the correct length for the triaxial cell. An aluminium drainage plate, designed to support the clay in the consolidometer during transfer and also to fit into the recess of the base piston of the triaxial apparatus, was then attached to the top flange of the lower half of the consolidometer. The cylinder was inverted and placed on the base piston of the triaxial apparatus, and the reaction frame (otherwise used to drive the tunnel) was used to provide the force required for the sample to be slowly extruded on the base piston, Fig. 2.7.

Before each test the pore pressure transducers were de-aired and calibrated to check on changes in their response, and then carefully threaded through the top plate and cylinder ready for insertion into the sample. The method used for placing the transducers was based on that used by others, e.g. Taylor (1984). After the preliminary tests,

further pieces of apparatus and tools were made and the procedure modified to allow the positions of the transducers in the sample to be known more accurately. The transducers were placed in horizontal holes about 8mm in diameter, cut by a casing greased on the inside with a drill bit used as a clay auger, Fig. 2.8. The transducers were pushed two millimetres into the clay to ensure that no voids existed between the porous stone and the clay. The opening behind the transducer was backfilled with kaolin slurry. Shallow grooves were cut vertically along the length of the sample to accommodate the transducer cables which were taken to the top of the sample to exit from the cell through the top plate.

Horizontal installation of pore pressure transducers placed the transducers in the best orientation for measurement of the radial pore pressure response and also allowed transducers to be located ahead of the face in the last test stage position. However, in the latter case the transducer would measure an average pore pressure across the diameter of its porous stone. A disadvantage of this method of installation is that the transducers were anchored radially by the cables, which may have caused larger pore pressure reductions to be measured on unloading than might otherwise have been observed.

After pore pressure transducer installation was complete, the triaxial cell was assembled by first lowering the cylinder (with vacuum applied to the membrane) over the sample and drawing the transducer cables through. The porous plastic plate and top plate were carefully positioned to avoid damaging the cables which were again pulled clear of the sample, Figs. 2.9(a) and (b). 'O' ring seals were placed at the interfaces of the cylinder with the base piston and top platen,

and the cell bolted together. The cylinder and base piston were filled with de-aired water via the cell pressure burette, and the top and base drainage plates flushed through with de-aired water from the back pressure burette. The sample was then reconsolidated in three loading increments to an isotropic effective stress of 800kPa.

2.5.3 Testing procedure

The procedure described in this section was used for all but the two preliminary tests which are described in Section 3.1.1. Observations and experience gained from the preliminary tests provided the basis for the development of this procedure. The initial stress levels to be applied in the Series I tests were also determined as a result of the first two tests.

Figure 2.10 illustrates the steps involved in the model test procedure. After reconsolidation to an equilibrium state at an isotropic effective stress of 800kPa, preparations were made to drive the model tunnel into the sample to the level required for the first stage of the test. First the cell pressure was reduced to about 300kPa (with the drainage taps closed) to minimise deformation and disturbance of the sample during tunnel driving. Reduction of the cell pressure to 300kPa lowered the stability ratio for the model tunnel. Under these stress levels only a very low rate of straining should take place during tunnel driving and subsequent removal of soil from the tunnel.

The tunnel was set up in the guide tube in the top plate, and the microswitch positioned to ensure that the tunnel was driven the

correct distance into the sample by the hydraulic jack on the reaction frame. The position of the tunnel was varied in some tests, depending on the diameter being used. Clay which had intruded into the tunnel during the drive was removed down to the face and the face support disc was installed with its inner plug. The frame providing reaction to the face support was bolted to the cell, Fig. 2.11, before adjusting the stress levels to provide the required stress state for the first stage of the test. After driving the tunnel, the sample was left for at least 24 hours to allow an equilibrium state to be achieved, which was indicated by the pore pressure transducers.

Once equilibrium had been reached, the model test could be performed. A data logger was programmed to record the events as rapidly as possible, a complete scan of all channels required about 2.5 seconds. The taps to the drainage plates were closed and the support frame and face support quickly removed from the tunnel. The LVDT with extension piece was positioned to monitor movement of the now unsupported tunnel face, which was permitted to deform for a period of time depending on the rate of intrusion. At the end of the deformation time period (end of test) the cell pressure was again reduced to minimise further clay intrusion into the tunnel.

Samples were taken from the clay in the tunnel and ahead of the face to obtain a water content profile, after which the tunnel was advanced to its subsequent position. The procedure described above was repeated until the final stage of testing in the sample had been completed. On completion of the final stage, the cell and back pressures were released and the apparatus disassembled, leaving the transducers and the tunnel embedded in the sample. These were

subsequently excavated by means of cutting a section across the sample; the end result is shown in Fig. 2.12.

3.1 Introduction

Two preliminary model tests were conducted using the 50.8mm diameter strain-gauged tunnel, before the main testing programme was planned, to allow some experience to be gained in the use of the apparatus and to assess the suitability of the proposed testing procedure for modelling an excavation process. A number of difficulties became apparent from these tests, which are discussed in Section 3.1.1 together with details of the tests and some of the observations made.

As a result of observations from the preliminary tests, the first series of tests (Series I) was performed to investigate the influence of the apparatus on the behaviour (i.e. scale effects), as well as the significance of the initial pore pressures and the tunnel diameter. The tests in this series are TT3 to TT8 and TT10 to TT12 inclusive and TT14. Details of these tests are summarized in Tables 3.1(a) and (b). A further series of tests (Series II) was conducted to provide additional evidence of the importance of pore pressure and load factor on the observed response. Details of the tests in Series II are given in Table 3.2.

A considerable number of tests were performed, some of which are of limited value due to experimental difficulties, particularly with the failure of transducers. Consequently representative data, selected to illustrate the observations generally applicable to all of the tests, will be discussed and compared in this chapter. Other data are

included in the analyses presented in Chapter 5. A full record of all the test data is given by De Moor (1989).

The purpose of this chapter is to describe the typical data as a guide to the full series of tests. Particular classes of behaviour will be contrasted and attention drawn to factors which may be relevant. Detailed discussion and analysis of the significance of these factors are presented in Chapter 5.

3.1.1 Preliminary tests

The samples used in these tests had been isotropically reconsolidated to an effective stress of 800kPa in the triaxial apparatus. Excavation of the tunnel face was modelled simply by driving the tunnel to the required position in the sample, removing the clay which had been displaced into the tunnel, and thereafter allowing the unsupported tunnel face to deform. If a large volume of clay intruded into the tunnel it was subsequently removed. Full details of the data from these tests can be found in De Moor (1985). However, a brief description is included here as an illustration of the influence of pore pressure and load factor on the model behaviour.

The stress levels applied to the models varied in the methods by which they were achieved as well as in magnitude. A summary of the test details is provided in Table 3.3. The stress histories of the two samples were also different, tunnel test 1 (TT1) was normally consolidated whereas TT2 had an OCR of about two.

For stage 1 of both tests, the initial pore pressures were equal to the head of water in the pore pressure burette (i.e. about 20kPa). For TT1 the drainage taps were open, whereas in TT2 the taps were closed. It was observed that a significantly larger volume (equivalent to approximately 85mm of deformation in 23 hours) of clay intruded into the tunnel during stage 1 of TT1 than during that of TT2, where only about 3mm of deformation occurred in 15 hours. These results are probably a consequence of the combination of the differences in drainage conditions and stress states. A much higher load factor of about 0.61 is associated with stage 1 of TT1 compared with 0.4 for that of stage 1 of TT2. The load factor was calculated based on the value of the critical stability ratio determined from a simplified analysis which is discussed in a Chapter 5.

Initial pore pressures for stages 2 and 3 of TT2 were produced simply as excess pore pressures caused by increasing the cell pressure, with the drainage taps closed, immediately before the tunnel was advanced for the given stage. A larger volume of clay intruded into the tunnel during stage 3 of TT2, where the initial load factor and pore pressure were higher than for stage 2 of TT2. The tunnel face was allowed to deform for about 24 hours in both tests during which the excess pore pressures close to the face dissipated to virtually constant values of about 40kPa, as shown for stage 3 in Figs. 3.1(a) and (b). Behind the tunnel face the transducers indicated that the pore pressures continued to reduce. The conditions obtained after about 24 hours in these tests were clearly not representative of a field situation.

The stress state applied to the sample for stage 2 of TT1 was the result of a cell pressure increase from 690kPa to 1020kPa, causing the

pore pressures to rise from about 20kPa initially to between 340kPa and 380kPa. The drainage taps were open to a pressure of 200kPa in the pore pressure burette and remained open for the first 30 minutes of the test. These stress changes, which were imposed immediately before the tunnel was advanced to the required position, implied an initial stability ratio of 6.4. Since the value determined at a later stage for N_{crit} was 6.6, the model may have been close to a collapse state. During the tunnel advance the volume of clay which entered the tunnel exceeded that occupied by the tunnel. Very rapid deformation continued after the clay had been removed, with further large volumes of clay being removed, which ultimately resulted in the membrane being drawn in too close to the tunnel face and subsequent failure. Figures 3.2(a) and (b) illustrate the marked difference between the rates of intrusion for the two stages of TT1 which had quite different stress levels.

Measurements of the water contents of the clay removed from the tunnel for tests TT2/3 and TT1/2 are shown in Figs. 3.3(a) and (b). It is interesting to note that water contents increased with time (the rate of increase becoming less with time) in TT2/3, whereas the water contents from the large volumes of clay removed during TT1/2 remained almost constant at a value close to that expected for an initial effective stress of 670kPa.

A number of conclusions were drawn from these preliminary tests:

- (a) the experimental procedure was itself unsatisfactory in terms of uncertainties about the stress state of the sample due to the excess pore pressures in the sample before driving the

tunnel, and also by the disturbance resulting from the tunnel advance;

- (b) additional perturbations to the stress state near the tunnel face were caused by the occasional removal of clay from the tunnel, thereby further complicating interpretation of the data;
- (c) a dependence on pore pressure and stress level was indicated for the rate of deformation at the tunnel face, i.e. the volume loss;
- (d) the length of time for which the tunnel face was allowed to deform required careful consideration.

In assessing the problems associated with the high rate of deformation and the implications of this for the testing programme as a whole, it was suggested that the rapid deformations could be a function of the apparatus and model arrangement. In TT1 the drainage taps remained open, providing a supply of water at a constant pressure to the sample. This simulated the condition of tunnel excavation towards an aquifer, a situation unlikely to be encountered in deep tunnels in a thick clay stratum. Although the drainage tap was closed at the base of the burette during TT2, the drainage plates and the pipework in the apparatus contained a supply of free water which could flow towards the zone of negative or low pore pressure at the tunnel face. It was thought that a large difference in pore pressure between the tunnel face and the drainage plate may lead to a significant flow of water towards the face with subsequent softening and deformation. The ratio

of the difference in pore pressure to the distance between the face and a drainage plate will be referred to as the overall pressure gradient (OPG), and is illustrated in Fig. 3.4. The existence of such an effect became one of the aspects investigated in the Series I tests.

3.2 Selection of initial stress conditions

3.2.1 Series I

The stress levels applied to the models in this series were determined by the conditions required to study the effect of the overall pressure gradients, and also by the need to allow a more controlled rate of deformation to occur, based on observations from the preliminary tests.

All the models were tested at an initial isotropic effective stress of 800kPa in a normally consolidated state, which corresponds to an in situ depth of 100m in a soil having an average bulk density of 18kN/m³ and K_0 equal to unity. For these tests, the initial pore pressures applied to the samples in equilibrium states before the start of the test were either 80kPa or 200kPa, depending on the position of the tunnel in the sample, i.e. the distance of the face from the base drainage plate. These pore pressures are much lower than in situ hydrostatic pore pressures at a depth of 100m, and the necessity for this simplification may be viewed as a limitation in the modelling technique.

The values of 80kPa and 200kPa were selected by considering the OPG between the tunnel face and base drainage plate at different positions in the sample. Consequently, a test with the tunnel face at a stage 1 position in the model and an initial pore pressure of 200kPa had a similar OPG to a stage 3 test with an initial pore pressure of 80kPa, as shown in Fig. 3.4. For stage 2 the same initial pore pressure was selected as for stage 3, so that the 'local' hydraulic gradients due to the initial pore pressure in the soil were similar for both stages. The OPG between the face and the base drainage plate for stage 2 was approximately half that for stages 1 and 3. The term 'local hydraulic gradient' refers to the pore pressure distribution or the loss in head per unit length which exists close to the tunnel face, and is quite distinct from the OPG. A summary of the stress levels applied in these tests is presented in Tables 3.1(a) and (b).

3.2.2 Series II

This second series of tests was designed to examine the influence of the initial pore pressure and load factor on the rate of tunnel face deformation. As in Series I, the kaolin samples were reconsolidated to an isotropic effective stress of 800kPa after transfer, but were then swelled back to lower effective stresses to allow a wider range of load factors to be investigated. Appropriate stress states were calculated using the method described in Section 4.4 for pre-selected values of pore pressures and load factors. A range of possible states based on this method are shown in Table 3.4. It should be noted that values obtained for the load factors were based on presumed undrained shear strengths for overconsolidated clays, which have since been recalculated using more appropriate strengths derived from subsequent

laboratory tests. The question of the selection of suitable strengths is discussed in detail in Chapter 4. The majority of the Series II tests were performed with the 12.7mm and 25.4mm diameter model tunnels to allow the effect of tunnel diameter to be studied further. A comprehensive summary of the tests in this series is presented in Table 3.2.

3.2.3 Position of tunnel face

In the Series I tests the locations of the tunnel face were varied, depending on tunnel diameter, to investigate the influence of the drainage plates and the overall pressure gradient. In some cases the 12.7mm diameter tunnel tests were positioned at distances into the sample relative to the top drainage plate which were geometrically similar to the 50.8mm diameter tests. Some additional tests were also performed in Series II, using the 12.7mm diameter tunnel, which was driven to positions above those intended for the larger diameter tunnel tests which were later conducted in the same sample. The arrangements of tunnel faces for all the different samples discussed in this chapter are shown in Figs. 3.5(a) and (b), indicating the appropriate test numbers for Series I and II.

The numbering system adopted throughout the dissertation for each test is such that the first number, which identifies the sample in which the tests was conducted is separated by / from a second number which refers to the position of the tunnel face. For example test 12/1A indicates that the test was performed in sample no. 12 at a position 31mm below the top drainage plate, as shown in Fig. 3.5(a).

3.3 Deformation of the tunnel face

3.3.1 Series I

Two different initial stress levels were modelled in this series. The initial values of the pore pressure were about 200kPa for stage 1 tests and about 80kPa for stage 2 and stage 3 tests, with an initial mean normal effective stress of approximately 800kPa. Details of the tests referred to in this section have been listed in Table 3.5, in order of discussion for ease of reference.

It should be noted that the length of time for each test was approximately the same, and it may not be relevant to make direct comparisons at similar times without first establishing an appropriate scaling relationship to identify the influence of tunnel diameter and stress state. In this chapter it is therefore intended only to attempt to identify classes of behaviour, and to highlight the similarities and discrepancies observed during the tests.

Deformation data in both series of tests could be obtained only onwards from about one to two minutes after the start of each test, as a result of the unloading procedure and the installation of the displacement transducer. Attempts to measure the deformation which had occurred during this time proved unreliable, but values of between 0.5mm and 6mm were noted, depending on the initial test conditions. Consequently offsets have been added to the displacement data such that zero deformation occurs at $t = 0$, for which it has been assumed that the rate of deformation between the start of the test and the first few measurements was constant and equal to that indicated by the

earliest part of the curve. This simplification disregards the initial immediate movements due to the removal of the tunnel face support. However, it is considered that the assumption made is unlikely to have a significant effect on the study of time dependent deformations.

Typical data are shown in Figs. 3.6(a) to 3.9(a) from the stage 1 tests for all three model tunnel diameters. Figures 3.6(a) and 3.7(a) show deformation of the 12.7mm diameter tunnel face against time for tests 14/1 and 12/1A respectively, which had virtually identical initial stress states. The tests are known to be different in only one respect, which was the position of the tunnel face in the sample. Tests 12/1A was at a distance of about 31mm below the top drainage plate compared with 125mm for test 14/1. Data from these tests are however in very close agreement, indicating that the proximity of the top drainage plate and the OPG are unlikely to be factors controlling the observed behaviour as previously suggested.

Figure 3.6(a) provides an illustration of the typical shape of the deformation-time curve. This shows that the rate of deformation was relatively slow for a short time initially, followed by a period during which the rate accelerated until a final virtually constant rate of deformation was reached before termination of the test. Although test 12/1A was not continued for as long as test 14/1, both deformation curves show an inward movement at the face of about 60mm after a time of 15 minutes.

Figures 3.8(a) and 3.9(a) allow comparisons to be made between the deformation of 25.4mm and 50.8mm diameter faces and that of a 12.7mm

diameter face, Fig. 3.6(a). Data from test 11/1 (Fig. 3.8(a)) indicated a slower rate of deformation compared with test 14/1, only 25mm of movement had occurred at a time of 15 minutes, although the overall shape of the curve is similar. The deformation curve, shown in Fig. 3.9(a), for the 50.8mm diameter tunnel test 10/1 is in very close agreement with that of test 11/1. This raises a question as to which of these tests has demonstrated an unexpected rate of deformation. It should be noted that although the stress states of the model samples were similar, the load factors varied significantly for each of the different diameter tunnel tests, with values of 0.44, 0.57 and 0.81 for the 12.7mm, 25.4mm and 50.8mm diameters respectively. The influence of both tunnel diameter and load factor is studied further in Chapter 5.

The behaviour of the face at a number of different locations in samples with an initial pore pressure of 80kPa is illustrated by Figs. 3.10(a) to 3.17(a). The smallest diameter tests (12/2A, 14/2, 14/3A and 14/3) at the tunnel face positions shown in Fig. 3.5(a), were all in close agreement, as shown in Figs. 3.10(a) to 3.13(a). These substantiate the evidence from the stage 1 data which suggested that the possible effects of the OPG and water supply from the drainage plates on the rate of deformation were insignificant. The data from the larger diameter tunnel tests, stages 2 and 3 in Figs. 3.14(a) to 3.17(a), may also be compared for this particular part of the investigation. The conclusions drawn, with respect to the tunnel face position, are the same as for the 12.7mm diameter tunnel.

The dependence of rate of deformation on tunnel diameter was again evident. Tests 14/2, 11/2 and 10/2, Figs. 3.11(a), 3.14(a) and

3.15(a), show that after a particular elapsed time, the deformation for the 25.4mm diameter tunnel was less than for the 12.7mm diameter tunnel yet similar to that of the 50.8mm tunnel. At a time of 15 minutes, the inward movement was about 18mm for the smallest tunnel and 7mm for the larger ones. Tests 11/3 and 10/3, shown in Figs. 3.16(a) and 3.17(a), also illustrate the unexpected consistency of the rate of deformation with respect to tunnel diameter. These values were considerably lower than those at similar times in stage 1 where the initial pore pressures were 200kPa. However, as noted previously, consideration needs also to be given to the differences in load factor resulting from the higher total stresses applied in the stage 1 tests.

3.3.2 Series II

Data from the Series I tests were grouped into types of test, i.e. stage 1 or stages 2 and 3, since the position of the tunnel face also dictated the stress levels applied. In Series II each of the various tests in a given sample is considered to be an entirely independent test, and the use of the term 'test stage' is discontinued.

Only some of the tests from this series can be directly compared due to the variations in tunnel diameter, pore pressure and load factor, although the attempts made to combine all the data using dimensional analysis are presented in Chapter 5. A list of the tests discussed in this section, with appropriate details, is given in Table 3.6.

Tests 16/2, 16/1 and 16/3 shown in Figs. 3.18(a) to 3.20(a) were conducted as an investigation into the changes in behaviour with variations in pore pressure at constant load factor. Initial pore

pressures of 56kPa, 200kPa and 350kPa were applied, which resulted in movements at the face of 6mm, 25mm and 86mm respectively after a time of 15 minutes. These data demonstrate a clear dependence of rate of intrusion on the magnitude of the initial pore pressure in the sample. The shape of the deformation curve for test 16/3 in Fig. 3.20(a) is dissimilar to those in the Series I tests in that the period during which the rate of deformation increased was very short, and is perhaps a consequence of the overconsolidated state of the clay.

Figures 3.6(a) and 3.21(a) show further evidence of the influence of initial pore pressure in tests 14/1 and 19/1A, where the load factors were reasonably close, 0.44 and 0.46. The pore pressure in test 19/1A was 400kPa, compared with 200kPa for test 14/1, which resulted in an estimated increase in deformation of 135% at ten minutes after the removal of face support for the higher pore pressure test.

The influence of the load factor with constant pore pressure may be examined in tests 17/1 and 17/2, Figs. 3.22(a) and 3.23(a), for which load factors were 0.59 and 0.64 respectively, as given in Table 3.2. This variation made an appreciable difference to the magnitude of movement observed ten minutes after the start of the test, when the volume of clay which had intruded into the tunnel was 25% greater for the higher load factor. Other tests which may be compared to reveal the same form of behaviour include tests 16/1 with 11/1, and 14/1 with 18/1A, shown in Figs. 3.19(a), 3.8(a), 3.6(a) and 3.24(a). For tests 16/1 and 11/1 the change in load factor from 0.49 to 0.57 led to a 35% increase in movement, whereas for tests 14/1 and 18/1A with load factors of 0.44 and 0.35 the difference in deformation was about 60%. Very similar initial stress states were applied to tests 19/1A and

18/3, shown in Figs. 3.21 and 3.25. The tunnel diameters, however, were 12.7mm and 25.4mm respectively, which resulted in a difference in load factor. A more rapid rate of deformation was obtained from the smaller diameter and lower load factor test. For these tests the influence of tunnel diameter and load factor are interdependent and therefore cannot be distinguished.

The majority of the tests have been performed at pore pressures significantly lower than hydrostatic pressure at a depth of 100m. However, two tests (of 12.7mm and 25.4mm diameter) were included to give an indication of the rates and magnitude of response at stress levels closer to anticipated field conditions at a depth of 100m, although the normally consolidated state of the sample may not be appropriate. The data from these tests, 19/3A and 19/3, are shown in Figs. 3.26(a) and 3.27(a), from which it may be seen that the deformation occurred extremely rapidly, and that no significant difference can be identified between the two different tests, which may be reasonable given the different load factors and tunnel diameters. The deformation curves show a tendency towards a reducing rate of deformation, which contrasts markedly with other test data and may be a consequence of the large volume of clay moving into the tunnel providing a measure of support at the tunnel face.

The comparisons drawn in this section between various tests have indicated, in a mostly qualitative manner, that for a given tunnel diameter both initial load factor and pore pressure combine to control the rate at which the face deforms into the tunnel. Analyses of the deformation data discussed in these sections and of the remaining

data, which incorporate these important factors, are presented in Chapter 5.

It may be concluded from the data described in this section that:

- (a) the influence of the OPG (investigated in Series I) on the deformation of the tunnel face is insignificant;
- (b) the rate of deformation appears to be a function of tunnel diameter, pore pressure and load factor;
- (c) rates of deformation observed in the 50.8mm diameter tunnel tests were found to be significantly different in comparison with the smaller diameter tunnel data; these data should be treated with caution in subsequent analyses.

3.4 Pore pressure response

3.4.1 Series I

As in the discussion of deformation behaviour for this series, the tests will be considered in two separate categories, i.e. stage 1 and stages 2 and 3, regardless of tunnel diameter. Table 3.5 should be referred to, particularly for pore pressure transducer details.

Comparisons of the responses indicated by pore pressure transducers (ppts) between different diameter tests will be made on the basis of geometric similarity (i.e. the distance of the transducer from the tunnel face is scaled by the radius, r_0 , of the tunnel). In tests

with the 12.7mm diameter tunnel it was considered necessary to position the pore pressure transducers at a greater distance from the tunnel face (in terms of geometrical similarity) than for the larger diameter tunnels. The influence of the transducer, which may be viewed as a rigid inclusion half the model tunnel diameter in size, would be minimized by the greater distance. As a result fewer transducers in the smallest diameter tests can be directly compared to the larger diameter tests.

Positions of the pore pressure transducers are expressed as the ratio of the distance, r , from the centre point of the tunnel face to the centre point of the front of the transducer divided by the radius, r_0 , of the tunnel, as shown in Fig. 3.28. Although r/r_0 allows the actual distance of a transducer from the centre point of the face to be determined it provides no indication of the orientation of the transducer relative to the face. Two further dimensions, g and h , defined as the vertical and horizontal offsets from the centre point of the tunnel face, are also shown in Fig. 3.28. The importance of these dimensions will become apparent in the later discussion of the data. It should be noted that the values of r or r/r_0 quoted throughout this dissertation may be subject to some experimental error, and may become quite significant in zones of very large hydraulic gradients close to the tunnel face. Values of r/r_0 for each transducer are shown on the figures, and are written beneath the pore pressure transducer identification number.

All stage 1 or 1A tests had an initial equilibrium pore pressure of approximately 200kPa. The positions of the tunnel face can be seen in

Fig. 3.5(a). In stage 2, 2A, 3 and 3A tests the initial pore pressure was about 80kPa.

Large and rapid variations in the pore pressures, which were observed during the removal of face support, may be the result of the experimental procedure. The effects of the various stages in the unloading procedure are shown clearly in Figs. 3.29(a) and (b). An initial sharp reduction in pore pressure was caused by the removal of the reaction frame, which was followed by an immediate partial dissipation before the inner plug in the face support was unscrewed and pulled out, resulting in a further reduction. The final unloading phase took place when the face support itself was pulled out of the tunnel. Subsequent longer term pore pressure changes were the result of dissipation of reduced pore pressures and changes in stress levels within the model sample.

It has also been noted that the pore pressure response during the unloading sequence may be dependent on the diameter of the tunnel. A comparison of tests 14/3 and 10/3 in Fig. 3.29(a) indicates a much slower response from the 50.8mm diameter tunnel test at a geometrically similar location on the central axis. In Figure 3.29(b) the response at r/r_0 of 2.6 perpendicular to the central axis is shown for tests 14/3A and 11/2. The changes for the smaller diameter test are larger and steeper, as shown in Fig. 3.29(a), and may indicate that the zones around the tunnel face affected by the unloading process are not geometrically similar. The reductions in pore pressure during the removal of the face support are considered in more detail in Chapter 5.

Tests 14/1 and 12/1A, Figs. 3.6(b) and 3.7(b), which were 12.7mm diameter tests at different distances from the drainage plates, are compared to assess the influence of these plates. Examination of these data suggests that significant differences due to the relative location of the drainage plate are unlikely to exist, as expected from the deformation results discussed in Section 3.3. A sudden reduction in pore pressure is shown in Fig. 3.6(b), as the support was removed from the tunnel face. The magnitude of the reduction was about 30kPa for pore pressure transducer 3441 (ppt3441) at r/r_0 of 2.6, whereas at r/r_0 of 4.2 (ppt2962) a smaller reduction of 20kPa was observed. A similar magnitude of response was recorded by transducers at the same locations in test 12/1A, Fig. 3.7(b), with reductions of 40kPa and 30kPa.

After the support had been fully removed in tests 14/1 and 12/1A, Figs. 3.6(b) and 3.7(b), the pore pressures at the r/r_0 values of 2.6 and 4.2 dissipated towards minimum values at a time of between 10 minutes and 15 minutes after the start of the test. Subsequently the pore pressures appeared to rise slowly and steadily, maintaining a difference of 20kPa to 30kPa between the transducers closest to the face in test 14/1. In contrast similar pore pressures throughout test 12/1A were measured at r/r_0 values of 2.6 and 4.2. Such a response is unlikely to be realistic, given the difference in the positions of the transducers. It can be seen from Fig. 3.7(b) and Table 3.5 that there was initially a discrepancy of 18kPa between the transducers, which if taken into account, would then indicate a similar trend of behaviour to that in Fig. 3.6(b). The lack of agreement between transducers due to variations in the calibrated zero values, which became apparent at

the initial equilibrium state in test 12/1A, was a common occurrence and has been commented on in Section 2.4.1.

At a greater distance ahead of the face ($r/r_0 = 5.8$), Fig. 3.7(b), ppt2933 showed very little change on unloading but measured the subsequent dissipation of the initial pore pressure of 211kPa to a value of about 160kPa at the end of the test. In test 14/1 the transducer located at about $20r_0$ showed virtually no response throughout the test, thereby giving a broad indication of the zone of influence for the given duration of this test.

Typical data for the 25.4mm diameter tests are from test 11/1, Fig. 3.8(b), from which it can be seen that two of the three transducers were at r/r_0 values smaller than for the 12.7mm diameter tests. A pore pressure reduction of about 170kPa was measured closer to the tunnel face (at r/r_0 of 1.4) by ppt3227 compared with a change of about -55kPa at r/r_0 of 2.6. The latter value is somewhat larger than the reduction of about 30kPa to 40kPa recorded at a geometrically similar distance in the smaller diameter tests. After the large and rapid changes in pore pressure caused by the removal of the face support, some dissipation of pore pressure to a peak value was observed before the pore pressures again reduced to minimum values at various times, the shortest time being for the transducer closest to the tunnel face. The minima reached by both the 12.7mm and 25.4mm diameter tests were of the order of 70kPa to 100kPa at r/r_0 of 2.6.

Figure 3.9(b) illustrates the response observed in test 10/1, one of the 50.8mm diameter tests. A reduction of about 30kPa at r/r_0 of 2.6 (ppt2937) compares favourably with the 12.7mm diameter tests, and from

Table 3.5 it may also be seen that the fall in pore pressures at r/r_0 of 1.4 and 1.8 compares reasonably well with those in test 11/1. This would indicate that the behaviour of ppt3225 in test 11/1 was possibly suspect, or that for some other unknown reason the initial change in pore pressure was larger than would otherwise be expected. Pore pressure changes after unloading at the face occurred more slowly in the largest diameter tests. Pore pressures at r/r_0 values of 1.4 and 1.8 were observed to rise more slowly before dissipating to minimum values as in test 11/1. However in tests 14/1 and 12/1A, Figs. 3.6(b) and 3.7(b), rising pore pressures immediately after unloading of the face were not observed, possibly the result of the r/r_0 values being greater than 1.8. In contrast to the behaviour in tests 14/1 and 12/1A the pore pressure at r/r_0 of 2.6 in test 10/1 rose to a peak before reducing to a minimum of about 160kPa. After minimum values were reached the pore pressure at all of the transducer locations tended to rise steadily, and at a slightly faster rate in test 10/1. The more rapid pore pressure rises in test 10/1 may be related to the higher load factor and the larger than anticipated rate of deformation.

The tests shown in Figs. 3.10(b) to 3.17(b) all belong to the Series I stages 2 and 3 category. Figures 3.10(b) to 3.12(b) illustrate the response observed in three 12.7mm diameter tests, in each of which the tunnel face was at a different location. The behaviour shown in these figures was generally consistent, both initially and in the longer term. On removal of face support, the initial reductions of pore pressure recorded at r/r_0 of 2.6 were 23kPa, 40kPa and 27kPa for tests 12/2A, 14/2 and 14/3A respectively. Reasons for the larger reduction recorded by ppt2834 in test 14/2 are not known, although a probable

cause is some inaccuracy in the value of r/r_0 . After the initial fall, the pore pressures were observed to rise quickly by between 5kPa and 10kPa, followed by dissipation towards apparently steady values of the order of 30kPa to 40kPa. The response observed at r/r_0 of 2.6 in test 11/2, Fig. 3.14(b), was initially similar to that of the 12.7mm diameter tests. However in the longer term the pore pressure remained constant at about 55kPa, whereas dissipation had occurred in the smaller diameter tunnel tests. Measurements from ppt2933 showed a different trend of behaviour to the other transducers in test 11/2 and also indicated a much lower initial value. It is probable that the transducer was not functioning correctly.

In test 10/2, Fig. 3.15(b), the pore pressure at r/r_0 of 2.6 rose steadily, after some initial reduction due to unloading. Transducers closer to the face in test 10/2 showed a similar response to those in test 10/1, although the time at which the minimum values were reached was greater in this case. The longer term behaviour was of steadily rising pore pressures instead of the apparently steady conditions observed at similar locations in the 12.7mm and 25.4mm diameter tests. A probable cause of this difference is the higher load factor, as noted for test 10/1.

The phrase 'apparently steady' requires further explanation. It appears from the data that this phrase may be applicable to the 12.7mm and 25.4mm diameter tests, where the initial pore pressures, load factor and rates of deformation are low. After some initial disturbance to the pore pressure equilibrium caused by the removal of face support, the pore pressures dissipated until a level was reached from which no further deviation could be discerned for the duration of

the test, hence the conditions were apparently steady. Given the drainage boundary conditions of the sample, the 'steady' condition could not be maintained for an infinite time and must be a transient phenomenon. After a time, when the pore pressure at the outer boundary had become less than the initial value, the pore pressure near the tunnel face would begin to reduce noticeably. These conditions are unlikely to be established in a sample with a low initial pore pressure and a 50.8mm diameter tunnel due to the higher load factor.

In a stage 3 type test it was possible to place pore pressure transducers ahead of the tunnel face on the central axis of the tunnel. Results from test 14/3, shown in Fig. 3.13(b), demonstrated that removal of the face support induced large reductions in pore pressure in the soil directly ahead of the face. The pore suctions rapidly dissipated as a result of the very high hydraulic gradients close to the tunnel face, as shown by ppt2944, and became positive once again before dissipating to an apparently steady value of 18kPa. Changes in pore pressure due to the removal of face support recorded where h is greater than r_0 are probably smaller than those where h is less than or equal to r_0 since the presence of the tunnel lining prevents the full effect of the removal of face support from being felt.

A comparison of stage 3 data on the central axis for all tunnel diameters revealed some inconsistencies between the magnitudes of pore pressure changes measured and the transducer positions. The 12.7mm diameter test data from test 14/3, Fig. 3.13(b), have already been discussed, the maximum pore suction measured being 130kPa at r/r_0 of

1.8. Figure 3.16(b) shows data from test 11/3, in which ppt2834 at r/r_0 of 1.0 clearly could not adequately measure the pore suction in the clay, although ppt3435 at r/r_0 of 2.0 momentarily sustained a suction of 140kPa, 40kPa greater than ppt2834. Measurement of pore suctions by the transducers is limited by cavitation in the porous stone or the gap between the stone and the diaphragm. In test 10/3, Fig. 3.17(b) the maximum pore suctions measured were 50kPa and 140kPa at r/r_0 values of 1.8 and 0.8 respectively, without any indication that a greater suction existed at these locations. The lack of agreement between these data calls into question the effect of the process of face support removal, and its influence on the observations. Further consideration to this problem is given in Chapter 5.

A number of conclusions may be drawn from the Series I data described in this section, as summarized below:

- (a) the influence of the OPG and the apparatus itself on the observed pore pressures is negligible;
- (b) at lower initial pore pressures, and hence lower initial load factors (stages 2A, 2, 3A and 3), the pore pressures showed dissipation towards apparently steady conditions, whereas a steadily rising trend was observed in the stage 1A/1 type tests;
- (c) pore pressure data from the 50.8mm diameter tunnel tests (as with the deformation data) have been shown to be significantly different in comparison with the smaller diameter tunnel data,

and may need to be treated with caution; use of the 50.8mm diameter tunnel in later analyses should be viewed with some scepticism.

3.4.2 Series II

As well as investigating the significance of initial pore pressure, this series also studied the influence of load factor on the rate of tunnel face deformation and pore pressure response. Different initial equilibrium pore pressures ranging from 50kPa to 820kPa were used, and variations in load factor were achieved by changes in stress level and stress history. The dependence of pore pressure response on stress history also complicates data interpretation with respect to the influence of initial pore pressure. The tests presented in this section are the same as those selected in Section 3.3.2 as being illustrative of the responses associated with changes in initial pore pressure and load factor. In this series only 12.7mm and 25.4mm diameter model tunnels were used, some doubt having arisen over the validity of the data from the 50.8mm diameter tunnel tests in Series I.

Figures 3.18(b) to 3.20(b) show data from three 25.4mm diameter tests (16/2, 16/1, and 16/3) performed in the same sample to investigate the influence of initial pore pressure with a similar initial load factor of approximately 0.5. In test 16/2, the clay was virtually normally consolidated, and the initial pore pressure was 56kPa. The decreases in pore pressure in test 16/2 were greater than in a similar 25.4mm diameter (test 11/2, Fig. 3.14(b)) with an initial pore pressure of 74kPa in Series I, which may be due to the smaller r/r_0 values in test

16/2. After rapid dissipation of the pore suctions, apparently steady values of between 10kPa and 20kPa were reached in test 16/2, which are similar to those close to the face in test 11/2.

An overconsolidated sample ($OCR \approx 1.5$) with an initial pore pressure of 200kPa was used in test 16/1, Fig. 3.19(b). At r/r_0 of 1.6 a change of approximately -150kPa was measured, whereas at r/r_0 of 2.0 a slightly lower reduction of 120kPa (compared with 135kPa in test 16/2) was recorded. After unloading, the pore pressures dissipated towards lower apparently steady values of the order of 30kPa to 50kPa, with some indication that they were beginning to increase towards the end of the test.

Test 16/3, Fig. 3.20(b), had an overconsolidation ratio of three (the highest used in this series) and an initial pore pressure of 350kPa. Large reductions in pore pressure were recorded by all of the transducers close to the face, as shown in Fig. 3.20(b). Very little dissipation took place since the pore pressures appeared to be close to the longer term equilibrium values of about 80kPa at r/r_0 of 2.0 as a result of the initial reductions at the removal of the face support. Both of the transducers ahead of the face on the central axis of the tunnel measured zero pore pressure towards the end of the test.

The comparison of these tests (16/2, 16/1 and 16/3) has attempted to demonstrate the dependence of the observed pore pressure response on the initial pore pressure (with a constant load factor). However, higher initial pore pressures at constant undrained shear strength imply higher total stresses and load factors. Consequently identical stress histories were not possible if a constant load factor was

necessary, and as a result the influence of the initial total stress and pore pressure on the immediate and subsequent pore pressure changes has been obscured by the differences in soil behaviour related to the overconsolidation ratio. Longer term pore pressure values at r/r_0 of about 2.0 ranged from about 20kPa to 80kPa for the initial pore pressure range of 50kPa to 350kPa.

Data from tests 17/1 and 18/3, Figs. 3.22(b) and 3.25(b), illustrate the differences in the magnitude of response at various locations around the tunnel face, and allow a more complete picture to be produced. The two tests may be combined due to the reasonable similarity of the initial conditions, as presented in Table 3.6. The significance of the relative magnitudes of the g and h dimensions can be demonstrated with data from these tests by comparing ppt2944 in test 17/1 with ppt3537 in test 18/3.

Attempts to assess the influence of load factor on the pore pressure response were complicated by the undefined effect of different stress histories. However trends of behaviour associated with different overconsolidation ratios may be identified, as illustrated by tests 16/3, 17/1 and 17/2 in Figs. 3.20(b), 3.22(b) and 3.23(b), in which the initial pore pressure was 350kPa. The details of the tests' initial conditions are given in Table 3.6. Test 16/3 was the most overconsolidated, and had the lowest load factor (0.5), whereas test 17/2 was virtually normally consolidated with the highest load factor (0.7). The initial reductions observed in test 17/2, Fig. 3.23(b), were considerably smaller than in test 17/1, and a direct comparison cannot be made to transducers in test 16/3 since the r/r_0 values were not identical. It is nevertheless clear that the reductions would be

greater in test 16/3 than for test 17/2. After unloading the transducers closest to the tunnel face in tests 17/1 and 17/2 (ppt2944, ppt2933 and ppt2962, ppt3102) showed a similar form of behaviour, although the pore pressures in the latter test were consistently 30kPa to 50kPa higher and also indicated a more rapid rate of increase. This type of response was contrasted by that seen in Fig. 3.20(b) for test 16/3 in which virtually no dissipation or pore pressure variations occurred after the initial removal of face support. These few data are insufficient to allow any statements to be made regarding the influence of load factor on pore pressure behaviour.

Tests 19/3A and 19/3, Figs. 3.26(b) and 3.27(b), used 12.7mm and 25.4mm diameter tunnels respectively with the same initial stress conditions, i.e. very high initial pore pressures. The load factors were not identical due to the different tunnel diameters. In test 19/3A it is difficult to separate the reduction in the pore pressures due to the removal of the face support from the rapid dissipation which caused a minimum value to be observed several minutes later. This may have been due to the different locations of the transducers, since similar problems were not found in test 19/3, or to the more rapid rate of dissipation in the smaller diameter tunnel test. In both tests the pore pressure rose rapidly after a minimum value had been reached, as observed in some other tests.

A number of conclusions may be drawn from the tests in this series:

- (a) the relationship between the magnitude of the pore pressure reductions at the end of the removal of the face support and

the initial pore pressure has not been clearly established due to the necessity of varying the stress states of the sample to maintain a constant load factor;

- (b) the influence of the load factor and the overconsolidation ratio of the sample is inter-related; lower load factors imply more highly overconsolidated soils with much larger pore pressure reductions than for normally consolidated samples;
- (c) the steepness of the hydraulic gradients around the tunnel face has been indicated by the significant differences in pore pressure measured by transducers at slightly different r/r_o values.

3.5 Water contents

At the end of each test, the cell pressure was lowered by about 60% to prevent further intrusion into the tunnel, after which samples were taken from the clay in the tunnel and from the clay ahead of the face for the measurement of water content. A number of difficulties were associated with this procedure. Clay samples for the water contents were unavoidably small, especially with the 12.7mm diameter tunnel, and may be accurate to $\pm 2\%$. The positions from which the samples were taken are probably known only to $\pm 5\text{mm}$, which has a significant effect on d/D for the 12.7mm diameter tests. It was concluded that the data in terms of the position of the sample and of the measured water contents may be unreliable, particularly for the 12.7mm diameter tests. Comparison of these data is limited still further by the variable durations of the tests. It is therefore suggested that the

data should be viewed accordingly and be considered only as an indication of the general trend of changes in water content at and close to the tunnel face. The data described in this section are from the tests discussed in the previous sections.

The flow of water towards the tunnel may be dependent on a number of factors, principally time, tunnel diameter, initial pore pressure and load factor. Data shown in Fig. 3.31 are all from the Series I tests, in which the samples were normally consolidated and only two different initial pore pressures were applied. The time to the lowering of the cell pressure at the end of the test is indicated on the figure; other test details are given in Table 3.5. The data appear to confirm that the longer the test duration the higher the water content, comparing tests 14/1 with 12/1A and 12/2A with 14/3A and 14/3. Figure 3.32 provides a further illustration of this from tests 17/1A and 19/1A, in which the initial pore pressures were similar (350kPa and 400kPa) and the duration of 17/1A was twice that of 19/1A. Water content at the tunnel face ($d/D = 0$) in test 17/1A was 6% higher.

In Fig. 3.31 the times for tests 14/1, 14/3A and 14/3 were reasonably similar and indicate that a higher initial pore pressure (test 14/1) caused higher water contents around the tunnel face. Another example of the importance of pore pressure is provided by tests 16/1 and 16/2, in which the load factors were very similar and pore pressures initially were 200kPa and 50kPa respectively. The data from these tests, in Fig. 3.33, show two curves representing a similar form of behaviour, with the water contents being highest in the tunnel just behind the tunnel face (inside the tunnel). Water contents ahead of the face decrease steadily until they approach the values appropriate

to the original stress state of the sample, found to be about 38% for an isotropic effective stress of 800kPa. Figure 3.33 shows that the water content in test 16/1 at the tunnel face was 50% compared with 43.5% for test 16/2 where the pore pressure initially was only 56kPa. Such a large difference in water content represents a considerable difference in the strength of the clay around the tunnel face, a fact reflected by the much larger deformations observed in test 16/1. Data from test 16/3, with a similar load factor to tests 16/1 and 16/2 but a pore pressure of 350kPa, might be expected to show even higher water contents. However this was not found to be the case, Fig. 3.33, where the water contents are shown to be quite similar to those from test 16/1. This response is probably linked to the different class of behaviour related to other aspects of the test discussed previously.

The influence of tunnel diameter can be clearly seen in Fig. 3.34 where data from tests 14/1, 11/1 and 10/1, all of approximately the same length of time, are illustrated. Higher water contents were obtained from the smaller diameter tests when compared with a larger diameter, for instance at the tunnel face the water contents were about 50.8%, 48% and 44% for the 12.7mm, 25.4mm and 50.8mm diameter tunnels respectively. Further evidence to support this observation is provided by the data from tests 10/2 and 11/2, in Fig. 3.35, which were obtained after a longer period of time.

All of the tests described so far have shown an increase in water content at the tunnel face, implying that sufficient time had elapsed during the test to allow dissipation of pore pressures induced by the 'excavation' process. The maximum increase in water content was obtained from samples some distance back from the face, inside the

tunnel. In tests 19/3A and 19/3 events occurred very rapidly as a result of the initial conditions applied. The water contents shown in Fig. 3.36 are of considerable interest since they demonstrate that very little softening occurred and that the large deformations observed represented an approximate state of 'undrained' collapse, as might be expected with load factors approaching unity.

3.6 Conclusions

The investigations described in this chapter have demonstrated a reasonably good repeatability. Given the large number of different operations within the preparation and testing stages, the testing procedures can be deemed satisfactory.

A greater variation of response has been observed in the pore pressure measurements than in the deformations which is probably a consequence of the additional inconsistencies which may have arisen as a result of the pore pressure transducer installation process. The ability of each transducer to respond to a given stress change in the sample in a similar manner may be less reliable than anticipated.

Direct comparisons between the tests have been limited to some extent by the interdependence of the larger number of variables involved in the investigation. Nevertheless it has been possible to compare a number of similar tests in this chapter and to make some general statements about the behaviour observed.

The dependence of the results on the tunnel diameter was shown to be inconsistent. Deformations associated with the 50.8mm diameter tunnel

appeared to be larger than might have been expected relative to those observed in the smaller diameter tests, and the pore pressure behaviour was not consistent with the 12.7mm and 25.4mm diameter tests. These observations cast considerable doubt over the validity of the 50.8mm diameter tunnel data and their subsequent use.

Tunnel diameter is also a major influence on the load factor in addition to the applied cell pressure, undrained shear strength and stress history. Hence the variations in load factor which would allow its influence to be studied necessarily also involved either a change in tunnel diameter or undrained shear strength, and hence stress history. Consequently a statement about the importance of the load factor cannot readily be made from a straightforward inspection of the data. The relevance of the load factor is discussed in Chapter 5.

An obvious dependence on the magnitude of initial pore pressure has been observed for the rate of deformation, although this has also been complicated by inevitable variations in stress history. No clear dependence on initial pore pressure has been established for the changes in pore pressure on removal of face support, which must also be strongly influenced by the stress history of the clay.

Measurements of water content at the end of each test have provided conclusive evidence of the changes in effective stress, or softening, which occur with time as the excess pore pressures brought about by the 'excavation' of the tunnel face dissipate. The significant variation of water content with tunnel diameter is an indication of the effect of scale on the rate at which events occurred in these models.

This study of the data as obtained from the model tests clearly indicates the need for the development of scaling relationships and a method of normalising the data to take account of the various controlling factors, as presented in Chapter 5.

4.1 Introduction

The successful prediction of the response of any form of engineering structure to imposed loading or boundary conditions is dependent on the constitutive model used to describe the behaviour of the material and the material parameters. Soil behaviour is more complex than that of most engineering materials due to its two phase nature (assuming full saturation), and is governed by the principle of effective stress. Consequently the selection of the most appropriate model to represent the behaviour with sufficient accuracy requires careful consideration. There are total stress theories available in continuum mechanics such as linear elastic and elastic-perfectly plastic which may provide simple predictions of soil behaviour. However total stress models are inadequate in complex loading situations, particularly where strain hardening or softening occurs or where time dependent dissipation of pore pressure is significant. A more suitable theory is that of critical state soil mechanics which is discussed later in this chapter. It is based on the principle of effective stress and was developed to provide an unified approach to the complex non-linear stress-strain response of soils. Within the framework of critical state theory, models such as Cam-clay have been developed to describe the behaviour of particular types of soil.

The time dependent deformation behaviour of clay at a tunnel face was one of the principal features investigated in the model tests, and has previously been described as being a creep phenomenon using visco-

plastic models. The same behaviour can also be analysed using coupled consolidation theory in critical state soil mechanics. The calculations involved in analyses with non-linear stress-strain relations, time dependency and complex geometry are performed using finite element programs.

In this chapter the basis of critical state soil mechanics will be briefly outlined. Numerical modelling of the small scale tunnel tests was undertaken using the CRISP finite element program developed at Cambridge (Britto and Gunn, 1987). The two soil models, modified Cam-clay which is based on critical state theory, and elastic-perfectly plastic with the Tresca yield criterion, used in the analyses are also discussed. The values selected for the parameters required by the program when using the models are presented and discussed. Analysis of the model test data required appropriate values of the undrained shear strength of the kaolin to be determined. Consideration is given to the selection of an appropriate strength and to a number of factors, such as stress history, which may affect its value.

4.1.1 Choice of material

Many of the earlier model tunnel test research projects at Cambridge have, as in this case, studied the mechanics of tunnel deformations without reference to a specific prototype. Under these circumstances the use of an industrially available soil, such as Speswhite kaolin powder produced by English China Clays Ltd., is acceptable.

The use of kaolin has a number of advantages in that the samples reconstituted from a slurry are consistent and controlled by the

preparation procedures employed, whereas good quality large field samples are difficult to obtain and are more variable in state. Previous experience at Cambridge has led to the development of the most suitable preparation methods. Kaolin has much higher coefficients of consolidation and permeability than in situ clays which are a considerable asset when the times required for sample preparation and testing are considered.

In recent years there has been some research into the fundamental stress-strain behaviour of kaolin, providing a reasonable body of data. The data base for the fundamental parameters of an in situ soil is likely to be much more limited.

4.2 Mathematical models

4.2.1 Critical state soil mechanics

Critical state theory provides a single framework within which the response of many types of soil with different stress states and stress histories can be analysed. The theory has provided a more realistic description of the behaviour of clays, in terms of the effective stress and pore pressure response to shearing and compression, by the inclusion of a yield surface. The fundamental principles of critical state soil mechanics formed the basis on which the Cam-clay models were developed.

The stress parameters used in critical state soil mechanics are the invariants p' , the mean normal effective stress and q , the deviator

stress, which are defined as:

$$p' = 1/3(\sigma'_1 + \sigma'_2 + \sigma'_3) \quad 4.1$$

$$q = 1/\sqrt{2}[(\sigma'_1 - \sigma'_2)^2 + (\sigma'_2 - \sigma'_3)^2 + (\sigma'_3 - \sigma'_1)^2]^{1/2} \quad 4.2$$

in a general three-dimensional effective stress state. Under axisymmetric triaxial stress conditions, $\sigma'_2 = \sigma'_3 = \sigma'_r$ and $\sigma'_1 = \sigma'_a$ such that

$$p' = 1/3(\sigma'_a + 2\sigma'_r) \quad 4.3$$

$$q = \sigma'_a - \sigma'_r \quad 4.4$$

where σ'_a is the axial stress (major principal stress) and σ'_r is the radial stress (minor principal stress). A third parameter, the specific volume, v , defined as $1 + e$, where e is the void ratio, is required to allow the state of the soil to be fully described.

The fundamental concept in critical state soil mechanics is the existence of a unique line in $q : p' : v$ space which is the locus of the critical or ultimate states for a particular soil. A critical state is reached when the soil continues to shear without further change in volume or effective stress. The critical state line is defined in $q : p'$ and $v : \ln p'$ space as shown in Fig. 4.1(a) and (b) by the equations

$$q = Mp' \quad 4.5$$

and

$$v = \Gamma - \lambda \ln p' \quad 4.6$$

where M = critical state friction constant

Γ = critical specific volume at $p' = 1$ (kPa)

λ = gradient of the critical state line in $v : \ln p'$ space.

In order to reach the critical state line the soil follows a stress path in $q : p' : v$ space which causes yielding or plastic straining to occur at some point depending on the initial state of the soil. The behaviour predicted from two possible initial stress states is described further. A normally consolidated soil lies on the yield surface and will yield further when a load increment is applied to it. During yielding the effective stress path moves towards the critical state line across an infinite series of expanding yield loci which form the yield surface of a particular soil. Overconsolidated samples which lie below the yield surface experience elastic (recoverable) strains until the effective stress path reaches the yield surface again. It has been found that the yield surface is also a state boundary surface, as discussed by Atkinson and Bransby (1978), which separates the soil states that are possible from those that are not, as shown in Fig. 4.2.

If the yield surface and state boundary surface are coincident it is also assumed that the behaviour below the state boundary surface is purely elastic. The isotropic compression line, which has a slope of $-\lambda$ shown to the right of the critical state line in Fig. 4.3, represents the intersection of the yield surface with the $q = 0$ plane, and as such represents a state boundary. As a sample is compressed along this line, irrecoverable or plastic strains occur. The one-dimensional (K_0) compression line, also shown in Fig. 4.3, is parallel to the critical state and isotropic compression lines, and represents

compression at a constant stress ratio ($q/p' > 0$) imposed by the condition of zero lateral strain.

Soil stress states which lie between the critical state line and the isotropic compression line in $v : \ln p'$ space are termed 'wet of critical', and samples at these states either compress or generate positive pore pressures on yielding when following a standard triaxial compression test stress path. Soils to the left of the critical state line are 'dry of critical' or more heavily overconsolidated, and would be expected to dilate or generate negative pore pressures during yielding under the same triaxial test conditions. On yielding these soils may reach a peak q/p' greater than the critical state value, which is then approached with strain softening and collapsing yield loci. In some cases where non-uniform pore pressures occur, a rupture failure occurs and the critical state is not reached. The surface defining the peak stress states dry of critical is known as the Hvorslev surface, as illustrated in Fig. 4.2.

If an element of soil experienced an unloading stress path its stress state would lie on one of an infinite number of the vertical elastic walls below the state boundary surface. An elastic wall is shown in Fig. 4.3 as a swelling line with a gradient of $-\kappa$ in $v : \ln p'$ space. Swelling and recompression take place along these lines without causing irrecoverable strains. The value of p' at the intercept of the swelling and isotropic compression line is known as the preconsolidation pressure p'_p , i.e. the maximum mean effective stress to which the soil on the swelling line has been isotropically compressed. A section along an elastic wall through the state boundary surface defines the shape of the yield locus, which separates

elastic stress states from states where plastic behaviour can also develop.

4.2.2 Cam-clay and modified Cam-clay

The Cam-clay model allows soil to be considered as an elasto-plastic material and uses plasticity theory to predict the behaviour during yielding. Cam-clay was developed at Cambridge based on the data from isotropic triaxial tests on isotropically normally and lightly overconsolidated clays, and has been particularly successful in the prediction of soil behaviour on the wet side of critical state, Schofield and Wroth, (1968). The equation of the yield locus was obtained assuming an associated flow rule to which the normality condition may be applied. The flow rule relates the input, output and dissipation of work during yielding and for Cam-clay is given by

$$\frac{d\epsilon_v^p}{d\epsilon_g^p} = M - \frac{q}{p'}, \quad 4.7$$

By applying the condition of normality and after some manipulation the Cam-clay yield locus shown in Fig. 4.4 is defined by

$$\frac{q}{Mp'} + \ln\left(\frac{p'}{p'_c}\right) = 1 \quad 4.8$$

where p'_c is the mean normal effective stress at the intersection of the yield curve and critical state line.

The model was originally developed for stress ratios less than M , but was later extended to include higher stress ratios, Roscoe and

Schofield (1963). The predictions in this region are not as reliable due to the over prediction of deviator stress when compared with experimental observations.

The shear strains at low stress ratios were found to be over predicted by the Cam-clay model due to the pointed shape of the yield surface, and an alternative yield locus was derived from a different flow rule or equation of work dissipation, (Roscoe and Burland, 1968). The equation of the elliptical yield locus of modified Cam-clay is given by

$$q^2 + M^2 p'^2 = 2M^2 p' p'_c \quad 4.9$$

The same parameters are used as for Cam-clay and the main difference lies in the separation between the critical state line and the isotropic compression line, which is given by $(\lambda - \kappa) \ln 2$ for modified Cam-clay instead of $\lambda - \kappa$ for Cam-clay, as shown in Fig. 4.3. The over prediction of strength at high stress ratios remains a difficulty in the Cam-clay models.

In both Cam-clay models the behaviour below the yield surface is defined by simple elastic relations, an assumption which may cause deformations to be poorly predicted by CRISP, for example. Much higher stiffnesses have been measured at very small strains, Richardson, (1988), and consequently a non-linear variation of stiffness with strain would provide a more realistic prediction of displacement. Other recent research, Pickles (1989), has shown that some plastic straining may occur as a stress path approaches the state boundary surface.

4.2.3 Elastic-perfectly plastic model

Models in which the yield criterion is also the failure criterion, such as that due to Tresca, are of limited value in the accurate prediction of soil behaviour. The stress-strain response is calculated in terms of total stress changes and cannot adequately model effective stress dependent soil deformations. However, in cases where the soil behaviour may be assumed to be undrained, the simple model has some merit in that it allows approximations of the response to be calculated without resorting to sophisticated numerical methods. In Chapter 5, simplified analyses using the thick cylinder and thick sphere closed form solutions are presented, in which the soil behaviour is modelled using the Tresca yield criterion defined by

$$\sigma_{\theta} - \sigma_r = 2c_u \quad 4.10$$

where σ_{θ} = circumferential principal stress

σ_r = radial principal stress

c_u = undrained shear strength.

The circumferential stress is the major principal stress where contraction of the thick cylinder occurs as the radial stress is decreased. Figure 4.5 contrasts the stress paths to failure predicted by the Tresca condition and the modified Cam-clay model for the axisymmetric conditions of the thick cylinder. For the Tresca criterion the separation between the total and effective stress paths, and hence the pore pressure, remains constant until the limiting shear stress is reached, after which the total stress and pore pressure reduce with the effective stress unchanged. Using modified Cam-clay

at an initial stress state 'wet of critical', the undrained effective stress path moves towards critical state, initially generating positive excess pore pressures which then are reduced as failure is approached and the total stress decreases. From an initially 'dry of critical' stress state the effective stress path rises vertically until the yield surface is reached. Subsequently the total stress reduces, and as the effective stress path moves towards critical state by strain softening, negative excess pore pressures are generated.

4.3 Soil parameters for the finite element analyses

4.3.1 Modified Cam-clay model

Analyses using the modified Cam-clay model in the finite element program CRISP require values for the four critical state parameters M , λ , κ and e_0 (equal to $\Gamma - 1$) to be specified in addition to an elastic constant which may be either the Poisson's ratio, ν' , or the shear modulus, G . For consolidation analyses the horizontal and vertical soil permeabilities are also necessary, whereas the bulk modulus of water, K_w , is specified for undrained analyses. Values used for these parameters are presented in Tables 4.1 to 4.3.

Ideally values for the frictional constant, M (the ratio q/p' at critical state), should be derived from laboratory stress path tests which are representative of the stress paths likely to be experienced by the finite elements. For example, at the model tunnel face the stress path for an element of soil directly ahead of the excavation is in extension. Other research workers (Al-Tabbaa, 1987, Atkinson et al, 1987 and Nadarajah, 1973) have found that the value of M is

dependent on the consolidation history of the sample and is not necessarily the same for compression and extension tests. Atkinson et al found that M values in compression and extension were identical for one-dimensionally compressed samples such that $M_c = M_e = 0.85$. Similar behaviour was observed by Nadarajah from anisotropically compressed samples of Spestone kaolin, which was reported to have very similar strength characteristics to that of Speswhite kaolin, Mair (1979). For isotropically compressed Speswhite kaolin, Atkinson et al reported values of $M_c = 0.95$ and $M_e = 0.80$ compared to Nadarajah's values for Spestone kaolin of 0.89 and 0.61, in compression and extension respectively.

If a constant value for the angle of shearing resistance at critical state, ϕ'_{cs} , is assumed, i.e. the Mohr-Coulomb failure criterion which is appropriate for a frictional material, the frictional constant M and ϕ'_{cs} may be related for compression and extension stress paths as shown below

$$M_c = \frac{6\sin\phi'_{cs}}{3 - \sin\phi'_{cs}} \quad 4.11$$

$$M_e = \frac{6\sin\phi'_{cs}}{3 + \sin\phi'_{cs}} \quad 4.12$$

A typical value of 21° , Phillips, (1986), has been used for ϕ'_{cs} which results in $M_c = 0.81$ and $M_e = 0.64$. Higher values of M and ϕ'_{cs} were presented by Al-Tabbaa (1987) based on results from one-dimensionally lightly overconsolidated triaxial samples. However, it is not clear from the data presented that the values quoted correspond to the critical states of the samples.

Recent research, Pickles (1989), has indicated that isotropically normally compressed samples, and K_0 normally compressed samples which were subsequently compressed to an isotropic normally compressed state lie on the same state boundary surface. Consequently, it may be assumed that the values for M obtained from isotropic tests are more appropriate.

Within the modified Cam-clay model it is assumed that the yield surface is symmetrical about the p' axis, i.e. M is a material constant, and only one value is required. The Cam-clay models were derived from the data of triaxial compression tests, and as such there may be no reason to assume that M is a constant. In selecting an appropriate M value the type of stress path experienced by elements of soil around the tunnel face must also be considered. Both extension and compression stress paths are anticipated, depending on the position of the element relative to the tunnel face. Consequently, the assumption that a constant ϕ'_{cs} and a variable M are appropriate led to the selection of 0.8 as the value of M for the CRISP analyses.

The gradients of the critical state line and the isotropic and one-dimensional normal compression lines are denoted by $-\lambda$ in $v : \ln p'$ space. Results from isotropically one dimensionally compressed triaxial samples of Speswhite kaolin presented by Atkinson et al (1987) indicate that a value of 0.19 is appropriate for both types of loading. In these tests the rate of loading was sufficiently slow to avoid the excess pore pressures which would otherwise have influenced the value of λ . Al-Tabbaa (1987) also tested Speswhite kaolin under isotropic and one-dimensional conditions and found the value of λ to

be identical to that given by Atkinson et al. Consequently a value of 0.19 was adopted for the finite element analyses.

The swelling and recompression line in $v : \ln p'$ space is assumed to be linear but has been observed to be dependent on the overconsolidation ratio and changes in stress path direction. Al-Tabbaa (1987) noted that a higher stiffness was obtained for the initial part of the unload/reload curve, the variation being greater for one-dimensional stress states than for isotropic conditions. Values of κ varied from about 0.02 at an OCR of two to about 0.04 for OCR of six for isotropic unloading conditions. For one-dimensional unloading κ varied from 0.03 to 0.07 for the same range of overconsolidation ratios. Other research workers, for example Richardson (1988), have obtained a value of 0.05 which appeared to be independent of K_0 or isotropic conditions. Since the nature and extent of the unloading during the model tests is not known, and the overconsolidation ratio is likely to vary considerably with distance from the tunnel face after some time during which dissipation of pore pressures and softening have occurred, a mean value of 0.05 has been selected as a generally appropriate value. A lower value of 0.02 has also been used in one analysis to demonstrate the significance of the parameter in the tunnel problem.

The parameter Γ locates the critical state line and the modified Cam-clay yield surface in $v : \ln p'$ space, and its value may be found by extrapolating the experimentally determined critical state line to

p' of 1kPa. Alternatively, if a particular soil model has been assumed, the value of Γ in modified Cam-clay may be found from

$$N - \Gamma = (\lambda - \kappa) \ln 2 \quad 4.13$$

where N is the specific volume on the isotropic normal compression line at $p' = 1\text{kPa}$. Al-Tabbaa (1987) obtained an average of 3.20 for N which results in a value of 3.10 for Γ , for modified Cam-clay. Values for Γ were reported by Richardson (1988) to be in the range of 3.10 and 3.16. The lower value of 3.10 was subsequently adopted for the analyses.

An elastic parameter is required to define the behaviour below the yield surface. The program requires a value for either ν' or G which remains constant throughout the analysis. Although it is assumed in the Cam-clay models that G is infinite, i.e. elastic shear strains are zero, this feature of the model cannot be implemented numerically and consequently elastic shear strains are calculated in CRISP. Since G is dependent on stress levels the selection of an appropriate value for an entire analysis is difficult. Consequently the use of a constant ν' parameter is preferable. A value of 0.3 was used based on the experimental relationship obtained by Wroth (1975) between plasticity index and Poisson's ratio for lightly overconsolidated clays.

For the consolidation analyses values are required for the horizontal and vertical permeabilities. Al-Tabbaa (1987) showed that permeability is a function of void ratio, e , and derived expressions

for the permeability of Speswhite kaolin in horizontal and vertical directions given by

$$k_h = 1.43e(2.09) \times 10^{-6} \text{ mm/s} \quad 4.14$$

$$k_v = 0.5e(3.25) \times 10^{-6} \text{ mm/s} \quad 4.15$$

These expressions were used to determine appropriate k_v and k_h values for the initial stress states applied in the analyses. The calculated values for the finite element analyses are given in Table 4.2. Within CRISP the value of the permeability is not updated with changes in void ratio, and remains a soil constant which may lead to some error in calculation. Values of the permeability for the initial stress states of the model tests were also calculated from equations 4.14 and 4.15. The equivalent isotropic permeability, which was required for the dimensional analysis, was obtained from

$$k = \sqrt{(k_v k_h)} \quad 4.16$$

In undrained analyses the calculation of pore pressure changes depends on the value of the bulk modulus of water K_w . Britto and Gunn (1987) suggest that values of K_w in the range of 50 to 500 times the bulk modulus, K' , of the soil should result in adequate predictions of undrained response. Lower values of K_w are likely to cause a partially drained pore pressure response, whereas higher values may result in numerical difficulties.

4.3.2 Elastic-perfectly plastic model

A small number of analyses were performed using the Tresca yield criterion of plasticity theory. Parameters defining the elastic properties of the soil were specified in terms of effective stresses, such that E' was dependent on the initial effective stress state of the sample, as shown below

$$E' = 3\nu p'(1 - 2\nu')/\kappa \quad 4.17$$

The same values were used for ν' and K_w as in the modified Cam-clay analyses. For the Tresca yield criterion, the limiting stress condition is equivalent to twice the undrained shear strength, c_u . The values used for this parameter were obtained from the critical state strength at failure, based on the same critical state parameters discussed in the previous section, and are shown in Table 4.2 for each of the analyses.

4.4 Undrained shear strength of kaolin

Although the time dependent behaviour in the model tunnel test is the primary concern of this research project, the initial conditions and 'undrained' response are characterized by the undrained shear strength in the simplified analyses. It is shown later in Chapter 5 that the undrained strength at the tunnel face has an influence on the longer term deformation behaviour.

Appropriate values for the undrained shear strength of kaolin at effective stress levels of 800kPa were not directly or readily

available in the literature. An empirical relationship was obtained by Ladd et al (1977) to relate the undrained shear strength to stress history and current stress level based on the results from a series of direct simple shear tests on K_0 consolidated samples from six different clays. They derived the expression

$$\frac{(c_u/\sigma'_{vc})_{oc}}{(c_u/\sigma'_{vc})_{nc}} = OCR^m \quad 4.18$$

where c_u/σ'_{vc} was the ratio of undrained shear strength to the current vertical effective stress, and m had a range of 0.75 to 0.85. It was noted that triaxial tests indicated that the increase in c_u/σ'_{vc} with OCR was the same or lower than that of expression 4.18.

Consequently a series of undrained triaxial compression tests were performed, and were complemented by those of Goulder (1988), for an initial isotropic state as in the model test, to establish a relationship between c_u/p' and OCR, and to investigate the influence of strain rate on undrained shear strength. Previous research has indicated that larger shear strengths may result from increased strain rates. For example Parry (1972) found that a 3% increase in shear strength may be observed when the strain rate is increased by an order of magnitude. It is likely that the strain rates in the model tests are significantly higher than those experienced by triaxial samples, and may therefore lead to the overpredictions of the initial stability ratio. The results of the tests, as shown in Fig. 4.6 have been plotted in logarithmic space to allow the value of m to be determined, assuming that the form of expression 4.18 is valid. The use of σ'_v was replaced by p' since the stress state investigated was isotropic. For the normally consolidated samples the ratio c_u/p' was found to be

0.23, and is in good agreement with the value predicted using the modified Cam-clay model. A gradient of 0.64 was obtained from the line in Fig. 4.6 which corresponds well with the value of 0.62 obtained by Nunez (1989), where c_u/σ'_v was plotted instead of c_u/p' . The expression used to calculate the undrained shear strengths for the analyses in Chapter 5 is given by

$$\frac{c_u}{p'} = 0.23 \text{ OCR}^{0.64} \quad 4.19$$

Expression 4.19 has been used to recalculate the load factors of the model tunnel tests. Initially, the stability ratio and equation 4.18 were used to calculate the stress states for a given initial load factor and pore pressure from the expression

$$\sigma'_v + u_o = LF \times N_{crit} \sigma'_v \frac{c_u(nc)}{\sigma'_{v(nc)}} \left[\frac{\sigma'_{v(max)}}{\sigma'_v} \right]^m \quad 4.20$$

using
$$N = \frac{\sigma'_v + u_o}{c_u}$$

$$N = N_{crit} LF$$

where $c_u(nc) = 180\text{kPa}$

$$\frac{c_u(nc)}{\sigma'_{v(nc)}} = 0.22$$

$$m = 0.75$$

$$\sigma' = p' \text{ (assumed for model tests)}$$

A summary of some of the possible stress states for different tunnel diameters was presented in Table 3.4.

The undrained shear strength is not regarded as a soil constant, but has been shown to vary with stress path and stress conditions. Consequently the strength would not be expected to be the same in extension as in compression and may be related, assuming that $\phi'_{cs} = \phi'_c = \phi'_e$ by

$$\frac{c_{uc}}{c_{ue}} = \frac{3 + \sin\phi'_{cs}}{3 - \sin\phi'_{cs}} \quad 4.21$$

If it is assumed that $\phi'_{cs} = 21^\circ$, and $c_{uc} = 185$ kPa, for a normally consolidated sample at $p' = 800$ kPa, the ratio c_{uc}/c_{ue} is 1.27. In view of the likely extension stress paths at the tunnel face expression 4.19, derived from the triaxial compression test results, may lead to a significant over predictions of strength for this particular case. These values have nevertheless been used since the discrepancy applied in the analyses is consistent throughout, and a more appropriate value is not available.

Data from the undrained triaxial tests at City University investigating the influence of strain rate showed that there may be a tendency for the shear strength to increase with strain rate. However, the scatter between the limited number of data points did not allow a clear relationship to be determined.

A further influence on the undrained shear strength of clay is the phenomenon known as cavitation, discussed by Bishop et al (1975) and Mair (1979). A reduction in the total stress applied to a sample of saturated soil may generate pore suctions in the sample. The magnitude of these suctions is dependent on the size of the pores and hence on the type of soil under consideration. Bishop et al found

that London clay samples could sustain much larger pore suctions than kaolin, which indicated that the behaviour was associated with failure of a meniscus in a capillary. The magnitude of pore suction at which such a breakdown occurred is related to the effective pore size of the soil. When such a loss of suction or cavitation occurs some of the pore water vaporizes and saturation is reduced. As a result the effective stress in the sample is decreased and consequently a lower undrained shear strength is measured. Tests were performed at Cambridge, Mair (1979) on samples at lower stress levels than those used by Bishop et al, the results of which are shown with Bishop's data in Fig. 4.7. Since the majority of the samples for the model tunnel tests were compressed to a mean normal effective stress of 800kPa, the data imply only a 3% reduction in strength is likely to have occurred during unloading in the model tests. However, sample no. 13, which was compressed to $p' = 2000\text{kPa}$, may have experienced a 23% loss of strength.

In summary, expression 4.19, which was derived from triaxial compression test data, has been used in the absence of other more appropriate data. It is assumed that the ratio c_{uc}/c_{ue} is constant and therefore the influence of the overestimated shear strength is consistent throughout the analyses. The values of c_{uc} used for the model test analyses in Chapter 5 are presented in Tables 3.1(a) and (b). On the basis of the data available, cavitation is only considered to be a problem for one set of tests (sample no. 13), and the strengths for these tests were reduced by the relevant percentage when analysed in Chapter 5.

5.1 Introduction

Representative model test data were presented in Chapter 3, and general statements made concerning the influence of the most relevant parameters such as load factor, initial pore pressure and tunnel diameter. In this chapter the pore pressure data, at the removal of the tunnel face support, are examined in more detail using the simplified analyses of the thick cylinder and thick sphere theories. From these analyses, an expression for the critical stability ratio is derived, which allows values of load factor to be obtained. The pore pressure response at the removal of face support is compared with values obtained for the idealized conditions. Discrepancies and limitations of the theoretical and experimental values are discussed with a view to making more realistic predictions.

Dimensional analysis is used to study the face deformation data and to develop a non-dimensional relationship between the deformation, tunnel diameter, initial pore pressure and load factor from different tests. Pore pressure changes with respect to time are examined on the same basis as the deformations using non-dimensional methods. Longer term pore pressure behaviour is considered in terms of steady seepage conditions.

5.2 Simplified analytical solutions

5.2.1 Thick cylinder analogue

The basis for using the thick cylinder solution to predict undrained behaviour around tunnels has been described in Chapter 1. Standard derivations of the solution for a thick cylinder of elastic-perfectly plastic material subjected to an internal pressure change may be found in texts on plasticity theory such as Calladine (1969) or Hoffman and Sachs (1953). A derivation, modified to suit the boundary conditions of the model tunnel tests, and extended to produce the equations used subsequently, is given in Appendix A. A number of simplifications and assumptions have been made in the analysis. Conditions of plane strain and axial symmetry are assumed based on the geometry of the problem. Figure 5.1(a) illustrates the idealized and model test geometry. An isotropic elastic-perfectly plastic model was used to describe the material behaviour, which is governed by the stress-strain equations of Hooke's law, and equilibrium and compatibility relations in the linear elastic range. Plastic behaviour or yielding has been defined by Tresca's yield criterion and the same equilibrium and compatibility equations as given for the elastic analysis. The Tresca yield condition for the tunnel problem is given by $\sigma_\theta - \sigma_r = 2c_u$, as discussed in Chapter 4.

Figure 5.2 illustrates the idealized stress distribution expected around the tunnel in a cylinder of finite radius, as a result of the soil model used and other simplifications. Removal of the tunnel boundary pressure σ_a (where $\sigma_a = \sigma_b$ initially and $N > (1 - a^2/b^2)$) causes the limiting shear stress to be reached and a zone of

plastically deforming material to be developed around the cavity. Within this plastic zone, the total stresses are reduced and vary logarithmically with radius. The distance from the central axis of the tunnel to the outer limit of plastically deforming material, at $r = c$, is known as the plastic radius, beyond which the behaviour is elastic. The magnitude of the plastic radius for a finite medium can be obtained from the expression

$$c = a \exp \frac{N - (1 - c^2/b^2)}{2} \quad 5.1$$

where c = plastic radius

a = current radius of the tunnel

N = stability ratio

b = radius of the sample

In a two phase saturated medium, such as clay, changes in the mean normal total stress would be fully reflected in the pore pressures. A reduction in mean normal total stress, p , would be accompanied by an identical reduction in pore pressure, the mean normal effective stress remaining constant as shown by the stress path in Fig. 5.3. The pore pressure change, \bar{u} , in the plastic zone is given by

$$\bar{u}/c_u = c^2/b^2 - 2\ln(c/r) \quad 5.2$$

or

$$\bar{u}/c_u = 2\ln(r/a) - N + 1 \quad 5.3$$

where \bar{u} = pore pressure change

c_u = undrained shear strength

r = radius at which \bar{u} is calculated

If the excavation occurred in an infinite medium the mean normal total stress in the elastic material would remain unchanged from its initial value, and therefore the pore pressure change in this zone would be zero. This result is due to the value of b in expressions A.20 and A.22 tending to infinity. However where the radius of the medium is finite, as in the model tests, a uniform increase in mean normal total stress, dependent on the ratio of the plastic radius to the radius of the material, occurs throughout the elastic zone.

Figure 5.4 shows that the idealized logarithmic pore pressure distribution, resulting from the removal of tunnel support pressure, has a slope of two when normalized with respect to the undrained shear strength. The radius at which $\bar{u}/c_u = 0$ is equivalent to the plastic radius in an infinite medium, or in a finite medium the plastic radius is located where the maximum value of \bar{u}/c_u occurs.

5.2.2 Thick sphere analogue

An alternative idealization of the model tunnel test conditions is illustrated in Fig. 5.1(b) where the unsupported tunnel face is represented by a hemispherical surface, and treated as part of the inner boundary of a spherical cavity in a finite medium. The centroid of the sphere is assumed to be located at a tunnel radius above the tunnel face, such that the assumed boundary and the actual unloaded boundary coincide only at the tunnel axis. The influence of this approximation on the values of $\ln(r/a)$ for the transducer positions used is insignificant. Soil behaviour was again represented by the elastic-perfectly plastic model with the Tresca yield criterion, and consequently the same limitations apply as discussed in Section 5.2.1.

The expression derived in Appendix B for the change in pore pressure within the plastic zone is given by

$$\bar{u}/c_u = c^3/b^3 - 4\ln(c/r) \quad 5.4$$

or

$$\bar{u}/c_u = 4\ln(r/a) + 4/3 - N \quad 5.5$$

where the symbols have the same meaning as in equations 5.1 to 5.3. From equation 5.4 it can be seen that the slope of the calculated lines in $\bar{u}/c_u : \ln(r/a)$ space is twice that of the thick cylinder theoretical lines. The onset of plastic behaviour occurs at a higher N value in the thick sphere and for an equivalent stress state the radius of the plastic zone in the thick cylinder is always greater than that of the thick sphere. This is consistent with the idea that a spherical cavity is a more stable structure since the area of shear surfaces mobilized is greater than for the cylinder. Results from model tunnel tests carried out by Mair (1979), in which the length of the unsupported heading was varied, showed that the critical stability ratio was significantly higher as the heading became more three dimensional, i.e. as the behaviour changed from being more cylindrical to more spherical in nature.

5.2.3 Comparison of experimental data with the thick cylinder and the thick sphere predictions

The volume of soil around the tunnel face has been divided into two zones, A and B, as shown in Fig. 5.5. In zone A it is considered that the response may be similar to that of the thick cylinder solution,

whereas in zone B it is probable that the thick sphere will give a better approximation.

Figure 1.11(a) indicated a radial stress $2c_u$ greater than the tunnel support pressure in the cylindrical volume of soil directly ahead of an excavation. For the model tests the tunnel face support pressure (axial stress) is zero, but it can be assumed that there is effectively a radial support pressure of $2c_u$ at radius $a = r_o$, which needs to be included in the calculation of stability ratio and plastic radius for the thick cylinder. The standard form of stability ratio, N , used in the model tests does not take the radial support ahead of the face into account, and is given by

$$N = \frac{P_o}{c_u} \quad 5.6$$

It is therefore suggested that a modified form of stability ratio N^* should be used to predict the pore pressure distribution for zone A conditions, where N^* is defined as

$$N^* = \frac{P_o - 2c_u}{c_u} \quad 5.7$$

or

$$N^* = N - 2 \quad 5.8$$

Experimental data from zone A, plotted in Fig. 5.6(a) with the predicted pore pressure distribution based on N^* , fall approximately within the zone defined by the thick cylinder analysis. There is a considerable scatter of data points which does not allow a clearly defined slope to be established, although in Fig. 5.6(a) (i) a general

value for the Series I data appears to be between 1.0 and 1.5 compared with two for the predicted slope. There is also some indication from the Series I tests that the slope decreases as $\ln(r/a)$ increases, and the experimental plastic radius appears to be larger than the calculated value due to the curvature of the line at larger values of $\ln(r/a)$.

The data plotted in Fig. 5.6(a) have been replotted in Fig. 5.6(b) using the dimensionless group $\bar{u}/c_u + N^* - 1$ derived from equation 5.3, together with a single line at a gradient of two which represents the distribution calculated from the thick cylinder closed form solution. The idealized line in Fig. 5.6(b) passes through the scatter of data points, which may indicate that the overall response from a large number of tests shows some agreement with the thick cylinder solution. However it was noted that the gradients between data points from transducers in the same test may fall on lines of different slopes and consequently show less correspondence. This variation in responses obtained indicates that there may be some error in measurement.

Values of $\ln(r/a)$ for the theoretical lines and experimental results have been calculated from the assumption that the current radius of the tunnel, a , is equal to r_0 , the initial radius. This simplification was unavoidable since radial deformations could not be measured, and is unlikely to have a significant effect on the distributions obtained since movements of only several millimetres were noted in the first two minutes after removal of the tunnel face support. Use of a tunnel radius which is larger than a , i.e. r_0 , in equation 5.1 would lead to an over prediction (of unknown magnitude) of the plastic radius and of the pore pressure reduction at a given radius. Another source of

discrepancy is the geometrical simplifications made, and brings into question the validity of the assumption that the unsupported model tunnel face may be adequately represented by an infinitely long unsupported cylindrical cavity, as shown in Fig. 5.1(a).

The pore pressure response in zone B for a number of the tests is shown in Fig. 5.7(a) with the predicted distribution based on the standard stability ratio, N . Data from some of the tests show some agreement with the spherical predictions with slopes of about four from tests 18/3 and 17/3; others indicate a slope closer to two. Unfortunately only a small number of tests had at least two or three transducers located ahead of the face, thereby adding to the difficulties encountered in making a reliable assessment of the slope of the line. It can also be seen from Fig. 5.7(a) that virtually all of the test data fall outside the predicted plastic radii by a considerable margin. Figure 5.7(b), in which the data are shown in a non-dimensional form with the single idealized line, demonstrates clearly that the pore pressure reductions measured were frequently significantly greater than predicted.

Calculation of the radius of the plastic zone, using equation 5.1 with N^* , for the cylindrical conditions indicated that the plastic zone extended beyond the radius of the sample for some stress states with the 50.8mm and 25.4mm diameter tunnels, for example as in tests 19/3, 19/3A and 17/3. Such tests were therefore implied to be in a state of undrained collapse. Since the instantaneous intrusion of large volumes of clay into the tunnel was not observed, equation 5.1 appears to lead to an over prediction of the size of the zone of plastic behaviour for the model test conditions, probably the result of the

lack of correspondence between the model test conditions and the thick cylinder. Smaller plastic zones were calculated for the thick sphere, an indication of its greater stability and also that it may be a more appropriate analogue for a tunnel heading where only the face is unsupported.

5.2.4 Influence of soil model on the closed form solutions

Experimentally a general form of response similar to that of the simplified analysis has been observed. However, significant differences exist between the magnitude of the observed and calculated pore pressure reductions, and some consideration should be given to the differences between the assumed and real soil behaviour. The simplified analysis has indicated that the reduction in pore pressure becomes greater with initial total stress or stability ratio but decreases with undrained shear strength, although the variation of c_u is small relative to total stress.

Examples of the disparity between the simplified and observed behaviour are shown in Fig. 5.6(a) where the reductions observed in the Series I tests such as 10/1, 11/1, 10/2 and 11/2 are all consistently smaller than the predicted changes. These observations (including the apparent curvature of the experimental lines in $\bar{u}/c_u : \ln(r/a)$ space) are evidence of the limitations associated with the use of a soil model which is necessarily simplified to allow a closed form solution to be obtained. In the elastic-perfectly plastic model with the Tresca criterion yield only begins when the deviator stress has reached its limiting value of $2c_u$, i.e. no pore pressure changes are

caused by shearing if the mean normal total stress and effective stress remain constant, as shown in Fig. 4.5(b).

A more realistic model for some circumstances is modified Cam-clay, a work hardening elasto-plastic model, which has been described in Chapter 4. Modified Cam-clay allows plastic strains to develop at lower shear stresses which may cause either positive or negative pore pressure changes to occur depending on the stress state of the soil. Typical stress paths indicating this class of behaviour are presented in Fig. 4.5(a). The difference in prediction compared with that of the Tresca model will also be influenced by the total stress path which may no longer be at constant p prior to reaching the maximum deviator stress. The Series I tests noted earlier, such as 10/1 and 11/1, had normally consolidated initial stress states. On the wet side of critical states modified Cam-clay predicts a reduction in mean effective stress during shearing and a smaller reduction in pore pressure, \bar{u} . Experimental observations are consistent with this form of behaviour. In other tests such as 16/1, 19/1A and 17/1, which were all lightly overconsolidated ($OCR < 2.0$), the measured pore pressure reductions were greater than those predicted using the elastic-perfectly plastic model, whereas slightly smaller reductions would be anticipated using modified Cam-clay. The effect of using different soil models to predict changes in pore pressure is considered further in Chapter 6.

5.2.5 Influence of experimental procedure

For tests in which the initial stress states were wet of critical, the magnitude of the pore pressure reductions and the slopes of lines in

zone A were substantially smaller than predicted for the thick cylinder. Although this may be partially or entirely due to the inadequacy of the soil model used, consideration should also be given to the accuracy of the pore pressure measurements made during the tests, and to how these may have been influenced by the experimental procedure. Typical pore pressure responses at the removal of face support, which illustrate the various types of response measured, are plotted at an enlarged time scale in Figs. 5.8(a) to (c). Large and rapid fluctuations occur, particularly in test 14/3 where the transducers were directly ahead of the tunnel face. The changes in pore pressure plotted in Figs. 5.6(a) and (b) are simply the difference between the initial pore pressure and the minimum value recorded during the removal of the face support. However, the minimum value measured may be that associated with only partial removal of support or may have been affected by very rapid dissipation due to the steep hydraulic gradients produced during the unloading procedure. Consequently the sharp rises in pore pressure observed in Figs. 5.8(a) to (c) may have masked the actual response. In cases where the reduction in mean normal total stress has created pore suctions, such as in Fig. 5.8(a), cavitation may occur in the transducer. As a result the suction measured by the transducer would be smaller than that of the surrounding soil.

The scatter of data in individual tests suggests that the experimental measurements may be a potential major source of disagreement between test data and theoretical values. Kutter et al (1988) have noted that the miniature pore pressure transducers over or under responded when anisotropic loading conditions were applied. The orientation of the transducer with respect to the major and minor principal stress

increments dictated whether the response was greater or less than that of the free field pore pressure. It has been noted that the values for the slope of the pore pressure distribution were generally larger in zone B than zone A, indicating a different form of behaviour, which may be related to the orientation of the pore pressure transducer.

5.2.6 N_{crit} and load factor

The critical stability ratio, N_{crit}, has been defined as the value of N at which the plastic radius, c, equals the sample radius, b, and for a tunnel radius, a, is obtained from the expression

$$N_{crit} = 2\ln(c/a) \quad (\text{cylinder}) \quad 5.9$$

or

$$N_{crit} = 4\ln(c/a) \quad (\text{sphere}) \quad 5.10$$

In calculating N_{crit} for the model tests, it was assumed that there was no displacement at the inner radius, i.e. $a = r_0$. Use of the undeformed radius results in the calculation of a value for N_{crit} which is lower than the true value. The load factor ($LF = N/N_{crit}$) gives an indication of how close the tunnel face is to undrained collapse (or the tunnel being instantaneously filled with clay), which would be anticipated at a value of unity.

In Section 5.2.3 it was indicated that the behaviour at the tunnel face is partly cylindrical and partly spherical, but as shown in Fig. 5.5 the spherical zone occupies a larger proportion of the volume of soil ahead of the tunnel face and may have a more significant influence on the behaviour. Consequently, equation 5.10 was adopted

in the calculation of N_{crit} for the different tunnel diameters, from which the load factors for the experimental tests were also obtained. A comparison of Figs. 5.6 (a) and 5.7(a) shows that the predicted plastic radii for the thick sphere are only slightly smaller than those of the thick cylinder based on the modified stability ratio N^* . The use of N_{crit} calculated from the thick sphere is therefore also likely to be a reasonable approximation for the zone of more cylindrical behaviour.

5.3 Non-dimensional groups

Dimensional analysis is a useful mathematical tool frequently used in modelling to determine relationships between the variables governing a particular problem. The fundamental principle of dimensional analysis, known as Buckingham's theorem, Langhaar (1951), states that the n variables on which a given phenomenon is dependent may be related in a dimensionally homogeneous equation containing $(n - r)$ dimensionless products, where r is the number of independent reference dimensions e.g. length (L), time (T) or mass (M). The n variables must also be totally independent, such that a complete set of dimensionless products can be produced, i.e. no member of the set may be derived from the other members.

The use of dimensional analysis is advantageous in experimental studies where the extent of the investigation may be reduced to include only the dimensionless products (which may be treated as variables) instead of the larger number of independent variables. Similarly, non-dimensional charts may be produced from the experimental data to replace a larger number of individual charts,

each illustrating the influence of one particular variable. Non dimensional charts should, if the dimensionless products have been correctly established, provide clear illustrations of the relationship between the dependent variable and the dimensionless products.

Data from the model tunnel tests and theoretical considerations indicated that the deformation of the tunnel face was a function of a large number of independent variables listed below:

δ	(L)	displacement at tunnel face
P_o	$\left(\frac{ML}{L^2T^2} \right)$	applied total stress
u_o	$\left(\frac{ML}{L^2T^2} \right)$	initial pore pressure
D	(L)	tunnel diameter
c_u	$\left(\frac{ML}{L^2T^2} \right)$	initial undrained shear strength
m_v	$\left(\frac{L^2T^2}{ML} \right)$	initial coefficient of volumetric compressibility
k	(L/T)	initial permeability
t	(T)	time
b	(L)	sample radius
γ_w	$\left(\frac{ML}{L^3T^2} \right)$	unit weight of water

These ten variables can be reduced to a set of seven independent dimensionless products given below as:

$$\begin{aligned}
 DP_1 &= \delta/D \\
 DP_2 &= P_o/c_u \quad (\text{stability ratio}) \\
 DP_3 &= u_o/c_u
 \end{aligned}$$

$$DP_4 = kt/D$$

$$DP_5 = kt/(m_v \gamma_w D^2)$$

$$DP_6 = b/D$$

$$DP_7 = \gamma_w D/c_u$$

5.3.1 Scaling laws for tunnels of different diameters (Series I)

The dimensionless products listed in the previous section have indicated how the factors of primary importance should be related. Consideration of the non-dimensional groups, together with an incomplete understanding of the behaviour observed, led to a step by step approach being adopted to establish an expression for the dependent parameter, the deformation of the tunnel face, δ . Initially only the data from the Series I tests were used in plotting values of the dimensionless products δ/D and $kt/(m_v \gamma_w D^2)$, as shown in Figs. 5.9 and 5.10. The group $kt/(m_v \gamma_w D^2)$ may be rewritten as $c_v t/D^2$ and is equivalent to the time factor, T_v , of consolidation theory. Since the initial values of p' , and hence k , m_v and c_u were constant, the effects of tunnel diameter and initial pore pressure may be studied in these figures.

It was thought that behaviour would be predominantly influenced by dissipation of the pore pressure changes induced by the removal of the face support. The term D^2 takes account of the time scaling factor n^2 used in physical modelling to correlate times associated with diffusion processes such as pore pressure dissipation and seepage in different scale models. A nominal value of $1 \text{ mm}^2/\text{s}$ was assigned to the parameter c_v for the purposes of this analysis, since the stress state at the start of each test was very similar. If different soils or

stress states were used, appropriate values of c_v would be needed to allow the data to be compared.

Typical plots for the stage 1 tests are shown in Fig. 5.9, from which it can be seen that there is a considerable difference between the data from the 12.7mm and 25.4mm diameter tunnel tests, with an even greater discrepancy between 25.4mm and 50.8mm diameter tunnel data. Comparisons of the Series I data in Chapter 3 have already indicated that the rate of deformation observed in 50.8mm diameter tunnel tests appeared to be greater than anticipated from the rates observed in the smaller diameter tests. This trend of behaviour has been confirmed in Figs. 5.9 and 5.10. The same non-dimensional groups were plotted in Fig. 5.10 for the stage 2 and stage 3 tests (i.e. with a lower initial pore pressure), and similar statements can be made regarding the effect of tunnel diameter. A comparison of Figs. 5.9 and 5.10 indicates that the initial pore pressure, u_0 , had a very significant effect on deformation and should be included in the dimensionless product or 'time factor'. The rates of deformation of the smaller diameter tunnel faces appeared to be directly dependent on initial pore pressure.

The data from Figs. 5.9 and 5.10 have been replotted in Fig. 5.11 (all stages) with a different dimensionless product $ktu_0/(D^2\gamma_w)$, which is derived from DP₃, DP₄ and DP₇ and continues to treat the time dependent response as one of pore fluid diffusion by the inclusion of D^2 . The dimensionless group $ktu_0/(D^2\gamma_w)$ will be referred to as the deformation time factor, T_δ , throughout this dissertation. Initial pore pressure, u_0 , and load factor both influence the steepness of the initial pore pressure gradients involved in the diffusion process. A

general observation made in Chapter 3 was that the pore pressure reductions resulting from the initial total stress changes dissipated quite rapidly, after which the pore pressures either tended towards steady values or began to rise again. These two phases of time dependent pore pressure response are discussed further in Section 5.4. The use of the coefficient of permeability may be more appropriate than c_v for the longer term behaviour, which does not appear to be consolidation diffusion. For the Series I tests the initial value of k remained constant. Data from stages 1, 2 and 3 (12.7mm and 25.4mm diameter tunnels) are seen to lie within a narrower range for a given tunnel diameter in Fig. 5.11, thereby supporting the use of the time factor, although the discrepancies which are a function of the tunnel diameter remain as observed in Figs. 5.9 and 5.10.

The larger than expected deformations in the 50.8mm diameter tests are probably due to the ratio of cover (distance between the outer boundaries of tunnel and sample) to tunnel diameter, $C/D = 100/50$, being insufficient to prevent the behaviour from being significantly affected by the constant stress boundary. In the analyses in Section 5.2.6 the ratio of the radius of the sample to that of the tunnel ($2 \times DP_6$) was used to obtain estimates of the value of N_{crit} (dimensionless) which is used with the initial stability ratio (DP_2) to form the non-dimensional load factor. For the Series I stage 1 tests the load factors (based on thick sphere theory, Section 5.2.6) were estimated to be 0.44, 0.57 and 0.81 for the 12.7mm, 25.4mm and 50.8mm diameter tunnels respectively. The value of 0.81 supports the hypothesis that the 50.8mm diameter tunnel was much closer to collapse due to the effects of the proximity of the stressed boundary. Consequently the load factor was incorporated into the group δ/D which

became $\delta/(D \times LF)$. Figure 5.12 indicates that significant differences between the data from the tests of the 12.7mm and 25.4mm diameter tunnels remained, demonstrating that an appropriate dimensionless product to take into account the influence of tunnel diameter and initial stress level on face deformation had not yet been established.

5.3.2 Scaling laws for tunnels of different diameters (Series II)

A more extensive assessment of the validity of the dimensionless products developed in Section 5.3.1 was made using the data from this series, where a much wider range of initial pore pressures and load factors was used. As a consequence of this greater variation the initial stress states of the sample were no longer constant, and the coefficient of permeability, k , was also a variable. Values of k were determined from the expressions for horizontal and vertical permeabilities of kaolin obtained by Al-Tabbaa (1987) and given in Chapter 4 by equations 4.14 and 4.15.

The parameters used to obtain the void ratio were the same as those given in Chapter 4 for the finite element analyses, and hence a value of k of 0.7×10^{-6} mm/s was obtained for a mean effective stress of 800kPa. Appropriate values corresponding to the initial conditions of the tests were incorporated into the dimensionless products before plotting.

Data from a number of tests were plotted on axes of $\delta/(D \times LF)$ against $ktu_o/(D^2\gamma_w)$, as shown in Fig. 5.13, with poor correlation as anticipated from the data in Fig. 5.12. The wider scatter shown in Fig. 5.13 compared with the Series I data indicated that some

modification to the non-dimensional groups was required. Further investigation of the dependence of deformation on load factor, as shown in Figs. 5.14 and 5.15, revealed that the response was approximately a function of the square of the load factor. In Fig. 5.14 the values of δ/D for the Series I and II tests have been plotted with load factor at a value of t/D^2 of 0.01min/mm^2 . The use of t/D^2 instead of $ktu_0/(D^2\gamma_w)$ is a simplification based on the assumption that the variation in k is insignificant. The influence of initial pore pressure has been taken into account by plotting lines of constant u_0 in Fig. 5.14. For a particular initial pore pressure the data were close to separate lines of an approximately parabolic shape, indicating increasing δ/D with higher initial pore pressure.

The parameters δ/D and LF were replotted in logarithmic space for initial pore pressures of 200kPa and 400kPa at $t/D^2 = 0.01\text{min/mm}^2$, as shown in Fig. 5.15. A linear variation was indicated, with slopes of 1.98 and 2.07 for a u_0 of 200kPa and 400kPa respectively. Values of δ/D and load factor for $ktu_0/(D^2\gamma_w)$ of 8×10^{-6} and 15×10^{-6} have been plotted in logarithmic space in Fig. 5.16, from which best fit slopes of 2.02 and 2.25 were determined for the scatter of data points. The use of load factor to the power of two was adopted, although it is noted that it may only be an approximation, particularly as the deformation time factor increases. The curves in Fig. 5.14 indicate a similar dependency of δ/D on load factor to that shown by Mair (1979) in Fig. 1.6, where volume loss was related to load factor. The model tests performed by Mair were virtually undrained, such that t/D^2 would be very small and such data would represent the shallowest of a series of curves of δ/D increasing with t/D^2 .

Some of the data from Fig. 5.13 have been replotted in Figs. 5.17-5.19 for the tests conducted in samples 17, 18 and 19 using the dimensionless product $\delta/(D \times LF^2)$. The range of load factors applicable to each set of plots is also given in the figures. The data are in much closer agreement, although there are some noticeable discrepancies. Figure 5.20 shows that the range of values obtained for many of the Series II tests and a number of the Series I tests deviates from a mean line by about $\pm 25\%$.

Tests 13/1A to 13/3 were separated from the other tests in Series I by a higher preconsolidation pressure of about 2MPa (compared with 800kPa for the other tests). During the tests the same stress levels were applied as in Series I tests. Data from these tests have been analysed in the same manner as before, the results of which are shown in Fig. 5.21. The deformation curves are considerably steeper than expected from the Series I tests. Several factors affecting the parameters used in the non-dimensional groups may account for part or all of this lack of agreement.

The value obtained for the permeability of kaolin at the appropriate stress state depends on the extrapolation of the expressions given by Al-Tabbaa (1987) beyond the range of stress states on which they were based. These expressions require a value for void ratio, which was determined using the parameters defined in Chapter 4, on the assumption that the slope of the normal compression line remains constant in $v : \ln p'$ space (at least up to a p' of 2MPa). An indication of the magnitude of the influence of void ratio may be given by calculating the permeability for void ratio higher than that obtained based on the assumptions stated previously. For instance, at

the end of consolidation to a p' of 2000kPa the void ratio is 0.756, using a λ of 0.19. If the value of λ is reduced to 0.15 between a p' of 800kPa and 2000kPa the void ratio becomes 0.793. The values of the coefficient of permeability, after swelling back to a p' of 800kPa, are 0.469mm/s for the constant λ value and 0.529mm/s for a reduced λ . The latter represents a 13% increase, which would bring the sample no. 13 tests into closer agreement with the Series I tests. Recalculation of the permeability based on the measured water content of about 32% resulted in an increase from 0.469×10^{-6} mm/s to 0.523×10^{-6} mm/s, which is very similar to that calculated for the reduced λ . It was, however, noted in Section 3.5 that the water contents were subject to some error, particularly for the 12.7mm diameter tunnel.

It has also been assumed that the empirical relationship suggested in Chapter 4 to determine the undrained shear strength of overconsolidated soils remains valid when extrapolated to these high stress levels. A value of approximately 330kPa was predicted using equation 4.19. Theoretical predictions of c_u can also be obtained within the framework of critical state soil mechanics, as described in Chapter 4, where the undrained shear strength is a function of water content. Two values of water content are possible; the first is theoretical, subject to the same assumptions as the permeability calculations, and the second is that measured from samples of clay removed from the sample as the tunnel was advanced before each test.

The theoretical value of the water content (assuming $G_s = 2.61$) is 28.9% which implies an undrained shear strength of 480kPa, whereas the measured value of water content was about 32% which indicates a strength of 311kPa. The latter value is only slightly lower than that

obtained from equation 4.19 and leads to small increase in load factor.

The influence of cavitation, discussed in Chapter 4, was found to be negligible for kaolin samples compressed to $p' = 800\text{kPa}$, Fig. 4.7. However, the same figure also indicated that samples compressed to much higher mean normal effective stresses were more susceptible to cavitation and reductions in undrained shear strength. From Fig. 4.7 the probable decrease in c_u for tests in sample no. 13 is about 23%. Revised values of N and LF were determined and the data in Fig. 5.21 have been replotted in Fig. 5.22. Much closer agreement is indicated, the difference having been reduced from a factor of about 2.6 to 1.3.

A series of model tests were performed in another triaxial apparatus, Baker (1988), with the sample size and tunnel diameter being a factor of about 2.5 smaller than that of the 50.8mm diameter tests. Data from the 19.1mm diameter tunnel tests have been plotted non-dimensionally with several 50.8mm diameter tests and a number of the 25.4mm and 12.7mm diameter tests in Fig. 5.23. Deformation curves for the 19.1mm diameter tunnel face were slightly shallower than those of the 25.4mm and 12.7mm diameter tests, and considerably lower than those of the 50.8mm diameter tests. This result is unexpected given the similarity of the geometrical conditions and applied stresses in these tests, and no explanation for the significant disparity has been found.

Several of the uncertainties concerning the data from the Series I and II tests, and the parameters used to present the model test data in the form shown in Fig. 5.20, have already been discussed in this

section, and may account for some or all of the deviation shown by the deformation curves. However, a significant simplification has been made throughout this analysis by the exclusion of any time dependent changes to the soil parameters. Both the undrained shear strength (and hence load factor) and permeability would be expected to change as the time dependent process of pore pressure diffusion produced a state of reducing effective stress around the tunnel face. The initial value of the undrained shear strength has been used throughout the analysis of the tests by means of the load factor, although the increased water contents measured at the end of each test, as discussed in Chapter 3, would clearly have resulted in a significantly lower "undrained" shear strength, at least in the soil close to the face. The increases in water content appeared to be functions of the initial pore pressures and tunnel diameter, although no quantitative analysis was possible, and were observed typically to extend ahead of the face for a distance of about twice the tunnel diameter. Since various combinations of pore pressure and tunnel diameter have been used in the tests, it is improbable that the rate of change of water content, undrained shear strength and load factor was consistent throughout the test series, and may have contributed to the divergence shown in Fig. 5.20.

5.4 Time dependent pore pressure response

The pore pressure responses from a range of tests were presented in Chapter 3, and illustrated in Figs. 3.6(b) to 3.27(b). General trends of behaviour after the face support had been removed appeared to be common to a number of tests. Two distinct phases of pore pressure response were observed, and are illustrated in Fig. 5.24. Dissipation

phase A lasted for the first few minutes of the test during which significant changes in pore pressure, either increases or reductions, were observed. In dissipation phase B two types of response were evident, in which the pore pressure was either almost constant or steadily rising. It should be noted that all of the pore pressure observations were highly dependent on the position of the transducer relative to the tunnel face, and also the accuracy with which the locations were known.

5.4.1 Dissipation phase A

Examination of the data presented in Figs. 3.8(b), 3.9(b) and 3.12(b) to 3.15(b) for the Series I tests indicates that the pore pressure reductions caused by the removal of the tunnel support pressure dissipated rapidly before reaching a peak value after which a further slower reduction was recorded, in some cases to a second minimum value. These changes were observed in all the stages of the 25.4mm and 50.8mm diameter tunnel tests at r/r_0 values < 2 , and in the 12.7mm diameter tests where the initial pore pressure was about 80kPa. The rate and time at which the dissipation changes occurred appears to be related to the diameter of the tunnel, the radius at which the transducer was located, and the initial pore pressure, although the rate at which events occurred in the 50.8mm diameter may have been influenced by the constant stress boundary of the sample.

At more remote transducers (e.g. $r/r_0 = 2.6$) where the initial pore pressure was 200kPa, the changes after removal of face support are of a continuing reduction to a minimum value. The time at which the minimum pore pressure level was reached is taken to be indicative of

the end of the transient changes, after which steadier conditions exist.

In the Series II tests, Figs. 3.18(b) to 3.27(b), the relationship between pore pressure behaviour, tunnel diameter, transducer location and initial pore pressure is further complicated by the dependence of pore pressure response on the state of the sample. However, there is some evidence to suggest that the dissipation towards a minimum value is more rapid with a higher initial pore pressure; for example, compare tests 11/1 and 17/2, Figs. 3.8(b) and 3.24(b). Attempts have been made to establish non-dimensional groups to relate the minimum point to the transducer location and initial test conditions. Data from Series I were plotted initially as shown in Fig. 5.25 using the time factor developed for the deformation behaviour, which demonstrated clearly that the $ktu_0/(D^2\gamma_w)$ term was inappropriate for correlating the pore pressure behaviour observed around different diameter tunnels.

Consideration of the radial nature of the tests suggested that the times at which the pore pressure minimum occurred and transducer locations might be related logarithmically. Consequently a non-dimensional time factor of the form $kt/(r_0 \ln(r/r_0))$ was developed and plotted with data from the Series I tests shown in Figs. 5.26(a) to (c). For a given initial test stress state, there is reasonable agreement between transducers at different positions and the value of the time factor at the minimum point. Minimum values were obtained at a larger time factor for the tests with lower initial pore pressure. Data from different diameter Series I tests also show some correlation.

Non-dimensional groups to relate tests with different stress states were investigated but it was not possible to show any clear relationships. It is likely that the behaviour after the removal of the face support is too complex to be analysed by dimensional methods. The pore pressure changes observed during the dissipation phase were a combination of the diffusion process of the flow of water towards the tunnel face and the stress changes which occurred to maintain an equilibrium state with the boundary conditions. It was suggested in Chapter 3 that the varying pore pressure with OCR during shearing prevented any relationship between stress levels from being identified.

5.4.2 Dissipation phase B

In the discussion of the pore pressure data in Chapter 3 the term 'apparently steady' was applied to the long term pore pressure response measured in a number of tests. This class of behaviour existed in tests where both the initial pore pressure in the sample and the load factor were low, such as in Series I stage 2 or 3 tests and tests 16/1 and 16/2 from Series II, which had $LF \leq 0.5$ and $u_0 \leq 200\text{kPa}$. The majority of other tests indicated pore pressures that were still rising towards the end of the test.

It was suggested that the steady pore pressures may be the result of a condition of steady seepage in the sample which could be maintained only until the pore pressure at the outer boundary became lower than the initial value. The validity of this hypothesis has been investigated by means of the radial flow net given by Taylor (1948), shown in Fig. 5.27(a). The flow net represents a well with an

impermeable cylindrical boundary, allowing water flow to the base of the well only, and would correspond to the steady seepage flow conditions of a model tunnel test. Taylor also noted that the geometry of the radial section had only a small effect on the results since virtually all of the head loss occurs close to the entrance of the well (corresponding to the face of the tunnel). Consequently only small differences should be expected in the comparison between the flow net and the model test data due to the geometrical differences.

A number of typical transducer positions have been indicated on Figs. 5.27(b) to (d) from the tests in which steady conditions were observed. In test 11/2 the transducers at r/r_0 of 1.4 and 2.6 measured pore pressures of about 23kPa and 53kPa respectively, compared to 49kPa and 66kPa estimated from the flow net. Values from the flow net again indicate higher pore pressures at r/r_0 of 1.6 compared with tests 16/1 and 16/2. The relevant values are 135kPa compared with 35kPa and 38kPa compared with 12kPa. Data from the 12.7mm diameter tests at r/r_0 of 2.6 show the pore pressure to be between 30kPa to 50kPa whereas the flow net indicates value of about 60kPa.

Predictions of pore pressure based on the flow net are consistently significantly higher than those measured in the model tests, a disparity which is unlikely to be entirely due to the geometry. A more probable cause is the difference in boundary conditions in the model tests. A zone of continually deforming soil exists around the tunnel and the region of soil affected by pore pressure changes is steadily extended. In the softened zone around the tunnel face the permeability, which is dependent on void ratio, will be larger than in

the more distant zones of soil. As a result a greater loss of head would occur in the outer zones of a model test than in a flow net assuming uniform permeability. Consequently steady seepage conditions cannot be established. It is concluded from these observations that although constant pore pressures exist under some circumstances, they do not correspond to pore pressure predicted from a seepage flow net or to a state of steady equilibrium.

5.5 Conclusions

Simplified analyses based on thick cylinder and thick sphere solutions of plasticity theory have been applied with limited success to the unsupported tunnel face. The idealized solutions were found to be inadequate principally in terms of geometrical representation and in terms of modelling the soil response to shearing.

Distributions of pore pressure with radius were obtained from the idealized solutions and compared with the experimental data. Two classes of behaviour have been identified which indicate that the soil surrounding the tunnel face may be divided into zones of approximately cylindrical and spherical behaviour. In the zone of cylindrical behaviour (zone A) the measured pore pressure reductions were found to show some agreement with predictions based on a thick cylinder and a modified stability ratio, N^* . Derivation of N^* was based on the radial support pressure of $2c_u$ ahead of the tunnel face indicated by a lower bound stress field. Directly ahead of the face, in zone B, the gradients of the pore pressure distribution compare more closely with predictions from a thick sphere analysis. A stability ratio, N ,

determined for full removal of support pressure is applicable in this zone.

Generally it was found that the measured pore pressures changes in zone A were smaller than in the thick cylinder analysis, whereas in zone B many of the reductions were significantly larger and more widespread than those predicted. The cause of this inconsistent variation has not been clearly identified, but it is considered that the pore pressure transducers have an influence on the measurements.

Within both zones the magnitude of the pore pressure response varied with the initial stress state of the clay, one of the most significant factors in the comparison between the experimental and idealized values. It was not possible to obtain a quantitative assessment of the relationship between stress state and pore pressure reduction from the tests performed.

From dimensional analysis, two dimensionless groups, $\delta/(D \times LF^2)$ and $ktu_0/(D^2\gamma_w)$, have been established which demonstrate the importance of load factor and initial pore pressure on time dependent deformation. The coefficient of permeability, k , has been included in the dimensionless time factor since the flow of water is likely to influence the rate of deformation. The relevance of k rather than c_v was indicated by the second of two distinct phases of pore pressure behaviour observed. In the first phase pore pressures dissipated rapidly to a minimum point. During the second phase steadily increasing pore pressure, or in some cases a constant pore pressure was measured, which could not be considered as the result of consolidation process.

Dimensional analysis has indicated a promising scaling relationship for the 12.7mm and 25.4mm diameter tunnels. Non-dimensionalized data from the 50.8mm diameter tests did not correspond well with the smaller tunnels. Higher rates of deformation were indicated, which may be the result of significant boundary effects in the 50.8mm diameter tests.

Data from a set of tests in which the preconsolidation pressure was 2000kPa (compared with 800kPa for the majority of tests) demonstrated the importance of the parameters c_u and k on the observed behaviour. At these high stress levels the relationships for the variation of c_u and k with stress level and stress state, derived from data at lower stress levels, may no longer be valid.

Non-dimensional groups have not been established for the time dependent and location dependent pore pressure behaviour, due to the complexity of the problem. A comparison of the almost constant pore pressures observed in some tests with a steady seepage flow net showed that the longer term conditions in the sample did not appear to correspond to steady seepage.

-

6.1 Introduction

Adequate representation of all the significant factors influencing the observed behaviour of a particular problem is as essential in numerical modelling as it is in physical modelling. In some cases sufficiently accurate analytical solutions may be obtained from a closed form approach, such as the thick cylinder and thick sphere analyses described in Chapter 5 which were used to study the initial 'undrained' behaviour of the model tunnel tests. However, it was found that although these simple solutions predicted the form of behaviour observed, the numerical values were in poor agreement with the experimental data, and only of limited value in this particular case. The undrained behaviour in a model tunnel test is too complex to be modelled with sufficient accuracy by the closed form solution in two respects. Firstly the geometry of the tunnel face is too difficult to be represented accurately in a 'hand calculation', and secondly the soil behaviour on shearing is stress state dependent. Changes controlling the time dependent behaviour of an elasto-plastic soil, as used in the model tunnel tests, are intractable as far as closed form solutions or 'hand calculations' are concerned.

A more appropriate analytical approach to the model tunnel problem is by the use of the finite element method, a technique which was originally developed for the analysis of problems in structural engineering based on continuum mechanics. Saturated soil is a two phase material, with non-linear stress-strain characteristics, the

behaviour of which is dependent on the effective stresses which may vary with time. Finite element programs have been developed specifically for geotechnical engineering with adaptations to take account of the two phase nature of soil by the inclusion of appropriate constitutive relations. Time dependency, complicated geometry and a more realistic soil model may all be incorporated into analyses using the finite element method.

For the analyses of the model tunnel tests a finite element program called CRISP was used, details of which are given by Britto and Gunn (1987). An important feature of this program, in relation to the class of behaviour investigated by the experimental work, is the inclusion of Biot's theory of coupled consolidation, i.e. the changes in excess pore pressure with time and soil strains are related. A number of soil models are available in the program, including modified Cam-clay which is based on work hardening plasticity, as described in Chapter 4. The three dimensional tunnel heading problem has been simplified by the axisymmetric conditions applied to the physical model, which allow the tests to be modelled numerically as a two dimensional angular sector.

Analyses presented in this chapter have been performed to study the behaviour of a plane strain idealized tunnel situation represented by a thick cylinder. The modified Cam-clay soil model and an elastic-perfectly plastic model were used in undrained analyses with different initial stress states to allow comparisons to be made between the predicted pore pressure changes as a function of the soil model. The finite element predictions were also compared with the closed form solutions based on the Tresca yield criterion used in Chapter 5.

Several consolidation analyses were also performed to study how the pore pressure behaviour with time, under the geometrically simpler conditions of a thick cylinder, varied with that of the model test analyses presented in Chapter 7. Several different load factors and initial pore pressures were used to indicate how these parameters influenced the predicted behaviour.

6.2 Details of the analyses

6.2.1 Development of thick cylinder finite element meshes

The configuration of elements used in the thick cylinder analyses is shown in Fig. 6.1(a) with an enlarged detail of the concentration of small elements at the inner boundary shown in Fig. 6.1(b). The thick cylinder was represented as a radial section of a disc of soil 7.5mm thick. The radii of the inner and outer boundaries, r_i and r_o , were 6.25mm and 125mm respectively, allowing the smallest diameter tunnel to be modelled under idealized plane strain cylindrical conditions. The nodes along the horizontal boundaries of the mesh were restrained in the vertical direction to apply the plane strain condition but were free to be displaced radially. Only the 12.7mm diameter tunnel was modelled since analyses of the larger diameters encountered numerical difficulties. This result is consistent with the 'hand calculations' discussed in Chapter 5 which showed that for the larger diameter tunnels, under certain initial stress conditions, a plastic radius larger than the outer radius of the sample was obtained with the Tresca yield criterion.

For the undrained analyses the mesh consisted of cubic strain triangles, each of which contained 16 integration points, at which the stresses were calculated. It has been shown that the use of these higher order elements becomes necessary to maintain numerical stability under conditions of undrained axisymmetric collapse, Sloan and Randolph (1982). The same element layout was used for the consolidation analyses, but in this case the use of the lower order linear strain triangles was acceptable. The mesh was developed to be suitable for both classes of analysis, to allow comparisons to be made directly.

6.2.2 Development of analysis procedure

At the start of the analysis in situ stresses were specified to be in equilibrium with the imposed boundary conditions. The support pressure at the inner boundary was reduced to zero in a large number of increments in the undrained analyses, with the magnitude of pressure reduction in each increment selected to ensure that the yield ratio remained within the recommended limits of 1.0 ± 0.05 . The yield ratio indicates the amount by which the yield locus has expanded during hardening or contracted during softening. Its value is obtained from the ratio of the preconsolidation pressure at the end of the load increment to the preconsolidation pressure at the start of the increment, assuming the soil to be yielding. For the consolidation analyses a number of very short time increments were used during the reduction of the inner boundary pressure. After the support pressure had been reduced to zero the analyses were continued on an incremental time basis, allowing dissipation of the pore suctions close to the unsupported boundary to take place. As the

large pressure gradients near the boundary decreased, the size of the time increments was steadily increased.

Flow of water towards the unsupported boundary caused the pore pressures to become positive in some cases, a condition which reduced the hydraulic gradients and the rate of flow towards the boundary. Positive pore pressures at the unsupported boundary lead to the physically unrealistic condition of negative effective stress which causes numerical problems since the element stiffnesses are obtained from the p' values. In such cases the analyses were performed again with a boundary condition of zero absolute pore pressure applied to the nodes along the unsupported boundary at the appropriate time to prevent the physically impossible state from developing.

6.2.3 Selection of soil model

For the undrained thick cylinder analyses two soil models, modified Cam-clay and elastic-perfectly plastic with the Tresca yield criterion, were used. These soil models were used to allow the results from the finite element calculations to demonstrate the influence of soil model on the predicted pore pressure behaviour, as well as to give a comparison with the closed form solution used in Chapter 5. Modified Cam-clay was used in the analyses of consolidation in a thick cylinder. A discussion of the parameters used was presented in Chapter 4, and details of these were summarized in Table 4.1.

6.3 Undrained analyses of a thick cylinder

Five analyses are presented which investigate the influence of overconsolidation ratio and soil model on the undrained response of the soil to the total removal of the support pressure at the inner boundary of a thick cylinder. Some quantitative as well as qualitative appreciation of the simplifications in the idealized thick cylinder calculations may also be obtained. Details of the stress states selected for the analyses are given in Table 6.1. Figures 6.2(a) to (c) show part of the deformed meshes for the modified Cam-clay analyses after complete removal of the support pressure, the larger radial displacement being for analysis TCU1 at the largest stability ratio. Values for the stability ratio, undrained shear strength and shear modulus based on the critical state parameters for modified Cam-clay, discussed in Chapter 4, are also presented in Table 6.1.

Calculations of displacement at the inner boundary based on the Tresca yield criterion, given by equation A-46 in Appendix A, are compared with those predicted by the modified Cam-clay finite element analyses in Table 6.1. Equation A-46 was derived by assuming that the cavity was contained in an infinite medium, i.e. the radius of the sample was much greater than the plastic radius. A hand calculated solution for a finite radius cannot be readily obtained.

Analysis TCU1, in which modified Cam-clay was used to model a normally consolidated soil, is compared with the elastic-perfectly plastic analysis TCU4 (with the Tresca yield criterion), and the hand calculated solution. The displacement predicted at the inner boundary using modified Cam-clay is a factor of 1.26 greater than that of the

'hand calculation', and a factor of 1.32 greater than TCU4. Larger displacements are anticipated for the analysis with normally consolidated modified Cam-clay due to the different assumptions made in the model to define plastic behaviour. Plastic strains occur with any shear stress in the modified Cam-clay model, whereas elastic behaviour is assumed until the limiting shear stress is reached in the elastic-perfectly plastic model. As the soil yields in analyses such as TCU1 the mean normal effective stress is reduced which leads to a reduction in the element stiffnesses and hence larger deformations.

The idealized solution using the Tresca yield criterion over predicted the displacement, by factors of 1.24 and 1.18, compared with analyses TCU2 and TCU3, which modelled overconsolidated soils. Different assumptions in the two models describing the soil behaviour after the maximum shear stress has been reached may be the cause of the disparity. Smaller deformations are to be expected for modified Cam-clay analyses with an OCR greater than two since the effective stress increases as pore suctions are generated during strain softening and consequently the element stiffnesses are also increased. For the elastic-perfectly plastic model a constant stiffness is assumed. However reasons for the disagreement between TCU2 with an OCR of two and the idealized calculations are less obvious.

Much closer agreement was obtained between the finite element computations and closed form solutions using the Tresca yield criterion, the difference being 4.5% in both cases. Theoretically these values should be identical, however some disparity is to be expected in view of the computational requirement for a finite bulk modulus of water in order to permit undrained behaviour to be modelled

in the finite element program. The closed form solution is also based on the assumption of an infinite outer radius, as given by equation A-46.

The pore pressure predictions under truly undrained conditions are also of some interest in view of the poor correlation between the idealized closed form solution and the experimental data, as demonstrated in Figs. 5.6(a) and (b). These analyses were intended to provide data for the fully undrained response which may also be compared with the unloading phase of the thick cylinder consolidation analyses discussed later. Figure 6.3(a) shows the distribution of non-dimensional pore pressure change, $\bar{u}/c_u + N - 1$, with $\ln(r/a)$. Under the idealized conditions described in Chapter 5 a slope of two is anticipated, whereas all three modified Cam-clay analyses predicted steeper slopes at low $\ln(r/a)$ values, which approached two as $\ln(r/a)$ increased. Smaller plastic radii were also predicted. It was found that the results had been significantly influenced by the specified value of K_w which was equivalent to $100K'$ and at the lower end of the range suggested by Britto and Gunn (1987). The changes in specific volume were examined and indicated that the analyses were not fully undrained, as a result of numerical problems. Other analyses were performed with various K_w values which indicated that a value of the order of $10K'$ was more appropriate. It appears that an optimum range of K_w values exists, which allows undrained behaviour to be modelled without numerical instability, and which may need to be assessed on a 'trial and error' basis.

Results from these analyses are plotted in Fig. 6.3(b). For analysis TCU1 ($OCR = 1.0$) the reduction in pore pressure was under predicted,

as anticipated from the discussion of the soil behaviour during shearing in Chapter 4, and also from the experimental observations. Analysis TCU4, with the same initial stress level as TCU1 but using the Tresca yield criterion, unexpectedly also indicated a consistently smaller pore pressure reduction (although much less significant than in TCU1) than that of the closed form solution.

The gradients of the predicted distributions for TCU2 and TCU3 were steeper than those based on idealized Tresca conditions. Pore pressure reductions in TCU2 were smaller than those given by the closed form solution. It was anticipated that the predictions from TCU2 would be equivalent to those of TCU5 and the closed form solution. However, TCU5 was in close agreement with the 'hand calculated' distribution and no reasons can be suggested for the discrepancy with TCU2 other than that it is simply a feature of the numerical procedures involved. On the dry side of critical state in TCU3 larger pore pressure reductions were predicted close to the unsupported boundary ($\ln(r/a) \leq 0.5$) compared to the idealized solution. At values of $\ln(r/a) > 0.5$ the pore pressure changes were under predicted. It may be more appropriate to compare the behaviour with that of TCU2, which although close to the idealized response, indicated that the slope was greater than two. In comparing TCU3 with TCU2 the pore pressure reductions are consistently over predicted, as expected from a dry of critical state and discussed in Section 4.2.3.

The most important results from these analyses are summarized below:

- a) careful selection of an appropriate K_w value is required to

allow truly undrained analyses to be performed without numerical difficulties;

- b) in comparison with the modified Cam-clay analyses the idealized closed form solution under predicted displacement for wet of critical states and over predicted for those dry of critical;
- c) significant differences in undrained pore pressure response were obtained using the modified Cam-clay soil model and the elastic-perfectly plastic model (Tresca yield criterion); over predicted reductions were obtained using the Tresca yield criterion in analyses representing soil at an OCR of less than two, whereas the changes were under predicted for an OCR greater than two;
- d) for an analysis on the dry of side of critical state the gradient of the pore pressure distribution with the logarithm of radius was steeper than the idealized value of two.

6.4 Consolidation analyses of a thick cylinder

6.4.1 Introduction

A number of consolidation analyses were carried out to provide some indication of the behaviour to be expected on and subsequent to the removal of the inner boundary support pressure for a problem with a simpler geometry than that of the model tunnel tests. The nature of a cylindrical response has been investigated since the experimental data in zone A (located beyond the tunnel radius, perpendicular to the

central axis) showed some agreement with the thick cylinder analogue. Various initial stress states were used to demonstrate the influence of load factor and initial pore pressure.

Five analyses were performed with the mesh used in the undrained analyses, shown in Fig. 6.1(a). Although the element layout was the same, the element type used in this case was the linear strain triangle for consolidation, in which the pore pressures are treated as unknown variables. The stress states were selected to allow the response from analyses using the modified Cam-clay model to be studied and are summarized in Table 6.2. The results from these analyses are considered firstly in terms of the 'undrained' response to the removal of the inner boundary support pressure, and secondly as the time dependent response.

6.4.2 Undrained response

Details of the displacement predictions from the finite element analyses at the end of unloading and from the closed form solution are given in Table 6.2. As expected the largest displacement was predicted for the analysis with the highest load factor (TCC1). For the two analyses with the lower load factors, (TCC2 and TCC5) the finite element predictions of displacement were slightly smaller than the closed form solution, whereas larger deformations were obtained with higher load factors.

Figure 6.4 shows that the initial displacement at the inner boundary after removal of the support pressure in the consolidation analyses may be a function of LF^2 , for $LF > 0.5$, although only a small number

of data points are available to support this hypothesis. A similar dependence on load factor was observed for the time dependent deformations in the model tests. Deformations predicted in the undrained analyses were significantly smaller than from the consolidation analyses, and a relationship with LF^2 has not been as clearly established.

Predicted changes in pore pressure, resulting from the removal of support pressure, are plotted in $\bar{u}/c_u + N - 1 : \ln(r/a)$ space in Fig. 6.5, together with the 'hand calculated' distribution based on the idealized Tresca criterion. There was some correspondence between the finite element analyses and the 'hand calculations', with the idealized line at a slope of two passing through the finite element distributions and taken to represent a mean distribution. For stress states initially on the wet side of critical the slopes were approximately similar to that of the idealized solution but became shallower as $\ln(r/a)$ increases, as observed experimentally. Steeper slopes are predicted for the analyses with an initial overconsolidation ratio greater than two. Similar behaviour was also predicted in the undrained analyses discussed earlier.

Reasonable agreement may be expected between the idealized solution and analyses TCC2 and TCC3, with an initial OCR of 1.6 (Fig. 6.5) as this is close to the condition of $OCR = 2.0$ where the behaviour should be elastic-perfectly plastic. A small over prediction was anticipated from the closed form solution compared with these two analyses. However, there was a significant difference between the analyses in that a larger non-dimensional pore pressure reduction was predicted for TCC3 than TCC2. This may be the result of the larger displacement

at the inner boundary during unloading in TCC3, which was greater than anticipated from the 'hand calculations'. Figures 6.6(a) and (b) show the radial distribution of pore pressure and specific volume at the end of unloading for the two analyses, and also the much larger plastic radius in TCC3. For analysis TCC3 the increase in specific volume close to the inner boundary was significantly greater than that of TCC2. However this behaviour was confined to a small localized zone with virtually no change in specific volume having occurred at a distance greater than r_0 from the inner boundary. The unexpected pore pressure distribution for TCC3, in Fig. 6.5, may be the result of water flowing towards the boundary from the elements close to those at the boundary due to the high hydraulic gradients. If water cannot flow into the draining elements rapidly enough (from other elements at larger radii) due to lower hydraulic gradients at a larger radius, then the specific volume would be reduced and the pore pressure reductions would be greater than anticipated.

The gradient of the closed form solution was less steep than those of TCC4 and TCC5, (Fig.6.5), in which more heavily overconsolidated soils were being modelled. The difference may also be explained by some drainage having taken place during removal of support pressure as a result of the large hydraulic gradients close to the inner boundary. Figures 6.7(a) and (b) show the changes in specific volume and pore pressure distribution with radius. An increase in specific volume close to the boundary is shown for both TCC4 and TCC5. At a small distance from the boundary the specific volume was lower than the initial value, to which it gradually returned at a greater radius. The extent of this reduction was considerably greater in TCC4 (higher pore pressure and load factor), as expected from the larger change in

pore pressure in Fig. 6.5. The variation in specific volume has probably been caused by the imbalance of water flow, as suggested earlier for the behaviour in TCC2 and TCC3. The changes in specific volume during very short unloading times support the suggestion in Chapter 5 that the pore pressure transducers may not have measured a truly undrained response.

6.4.3 Consolidation behaviour

The stress levels used in three of the five analysis, particularly in terms of pore pressure, were lower than would be expected for in situ deep tunnel conditions. Consequently analysis TCC1, in which the initial mean effective stress and pore pressure were both equal to 600kPa, was performed to model a more realistic in situ stress level. Table 6.2 shows that its stability ratio of 6.85 exceeds the critical value of 5.99, which is based on no displacement at the inner boundary, i.e. $a = r_o$. This assumption leads to the calculation of a smaller N_{crit} , as discussed in Chapter 5. In practical terms such high load factors would not exist and some form of support would be provided for greater stability.

The finite element analysis predicted a displacement of about 5mm at the inner boundary during the removal of the support pressure, after which almost no further deformation occurred, as shown in Fig. 6.8. The initial displacement is equivalent to a volume loss of 96%. The cylinder appeared to have 'locked up', having shown virtually undrained collapse. The mean effective stress path for element 17, Fig. 6.9 moved away from the critical state line at almost constant q , and almost no softening was predicted as shown in Fig. 6.10. Analysis

TCC1 experienced considerable numerical difficulties and has been included here to demonstrate the limitations in modelling behaviour which involves large displacements and extremely steep stress gradients. An analysis with increased number of increments was also performed but without a noticeable improvement.

The other four analyses were performed at lower stress levels, with two different overconsolidation ratios and different initial pore pressures, as summarized in Table 6.2. Values for the deformation time factor, T_δ , are also given in Table 6.2. The behaviour of analyses TCC2 and TCC5 with the lower pore pressures and load factors, is studied first, after which comparisons are made with the predictions for TCC3 and TCC4 to indicate the significance of initial pore pressure and load factor.

Almost constant rates of deformation occurred at the inner boundary in analyses TCC2 and TCC5, Fig. 6.11(a), with a higher rate predicted for TCC5. The time dependent deformation predictions (i.e. from which the initial displacements have been subtracted), which are plotted in Fig. 6.11(b) using the non-dimensional groups developed in Chapter 5, were found to coincide for TCC2 and TCC5. The deformation time factors at the end of these analyses were about 10×10^{-6} , considerably less than those of the 12.7mm diameter tunnel tests. Dissipation of the pore suctions at node 4, on the inner boundary (see Fig. 6.1(b)), was more rapid in TCC5 than TCC2, as expected from the higher initial pore pressure and larger hydraulic gradient close to the boundary. Figure 6.12 shows that steady values were achieved after about 12 seconds compared with 30 seconds for TCC2. A gradual small reduction in pore pressure occurred after about 30 seconds in analysis TCC5 (OCR = 3.0),

whereas a constant pore pressure was predicted in TCC2. At element 17 in Fig. 6.13, the behaviour was similar to that of node 4, although the gradual reduction in pore pressure after partial dissipation in TCC5 was more pronounced than at node 4. This difference in pore pressure behaviour for TCC2 and TCC5 is probably the result of the more rapid increase in specific volume or dilation in TCC5, as illustrated in Fig. 6.14.

Figures 6.15(a) and (b) illustrate the stress paths experienced by element 17 during analyses TCC2 and TCC5, which had overconsolidation ratios of 1.6 and 3.0 respectively. Both figures show constant p and p' before the yield surface was reached, after which the effective stress paths moved across the yield surface towards the critical state line. In TCC5, Fig. 6.15(b), the critical state line was approached but not reached before the direction of the effective stress path changed during the consolidation phase of the analysis. During the early stages of consolidation in both analyses the effective stress path moved away from the critical state line into the dry of critical region, and gradually tended back towards critical state as consolidation continued. At the end of the analyses, TCC5, which modelled a higher overconsolidation ratio and had a larger initial pore pressure, had softened considerably more than TCC2, as reflected in the changes in specific volume with time shown in Fig. 6.14.

Analyses TCC3 and TCC4 were performed using the same overconsolidation ratios as TCC2 and TCC5, but with higher initial pore pressures, and consequently higher load factors which caused significant differences to develop. The deformations at the inner boundary, Fig. 6.11(a), increased steadily (at different rates) in these analyses up to a

value of about 5mm, after which the rate was much reduced, with the cylinder becoming 'locked up' as in TCC1, when its internal diameter had reduced to only about 2.5mm. These displacements were much larger than those predicted in TCC2 and TCC5, which had lower initial pore pressures and lower load factors. In Fig. 6.11(b), the time dependent deformation curves (in non-dimensional space) from TCC3 and TCC4 are in poor agreement with those from the analyses with lower initial pore pressures and load factors.

At the inner boundary in analysis TCC4 ($OCR = 3.0$), Fig. 6.16, the pore suction dissipation behaviour at node 4 was different to that in TCC3. Only partial dissipation in TCC4 occurred before a constant value was maintained during the period which coincided with the rapid displacement and associated dilation, Fig. 6.11(a). The rate of deformation was initially much more rapid in TCC3, with only a small amount of pore pressure dissipation. As the rate of deformation in TCC3 was significantly reduced soon after unloading due to the large volume loss, the pore pressure rose continuously and it became necessary to introduce a zero pore pressure boundary condition at the inner radius part way through the analysis. Similar pore pressure behaviour to that at the inner boundary was observed in element 17, Fig. 6.17.

The stress paths for analyses TCC3 and TCC4 in Figs. 6.18(a) and (b) show that the mean total stress began to increase at the time when the deformation at the inner radius had reached a maximum value. Drainage towards the zone of pore suction as the cylinder deformed had increased the specific volume in that zone in equilibrium with the boundary conditions. Subsequently, as the cylinder locked up, the

displacement boundary condition at the inner boundary was effectively altered although water continued to flow towards the zone of low pore pressures at the 'unsupported' boundary. The increased volume of water could not be accommodated by the soil swelling since the inner radius had become very small and no further displacements were being predicted. Consequently the pore pressure and mean normal total stress increased, as shown in Figs. 6.18(a) and (b).

The mean effective stress paths in Figs. 6.18(a) and (b) moved away from the critical state line continuously as the cylinder locked up and the pore pressures rose, in contrast to the analyses with lower initial pore pressures where the stress paths eventually changed direction and moved back towards the critical state line. Changes in direction of the effective stress paths away from the critical state line during consolidation may be represented in $v : p'$ space, as shown in Fig. 6.19. The specific volume (or water content) increases were small as p' was reduced, with the result that the stress paths moved away from critical state into the dry of critical region.

The relatively small increases in specific volume may have been caused by an imbalance of the water flowing into and out of elements at various distances from the inner boundary, as illustrated in Figs. 6.20(b) and (d) by the highly localized softened zone. Water was drawn from the inner elements by the large hydraulic gradients, established as a result of the removal of the support pressure, to dissipate the pore suctions at the inner boundary, shown in Figs. 6.20(a) and (c). Further from the inner boundary the hydraulic gradients were much less steep, and although the supply of water to the inner elements was being provided across a larger area, the rate

of inflow may have been lower than that required to balance the volume of water flowing out. As a result the element has remained at a high stress ratio, as shown in Figs. 6.18(a) and (b). Figures 6.20(b) and (d) show that there is a region beyond the softened zone, in which the specific volume was lower than the initial value. As the softening close to the inner boundary continued, the outer radius of the softened zone increased, particularly for analyses TCC3 and TCC4 which had the highest initial pore pressures or overconsolidation ratios. The most significant zone of reduced specific volume was predicted in TCC2 which had the lowest initial pore pressure and hydraulic gradients.

The most important observations made from these analyses are summarized below:

- a) the 'undrained' responses during the removal of support pressure were similar to those of the undrained analyses, but there were indications that some drainage and softening at the inner boundary during this very short time had affected the pore pressure distribution;
- b) initial deformations during support pressure removal have been shown to be strongly influenced by load factor, for $LF > 0.5$, and it is suggested that they are a function of LF^2
- c) analyses which had low initial pore pressures and load factors ($u \leq 200\text{kPa}$, $LF \leq 0.6$) deformed at a relatively constant rate and were shown to be in close agreement when plotted in the non-dimensional groups developed for the experimental data;

- d) analyses which had higher initial pore pressure and load factors deformed rapidly until a maximum displacement of about 80% of the initial radius or a volume loss of 96% had been reached, after which almost no further movement occurred;
- e) the rate of deformation at the inner boundary and the initial stress state influence the time dependent pore pressure behaviour; the more rapid displacement leads to a high rate of dilation close to the boundary and reduced dissipation of pore pressure suctions;
- f) continued pore pressure rises with time are associated with the large displacements at the inner boundary having reached a maximum (collapse state) in the analyses which had large initial load factors;
- g) the variation in specific volume with radius is highly non-uniform, with a softened zone close to the inner boundary; there is evidence that specific volume changes are negative for elements adjacent to this zone due to the variations in the hydraulic gradient with radius.

6.4.4 Comparison with experimental data

Direct quantitative comparisons of the finite element analyses cannot be made with the experimental data since the thick cylinder is not equivalent to an unsupported model tunnel face. The analyses could only be performed to represent a 12.5mm diameter cavity and were not intended to model any given test. However, some statements can be

made concerning the extent to which the same class of behaviour was observed in the model tests.

The analyses have shown two different types of pore pressure behaviour which were also indicated in the model tests. In cases where the load factor and initial pore pressure were low, the pore pressures changes caused by the removal of the face support pressure dissipated towards relatively constant but slightly negative values. For higher load factors and pore pressures there was some initial dissipation followed by a further reduction for a short time, after which the pore pressures rose steadily as the volume losses became very large. Steadily increasing pore pressures were measured in some model tests, particularly where a considerable volume of clay had intruded into the tunnel, and may have provided some support at the face. The relationship between load factor, initial pore pressure and rate of deformation has not been clearly established by the analyses, although some agreement with the non-dimensional groups used for the model tests has been shown for low values of these parameters.

6.5 Conclusions

Thick cylinder analyses have been used to investigate the undrained pore pressure and deformation behaviour using modified Cam-clay and an elastic-perfectly plastic model with the Tresca yield criterion, and to indicate the limitations of the idealized 'hand calculations'. Results from the modified Cam-clay analyses have clearly shown that the closed form solution over predicted the pore pressure changes for cases where the OCR of the soil being modelled was less than two, and under predicted for an OCR greater than two, in agreement with some of

the experimental observations. For the analyses modelling a more heavily overconsolidated soil the gradient of the pore pressure distribution was greater than two, whereas for a lightly overconsolidated soil the gradient was closer to two, i.e. the gradient of the simplified solution. Reasonably close agreement was found between the 'hand calculations' and the finite element computations using the Tresca yield condition. Some variation is to be expected due to the different assumptions made for the boundary conditions and the bulk modulus of water.

The removal of support pressure during the consolidation analyses has also been considered in terms of an 'undrained' response. Similar classes of behaviour to the undrained analyses were observed generally, although the pore pressure distribution may have been affected by some specific volume changes, which occurred as a result of the large hydraulic gradients established during the very short unloading time. Analyses which had a high initial pore pressure were particularly affected by this behaviour, and provided some evidence to support the suggestion in Chapter 5 that the pore pressure transducers located at some radial distance from the central axis may not have measured a truly undrained response. Deformations during the unloading phase of the analyses have been shown to be related to LF^2 , although this relationship has been based on only a very small number of data points.

Two classes of pore pressure behaviour have been predicted in the CRISP consolidation analyses of the thick cylinder. In cases where the pore pressure and load factor are low ($u_0 \leq 200\text{kPa}$, $LF \leq 0.6$) the cylinder deforms steadily by a significant amount ($\approx 20\%$ of initial

radius) at the inner boundary and the pore pressures dissipate and tend towards virtually steady conditions. Higher pore pressures and load factors lead to 'locking up' of the mesh after large displacements ($\approx 80\%$ of initial radius, equivalent a volume loss of 96%) at the inner boundary have occurred. This results in the generation of positive pore pressures which also tend towards an equilibrium condition after some time. Experimentally the rapid intrusion of clay into the tunnel may be equivalent to the 'locking up' effect of the analyses, since it has been generally observed that rising pore pressures in the later stages of the tests occurred only in tests with high load factors and large deformations at the tunnel face. Increasing pore pressures in the model tests may have been due to some support being provided by the volume of clay in the tunnel, and to the increasing length of the drainage path from unsupported face to the transducer.

Continued softening close to the inner boundary was predicted in all of the analyses. At the end of the analyses the largest increase in specific volume had occurred where either the initial pore pressure or the overconsolidation ratio was highest. Significant zones of specific volume reductions were also obtained where the initial pore pressures and hydraulic gradients were low.

Use of the thick cylinder analogue in the consolidation analyses has demonstrated the complexity of the stress changes at an unsupported boundary which lead to time dependent deformations. Comparisons of these analyses to the model tunnel tests is limited, largely due to the differences in geometry. Time dependent deformation of the thick cylinder may become restricted by the finite radius of the cavity,

whereas the model tunnel is unrestrained by any geometrical feature. A thick cylinder is a less stable structure than the three dimensional tunnel face, as a result of which only a cavity equivalent to the 12.7mm diameter tunnel could be analysed. Consequently the usefulness of the analogue is confined to providing a qualitative understanding of the time dependent behaviour around an unsupported cavity.

7.1 Introduction

A simplified representation of the model tunnel tests by a thick cylinder has been analysed and discussed in Chapter 6. The finite element program CRISP described in the previous chapter, was also used to model the experimental tunnel tests in more representative detail and aspects of these analyses are now presented. Some difficulties arose from the more complex geometry of the model tunnel tests which required the development of a suitable mesh and procedure for the numerical computations.

Analyses of the model tunnel tests involving different initial stress states were carried out to gain a better understanding of the changes occurring during such a test, particularly in terms of the flow of pore water and the associated time dependent effects. Deformation at the tunnel face and pore pressure changes are examined closely, and the overall performance of the analyses is assessed.

7.2 Details of the analyses

7.2.1 Development of the model tunnel test meshes

Although it was concluded in Chapter 5 that the 50.8mm diameter tunnel tests were significantly affected by the relatively low cover to diameter ratio (C/D), it was decided to include a 50mm diameter tunnel mesh to study the influence of C/D in the finite element analyses.

The layout of elements used to represent the 50.8mm diameter model tunnel tests is shown in Fig. 7.1(a) with an enlarged detail of the tunnel face in Fig. 7.1(b). The cylindrical soil sample and model tunnel were discretized as a radial section (due to the axisymmetry of the model) which was 600mm in height and had a radius of 125mm. Along the upper edge of the mesh the nodes were restrained in the vertical direction and a uniform stress was applied to the base of the mesh and the outer vertical boundary, to model the conditions applied in the triaxial apparatus. The axisymmetry of the tunnel problem required zero displacement across the central axis, consequently the nodes along the inner vertical boundary were restrained in the radial direction.

Displacement fixities were also used to model the effect of the lining by restraining radial movement in the tunnel cavity; it should be noted that the lining itself was not incorporated. An analysis with a preliminary mesh indicated that the deformation of elements into the tunnel was being restricted by the influence of this radial restraint on elements close to the tunnel face. This differs from small scale model and prototype tunnelling conditions where the soil would be free to deform radially in towards the central axis and to deform around the leading edge of the lining. In this method of analysis, the displacement fixity introduced effectively limits the movement of soil at the circumference of the tunnel face, as indicated in the preliminary analysis. Figure 7.2(a) illustrates the mesh adopted for the preliminary analysis, which was fairly coarse in regions close to the tunnel face. The result was restricted and non-uniform deformations at and ahead of the tunnel face as clearly indicated by Fig. 7.2(b).

The finer mesh, of the form shown in Figs. 7.1(a) and 7.1(b), was developed in an attempt to minimise the influence of unrealistic restraints. A large number of very small elements were concentrated at the radially fixed node, i.e. at the intersection of the restrained boundary, representing the lining and the unsupported face, in an attempt to introduce a greater freedom of movement and to allow a more uniformly deformed mesh to develop around the tunnel face. Small elements with low aspect ratios were used close to the unsupported boundary, where it was anticipated that large pore pressure and stress gradients would result from the rapid removal of face support.

- Two additional meshes were created to allow the 25.4mm and 12.7mm diameter tunnel tests to be modelled and are shown in Figs. 7.3(a) and 7.3(b). These meshes were reduced scale versions of the largest diameter tunnel mesh, with elements added around the scaled boundaries to maintain the overall dimensions of the original mesh. Since the size and position of the elements relative to the tunnel face in each reduced mesh was geometrically similar, a direct comparison of the behaviour of different diameter tunnels may be made.

7.2.2 Development of analysis procedure

All of the analyses were concerned only with the behaviour during and after the removal of support pressure from the tunnel face. No attempt was made to model any of the preparation stages, or the actual experimental process of removing the rigid support at the tunnel face.

At the start of the analysis in situ stresses were specified to be in equilibrium with the imposed boundary conditions. The support

pressure at the tunnel face was reduced to zero in a number of very short time increments, each pressure reduction being sufficiently small to prevent excessive changes in yield ratio, as discussed in Chapter 6 for the thick cylinder analyses. Reduction of face support pressure was completed in about three seconds for the 50mm diameter tunnel analyses, so that the conditions at the start of an analysis would be as close to undrained as possible. After the support pressure had been reduced to zero, the analyses were continued on an incremental time basis with the introduction of a zero pore pressure boundary condition along the tunnel face if required; this was discussed in Section 6.2.2.

The stop/restart facility in CRISP is advantageous for analyses in which boundary conditions, material parameters or time increments may need to be altered at several different stages during the analysis since these changes may then be implemented without having to start the analysis again at the first increment. This facility was found to be particularly useful in the original analysis when appropriate sizes of unloading increments and time increments were established to ensure that the yield ratio remained within the recommended limits of 1.00 ± 0.05 , and that no oscillations in pore pressure occurred during consolidation.

For analyses in which different diameter tunnels were to be compared, a scale factor for the time increments was required. A scale factor n was discussed in Chapter 2, where it was defined as the ratio of the linear dimensions of the prototype to the model e.g. D_p/D_m , where D is the tunnel diameter. Similarly the scale factor n_f relates the sizes of the tunnels in the finite element meshes, for example to compare

the 50mm and 25mm tunnels, n_f is obtained from $D_{50}/D_{25} = 2$. It was also shown in Chapter 2 that the scale factor for diffusion events was n^2 . Consequently the magnitude of each time increment was scaled by n_f^2 between analyses of different diameter tunnels. Analyses were continued for the same number of increments, so that the total times also varied by a factor n_f^2 .

7.2.3 Selection of soil model

Initially modified Cam-clay was used throughout the entire mesh representing the physical model tunnel tests. However, it was found that the small elements at the edge of the tunnel and just ahead of the tunnel face experienced large strains early in the analyses, which were severe enough to prevent the analysis from being continued as a result of numerical problems. The numerical difficulties originated at the small group of elements within the shaded area shown in Fig. 7.4. Since the elements in this area were of little importance to the analysis as a whole, they were replaced by elastic elements which had a stiffness modulus about eight times greater than that of the modified Cam-clay elements; the analysis was then able to proceed without the numerical difficulties.

7.3 Analyses of the model tunnel tests

A number of analyses have been performed to study some of the factors considered to influence the behaviour observed in the model tests, with some additional analyses designed only to establish the effect of the analysis procedure on the results. A full list of the analysis details is presented in Table 7.1, in which the analyses are grouped

and listed in the order in which they are discussed in this chapter. Rates of deformation of the tunnel face and pore pressure changes with time are of particular interest to permit comparisons to be made with the experimental data. The value of the deformation time factor, T_δ , at the end of each analysis is also given in Table 7.1. Other time dependent changes in specific volume and effective stress are important in understanding the behaviour at an unsupported tunnel face.

7.3.1 Series I Stage 1 analyses

Three analyses were performed to model the Series I stage 1 tests, which investigated the influence of tunnel diameter and the cover to tunnel diameter ratio, C/D . For these analyses, which have been labelled as SI50, SI25, and SI13, the meshes used were those shown in Figs. 7.1 and 7.3(a) and (b), with the geometrically similar element layouts near the tunnel face. The analyses of the smaller diameter tunnels, SI25 and SI13, were performed with the size of the time steps reduced by the scale factor n_f^2 .

Both of analyses SI25 and SI13 experienced some numerical difficulties in the latter stages, particularly SI13, as indicated by the non-uniform distortion of the mesh in Fig. 7.5(a) and (b), which were not apparent from the deformed mesh at a larger deformation time factor in SI50, Fig. 7.6(a). These problems may be the result of the time scale factor (n_f^2) applied to the time increments of the smaller diameter tunnel analyses since analysis SI25 also showed some signs of numerical difficulties, but at a larger deformation time factor than in SI13. Analysis SI50 continued with less severe numerical

difficulties for the intended number of increments. The 12.5mm and 25mm diameter tunnel analyses were performed again, with the size of time increments halved, and have been labelled as SI13T and SI25T. No further numerical problems were encountered, as shown by the deformed meshes at a common T_δ of 4.4×10^{-6} in Fig. 7.6(a) to (c). This value of T_δ at the end of these analyses is significantly less than that of the model tests.

The deformed meshes indicate that the most significant zone of movement was confined to a hemisphere ahead of the tunnel face. Figure 7.6(d) shows that this zone, extending in the direction of the central axis to a distance $1.5r_0$ ahead of the tunnel face, contained the elements most severely affected by time dependent events. Beyond the softened zone the elements were in a state of yielding. In these and subsequent analyses, the elements around the tunnel face are shown in various figures to be yielding, softening, elastic or at critical state. Elastic behaviour has been specified as that for which the yield ratio, YR, was less than 0.99. The remaining states have a $YR \geq 0.99$ with $q/p' < 0.95M$ indicating hardening, $q/p' > 1.05M$ for softening and $0.95M \leq q/p' \leq 1.05M$ for critical state.

Node 52 lies on the central axis at the tunnel face, as illustrated by Fig. 7.1(b), and is equivalent to the displacement measurement point in the physical model tests. Values of the initial displacement, δ_i , predicted during removal of support have been subtracted from the data presented in all plots showing deformation responses with time, as in the analyses of the experimental data. The deformations which occurred at node 52 in the three analyses have been plotted in Fig. 7.7 in the dimensionless $\delta/D : c_v t/D^2$ space, where c_v was assigned a

nominal value of $1\text{mm}^2/\text{s}$. Initially the slopes of the displacement curves were quite similar for all tests, but analysis SI50 diverged from the others after a time factor ($c_v t/D^2$) of about 0.06. The value of δ/D at a time factor of 0.35 was 0.088 for SI50, compared with a δ/D of 0.062 for SI25T and SI13T, which provided some evidence that the 50mm diameter tunnel analysis had been slightly affected by the geometrically closer constant stress boundary. The same trend of behaviour was shown experimentally for small time factor values in Fig. 5.9.

The deformation data have been replotted in Fig 7.8, using the dimensionless deformation group (including load factor) developed in Chapter 5. The time factor $c_v t/D^2$ is equivalent to T_δ for these analyses since the tunnel diameter, D , is the only variable. None of the deformation curves coincided, in contrast to the experimental results where similar deformation curves were obtained from the 25.4mm and 12.7mm diameter tunnels. The different values of N_{crit} (and hence load factor) calculated for the model tunnel tests to take account of the sample diameter/tunnel diameter ratio may not be applicable in these analyses. It is probable that the use of the thick sphere analogue to determine the value of N_{crit} is not as appropriate for these meshes due to the influence of the unrealistic radial constraints at the tunnel face.

The dissipation of pore suctions after removal of the support pressure at node 52, shown in Fig. 7.9, occurred very rapidly with pore pressure becoming slightly positive at a time of about 130 seconds. The elements at the tunnel face and close to the central axis became numerically unstable and may have been the cause of the sudden change

in response predicted at this time (130 seconds in SI50) for other elements close to the tunnel face. Attempts to lessen the difficulties by introducing a zero pore pressure boundary condition at the tunnel face partway through the analysis resulted in very little improvement. Subsequently the pore pressure became negative again, and remained at about -50kPa until the end of the analysis. Negative pore pressures at the unsupported boundary were also observed in the thick cylinder analysis TCC2, Fig. 6.12, which had an initial pore pressure of 100kPa and an OCR of 1.6. Although SI50, SI25T and SI13T were clearly affected by numerical problems at the tunnel face, it is considered that the overall effect on the predicted class of behaviour was not sufficiently severe to invalidate the analyses.

A small number of elements, identified in Fig. 7.1(b), were selected to illustrate the behaviour generally observed at various points in the mesh. Element 25 was selected to illustrate the behaviour at a distance of about $r/r_0 = 1$ ahead of the tunnel face on the tunnel axis. In the analyses generally this distance appeared to be beyond the zone affected by the numerical problems very close to the face. However, for the Series I stage 1 analyses the effects of the numerical difficulties were more widespread and appeared to extend to this element.

The pore pressure response at element 25 in SI50 is presented in Fig. 7.10, which shows an initial reduction of about 280kPa. Subsequently the pore pressure rose rapidly, followed by a steady reduction before the sudden step in the analysis occurred at a time of about 130 seconds, which corresponded to the change in pore pressure at the tunnel face in Fig 7.9. Thereafter the pore pressure began to rise

again for a short time before decreasing at a steady rate for the remainder of the analysis. The change in direction of pore pressure response at about 60 seconds may have been the result of the large gradients and pore suctions at the face drawing water away from adjacent zones, such as in the region of element 25, at a greater rate than that which these zones were being supplied with water from other more remote elements. This effect, due to the difference in hydraulic gradients, was suggested in Chapter 6.

The stress paths associated with the removal of support pressure and subsequent changes in water contents at element 25 are illustrated in Fig. 7.11. Yielding occurred as the effective stress path approached the critical state line while the face support pressure was removed. After yielding the effective stresses followed a similar path to that predicted by the thick cylinder consolidation analyses, Section 6.4.3. Figure 7.11 shows that the stress path moved into the dry of critical region before softening towards the critical state line as consolidation continued. The discontinuity in the stress path may have been the result of the numerical problems influencing the rate of flow of pore water towards the face such that rate of softening was reduced, as indicated by the reduced slope of the specific volume curve for SI50 in Fig. 7.12.

The behaviour in analyses SI25T and SI13T was generally similar to SI50 with the exception of the reduced softening shown in Fig. 7.12, where the increase in specific volume has been plotted against time factor to allow a direct comparison between the analyses. The increase in specific volume was about 25% higher in SI50. A comparison of Fig. 7.12 with Fig. 7.7 demonstrates clearly that the

increased deformation in SI50 is a function of the more highly softened soil around the tunnel face.

Element 33 was located at the same distance ahead of the face as element 25, but was almost in line with the tunnel boundary, as indicated in Fig. 7.1(b). A smaller pore pressure reduction of about 110kPa was calculated, which dissipated towards a steady value about 20kPa above the pore pressure predicted after unloading, as shown in Fig. 7.10. The behaviour of this element was quite different to that of element 25 since virtually no softening occurred, as demonstrated by the specific volume changes and stress paths in Figs. 7.13 and 7.14. A much smaller reduction in total stress was experienced by element 33 at the removal of the support pressure, which resulted in a pore pressure change to a level close to the virtually steady longer term conditions. Consequently only small changes in water content were needed to maintain the stress equilibrium. From the seepage flow net in Fig. 5.27(a) a pore pressure of about 110kPa was expected, a value similar to that shown in Fig. 7.10. However at element 25 a pore pressure of about 90kPa is indicated for steady seepage, but a steadily decreasing pore pressure of less than 30kPa was predicted in SI50.

Two elements, 48 and 50, were located at a similar distance ahead of the tunnel face to that of element 33 but at a radial distance perpendicular to the central axis of r/r_0 of between 1.4 and 2.0, as shown in Fig. 7.1(b). Element 48 lies within zone B, defined in Chapter 5, whereas element 50 is located in zone A. At element 48 only a very small pore pressure reduction was predicted at the removal of face support pressure, Fig. 7.15, compared with a measured decrease

of about 150kPa at ppt3106 in Fig 3.9(b). Experimentally at r/r_0 of 2.0 in zone A significant reductions in pore pressure were measured, instead of which a small rise in pore pressure was predicted at element 50. The changes predicted for these elements were negligible relative to those directly ahead of the face, an indication of the very large gradients which existed across the more limited zone of influence adjacent to the tunnel face, illustrated by the pore pressure distribution in Fig. 7.16(a). Zones A and B were effectively separated by the 200kPa contour line, i.e. $\bar{u} \approx 0$, in Fig. 7.16(a). The effect of the stiff elastic elements and of the radial restraint was shown by the rise in pore pressure in zone A. It was also noted that the longer term pore pressure behaviour of element 12 in Fig. 7.15, at a distance of about $r/r_0 = 2$ directly ahead of the face, was slightly lower than that of element 50, a distribution similar to that of the seepage flow net. Figure 7.16(b) illustrates the pore pressure distribution obtained towards the end of the analysis, which may be compared with the seepage flow net in Fig. 5.27(a). The distribution was confined to a smaller zone than that shown in the radial flow net, a consequence of the different boundary conditions. A constant value of 200kPa has been imposed at the outer equipotential in the radial flow net, and in some analyses a negative pore pressure was predicted at the tunnel face, whereas zero pore pressure is assumed in the flow net.

The analyses indicated that there was some evidence of boundary effects in analysis SI50, arising from the relatively low C/D value. The deformation curves plotted in non-dimensional space, in Fig. 7.7, demonstrated a significant difference between SI50, SI25T and SI13T. However, contours of the total stress distribution at $T_0 = 4.4 \times 10^{-6}$,

shown in Figs. 7.17(a) to (c), were very similar, indicating that the constant stress boundary may only have had a minor effect on the predictions.

A comparison of the Series I stage 1 analyses modelling three different diameter tunnels has demonstrated a number of points summarized below:

- a) the deformation at the tunnel face in SI50 (50mm diameter tunnel mesh) was significantly greater than in SI25T or SI13T, although the difference was much less pronounced than that observed experimentally; the larger deformation was linked with a greater amount of softening;
- b) the use of n_f^2 to scale the size of the time increments between analyses of different diameter tunnels produced unsatisfactory results, a greater reduction in the magnitude of the time steps proved more successful;
- c) load factors calculated using the same assumptions as for the experimental conditions may not give appropriate values to relate tunnels of different diameters in the finite element computations;
- d) although affected by some numerical problems, the analyses indicated the class of behaviour associated with rapidly varying stress distributions around an unsupported tunnel face;

- e) in contrast to the experimental observations, the stress changes were confined to a localized zone directly ahead of the face; reductions in stresses perpendicular to the central axis of the tunnel were severely limited by the displacement boundary condition introduced to simulate the tunnel lining; in zone A, identified from the experimental data, pore pressure increases instead of reductions were predicted in these analyses.

7.3.2 Influence of pore pressure

Analyses SI50, SI25T and SI13T have indicated that the selection of time increments based on a scale factor n_f^2 for a diffusion process may not be satisfactory for a mesh which has been reduced by a scale factor n_f . Since the numerical difficulties experienced with the 50mm diameter tunnel mesh were much less severe than with the smaller diameter meshes, its use was continued in the investigation of the influence of different initial stress states.

Analysis SI50 is compared with analysis KAP05 which had an initial pore pressure of 400kPa and an OCR of 2.0; further details are given in Table 7.1. Figures 7.6(a) and 7.18(a) show the deformed meshes at a deformation time factor of 4.4×10^{-6} in which KAP05 deformed about the same amount as the tunnel face in SI50. At a larger deformation time factor, $T_6 = 15.1 \times 10^{-6}$, the mesh for KAP05 was more severely deformed close to the tunnel face, Fig 7.18(b). The analysis has extended the finite element calculations beyond the recommended limits, a consequence of using a finite element program intended for small strain situations. The distortion which occurred at this time

factor clearly indicates that a number of elements, particularly those close to the elastic elements, should be disregarded as far as meaningful results in the analysis are concerned. Since the behaviour of a few elements at the face is not of primary importance, the analysis may still be assumed to be valid, and shows significant time dependent changes. Directly ahead of the tunnel face, in Fig. 7.18(b), large volumetric changes (swelling) occurred where some element dimensions have become significantly elongated parallel to the tunnel axis. Figure 7.18(c) shows a slightly larger zone of softened elements compared to that of SI50, Fig 7.6(d). The elements surrounding the softened zone, in Fig 7.18(c), remained elastic.

Deformations at the tunnel face from the two analyses were plotted in non-dimensional space, using the deformation time factor developed in Chapter 5, as illustrated by Fig. 7.19. Close agreement exists between SI50 and KAP05, although it should be noted that the load factors for these analyses were similar.

The pore pressure distributions close to the central axis (immediately after unloading) have been plotted for these analyses in $(\bar{u}/c_u + N - 4/3) : \ln(r/a)$ space) as shown in Fig. 7.20. For values of $\ln(r/a)$ of less than about one in SI50 the distribution was linear with a gradient of about four, which decreased as the outer limit of the plastic zone was approached. As expected a greater pore pressure reduction was predicted for the analysis of overconsolidated soil behaviour, KAP05. The overall slope was also approximately four, although at several elements larger reductions were predicted. These data provide some evidence to support the suggestion in Chapter 5 that the thick sphere is a more appropriate analogue for the tunnel face.

At element 25 the initial reduction in pore pressure, Fig. 7.21, of about 420kPa, compared with 280kPa in SI50, dissipated partially before remaining constant for about 200 seconds. At the tunnel face the pore suctions in KAP05 dissipated less rapidly than in SI50, Fig. 7.22, and at the same time decreased the hydraulic gradients causing flow towards the face. The consequent reduction of the flow of water towards the face may have influenced the rate of pore pressure dissipation at elements such as element 25, which gradually reduced to equilibrium values of about zero. These steady conditions were also evident from the changes in specific volume at element 25, in Fig. 7.23, which increased at a relatively slow rate after the pore pressure had reached a constant value.

An elastic-perfectly plastic response is shown in Fig. 7.24 where the effective stress path rose directly to the critical state line before moving into the dry of critical zone, as in analysis SI50, Fig. 7.11. In contrast to SI50, element 25 softened sufficiently (at a larger T_δ) to cause the stress path to return to the critical state line towards the end of the analysis. An indication of the difference between SI50 and KAP05 may be obtained by studying the response at element 33, which was relatively unaffected in SI50, Fig. 7.14. In KAP05 element 33 softened gradually, and finally reached the critical state line with a higher specific volume than element 25, Figs. 7.13 and 7.23. Other elements more significantly affected than in SI50 were 12 and 48, which reached the yield surface and began to soften, demonstrating that a much greater volume of soil had become affected by the 'excavation' of a tunnel face under conditions of relatively high in situ pore pressures and by the larger deformation time factor to which the analysis was continued.

A number of the points noted in the comparison of analyses SI50 and KAP05 are given below:

- a) rates of deformation of the tunnel face, when compared using the non-dimensional groups from Chapter 5, were in close agreement;
- b) the pore pressure distribution along the central axis had a gradient of about four in both SI50 and KAP05, and provided evidence that the thick sphere may be a more suitable analogue than the thick cylinder;
- c) the finite element mesh in KAP05 became severely distorted by the substantial volumetric strains in the elements close to the tunnel face at a large time factor;
- d) the larger time factor, to which KAP05 was continued, allowed an element at a distance $r/r_0 = 1$ ahead of the tunnel face to soften and gradually reach the critical state line;
- e) the longer term influence of higher initial pore pressure has been a more widespread increase in specific volume, and significant changes were calculated for elements which had remained virtually unchanged in SI50.

7.3.3 Influence of load factor

Analysis LF5 had a similar initial pore pressure to SI50, and was undertaken to study the influence of overconsolidation and load

factor; details of the parameters are given in Table 7.1. Figures 7.6(a) and 7.25(a) illustrate the deformed meshes at similar deformation time factors towards the end of the analyses and show that the deformation in SI50 was about twice that of LF5. The softened zone ahead of the tunnel face, Fig. 7.25(b), was smaller than in SI50, Fig. 7.6(d), as expected from the lower load factor and deformation. In non-dimensional space there was good agreement between deformation curves for the two analyses, which had a significant difference in load factor, as shown in Fig. 7.19. The form of deformation curve was similar to that obtained experimentally, with steadily increasing deformation at large time factors.

Data from LF5 have also been plotted in Fig. 7.20 to show the pore pressure distribution in $\bar{u}/c_u + N - 4/3 : \ln(r/a)$ space. In this case the slope was linear with a gradient of slightly less than four for a smaller range of $\ln(r/a)$ (< 0.6), beyond which the gradient decreased, and was indicative of the smaller plastic zone associated with a lower load factor. The pore pressure reductions were greater than those predicted using the closed form solution, as expected from the dependence of pore pressure response on overconsolidation ratio, discussed in Section 6.3. Estimates of the extent of the plastic zones for analyses SI50, KAP05 and LF5 may be obtained from Fig. 7.20. Comparisons of analyses SI50 and KAP05 with the closed form solution lines B and D in Figs. 5.7(a) (i) and (ii) show reasonable agreement, although there is less agreement between LF5 and line E in Fig. 5.7(a) (iii). In all cases the experimental plastic radii were considerably larger.

At element 25 in LF5, the reduction in pore pressure after full removal of support pressure, shown in Fig. 7.26, was much smaller than that of SI50. As before, the pore pressure rose while the pore suctions at the face were being dissipated, and afterwards reduced, again possibly towards steady values. At a time of about 900 seconds, Fig. 7.26, the pore pressure at elements 25 and 33 in both analyses reached almost identical levels, but were not yet at a steady value unlike those in KAP05.

Figure 7.27 shows that the mean effective stress path for element 25 rose towards the yield surface, and that p' remained constant as expected, with elastic behaviour during the unloading stage of the analysis. From the start of the removal of support pressure, the total stress path showed a reduction in mean normal total stress, as also predicted in KAP05. In contrast to SI50, Fig. 7.11, the yield surface was not reached until some 100 seconds of the consolidation stage had been completed. The difference in behaviour is consistent with the lower load factor and plastic strains in LF5. After having reached the yield surface, the effective stress path steadily moved away from the critical state line with decreasing mean effective stress and increasing stress ratio, a similar class of behaviour to that predicted in the less overconsolidated analyses. Continued softening of element 25 is shown in Fig. 7.28, as expected with a steady approach to the critical state line. A greater amount of softening was indicated in LF5 than SI50, which is in agreement with the predictions in the thick cylinder analyses where the largest increases in specific volume were related to the highest initial pore pressure and overconsolidation ratio. Element 33 showed virtually no

softening, a further indication of the much reduced zone of influence in LF5.

Other elements such as 12 and 48, as located in Fig. 7.1(b), discussed in the previous analyses were only slightly affected by the changes at the tunnel face and also demonstrated the more limited zone of influence when the load factor is significantly reduced.

Observations arising from the comparison of analyses SI50 and LF5 are summarized below:

- a) displacement of the tunnel face has been plotted in non-dimensional space in agreement with the results from SI50 and KAP05, demonstrating the influence of load factor on the rate of deformation;
- b) a smaller plastic radius was indicated by the pore pressure distribution after the removal of the support pressure;
- c) the influence of load factor was obscured, as in the experimental tests, by the influence of the overconsolidation ratio; increases in specific volume were larger than in SI50 but were also more localized.

7.3.4 Influence of kappa

The selection of an appropriate κ value was based on the discussion in Chapter 4, in which it was noted that the slope of the swelling line in $v : \ln p'$ space was not constant. Analysis KAP02, in which κ had a

lower value of 0.02, was performed to examine the importance of this parameter on the finite element modelling of the tunnel tests, since the swelling characteristics of the soil were particularly important. Although the slopes of swelling line were different in KAP05 and KAP02, the specific volume, and hence also k and c_u were the same (for these particular values of κ) at the initial in situ mean effective stress of 400kPa. This is possible due to the greater separation between the critical state line and the isotropic compression lines, given by $(\lambda - \kappa)\ln 2$, for modified Cam-clay which is equivalent to the difference in specific volume increases on swelling back to an effective stress of 400kPa.

Figures 7.18(a) and 7.29(a) illustrate the deformed meshes at equal deformation time factors towards the end of each analysis in which a smaller deformation occurred in KAP02 compared with KAP05. Deformation at the tunnel face has been compared in Fig. 7.19 with KAP05 and other analyses. Since both non-dimensional groups have identical values for KAP02 and KAP05, a shallower deformation curve has been shown for KAP02. A difference of this nature may be expected since κ and p' control the elastic stiffness of the soil, and a greater restraint would be applied by the stiffer elastic elements surrounding the plastically deforming zone in KAP02. A comparison of Figs. 7.18(c) and 7.29(b) shows that the zones of softened elements for these analyses were almost identical.

The pore suction at the tunnel face was dissipated more rapidly and to a higher value in analysis KAP02 than KAP05, Fig. 7.30, a consequence of the higher c_v associated with a lower κ value and a lower compressibility of the soil. These differences in behaviour were also

reflected in the response predicted at element 25, Fig. 7.31, where the pore pressure in KAP02 rose more rapidly and to a higher value than that of KAP05 before dissipating slowly towards equilibrium values of about zero in both analyses. A longer dissipation time towards the steady values was predicted for KAP02 as a result of the larger specific volume changes required to achieve stress equilibrium. The rate of water flow is modified as the hydraulic gradients change with the equilibrium stress state.

A significantly larger increase in specific volume was predicted for the lower κ value at element 25, Fig. 7.32. This may be due to the pore pressure conditions at the tunnel face where the pore pressure reduced steadily from about 0kPa to -100kPa in KAP05, possibly as a result of the continued large displacement, which may have caused a greater flow of water out of element 25 than in KAP02. Figure 7.33 shows the volumetric changes in $v : p'$ space. Both stress paths moved away from the critical state line into the dry of critical region. In analysis KAP05, with the larger κ , the stress path returned to the critical state line at a higher p' and lower specific volume than in KAP02. Such behaviour may be the result of the greater support being provided by the outer elements with a higher stiffness in KAP02.

Some difference in the mean effective stress paths can be seen in Fig. 7.34, where the stress ratio remained higher in KAP02 than in KAP05 before eventually moving down onto the critical state line. The higher q/p' values in KAP02 are associated with the higher pore pressure levels and the slower increase in specific volume, which may be the result of lower hydraulic gradients between element 25 and the more remote elements providing a supply of water.

At element 33 the equilibrium pore pressure did not appear to have been reached at the end of KAP02, in contrast to that of KAP05, as shown in Fig. 7.31. The element had not softened sufficiently to reach the critical state line, and the specific volume was steadily rising, Fig. 7.32, whereas the element appeared to be approaching an equilibrium state in KAP05. At other elements, such as 48, a similar trend of slower changes compared to KAP05 was observed throughout.

The effects of varying the value of κ are summarized below:

- a) smaller deformations were predicted for the analysis (KAP02) having the lower κ value
- b) larger increases in specific volume were required in KAP02 before a critical state was reached, i.e. a higher stress ratio could be maintained for a given specific volume;
- c) at a given deformation time factor, a similar zone of soil ahead of the tunnel face was in a state of softening, although the magnitude of specific volume changes was dependent on location relative to the tunnel face, as well as κ .

7.3.5 Influence of analysis procedure

The inclusion of a number of stiff elastic elements to model the soil close to the tunnel lining is shown in Fig. 7.4 and was discussed in Section 7.2.3. An elastic stiffness about eight times greater than that of the modified Cam-clay elements was used for these elements. The effect of the elastic elements was investigated by comparing KAP05

with STF1. Analysis STF1 was in all respects the same as KAP05, except that the stiffness of the elastic elements was reduced to a value equivalent to the initial stress level of the surrounding modified Cam-clay elements. Severe numerical difficulties, which prevented the analysis from proceeding, were encountered much earlier in STF1 than KAP05, although the analysis continued for an adequate number of increments to allow the results to be compared with KAP05. Figures 7.35 to 7.37 demonstrate that the stiffness of the elastic elements had a negligible effect on the behaviour predicted.

An observation common to all the analyses discussed so far concerns the pore pressure reductions predicted at elements such as 48, Fig. 7.15, at some small distance ahead of the tunnel face and at a radial distance r/r_0 of about 1.4 perpendicular to the central axis. Large reductions observed experimentally have not been modelled in the analyses, a discrepancy also noted by White (1987), who suggested that the difference might be due to the pore pressure transducers modifying the behaviour locally. White analysed a centrifuge model test of an unsupported axisymmetric shaft and found poor agreement between the numerical and physical models. He carried out a further analysis in which an impermeable element with a much higher stiffness represented the stiff inclusion of a pore pressure transducer. The transducer was therefore modelled as a stiff ring with restricted displacement in the radial direction due to the assumption of axisymmetry and its relatively high stiffness, and it may have corresponded to a transducer restrained by its cable.

Two analyses, D13 and SRN1, were performed to investigate the effect of such an inclusion. Element 66 at a typical transducer location,

shown in Fig. 7.1(b), was made virtually impermeable and had an elastic stiffness of 4140MPa in analysis SRN1, whereas the material parameters of this element were unaltered in D13. The mesh representing the 12.7mm diameter tunnel was used since the size of elements at the appropriate location in this mesh were similar to the size of the transducer. The initial stress state of these analyses was similar to that of KAP05, except for a slightly higher p' , and details are given in Table 7.1.

Figures 7.38(a) and (b) compare the pore pressure reductions predicted in the two analyses for elements 65 and 47 in front of the stiff element. Without the stiff ring (D13) the initial reduction at element 65 was negligible, and at element 47 the reduction was about 60kPa. In analysis SRN1 these reductions were increased to about 80kPa and 120kPa respectively. Other elements in the vicinity also experienced larger reductions. With increasing time the pore pressures at elements 65 and 47 reached almost the same values in both analyses.

The stiff inclusion caused a redistribution of total stresses to occur, a higher load being carried by the stiff element and a lower total stress in adjacent elements. Consequently the changes in pore pressure were larger locally, such as those experienced by elements 65 and 47. The influence of the stiff ring on the specific volume changes and the stress paths is shown in Figs. 7.39 and 7.40. In SRN1 the specific volume increased as water flowed towards elements 65 and 47 during the removal of face support pressure as the pore pressure was reduced by the transfer of total stress to the adjacent stiff ring. By contrast the specific volume at elements 65 and 47 decreased

in D13, a response which may be the result of the steeper hydraulic gradients between the unsupported tunnel face and these elements which remained at a higher pore pressure than in SRN1. In the longer term the specific volume changes at elements 47 and 65 tended towards similar values in both analyses.

The inflow of water at element 65 in SRN1 caused the effective stress path shown in Fig 7.40 to decrease instead of remaining constant prior to yielding, as anticipated and as predicted by D13. The total stress paths also indicated the significant difference imposed by the stiff ring on adjacent elements with the large decrease in total stress in analysis SRN1.

At the tunnel face the stiff ring appeared to have a similar but smaller effect to that found in KAP02, where a lower value of κ was used. After rapid initial dissipation at the tunnel face the pore pressure tended to reduce towards equilibrium values of about -40kPa in D13, but only to -20kPa in SRN1, Fig. 7.41, a response similar to that in Fig. 7.31. At element 25 the changes in pore pressure, Fig. 7.42, were slower in SRN1, as they were in KAP02, with the associated differences in rates of specific volume increase and variations in stress paths. At the end of the analyses the deformation at the tunnel face in SRN1 was about 25% less than D13, indicating the support being provided by the stiff ring. Although modelling a pore pressure transducer as a stiff ring may be beneficial in obtaining a more appropriate pore pressure response for comparison with experimental data, the results from D13 and SRN1 suggest that a stiff ring should not be included as standard procedure due to its wider influence.

Investigation of the treatment of particular difficulties in the analyses has shown that:

- a) the increase in stiffness (by a factor of eight) of the elastic elements at the intersection of the tunnel boundary with the tunnel face had a negligible effect on the predicted behaviour and allowed the analyses to proceed for a larger number of increments;
- b) larger pore pressure reductions were predicted (during the removal of the face support) local to a stiff element which had been included to model a pore pressure transducer;
- c) the stiff element (or stiff ring due to the axisymmetry of the problem) modified the behaviour locally, influencing the stress paths and the specific volume changes in adjacent elements;
- d) the presence of a stiff ring to model a pore pressure transducer influences the behaviour throughout the zone ahead of the tunnel face, and should only be incorporated to study pore pressure responses in the vicinity of a pore pressure transducer.

7.4 Comparison with experimental data

Analysis SI50, which modelled some of the Series I stage 1 tests, may be compared with test 10/1 in which the 50.8mm diameter tunnel was used. The agreement between the predicted and measured pore pressure values is poor, as seen in Fig. 7.43, in which elements 48 and 50

represented ppt3106 and ppt3435 respectively. A small rise was predicted at element 50, whereas experimentally a reduction of about 90kPa was measured at ppt3435. Although elements such as 48 and 50 did not predict the experimental behaviour well, the elements along the central axis such as 25 in SI50, Fig. 7.43, showed a more similar qualitative response to that of the pore pressure transducers. The pore pressure changes occurred over a much longer time period experimentally.

Test 15/1, also a 50.8mm diameter tunnel test, was modelled by KAP05 in which the initial effective stresses and pore pressures were 400kPa. Elements 48 and 50 in zone A represented ppt2933 and ppt2962 respectively, as shown in Fig. 7.44. There was little agreement between the experimental response and finite element predictions at these elements. However the response of element 25, directly ahead of the face, Fig. 7.44, showed some similarity to that of the pore pressure transducers at some distance perpendicular to the central axis.

The response of three pore pressure transducers located directly ahead of the face in test 18/3 (25.4mm diameter tunnel) is shown in Fig. 7.45. Element 25 and ppt3537 were both located at r/r_0 of about one ahead of the face on the central axis, and showed a similar reduction in pore pressure at the end of the removal of the support pressure. Experimentally there was only a very small rise and subsequent fall in pore pressure (ignoring the erratic changes due to the experimental procedure) unlike that at element 25. Transducers 2944 and 3536 at r/r_0 of 2.6 and 3.8 respectively measured larger initial reductions

than for example those predicted at element 12 at r/r_0 of about two, shown in Fig 7.45.

Deformation data from tests 10/1 and 11/1 and analyses SI50 and SI25T are compared using the non-dimensional group $\delta/(D \times LF^2)$ in Fig. 7.46. A considerable disparity exists between the measured and predicted displacements, particularly at the 50.8mm diameter tunnel face. Reasons for this difference may be the restraining effect of the outer elements, and the more noticeable influence of the constant stress boundary experimentally. CRISP predicted only 3.6mm of displacement compared with 20mm in the model test 10/1 at T_δ of about 4.5×10^{-6} , an under prediction by a factor of 5.6. Predictions from SI25T compared with the experimental values from test 11/1 were only a factor of about two smaller. The results in Fig. 7.46 demonstrate that the use of the load factor, as calculated in Chapter 5, may not be appropriate for comparing the displacements from different diameter tunnels for these analyses, and also indicate the effect of the constant stress boundary on the experimental 50.8mm diameter tunnel data.

The deformation of the tunnel face in KAP05 was under predicted when compared with test 15/1, in Fig. 7.47, by a factor of about 4.7, which is similar to the under prediction in SI50. The 25.4mm diameter tunnel was used in test 18/3, which had an initial stress state similar to test 15/1. At equal time factors, the value of $\delta/(D \times LF^2)$ was 2.33 compared with 0.91 for KAP05, values which differ by a factor of about 2.6. This lower factor is in agreement with the observations made concerning the data presented in Fig. 7.46.

A number of factors may have contributed to the poor prediction of deformation. The radial support provided by the displacement fixity representing the tunnel lining restricted radial movement ahead of the face, and limited the extent of the plastic zone. Consequently smaller radial movements occurred towards the tunnel face. The soil model used is another reason for the under predictions. Elastic behaviour is assumed below the yield surface in the modified Cam-clay model, which causes the outer elements to provide greater support than would be expected in real soil behaviour. On cutting a section through the sample, it was noted that cracks had opened up around the tunnel face, as shown in Fig. 2.12. Such cracks may be an indication of the formation of slip planes during the tests, which were not modelled in the finite element analyses, and may be a further cause of the poor correspondence between the test data and the analyses.

The major findings of the comparisons of experimental data with finite element predictions are given below:

- a) pore pressure increases were calculated in zone A (perpendicular to the central axis), an indication that the shape of plastic zone in this region was significantly different from the model tests in which pore pressure reductions were measured;
- b) large pore pressure reductions were predicted in zone B, although the extent of these was also not as great as those measured experimentally;

- c) deformations were consistently under predicted throughout the analyses;
- d) the magnitude of the under prediction varied depending on the diameter of the model tunnel and analysis being compared, as a result of the influence of the constant stress boundary;
- e) the use of the non-dimensional group $\delta/(D \times LF^2)$ developed from experimental data may not be suitable for comparing predicted displacements for different diameter tunnels.

7.5 Conclusions

The analyses have generally provided data to assist with the development of a better understanding of the complex changes which take place during the excavation and subsequent deformation with time in the model tunnel tests. Deformations occurring with time at a tunnel face have been clearly shown to be a function of dissipating pore suctions and increases in specific volume which lead to loss of strength and softening towards critical state. Limitations of some aspects of the finite element program used have also become evident.

The investigation of the influence of tunnel diameter showed that the predicted response appeared to be affected by the proximity of a constant stress boundary, although to a lesser extent than in the model tests. These analyses also indicated that the use of the n_f^2 time scale factor may not be appropriate for cases where the initial stress state is normally consolidated, since the smaller diameter tunnels with identical stress states encountered numerical

difficulties at earlier stages in the analyses. These problems were overcome by reducing the size of the time increments, which suggests that the changes taking place were not simply due to a diffusion process. Analyses modelling a soil with an overconsolidation ratio of two in which the same time scale factor n_f^2 was applied did not encounter such numerical problems.

The investigation of the influence of load factor and initial pore pressure for a given tunnel diameter provided some further evidence to support the non-dimensional groups developed in Chapter 5. However the calculation of load factor using N_{crit} , as determined in Chapter 5, may not be appropriate for these analyses, since its inclusion resulted in a greater separation between the deformation curves for different diameter tunnels. In contrast to the experimental behaviour, the shallowest curve in non-dimensional space was obtained from the 50mm diameter analysis.

The pore pressure changes at the tunnel face appeared to be related to the rate of deformation at the face. The subsequent rates of softening and pore pressure change with time at locations some distance from the face seemed to be significantly influenced by the behaviour at the face, as shown particularly by the analyses in which the influence of κ was studied.

An investigation of the influence of the pore pressure transducers on the measured changes, by the inclusion of a stiff ring to represent the transducer, indicated that such an inclusion caused a localized disturbance to the stress distribution. As a result larger pore pressure reductions were predicted in the vicinity of the stiff ring

at the end of the removal of support pressure. This implies that the larger than anticipated experimental pore pressure changes shown in Fig. 5.7(a) may be at least in part the result of load transfer to the transducers. The influence of the stiff ring was not confined to the adjacent elements, but significantly affected the deformation of the tunnel face and the pore pressure response ahead of the face. Consequently it is suggested that the use of this procedure should be restricted to the study of pore pressure response at individual elements.

In comparison with the experimental measurements, the finite element analyses consistently under predicted the plastic radius or the extent of zone around the tunnel face which was affected by pore pressure changes at the end of support pressure removal. Along the central axis there was some agreement between the extent of the plastic zone predicted and the closed form solution for the thick sphere.

Displacement predictions from the CRISP analyses using the 50mm diameter tunnel mesh under predicted the 50.8mm diameter model tunnel test data by a factor of between four and six. Results from the analyses of smaller diameter tunnels compared with the experimental data differed by a factor of between two and three. These data support the suggestions in Chapters 3 and 5 that the largest diameter model tunnel tests were significantly affected by the constant stress boundary.

Numerical problems related to the unavoidably restricted deformation at the intersection of the tunnel circumference and the tunnel face were overcome by the use of some elastic elements. However, the

restraint remained and was the probable cause of some significant differences found between the experimental and analytical results. The shape of the zone affected by the removal of face support is different to that based on experimental data. Two zones of influence were established with the experimental data, whereas from the analyses only one zone, equivalent to a reduced zone B in Fig. 5.5, was significant. The elements close to the tunnel face restricted radial movement into the tunnel so that the flow of soil into the tunnel could not be modelled. A large measure of support was provided by these elements with the result that much smaller pore pressure reductions were observed due to the smaller total stress changes.

The radial restriction may also have been a contributory factor to the disparity found between the predicted and measured deformations at the tunnel face. Some constraint was also provided by the surrounding elements as a result of the soil model used. There is some experimental evidence that slip planes may have formed ahead of the tunnel face, which were not modelled in the analyses, and may be a further reason for the poor correspondence.

The analysis of problems in which large pressure gradients are caused by excavation processes can be successfully performed with adequately small time steps and a sufficiently refined mesh. Increases in specific volume and softening towards critical state, close to the unsupported boundary, have been shown in analyses modelling soils which were initially either wet or dry of critical state. Careful consideration of pore pressure boundary conditions is essential if the numerical difficulties are to be minimised. Particular problems, such as the additional restraint introduced by boundary conditions imposed

to represent the tunnel lining, required special treatment. For example, the use of a small number of elements having elastic properties, instead of modified Cam-clay, avoided the numerical problems which would otherwise have arisen.

8.1 Deformations and pore pressure behaviour around an unsupported tunnel face in clay

At the instant of excavation the behaviour of the soil close to the tunnel face is undrained and an inevitable undrained deformation is observed as a result of stress relief. The reduction in total stress at the excavated boundary is accompanied by a reduction in pore pressure and the introduction of large hydraulic gradients which cause flow of water from zones of high (or unchanged) pore pressure to those of low pore pressure close to the face. Consequently the pore pressure and water content at and close to the boundary begin to rise causing the effective stress and the soil strength to be reduced. The change in effective stress level is then dependent on the rate of pore water migration, and the deformation, which is the inevitable result of a change in effective stress, also becomes time dependent.

The small scale model tests have confirmed that this mechanism is the cause of the time dependent behaviour often observed in the field. Water contents of clay samples taken from the model after a test showed a steady increase in the vicinity of the face, which was dependent on the duration of the test. Pore pressure measurements demonstrated the dissipation of the pore pressure reductions and subsequent changes associated with the stress equilibrium being maintained. The zone of soil within which significant changes in stress level and in which significant flow of water may occur is small relative to the overall volume of the sample. Consequently events at

the model tunnel face may be considered to be due to local drainage with the overall conditions in the model sample remaining undrained for the time period during which the tunnel face was unsupported. Similarly during the construction of experimental galleries at Mol the Boom clay stratum would remain globally undrained.

Rates and magnitude of deformation at the model tunnel face are influenced by the initial pore pressure, the permeability of the soil, the load factor and the tunnel diameter. The influence of permeability, pore pressure and tunnel diameter have been combined in a dimensionless deformation time factor, $T_\delta = ktu_0/(D^2\gamma_w)$. These factors have been identified based only on tests using kaolin, and consequently other soil parameters which may also be important have not been investigated. The stability of the tunnel face under undrained conditions is assessed by the value of the load factor. The same parameter has been used to correlate the time dependent deformation (at a given deformation time factor) from tests with different initial stress states and tunnel diameters, and a second dimensionless group $\delta/(D \times LF^2)$ has been established. Variations in load factor are closely related to the initial pore pressure by its influence on stability ratio, and to the value of the critical stability ratio, N_{crit} .

Typical values obtained for the dimensionless groups from the model tests have been correlated with the conditions at Mol. It is assumed that the water table is at ground level, that the permeability of the Boom clay has a value of 10^{-12}m/s and that the load factor is 0.5. At a deformation time factor of 30×10^{-6} , which is equivalent to about 1000 hours at Mol, the anticipated deformation at the tunnel face

would be about 9m, assuming that all relevant soil parameters have been considered in the dimensionless groups. After a time of 100 hours, the expected deformation would be 0.6m. Such large displacements were not observed in the experimental drift at Mol, where the face has been unsupported for about two years with a movement of only about 200mm. At this particular location the pore pressures are at present only about 1000kPa, much lower than hydrostatic, possibly due to drainage into instrumentation casings, or a side effect of the ground freezing used in the construction of the underground research laboratory. Water content measurements from samples taken from this location were about 3% lower than expected. Consequently the load factor may have been significantly lower than anticipated, with the resultant reduced deformation. Evaporation of moisture from the surface of the tunnel face would lead to pore suction at the face, which may have contributed to the greater stability. This time dependent process was not modelled in the experimental tests and may have led to an artificially high rate of softening at the model tunnel face.

Stress changes at the removal of support pressure lead to large hydraulic gradients (of the order of 700), which exist only for a short time close to the model tunnel face. As the pore pressure reductions dissipate the hydraulic gradients also reduce and become dependent on the magnitude of the initial pore pressure. The model tests have shown that after an initial time period, during which both the deformation and pore pressure response was transient, the longer term conditions were associated with a steady rate of increase in deformation and pore pressure. The steady nature of this behaviour indicated that the coefficient of permeability was a more appropriate

parameter to use in order to define the predominant phase of pore water flow, although the coefficient of consolidation may be the controlling parameter during the early dissipation phase. Identification of the importance of load factor for pore pressure behaviour has not been established in the model tests since a variation in load factor was often also associated with a change in the stress history of the sample.

Simplified analyses based on the thick cylinder and thick sphere closed form solutions from plasticity theory have been used to obtain pore pressure distributions, assuming undrained conditions at the removal of face support. Both the cylinder and sphere were found to be only very approximate geometric representations of the tunnel face. Two zones of behaviour were identified experimentally. One zone, extending in a radial direction perpendicular to the central axis of the tunnel, showed pore pressure behaviour similar in certain respects to the thick cylinder predictions. In the second zone, radial in the direction of the central axis, measured pore pressures were in better agreement with predictions from the thick sphere analogue.

A major source of disparity between the behaviour predicted by the closed form solution and that observed experimentally is the assumption that an elastic-perfectly plastic model can adequately represent the soil response to the excavation. Pore pressures changes during yield prior to reaching the limiting shear stress cannot be predicted by the idealized analysis. Modified Cam-clay is a more appropriate soil model to use for predicting the pore pressure changes during yielding, but cannot be incorporated into a closed form solution. Finite element analyses of an undrained thick cylinder,

using the modified Cam-clay soil model, have provided a more realistic predicted pore pressure distribution which takes soil stress state into account. These analyses showed that the closed form distributions over predicted the pore pressure changes for soil initially at a wet of critical state, and under predicted for a more heavily overconsolidated soil. The gradient of the idealized pore pressure distribution with the logarithm of radius may be taken to represent a mean value for the variable slopes obtained from the analyses using modified Cam-clay. Pore pressure changes along the central axis of the model tunnel analyses have also provided some evidence to support the use of the thick sphere analogue to predict behaviour ahead of the face. The slopes of the pore pressure distributions were similar to that of the idealized solution, although the extent of the plastic zone was slightly smaller.

Analyses of time dependent behaviour of a thick cylinder and of the model tunnel tests using the finite element method have shown the complexity of the stress changes and volumetric strains which occur with time close to an unsupported boundary. The magnitude and rate of these changes is strongly influenced by the initial stress state. Although numerical modelling of the tunnel tests has been successful in demonstrating the mechanics of time dependent behaviour, the predictions are only of limited value in direct comparisons with the experimental results. Deformation, pore pressure changes and the extent of the plastic zone were all significantly under predicted, a consequence of the soil model used and also of the limitations inherent in the finite element program. The program cannot adequately model the large strains observed in the experimental tests. The boundary conditions at the model tunnel face, which allow the soil to

deform freely into the cavity around the leading edge of the lining, could not be modelled satisfactorily in the program. Instead, unavoidable displacement restraints imposed in the analyses have contributed significantly to all aspects of the under predictions.

8.2 Recommendations for further research

The model tests in this dissertation have been restricted to only one soil. A dimensionless time factor developed on this basis cannot include the influence of material properties such as κ , k and c_v . The significance of κ , which defines the swelling characteristics of the soil, has been indicated by the finite element analyses. Further tests are required using a range of soils with different κ , k and c_v to confirm or establish the importance of these parameters to the time dependent deformations. Such tests should be undertaken with a wider range of tunnel diameters, possibly in a larger diameter soil sample, to confirm the applicability of the suggested scaling relationships and to establish a more comprehensive set of dimensionless groups.

In the model tests undertaken for this research project the variations in load factor were often related to a difference in stress history. A further series of tests is needed to demonstrate the influence of stress history with respect to the undrained pore pressure response. The influence of the transducers on the measured values during the unloading stage also needs to be clearly indentified. These tests may also clarify the time dependent pore pressure behaviour, particularly if the positions of the pore pressure transducers are controlled to a greater accuracy. Some consideration of the influence of cavitation is necessary especially for soils which have been subjected to the

high stress levels associated with very deep tunnels at depths greater than 100m.

The magnitude of lining loads is of great importance to the economic feasibility of deep tunnelled repositories. An increased understanding of the soil-lining interaction is needed particularly in terms of how the lining loads are influenced by convergence prior to lining installation, and the drainage boundary condition imposed by the lining. Small scale modelling of such behaviour would require the development of a more sophisticated model tunnel with features such as an overcutting bead and a facility to control drainage through the tunnel lining. Finite element analyses may be valuable particularly where the significance of convergence is concerned, and also in assessing the influence of the drainage conditions.

APPENDIX A - Expressions for thick cylinder solution

The derivation of the equations used in the thick cylinder analysis discussed in Chapter 5 is presented in this Appendix. Figure 5.2 illustrates the dimensions and boundary conditions applied, which are appropriate to the modelling of tunnel behaviour.

Derivation of pore pressure distribution expressions

Elastic analysis

Stress-strain relations (Hooke's law):

$$\epsilon_r = \frac{1}{E}(\sigma_r - \nu\sigma_\theta - \nu\sigma_z) \quad \text{A-1}$$

$$\epsilon_\theta = \frac{1}{E}(\sigma_\theta - \nu\sigma_r - \nu\sigma_z) \quad \text{A-2}$$

$$\epsilon_z = \frac{1}{E}(\sigma_z - \nu\sigma_r - \nu\sigma_\theta) \quad \text{A-3}$$

Assuming plane strain conditions

$$\epsilon_z = 0 \quad \text{A-4}$$

and hence $\sigma_z = \nu(\sigma_r + \sigma_\theta)$ A-5

Compatibility equations:

$$\epsilon_r = du_r/dr \quad \text{and} \quad \epsilon_\theta = u_r/r \quad \text{A-6 and A-7}$$

where u_r is a small radial displacement from a point originally at radius r .

Equilibrium equation (only non-trivial one):

$$\frac{d\sigma_r}{dr} = \frac{\sigma_\theta - \sigma_r}{r} \quad \text{A-8}$$

Substituting equations A-5 and A-8 into equations A-1 and A-2 to obtain

$$\epsilon_r = \frac{(1 + \nu)}{E} \left[\sigma_r(1 - 2\nu) - \nu r \frac{d\sigma_r}{dr} \right] \quad \text{A-9}$$

$$\epsilon_\theta = \frac{(1 + \nu)}{E} \left[\sigma_r(1 - 2\nu) + (1 - \nu)r \frac{d\sigma_r}{dr} \right] \quad \text{A-10}$$

From equations A-6 and A-7, eliminate u_r

$$\frac{du_r}{dr} = \epsilon_r = \frac{d(r\epsilon_\theta)}{dr} \quad A-11$$

$$\therefore \epsilon_r = \epsilon_\theta + r \frac{d\epsilon_\theta}{dr} \quad A-12$$

where

$$\frac{d\epsilon_\theta}{dr} = \frac{(1 + \nu)}{E} \left[\frac{d\sigma_r}{dr} (1 - 2\nu) + (1 - \nu) \frac{d\sigma_r}{dr} + (1 - \nu)r \frac{d^2\sigma_r}{dr^2} \right] \quad A-13$$

Substituting A-9, A-10 and A-13 into A-12, a second order differential equation is obtained

$$\frac{r^2 d^2\sigma_r}{dr^2} + \frac{3rd\sigma_r}{dr} = 0 \quad A-14$$

for which the general solution is

$$\sigma_r = A/r^2 + B \quad A-15$$

By substituting in boundary conditions for the elastic zone into A-15 such that at the outer boundary, $r = b$, $\sigma_r = P_o$ and at the plastic radius $r = c$, $\sigma_r = \sigma_c$

$$P_o = A/b^2 + B \quad A-16$$

$$\sigma_c = A/c^2 + B \quad A-17$$

hence

$$A = \frac{P_o - \sigma_c}{(1/b^2 - 1/c^2)} \quad A-18$$

and

$$B = P_o - 1/b^2 \frac{(P_o - \sigma_c)}{(1/b^2 - 1/c^2)} \quad A-19$$

By substitution into A-15, the general expressions for radial and circumferential stresses become

$$\sigma_r = P_o - (P_o - \sigma_c) \frac{(1/b^2 - 1/r^2)}{(1/b^2 - 1/c^2)} \quad A-20$$

and

$$\sigma_\theta = \sigma_r + \frac{rd\sigma_r}{dr} \quad (\text{from A-8}) \quad A-21$$

$$\sigma_\theta = P_o - (P_o - \sigma_c) \frac{(1/b^2 + 1/r^2)}{(1/b^2 - 1/c^2)} \quad A-22$$

At the plastic radius the Tresca yield criterion applies such that

$$\sigma_{\theta} - \sigma_r = 2c_u \quad \text{A-23}$$

and by subtraction of A-20 from A-22

$$P_0 - \sigma_c = c_u(1 - c^2/b^2) \quad \text{A-24}$$

It is assumed that $b \gg c$ and therefore the term c^2/b^2 is not negligible.

From A-20 and A-22 it can be seen that

$$\sigma_{\theta} + \sigma_r = \text{constant} \quad \text{A-25}$$

and therefore the mean total stress, P , also remains constant in the elastic zone

$$P = \frac{\sigma_{\theta} + \sigma_r + \sigma_z}{3} \quad \text{A-26}$$

where $\sigma_z = \nu(\sigma_r + \sigma_{\theta})$

and assuming constant volume

$$\nu = 0.5$$

Plastic analysis

For plastic behaviour the equilibrium equations, compatibility conditions and the yield criterion are considered. Substitution of equation A-23 into equation A-8 gives

$$\frac{d\sigma_r}{dr} = \frac{2c_u}{r} \quad \text{A-27}$$

and integrating

$$\sigma_r = 2c_u \ln r + F \quad \text{A-28}$$

where F is a constant of integration, and by substituting boundary conditions at $r = a$ and $r = c$ an expression for the stress distribution in the plastic zone can be obtained.

At the inner radius a , $\sigma_r = P_i$

hence $P_i = 2c_u \ln a + F \quad \text{A-29}$

$$\sigma_r = P_i + 2c_u \ln(r/a) \quad \text{A-30}$$

$$\sigma_{\theta} = P_i + 2c_u[1 + \ln(r/a)] \quad \text{A-31}$$

An expression for the plastic radius is obtained by substituting the boundary conditions at the plastic radius $r = c$, $\sigma_r = \sigma_c$ into A-28 and

using A-24

$$N = [2\ln(c/a) + 1 - c^2/b^2] \quad A-32$$

where

$$N = \frac{P_o - P_i}{c_u} \quad A-33$$

hence

$$c = a \cdot \exp \left[\frac{N - (1 - c^2/b^2)}{2} \right] \quad A-34$$

If $b \gg c$ then $c^2/b^2 \rightarrow 0$ and A-34 reduces to

$$c = a \cdot \exp \left[\frac{N - 1}{2} \right] \quad A-35$$

The value of N_{crit} , the value of the stability ratio at which the plastic radius is equal to that of the sample, i.e. $c = b$, is determined by

$$N_{crit} = 2\ln(c/a) \quad A-36$$

The mean of total stress P in the plastic zone is determined from

$$P = \frac{\sigma_r + \sigma_\theta + \sigma_z}{3} \quad A-37$$

which assuming $\nu = 0.5$ for undrained conditions in equation A-5 becomes

$$P = \frac{\sigma_r + \sigma_\theta}{2} \quad A-38$$

and hence

$$P = P_i + c_u + 2c_u \ln(r/a) \quad A-39$$

For undrained conditions the change in pore pressure, \bar{u} , is taken to be equal to the change in total stress which is initially P_o throughout the cylinder and may be written as

$$\bar{u} = c_u [2\ln(r/a) + 1 - N] \quad A-40$$

or

$$\bar{u} = c_u [c^2/b^2 - 2\ln(c/r)] \quad A-41$$

Derivation of displacement expressions

Expressions for the displacement at any point within the cylinder can also be obtained from elastic and plastic analyses using the equations of compatibility and conditions of constant volume.

Elastic zone

From equations A-2, A-5 and A-7

$$\epsilon_{\theta} = \frac{u_r}{r} = \frac{(1 + \nu)}{E} [\sigma_{\theta}(1 - \nu) - \nu \sigma_r] \quad A-42$$

which becomes by substituting from equations A-20, A-22 and A-24

$$\frac{u_r}{r} = \frac{c_u}{2G} \frac{c^2}{r^2} \quad A-43$$

Assuming that $\nu = 0.5$ for undrained conditions and $b \gg c$

at $r = c$

$$u_c = c \cdot c_u / 2G \quad A-44$$

Plastic zone

It is assumed that the volume of the plastic zone remains constant, i.e. the displacement at any radius is compatible with the displacement at the plastic radius.

Hence

$$\pi[(c + u_c)^2 - (r + u_r)^2] = \pi(c^2 - r^2) \quad A-45$$

and from equation A-43

$$\frac{u_r}{r} = \frac{c_u}{2G} \frac{c^2}{r^2} \quad A-46$$

By substituting the expression for the plastic radius (A-34) for which $b \gg c$, equation A-46 becomes

$$\frac{u_r}{r} = \frac{c_u}{2G} \frac{a^2}{r^2} \exp(N - 1) \quad A-47$$

The displacement at the inner boundary is $u_a = a_0 - a$, where a_0 is the initial inner radius, which allows the deformed radius to be approximated by

$$a = \frac{a_0}{1 + \frac{c_u}{2G} \exp(N - 1)} \quad \text{A-48}$$

Equation A-48 is an approximation of the displacement since the plastic radius is dependent on the magnitude of the inner radius. Use of equation A-35 avoids the necessity of introducing a second unknown variable into the expression.

APPENDIX B - Expressions for thick sphere solution

The equations for the thick sphere analysis discussed in Chapter 5 are derived in this Appendix.

Elastic analysis

Stress-strain relations:

$$\epsilon_r = \frac{1}{E} (\sigma_r - 2\nu\sigma_\theta) \quad \text{B-1}$$

$$\epsilon_\theta = \frac{1}{E} (\sigma_\theta(1 - \nu) - \nu\sigma_r) \quad \text{B-2}$$

Compatibility equations:

$$\epsilon_r = du_r/dr \quad \text{and} \quad \epsilon_\theta = u_r/r \quad \text{B-3 and B-4}$$

Equilibrium equation (only non-trivial one):

$$\frac{d\sigma_r}{dr} = \frac{2(\sigma_\theta - \sigma_r)}{r} \quad \text{B-5}$$

Substituting B-5 into B-1 and B-2

$$\epsilon_r = \frac{1}{E} \left[\sigma_r(1 - 2\nu) - \nu r \frac{d\sigma_r}{dr} \right] \quad \text{B-6}$$

$$\epsilon_\theta = \frac{1}{E} \left[\sigma_r(1 - 2\nu) + (1 - \nu) \frac{r}{2} \frac{d\sigma_r}{dr} \right] \quad \text{B-7}$$

Solving for ϵ_r and ϵ_θ in terms of σ_r and σ_θ , from equations B-3 and B-4

$$\frac{du_r}{dr} = \epsilon_\theta + r \frac{d\epsilon_\theta}{dr} = \epsilon_r \quad \text{B-8}$$

where

$$\frac{d\epsilon_\theta}{dr} = \frac{1}{E} \left[\frac{d\sigma_r}{dr} (1 - 2\nu) + \frac{(1 - \nu)}{2} \frac{d\sigma_r}{dr} + (1 - \nu) \frac{r}{2} \frac{d^2\sigma_r}{dr^2} \right] \quad \text{B-9}$$

Substituting B-7 and B-9 into B-8 a second order differential is obtained

$$\frac{r^2 d^2\sigma_r}{dr^2} + \frac{4rd\sigma_r}{dr} = 0 \quad \text{B-10}$$

for which the general solution is

$$\sigma_r = A/r^3 + B \quad \text{B-11}$$

By substituting in boundary conditions for the elastic zone into B-11 such that at the outer boundary, $r = b$, $\sigma_r = P_o$ and at the plastic radius $r = c$, $\sigma_r = \sigma_c$

$$P_o = A/b^3 + B \quad \text{B-12}$$

$$\sigma_c = A/c^3 + B \quad \text{B-13}$$

hence

$$A = \frac{P_o - \sigma_c}{(1/b^3 - 1/c^3)} \quad \text{B-14}$$

and

$$B = P_o - \frac{(P_o - \sigma_c)}{(1 - b^3/c^3)} \quad \text{B-15}$$

The distribution of radial and circumferential stresses is given by

$$\sigma_r = P_o - (P_o - \sigma_c) \frac{(1/b^3 - 1/r^3)}{(1/b^3 - 1/c^3)} \quad \text{B-16}$$

$$\sigma_\theta = P_o - (P_o - \sigma_c) \frac{(1/b^3 + 1/2r^3)}{(1/b^3 - 1/c^3)} \quad \text{B-17}$$

At the plastic radius the Tresca yield criterion is applied such that

$$\sigma_\theta - \sigma_r = 2c_u \quad \text{B-18}$$

which gives

$$P_o - \sigma_c = 4/3c_u(1 - c^3/b^3) \quad \text{B-19}$$

The mean total stress, P , remains constant in the elastic zone where

$$P = \frac{\sigma_r + 2\sigma_\theta}{3} \quad \text{B-20}$$

since it can be seen from equations B-16 and B-17 that

$$\sigma_r + 2\sigma_\theta = \text{constant} \quad \text{B-21}$$

Plastic analysis

In the plastic zone the behaviour is governed by the equilibrium equations, compatibility conditions and the yield criterion.

Substitution of equation B-18 into B-5 gives

$$\frac{d\sigma_r}{dr} = \frac{4c_u}{r} \quad \text{B-22}$$

and integrating

$$\sigma_r = 4c_u \ln r + F \quad \text{B-23}$$

where F is a constant of integration.

By substituting boundary conditions at $r = a$ and $r = c$, an expression for the stress distribution in the plastic zone can be obtained.

At the inner radius a , $\sigma_r = P_i$

and hence

$$P_i = 4c_u \ln a + F \quad \text{B-24}$$

$$\sigma_r = P_i + 4c_u \ln(r/a) \quad \text{B-25}$$

$$\sigma_\theta = P_i + 2c_u[1 + 2\ln(r/a)] \quad \text{B-26}$$

An expression for the plastic radius is obtained from the boundary conditions at the plastic radius, $r = c$, $\sigma_r = \sigma_c$ and by substitution into B-19

$$N = 4[\ln(c/a) + 1/3(1 - c^3/b^3)] \quad \text{B-27}$$

where

$$N = \frac{P_o - P_i}{c_u} \quad \text{B-28}$$

and hence

$$c = a \cdot \exp \left[\frac{N - 4/3(1 - c^3/b^3)}{4} \right] \quad \text{B-29}$$

If $b \gg c$ then $c^3/b^3 \rightarrow 0$ and equation B-29 reduces to

$$c = a \cdot \exp \left[\frac{N - 4/3}{4} \right] \quad \text{B-30}$$

The value of N_{crit} , the stability ratio at which the plastic radius is equal to that of the cylinder is determined by

$$N_{crit} = 4\ln(c/a) \quad \text{B-31}$$

The mean of total stress P in the plastic zone is determined from

$$P = \frac{\sigma_r + 2\sigma_\theta}{3} \quad \text{B-32}$$

hence

$$P = P_i + 4c_u \ln(r/a) + 4/3c_u \quad \text{B-33}$$

For undrained conditions the change in pore pressure is taken to be equal to the change in total stress, which is initially P_0 throughout the cylinder and may be written as

$$\bar{u} = c_u[4\ln(r/a) + 4/3 - N] \quad \text{B-34}$$

or

$$\bar{u} = 4c_u[c^3/3b^3 - \ln(c/r)] \quad \text{B-35}$$

REFERENCES

- Al Tabbaa, A. (1987). Permeability and stress-strain response of Speswhite kaolin. Ph.D. Thesis, Cambridge University.
- Atkinson, J.H. and Bransby, P.L. (1978). The Mechanics of Soils. McGraw-Hill, London.
- Atkinson, J.H. and Potts, D.M. (1977). Subsidence above shallow tunnels in soft ground. Jour. Geotech. Eng. Div., Proc. ASCE, Vol. 103, No. GT4, pp307-325.
- Atkinson, J.H., Richardson, D. and Robinson, P.J. (1987). Compression and extension of K_0 normally consolidated kaolin clay. Jour. Geotech. Engg., Proc. ASCE, Vol.113, No. 12, pp1468-1482.
- Baker, R.T. (1988). Face stability of deep tunnel excavations. Final Year Project. City University.
- Beaufays, R., Buyens, M., De Bruyn, D., Meynendonckx, P., Neerdael, B., Noynaert, L., Voet, M. and Volckaert, G. (1987). The Hades Demonstration and Pilot Project. 2nd Semester Report, Contract F11W-004B(B).
- Bishop, A.W. Kumapley, N.K. and El-Ruwayih, A. (1975). The influence of pore water tension on the strength of clay. Phil. Trans, Royal Society, London, A, volume 278, pp 511-554.
- Bohlke, B.M. and Monsees, J.E. (1988). Design criteria for an underground nuclear waste repository. Tunnels and Tunnelling, June 1988.
- Bonne, A. and Neerdael, B. (1986). Disposal of radwaste in clay: the experience gained in Belgium. Proc. Transactions ENC '86. Genève, June 1986.
- Britto, A.M. and Gunn, M.J. (1987). Critical State Soil Mechanics via Finite Elements. Ellis Horwood Ltd., Chichester.
- Broms, B.B. and Bennermark, H. (1967). Stability of clay at vertical openings. Jour. Soil Mech. Fdn. Eng. Div., Proc. ASCE, Vol. 93, No. SMI, pp 71-94.
- Calladine, C.R. (1969). Engineering Plasticity. Pergamon Press, Oxford.
- Clough, G.W. and Schmidt, B. (1981). Design and performance of excavations and tunnels in soft clay. In Soft Clay Engineering. Elsevier.
- Davis, E.H., Gunn, M.J., Mair, R.J. and Seneviratne, H.N. (1980). The stability of shallow tunnels and underground openings in cohesive materials. Geotechnique, 30 (4), 397-416.

- De Beer, E.E. and Buttiens, E. (1966). Construction de réservoirs pour hydrocarbures liquéfiés dans l'argile de Boom à Anvers. Étude des mouvements du sol provoqués par cette réalisation. Travaux. Sept. 1966, pp 1087-1093, Oct. 1966, pp 1167-1174.
- De Bruyn, D., Neerdael, B., Gonze, P., Rossion, J.P. and Rousset, G. (1986). Contribution to the study of the time dependent behaviour of clay at great depth. Application in view of the construction of a waste disposal facility in the Boom clay formation. Proc 2nd. Int. Symp. on Numerical Models in Geomechanics (NUMOG II), Gent, April, 1986.
- De Moor, E.K. (1985). Model studies related to the behaviour of deep tunnel excavations. First Year Report. Geotechnical Engineering Research Centre Research Report, GE/85/25, The City University.
- De Moor, E.K. (1987). Geotechnical aspects of tunnel construction in deep clay for radioactive waste disposal. Ground Engineering, Sept. 1987.
- De Moor, E.K. (1989). Data report on a programme of small scale model tunnel tests. Geotechnical Engineering Research Centre Research Report, GE/89/03, City University.
- Farmer, I.W. (1978). Case histories of settlement above tunnels in clay. Proc. Conf. on Large Ground Movements and Structures, Cardiff, July 1977, Ed. J.D. Geddes, publ. Pentech Press, London, pp357-371.
- Funcken, R., Gonze, P., Vranken, P., Manfroy, P. and Neerdael, B. (1983). Construction of an experimental laboratory in deep clay formation. Proc. Eurotunnel '83 conf., Basle, Switzerland.
- Gioda, G. (1982). On the non-linear squeezing effects around circular tunnels. Int. Jour. for Num. and Anal. Meth. in Geomech., 6, 21-46.
- Goulder, S.J. (1988). Effects of strain rate and stress history on the undrained shear strength of kaolin. Final Year Project. City University.
- Hoffman, O. and Sachs, G. (1953). Introduction to the Theory of Plasticity for Engineers. McGraw-Hill Book Company Inc.
- Horseman, S.T., Winter, M.G. and Entwistle, D.C. (1986). Geotechnical characterisation of Boom clay in relation to the disposal of radioactive waste. British Geological Society / National Environmental Research Council Report FLPV 86-12, BGS. Keyworth, UK.
- Hudson, J.A. and Boden, J.B. (1982). Geotechnical and tunnelling aspects of radioactive waste disposal. Proc. of Conf. Tunnelling '82, pp271-281.
- Keedwell, M.J. (1984). Rheology and Soil Mechanics. Elsevier Applied Science Publishers, London.

- Kutter, B.L., Sathialingam, N. and Herrmann, L.R. (1988). The effects of local arching and consolidation on pore pressure measurements in clay. Proc. of the Int. Conf. on Geot. Centrifuge Modelling, Paris, pp115-118. A. A. Balkema.
- Ladd, C.C., Foott, R., Ishihara, K., Schlosser, F. and Poulos, H.G. (1977). Stress-deformation and strength characteristics. Proc. 9th. Int. Conf. on Soil Mech. and Fdn Engg., Tokyo, Vol. 2, pp 421-494.
- Langhaar, H.L. (1951). Dimensional Analysis and Theory of Models. Chapman and Hall, London.
- Lo, K.Y., Ng, M.C. and Rowe, R.K. (1984). Predicting settlement due to tunnelling in clays. Tunnelling in Soil and Rock. Proc. of Geotech '84, publ. ASCE, pp46-76.
- Lopez, R.S., Cheung, S.C.H. and Dixon, D.A. (1984). The Canadian program for sealing underground nuclear fuel waste vaults. Can. Geotech. Journal. Vol. 21, pp 593-596.
- Mair, R.J. (1979). Centrifugal modelling of tunnel construction in soft clay. Ph.D Thesis, Cambridge University.
- Manfroy, P., Neerdael, B. and Buyens, M. (1987). Construction of an underground laboratory and experimental programme. Chapter IX in R & D programme on radioactive waste disposal into geological formations (study of a clay formation). Report EUR11025EN.
- Myer, L.R., Brekke, T.L., Korbin, G.E., Kavazanjian, E. and Mitchell, J.K. (1977). Stand-up time of tunnels in squeezing ground. Report to the U.S. Dept. of Transportation, No. DOT-TST-77-59.
- Nadarajah, V. (1973). Stress-strain properties of lightly overconsolidated clays. Ph.D Thesis, University of Cambridge.
- Neerdael, B., De Bruyn, D., Voet, M., André-Jehan, R., Bouilleau, M., Ouvry, J.F. and Rousset, G. (1987). In situ testing programme related to the mechanical behaviour of clay at depth. 2nd Int. Symp. on Field Measurements in Geomechanics. Kobe, Japan, April 1987.
- Nunez, I.L. (1989). Centrifuge model tension piles in clay. Forthcoming Ph.D Thesis, Cambridge University.
- Parry, R.H.G. (1972). Stability analysis for low embankments on soft clays. Proc. Roscoe's Memorial Symp. Foulis, pp643-668
- Peck, R.B. (1969). Deep excavations and tunnelling in soft ground. Proceedings of 7th International Conference on Soil Mechanics, Mexico. pp. 226-290. State of the Art Vol.
- Phillips, R. (1986). Ground deformation in the vicinity of a trench heading. Ph.D Thesis, Cambridge University.

- Pickles, A.R. (1989). The application of critical state soil mechanics to predict ground deformation below an embankment constructed on soft alluvium. Forthcoming Ph.D Thesis, City University.
- Rebull, P.M. (1972). Earth responses in soft ground tunnelling. Proc. Spec. Conf. Performance of Earth and Earth supported structures, Purdue University, Lafayette, Ind., 1:1517-1535.
- Richardson, D. (1988). Investigation of threshold effects in soil deformations. Ph.D Thesis, The City University.
- Roscoe, K.H. and Burland, J.B. (1968). The generalised stress-strain behaviour of 'wet' clay. In Engineering Plasticity, Eds. J. Heyman and F.A. Leckie, Cambridge University Press, pp535-609.
- Roscoe, K.H. and Schofield, A.N. (1963). Mechanical behaviour of an idealized 'wet-clay'. Proc. 2nd European Conf. Soil Mech. Fdn. Engg., Wiesbaden, Vol. 1, pp47-54.
- Schittkat, J. (1983). Geology and geotechnique of the Scheldt surge barrier. Characteristics of an overconsolidated clay. Proc. 8th Int. Harbour Congress Antwerp, 2, 121-135.
- Schofield, A.N. and Wroth, C.P. (1968). Critical State Soil Mechanics. McGraw Hill, England.
- Seneviratne, H.N. (1979). Deformations and pore pressure dissipation around shallow tunnels in soft clay. Ph.D Thesis, Cambridge University.
- Sloan, S.W. and Randolph, M.F. (1982). Numerical prediction of collapse loads using finite element methods. Int. Jour. for Num. and Anal. Math in Geom. Vo. 6, pp 47-76.
- Taylor, D.W. (1948). Fundamentals of Soil Mechanics. John Wiley and Sons, Inc. New York.
- Taylor, R.N. (1984). Ground movements associated with tunnels and trenches. Ph.D Thesis, Cambridge University.
- Taylor, R.N. (1987). Modelling in Ground Engineering. Chapter 58 in Ground Engineer's Reference Book. Ed. F.G. Bell. Butterworths, London.
- Terzaghi, K. (1936). Discussion, Section J: Earth pressure against retaining walls, excavation sheeting, tunnel linings, etc. Paper J8, Proc. 1st Int. Conf. Soil Mech. Fdn. Engg., Cambridge, Mass., Vol 3, pp 152-155.
- Wroth, C.P. (1975). In-situ measurement of initial stresses and deformation characteristics. State of the Art report, Session IV, ASCE GED Speciality Conference on In-situ Measurement of Soil Properties, Raleigh, North Carolina, Vol.2, 181-230.

White, T.P. (1987). Finite element calculations involving the yielding of dilatant soils. M.Phil Thesis, Cambridge University.

Test No.	p (kPa)	p' (kPa)	u (kPa)	OCR	c _u (kPa)	N	LF
3/1	959	765	194	1.0	184	5.21	0.81
3/2	886	807	79	1.0	194	4.57	0.71
3/3	862	780	82	1.0	187	4.61	0.72
4/1	959	767	192	1.0	184	5.21	0.57
4/2	872	792	80	1.0	190	4.59	0.50
4/3	870	791	79	1.0	190	4.58	0.50
5/1	963	767	196	1.0	184	5.23	0.57
5/2	880	804	76	1.0	193	4.56	0.50
5/3	861	779	82	1.0	187	4.60	0.50
6/1	not tested						
6/2	883	809	74	1.0	194	4.55	0.49
6/3	852	772	80	1.0	185	4.61	0.50
7/1	970	775	195	1.0	186	5.22	0.81
7/2	900	824	76	1.0	198	4.55	0.71
7/3	862	779	83	1.0	187	4.59	0.71
8/1	959	766	193	1.0	184	5.21	0.81
8/2	886	808	78	1.0	194	4.57	0.71
8/3	857	779	78	1.0	187	4.58	0.71
10/1	961	766	195	1.0	184	5.22	0.81
10/2	891	815	76	1.0	196	4.55	0.71
10/3	864	784	80	1.0	188	4.60	0.71

Note: Values of c_u obtained from expression 4.19, based on undrained triaxial compression tests described in Chapter 4

Table 3.1(a) Summary of initial stress states for Series I tests

Test No.	p (kPa)	p' (kPa)	u (kPa)	OCR	c _u (kPa)	N	LF
11/1	964	771	193	1.0	185	5.21	0.57
11/2	883	809	74	1.0	194	4.55	0.49
11/3	865	783	78	1.0	188	4.60	0.50
12/1A	965	767	198	1.0	184	5.24	0.44
12/2A	879	799	80	1.0	192	4.58	0.38
12/3A	858	778	80	1.0	187	4.59	0.38
14/1A	not tested						
14/2A	885	805	80	1.0	193	4.59	0.38
14/3A	862	784	78	1.0	188	4.59	0.38
14/1	969	770	199	1.0	185	5.24	0.44
14/2	866	779	80	1.0	187	4.63	0.39
14/3	869	782	87	1.0	188	4.62	0.39
13/1A	963	766	197	2.50	324	2.97	0.25
13/2A	892	813	79	2.35	332	2.69	0.22
13/3A	874	792	82	2.41	328	2.66	0.22
13/1	961	768	193	2.49	324	2.97	0.25
13/2	883	805	78	2.38	330	2.68	0.22
13/3	855	775	80	2.47	326	2.62	0.22

Note: Values of c_u obtained from expression 4.19, based on undrained triaxial compression tests described in Chapter 4

Table 3.1(b) Summary of initial stress states for Series I tests and tests performed in sample no. 13

Test No.	p (kPa)	p' (kPa)	u (kPa)	OCR	c _u (kPa)	N	LF
15/1A	808	406	402	1.97	148	5.46	0.46
15/1	802	400	402	2.00	148	5.42	0.84
15/2	438	236	202	3.39	121	3.62	0.56
15/3	512	457	55	1.75	155	3.30	0.51
16/1A	743	542	201	1.48	166	4.48	0.37
16/1	756	556	200	1.44	167	4.53	0.49
16/2	815	759	56	1.05	188	4.34	0.47
16/3	616	266	350	3.01	126	4.89	0.53
17/1A	894	544	350	1.47	166	5.39	0.45
17/1	900	550	350	1.45	167	5.39	0.59
17/2	1123	771	352	1.04	189	5.94	0.64
17/3	1306	803	503	1.00	193	6.77	0.74
18/1A	652	454	203	1.76	155	4.21	0.35
18/2A	646	451	195	1.77	154	4.19	0.35
18/3A	1047	582	465	1.37	170	6.16	0.51
18/2	1048	578	465	1.38	170	6.16	0.67
18/3	833	435	398	1.84	152	5.48	0.60
19/1A	839	438	401	1.83	153	5.48	0.46
19/2A	904	600	304	1.33	172	5.26	0.44
19/3A	1624	804	820	1.00	193	8.41	0.70
19/2	916	621	295	1.29	174	5.26	0.57
19/3	1624	804	820	1.00	193	8.41	0.91

Note: Values of c_u obtained from expression 4.19, based on undrained triaxial compression tests described in Chapter 4

Table 3.2 Summary of initial stress states for all Series II tests

Test No.	Stage No.	Initial cell pressure (kPa)	Initial back pressure (kPa)	Length of tunnel driven (mm)	Volume occupied by length of tunnel (cc)	Volume of clay removed to reach face (cc)	Drainage conditions	Comments
1	1	760	approx. 20kPa due to level of water in pwp burette	128.7	261.0	255.0	tap to pwp burette OPEN	
	2	1020	200	118.7	240.6	see comments	tap to pwp burette CLOSED until $t = 62$ mins.	rate of intrusion of clay into tunnel too rapid to allow loss to be calculated. At $t = 62$ mins cell pressure reduced to approx. 800kPa and pwp to approx. zero
2	1	390	approx. 20kPa due to level of water in pwp burette	116.2	235.5	227.0	tap to pwp burette CLOSED	pwp burette base tap closed immediately before start of stage and remained closed throughout each stage of the test
	2	510	see comments stage 1	123.4	250.1	276.0	tap to pwp burette CLOSED	
	3		see comments stage 1	142.0	287.8	352.0	tap to pwp burette CLOSED	

Table 3.3 Summary of events during tests nos. 1 and 2

u (kPa)	LF	0.30	0.35	0.50	0.60	0.70	0.80	*
50		531 352	668 449	1116 764				
100		461 280	598 378	1048 695				
150		386	526 302					
200		306	451 215	907 549	782			
250			369		708			
300			275	759 386	631			
350				264	549	1367 804		
400	KEY				461			
450	123	possible p' for 12.7mm dia. tunnel			861			
	123	possible p' for 25.4mm dia. tunnel			358	630		
500					778 186		829	

Table 3.4 Values of p' (in kPa) required for given load factors and initial pore pressures

Test No.	Tunnel dia. (mm)	Fig no. for data	Initial stress state			LF	ppt no.	r/r_o	\bar{u} (kPa)	Final u (kPa)
			u (kPa)	p' (kPa)	OCR					
14/1	12.7	3.6	190	770	1.0	0.44	3441	2.6		86
			205				2962	4.2		109
12/1A	12.7	3.7	198	767	1.0	0.44	3106	2.6	40	98
			211				3102	4.2	13	159
			180				2933	5.8	30	100
11/1	25.4	3.8	194	771	1.0	0.57	3227	1.4	172	40
			196				2936	1.8	81	82
			180				3225	2.6	57	98
10/1	50.8	3.9	194	766	1.0	0.81	3106	1.4	159	68
			195				3435	1.8	92	90
			195				2937	2.6	28	164
12/2A	12.7	3.10	76	799	1.0	0.38	2933	2.6	23	35
			83				3441	6.0	23	38
14/2	12.7	3.11	88	779	1.0	0.38	2834	2.6	39	37

Table 3.5 Summary of model tunnel test data from representative tests in Series I

Test No.	Tunnel dia. (mm)	Fig no. for data	Initial stress state			LF	ppt no.	r/r_o	\bar{u} (kPa)	Final u (kPa)
			u (kPa)	p' (kPa)	OCR					
14/3A	12.7	3.12	77	784	1.0	0.38	3102	2.6	27	28
			71				3441	5.2	20	33
			85				2962	6.2	11	58
14/3	12.7	3.13	85	782	1.0	0.38	2944	1.8	208	18
			90				2933	2.6	52	43
11/2	25.4	3.14	81	809	1.0	0.49	2937	1.4	79	21
			60				2933	1.8	39	32
			80				3106	2.6	27	27
10/2	50.8	3.15	82	815	1.0	0.71	2962	1.4	97	27
			79				2936	1.8	53	43
			80				2939	2.6	14	83

Table 3.5 (continued) Summary of model tunnel test data from representative tests in Series I

Test No.	Tunnel dia. (mm)	Fig no. for data	Initial stress state			LF	ppt no.	r/r_o	\bar{u} (kPa)	Final u (kPa)
			u (kPa)	p' (kPa)	OCR					
11/3	25.4	3.16	80	783	1.0	0.50	2834	1.0	180	-4
			85				3435	2.0	220	12
			86				2939	1.4	80	24
			82				3102	1.8	50	33
			82				2962	2.6	35	40
10/3	50.8	3.17	84	784	1.0	0.71	2933	0.8	218	-4
			77				3441	1.8	130	0
			90				3227	1.4	89	18
			82				2834	1.8	46	33
			74				3225	2.6	18	69

Table 3.5 (continued) Summary of model tunnel test data from representative tests in Series I

Test No.	Tunnel dia. (mm)	Fig no. for data	Initial stress state			LF	ppt no.	r/r_o	\bar{u} (kPa)	Final u (kPa)
			u (kPa)	p' (kPa)	OCR					
16/2	25.4	3.18	56	759	1.05	0.49	3435	1.6	93	11
			53				3102	2.2	6	21
			60				2962	2.0	135	12
16/1	25.4	3.19	207	556	1.44	0.47	3441	1.6	150	33
			195				2936	2.2	85	48
			200				2944	2.0	120	40
16/3	25.4	3.20	347	266	3.01	0.53	2834	1.2	409	-2
			348				3106	2.0	368	7
			367				2933	2.0	370	76
19/1A	12.7	3.21	401	438	1.83	0.46	2944	2.7	104	146
			399				2933	3.8	63	193
17/1	25.4	3.22	349	550	1.45	0.59	2944	1.4	304	66
			339				2933	2.4	206	88
			352				3435	4.2	79	149

Table 3.6 Summary of model tunnel test details from representative tests in Series II

Test No.	Tunnel dia. (mm)	Fig no. for data	Initial stress state			LF	ppt no.	r/r_o	\bar{u} (kPa)	Final u (kPa)
			u (kPa)	p' (kPa)	OCR					
17/2	25.4	3.23	354	771	1.04	0.64	2962	1.4	206	116
			351				3102	2.4	181	128
			358				3441	3.8	94	180
18/1A	12.7	3.24	199	454	1.76	0.35	3106	2.6	50	71
			198				2936	5.9	46	83
18/3	25.4	3.25	401	435	1.84	0.6	3537	1.6	421	2
			402				2944	2.6	269	79
			392				3536	3.8	195	125
19/3A	12.7	3.26	818	804	1.0	0.7	3106	5.2	188	630
			820				2936	4.6	306	556
19/3	25.4	3.27	817	804	1.0	0.91	3393	5.5	199	688
			820				3435	3.4	309	542

Table 3.6 (continued) Summary of model tunnel test details from representative tests in Series II

M	λ	κ	Γ	ν'
0.8	0.19	0.05	3.10	0.3

Table 4.1 Modified Cam-clay parameters describing the behaviour of Speswhite kaolin

Analysis No.	$k_v \times 10^{-6}$ (mm/s)	$k_h \times 10^{-6}$ (mm/s)	Analysis No.	$k_v \times 10^{-6}$ (mm/s)	$k_h \times 10^{-6}$ (mm/s)
TCC1	0.42	1.27	SI50	0.39	1.23
TCC2	0.43	1.29	SI25(T)	0.39	1.23
TCC3	0.43	1.29	SI13(T)	0.39	1.23
TCC4	0.48	1.39	KAP05	0.45	1.33
TCC5	0.48	1.39	LF5	0.48	1.40
			KAP02	0.45	1.33
			STF1	0.45	1.33
			D13	0.44	1.31
			SRN1	0.44	1.31

Table 4.2 Seepage parameters for Speswhite kaolin used in the finite element analyses

Analysis No.	Soil model	E' (kPa)	ν'	K_w (kPa)	c_u (kPa)
TCU1	modified Cam-clay		0.3	320000	
TCU2	modified Cam-clay		0.3	160000	
TCU3	modified Cam-clay		0.3	53000	
TCU4	Tresca	37000	0.3	320000	189
TCU5	Tresca	18800	0.3	160000	160

Table 4.3 Parameters used in the undrained thick cylinder finite element analyses

Analysis No.	Soil model	p (kPa)	p' (kPa)	u (kPa)	OCR	N	c _u (kPa)	G (kPa)	u _a ^{*1} (mm)	u _a ^{*2} (mm)
TCU1	modified Cam-clay	1000	800	200	1.0	5.29	189	14250	2.04	2.58
TCU2	modified Cam-clay	600	400	200	2.0	3.75	160	7260	0.93	0.75
TCU3	modified Cam-clay	465	265	200	3.0	3.30	141	4860	0.80	0.68
TCU4	Tresca	1000	800	200	–	5.29	189	14250	2.04	1.95
TCU5	Tresca	600	400	200	–	3.75	160	7260	0.93	0.89

*1 closed form solution

*2 finite element

Table 6.1 Initial stress states and final displacements for the undrained thick cylinder analyses

Analysis No. ^{*3}	p (kPa)	p' (kPa)	u (kPa)	OCR	N (LF)	c _u (kPa)	G (kPa)	u _a ^{*1} (mm)	u _a ^{*2} (mm)	$ktu_o/(D^2\gamma_w)$ x10 ⁻⁶
TCC1	1200	600	600	1.33	6.85 (1.14)	175	10767	4.61	5.70	27.85
TCC2	600	500	100	1.6	3.59 (0.6)	167	9016	0.69	0.61	4.85
TCC3	850	500	350	1.6	5.09 (0.85)	167	9016	2.23	3.39	17.53
TCC4	615	265	350	3.0	4.36 (0.73)	141	4860	1.86	1.91	18.61
TCC5	465	265	200	3.0	3.30 (0.55)	141	4860	0.80	0.65	10.55

*1 closed form solution

*2 finite element

*3 modified Cam-clay used in each analysis

Table 6.2 Initial stress states and displacements at the end of removal of face support and final time factors for the thick cylinder consolidation analyses

Analysis No.	Tunnel dia. (mm)	p (kPa)	p' (kPa)	u (kPa)	OCR	c _u (kPa)	N	LF	$ktu_o/(D^2\gamma_w) \times 10^{-6}$
SI50	50.0	960	765	195	1.0	181	5.3	0.82	4.82
SI25(T)	25.0	960	765	195	1.0	181	5.3	0.58	6.79
SI13(T)	12.5	960	765	195	1.0	181	5.3	0.44	6.79
SI50	50.0	960	765	195	1.0	181	5.3	0.82	4.82
KAP05	50.0	800	400	400	2.0	160	5.0	0.78	15.22
SI50	50.0	960	765	195	1.0	181	5.3	0.82	4.82
LF5	50.0	440	240	200	3.2	134	3.3	0.52	5.91
KAP05	50.0	800	400	400	2.0	160	5.0	0.78	15.22
KAP02	50.0	800	400	400	2.0	160	5.0	0.78	15.22
KAP05	50.0	800	400	400	2.0	160	5.0	0.78	15.22
STF1	50.0	800	400	400	2.0	160	5.0	0.78	6.27
D13	12.5	840	440	400	1.8	162	5.2	0.43	14.95
SRN1	12.5	840	440	400	1.8	162	5.2	0.43	14.95

Table 7.1 Details of finite element analyses of the model tunnel tests

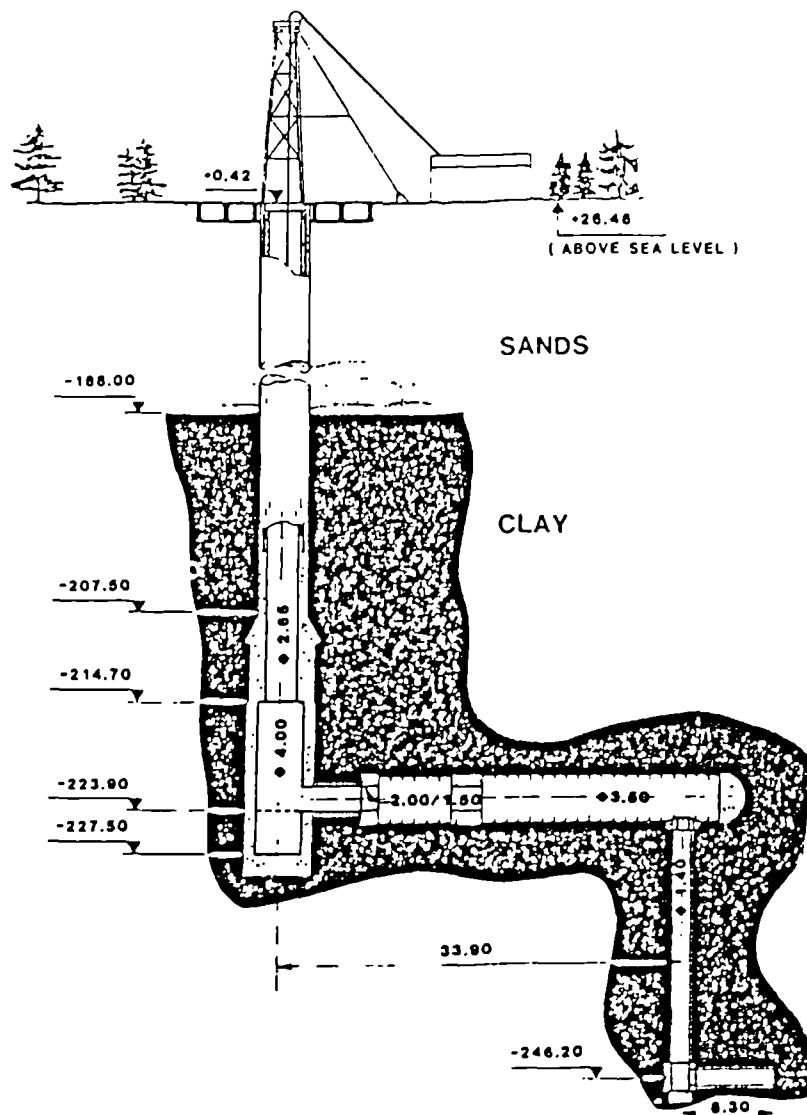


Figure 1.1 The Underground Research Laboratory at Mol (after Manfroy et al, 1987)

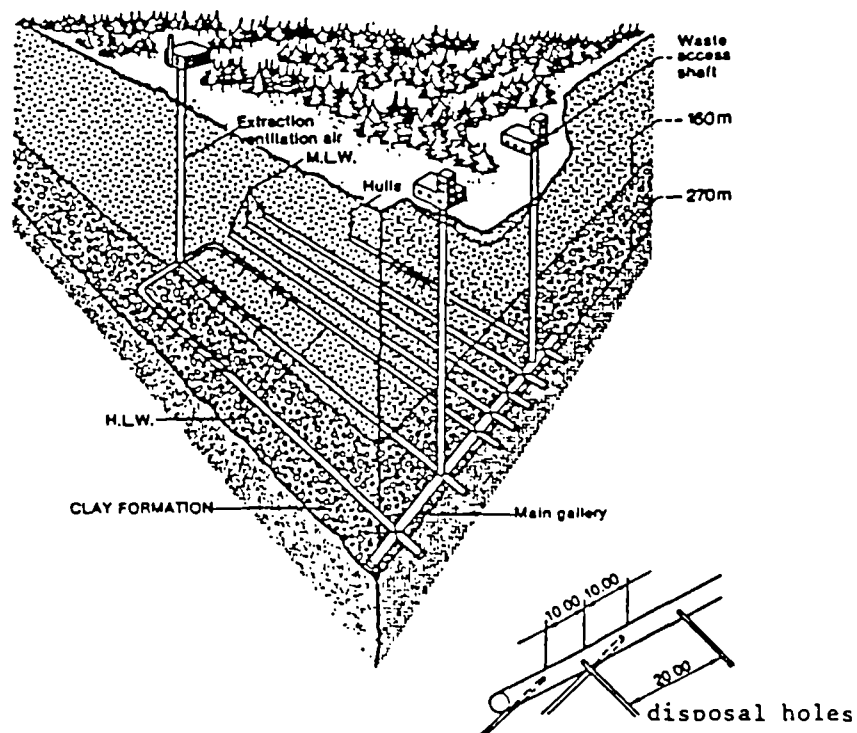


Figure 1.2 Concept of a tunnelled repository in a deep clay formation (after Bonne and Neerdael, 1986)

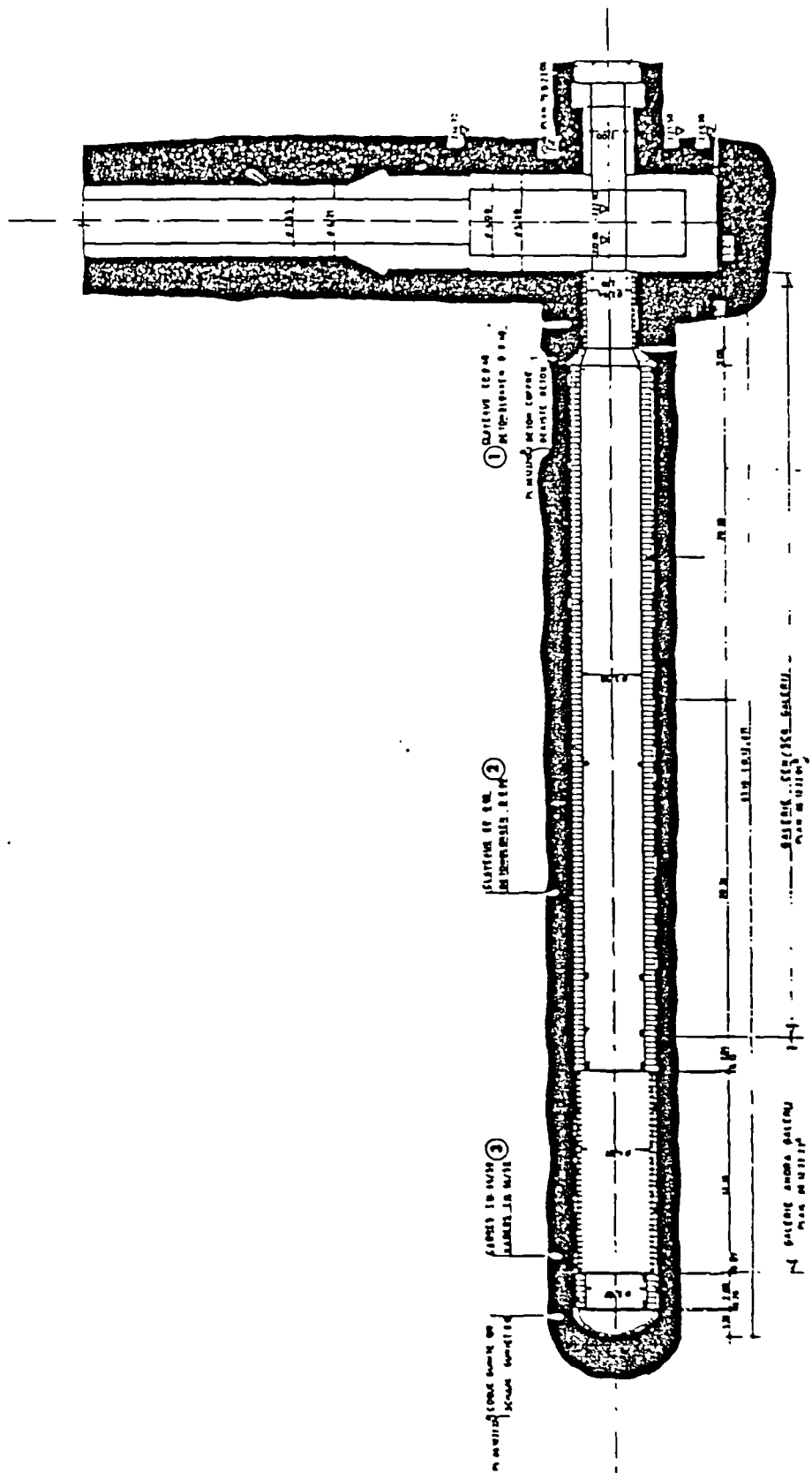


Figure 1.3 The test drift at Mol (after Beaufays et al, 1987)

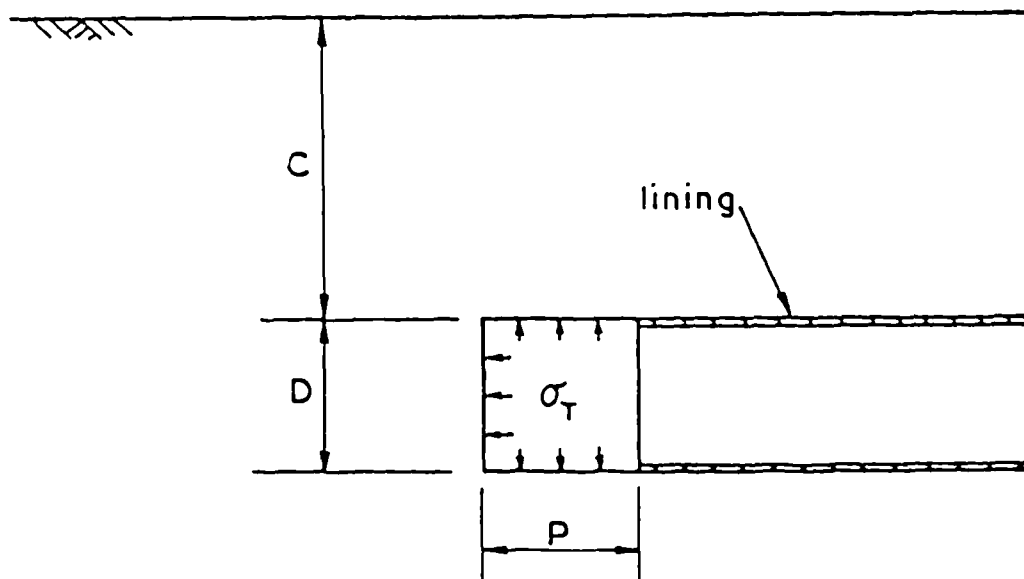


Figure 1.4 Idealized representation of heading during tunnel construction (after Mair, 1979)

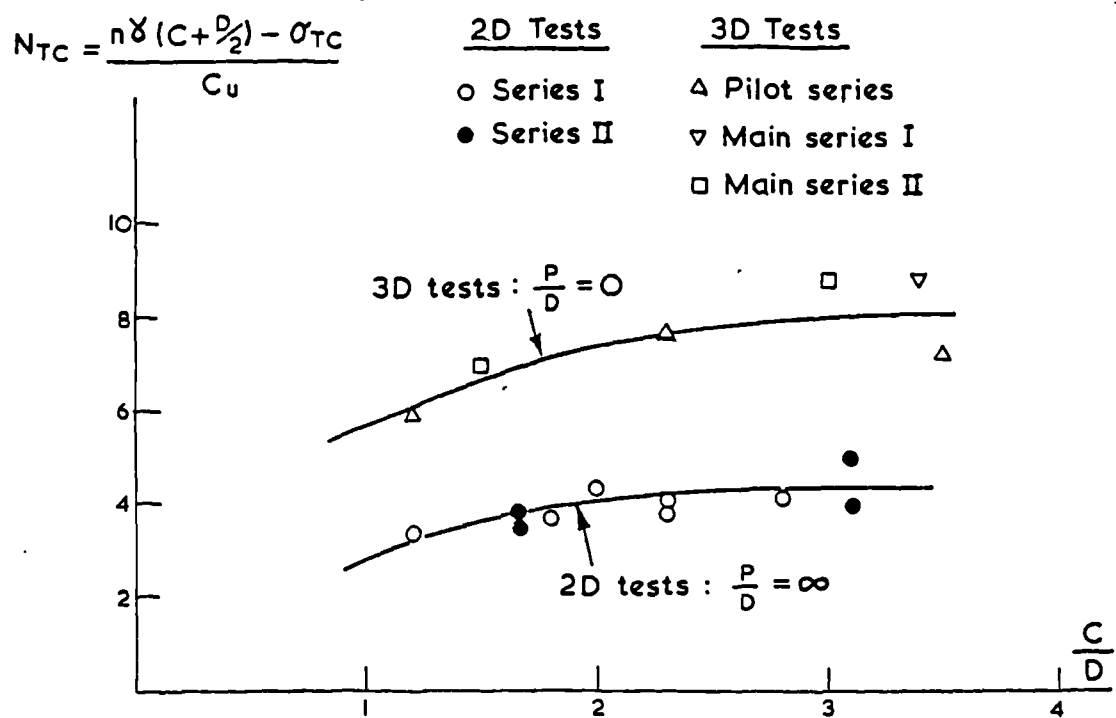


Figure 1.5 Variation of N_{crit} with tunnel geometry (after Mair, 1979)

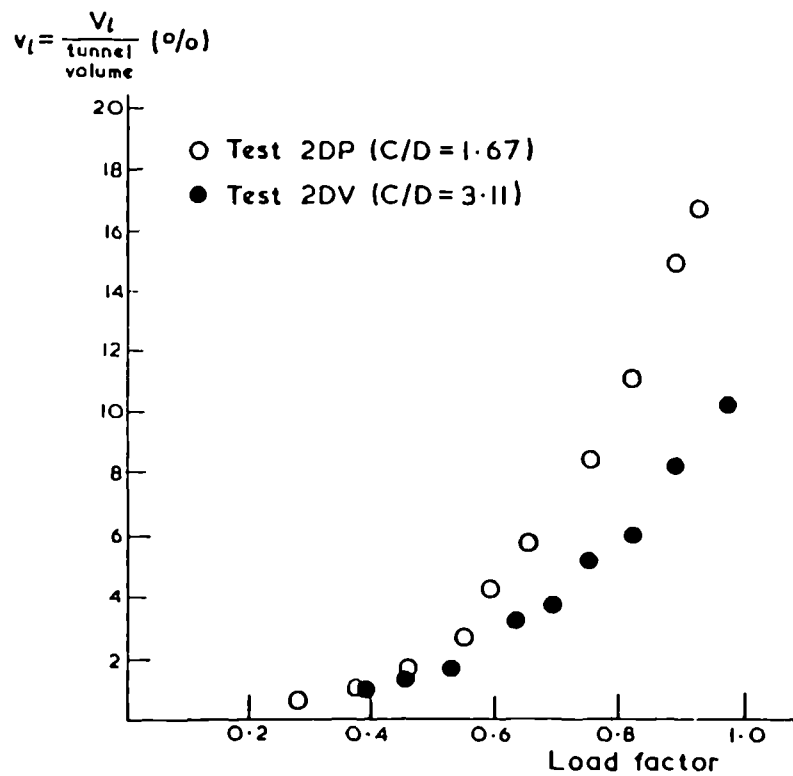


Figure 1.6 Variation of volume loss with load factor (after Mair, 1979)

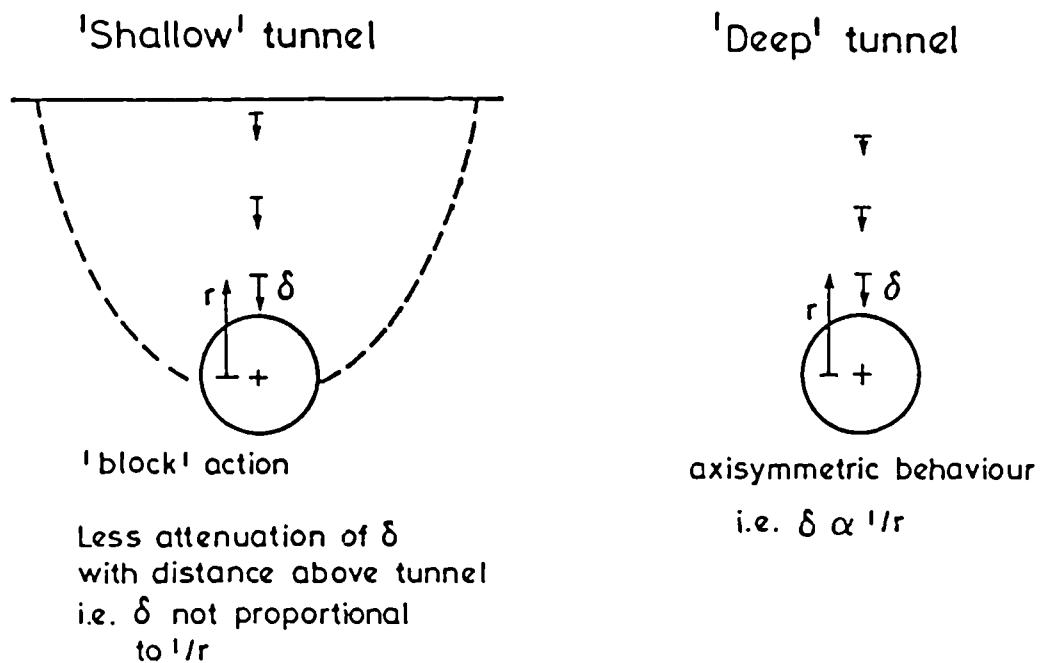


Figure 1.7 Deformation around shallow and deep tunnels

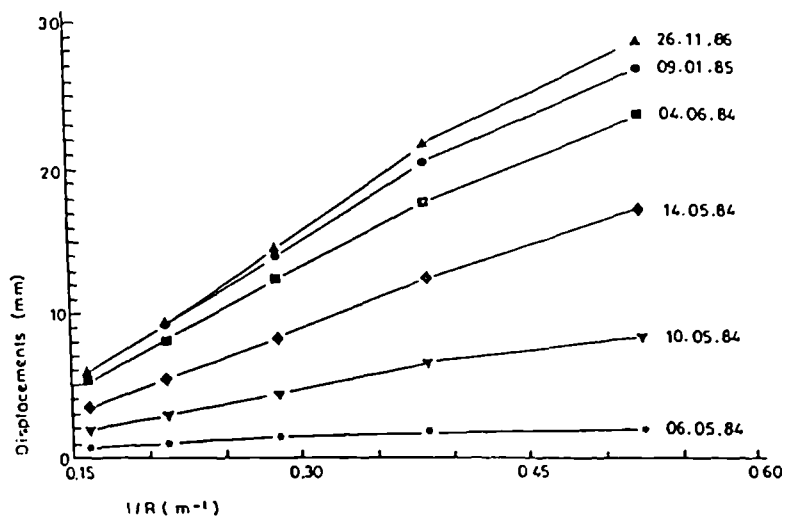


Figure 1.8 Deformation data from the experimental drift (after Neerdael et al, 1987)

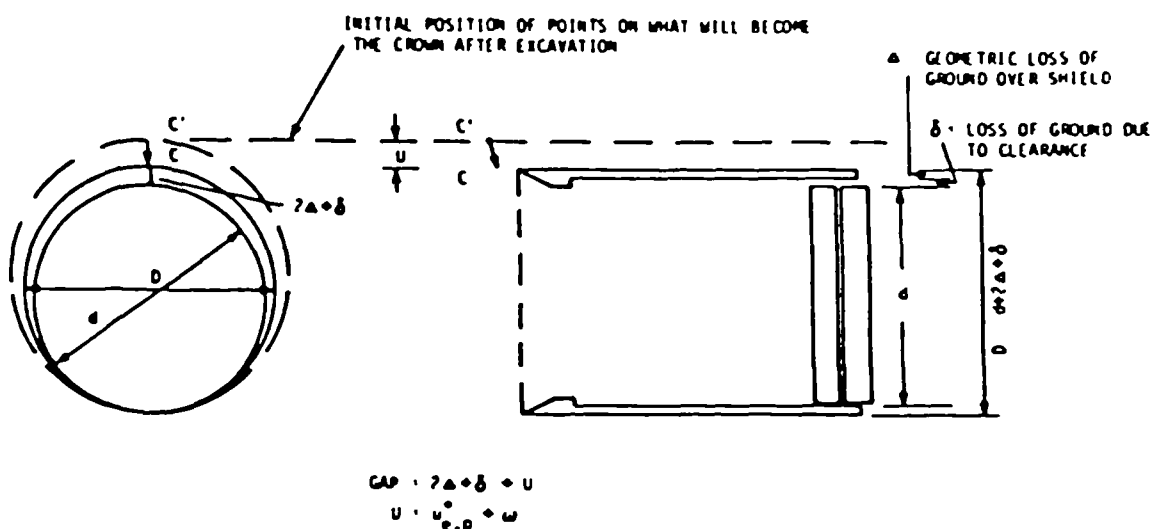


Figure 1.9 Components of deformation caused by tunnel construction (after Lo et al, 1984)

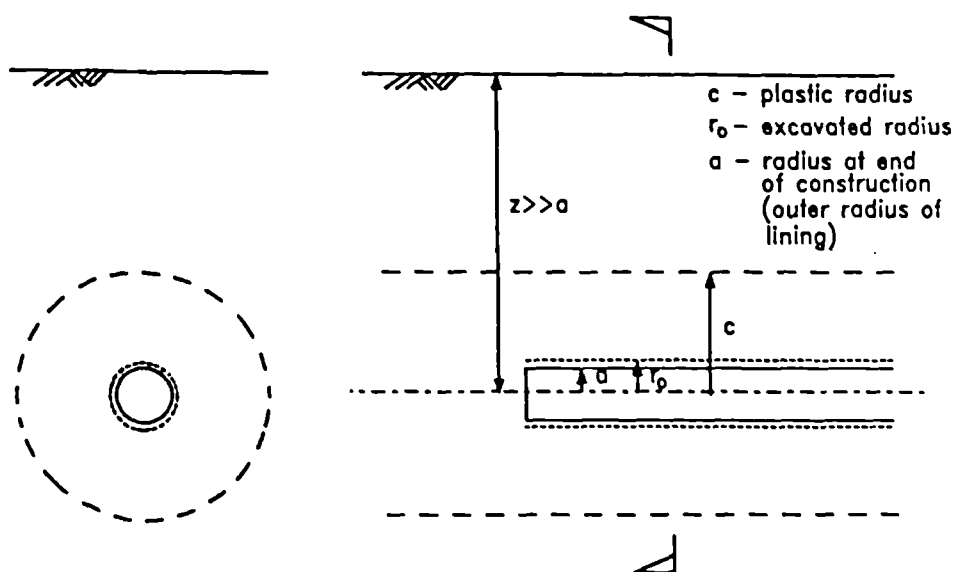


Figure 1.10 Thick cylinder analogue for in situ tunnel behaviour

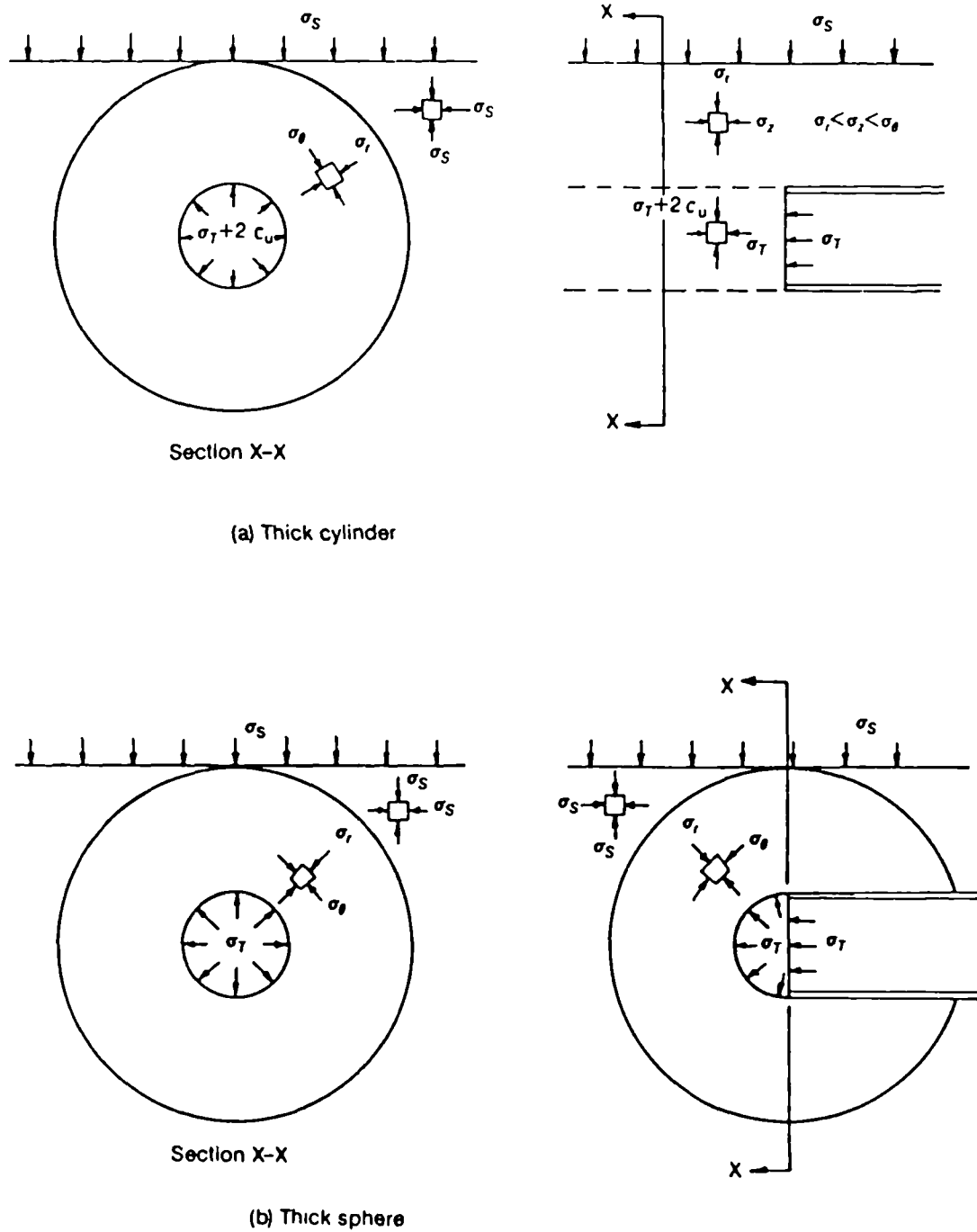


Figure 1.11 Lower bound stress fields for the circular tunnel heading
(after Davis et al, 1980)

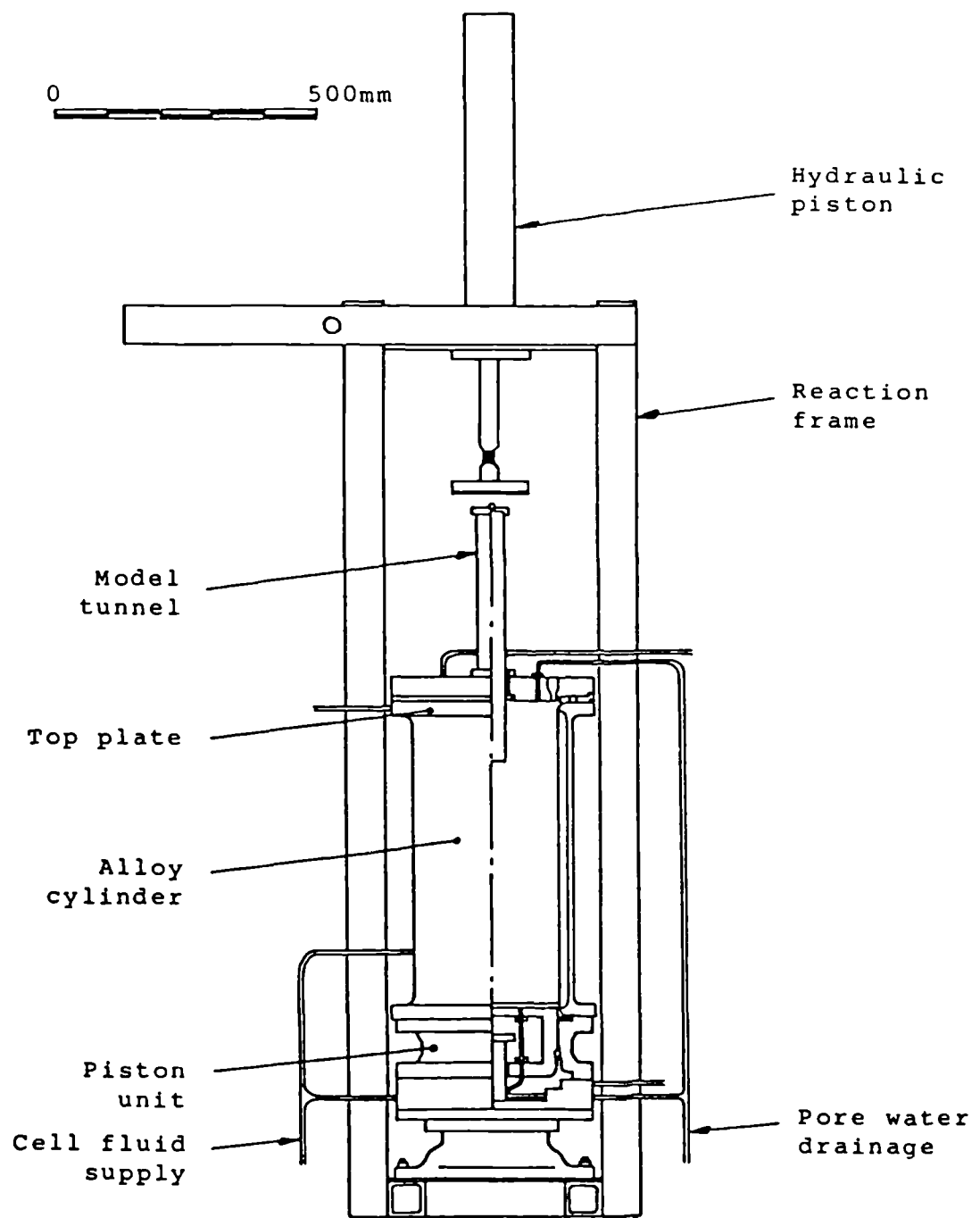


Figure 2.1 The triaxial apparatus

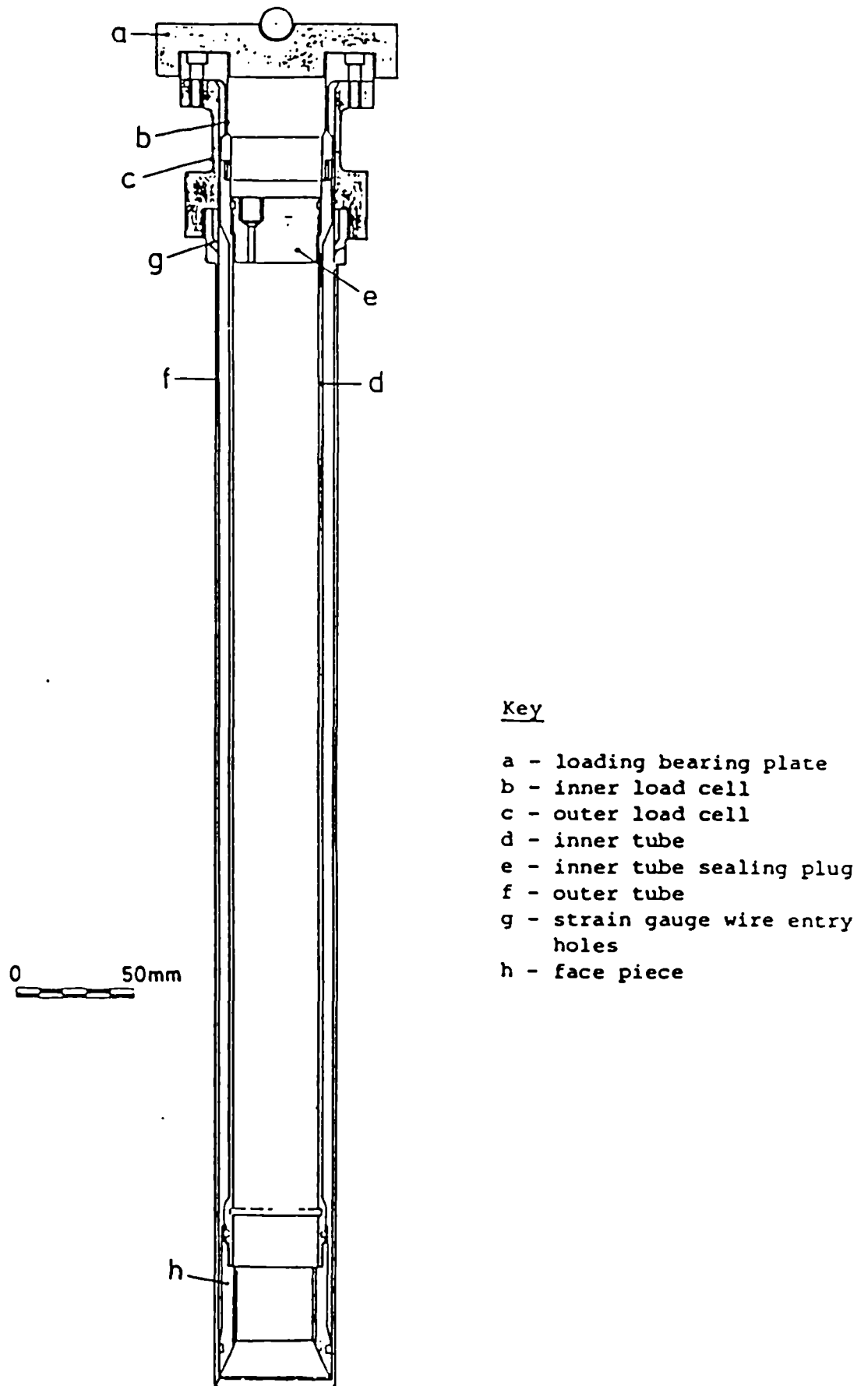


Figure 2.2 Strain-gauged model tunnel

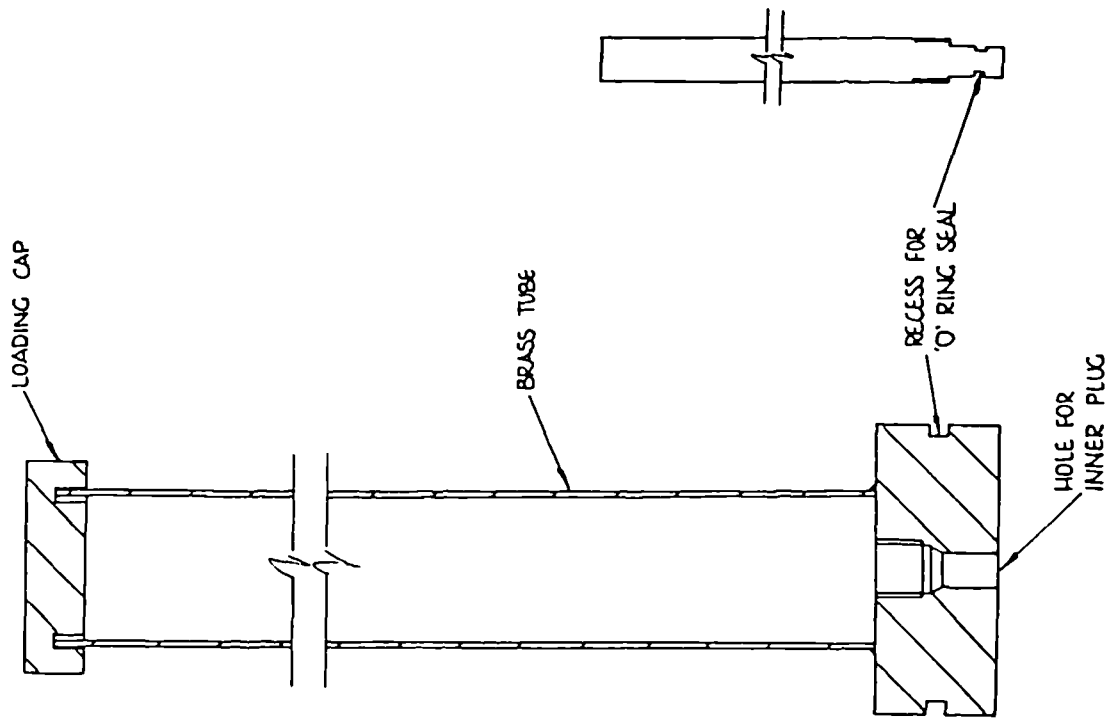


Figure 2.3 Tunnel face support

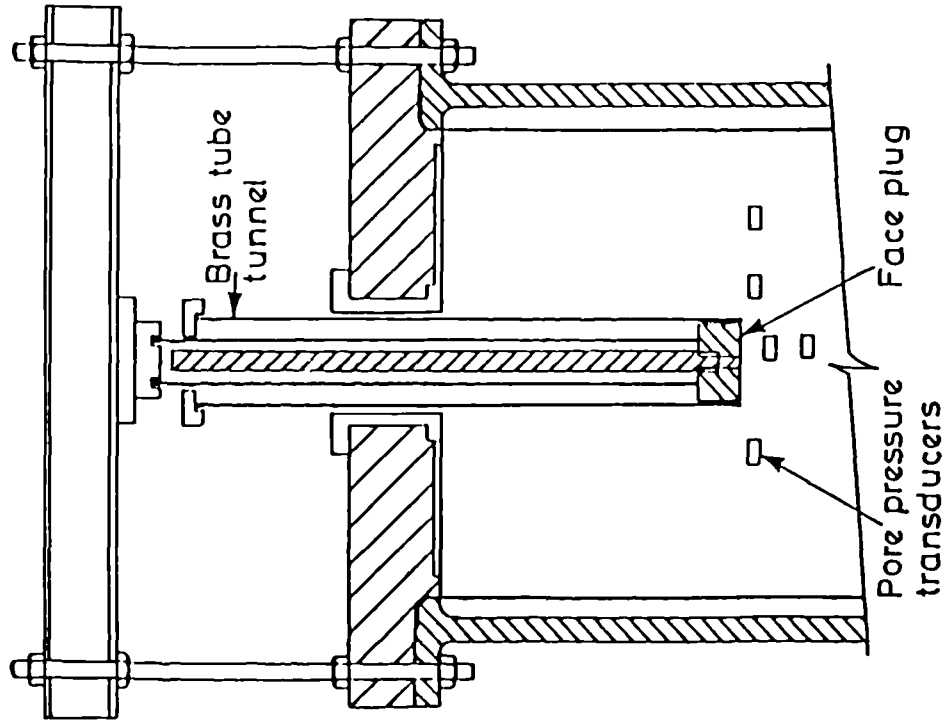


Figure 2.4 Arrangement of tunnel face support apparatus prior to a tunnel test

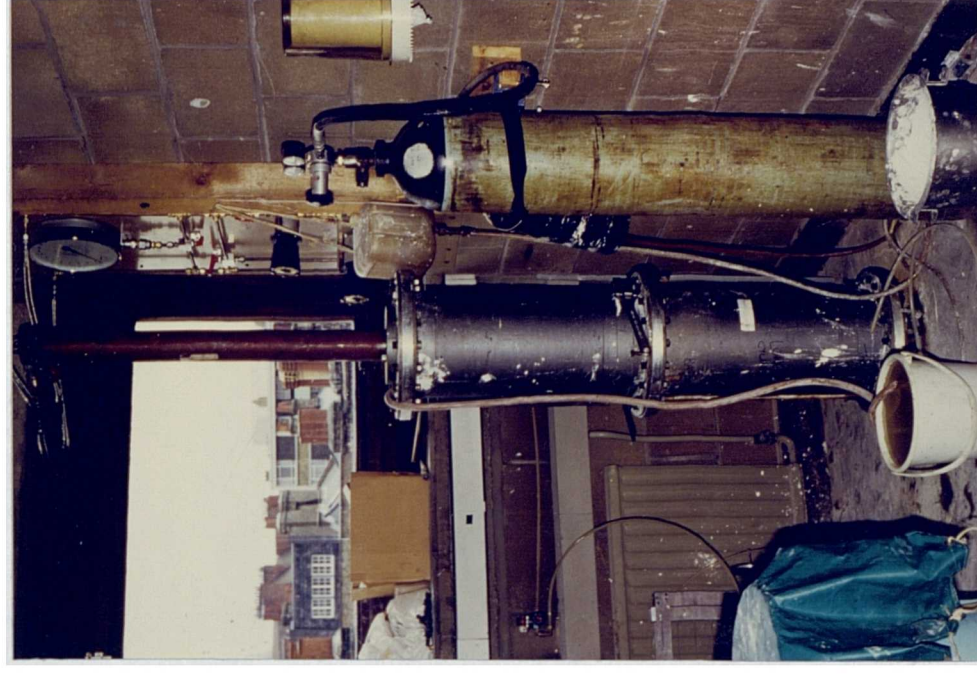


Figure 2.6 Consolidometer used in sample preparation

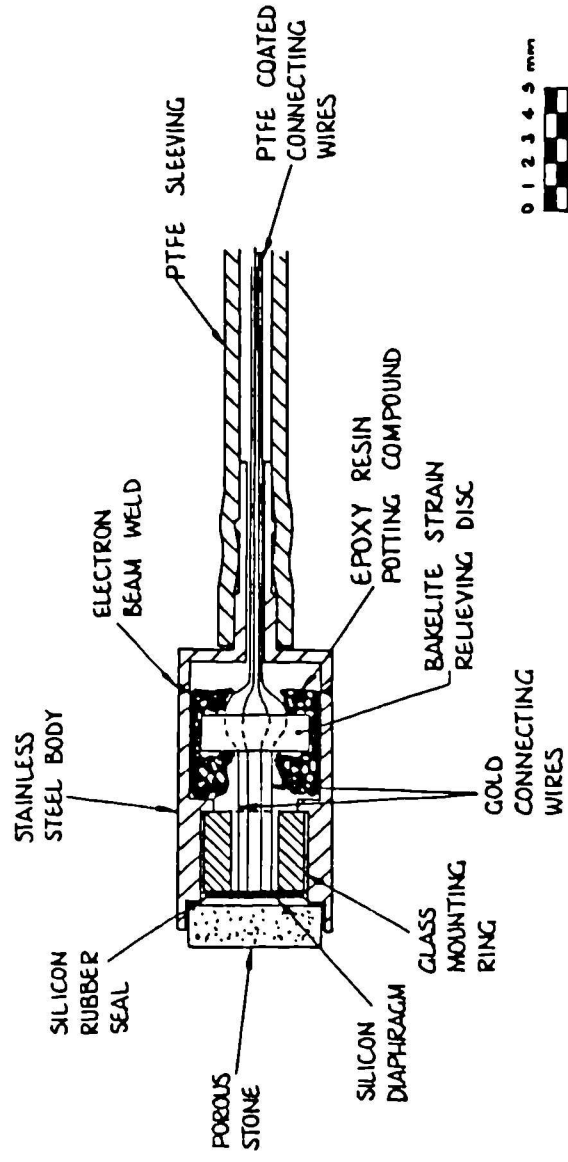


Figure 2.5 Section through a miniature pore pressure transducer

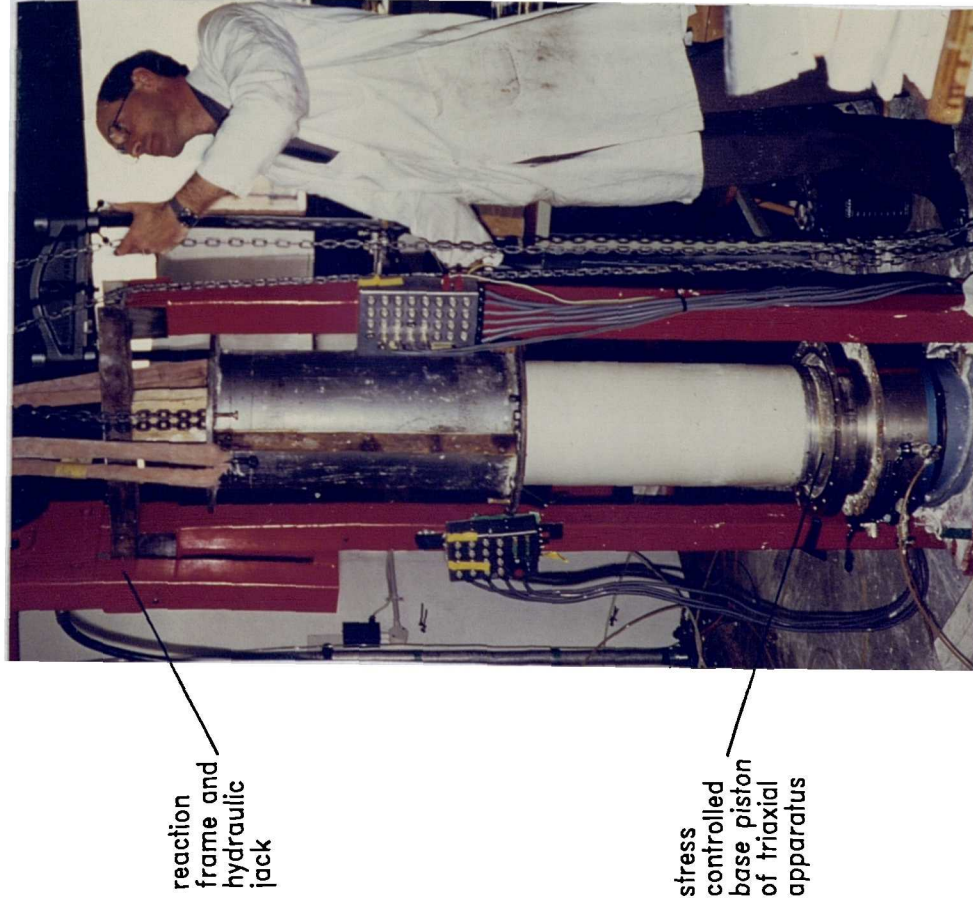


Figure 2.7 Transfer of sample to triaxial apparatus

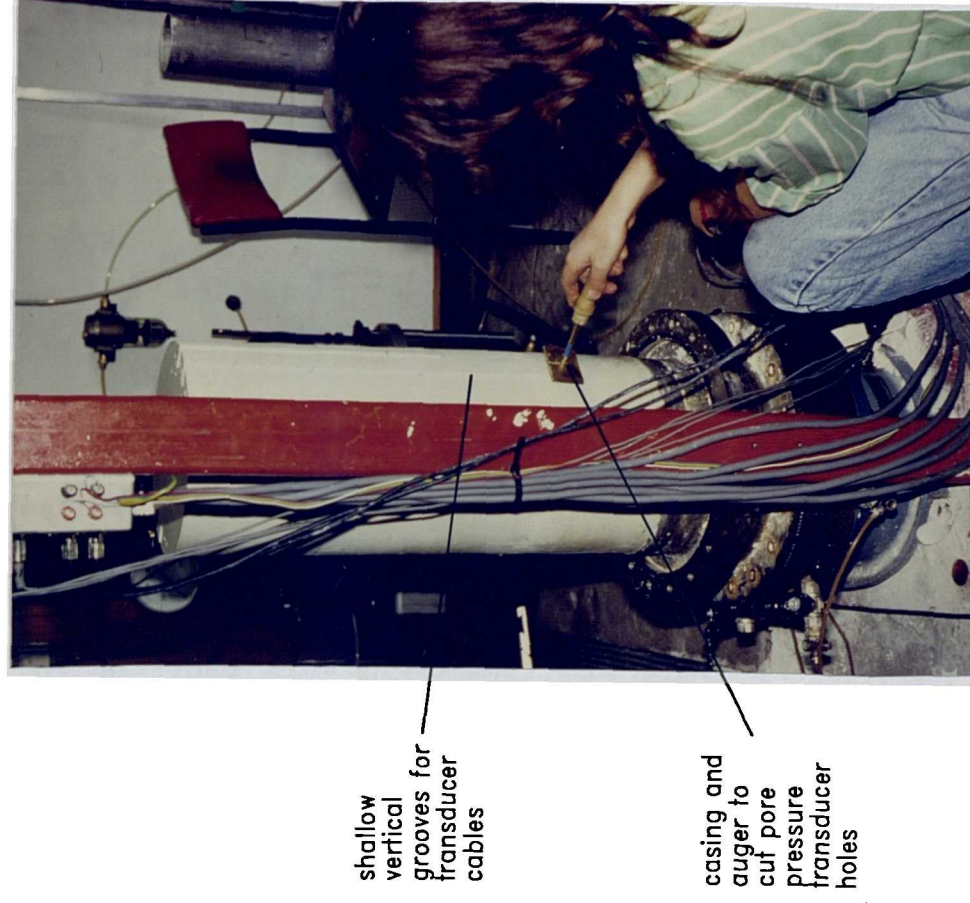


Figure 2.8 Insertion of pore pressure transducers

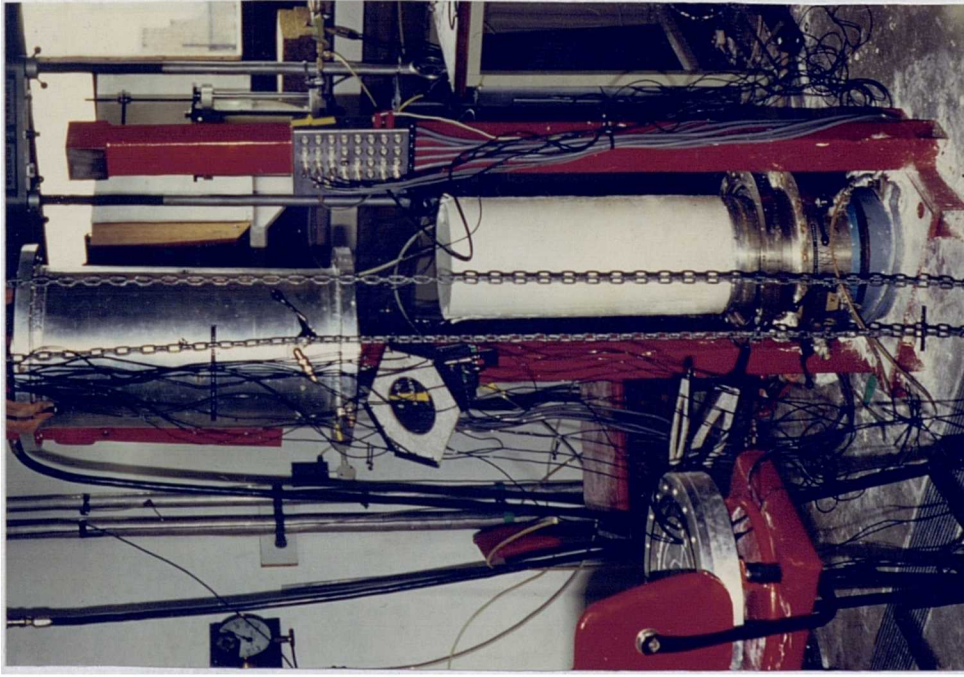


Figure 2.9(a) Assembly of triaxial apparatus

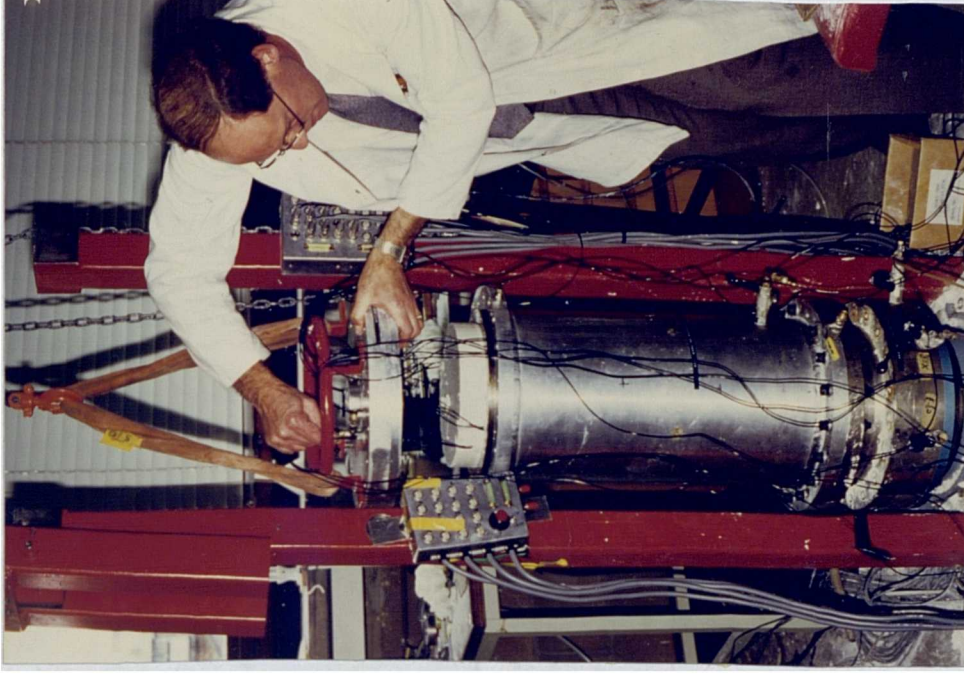
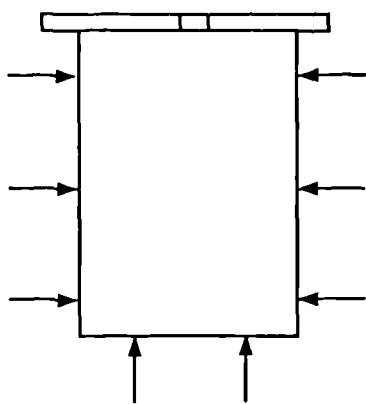


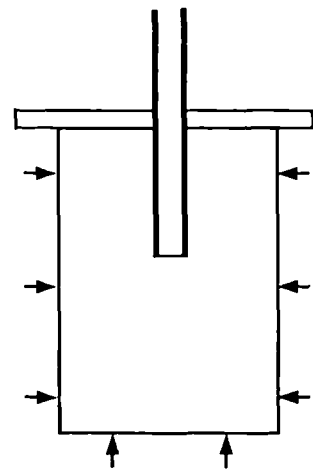
Figure 2.9(b) Assembly of triaxial apparatus

①



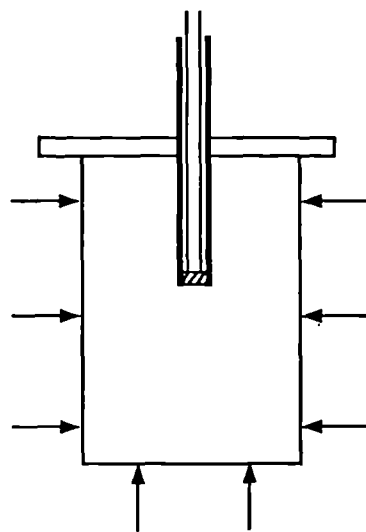
Isotropic consolidation
to $p' = 800\text{kPa}$

②



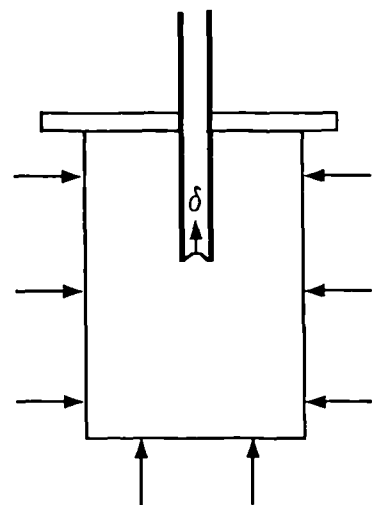
Total stress reduced and
model tunnel advanced

③



Tunnel face supported and
isotropic reconsolidation
to required initial stress
state p'_0, u_0

④



Face support removed,
deformation and pore
pressure changes
monitored

Figure 2.10 Summary of model test procedure

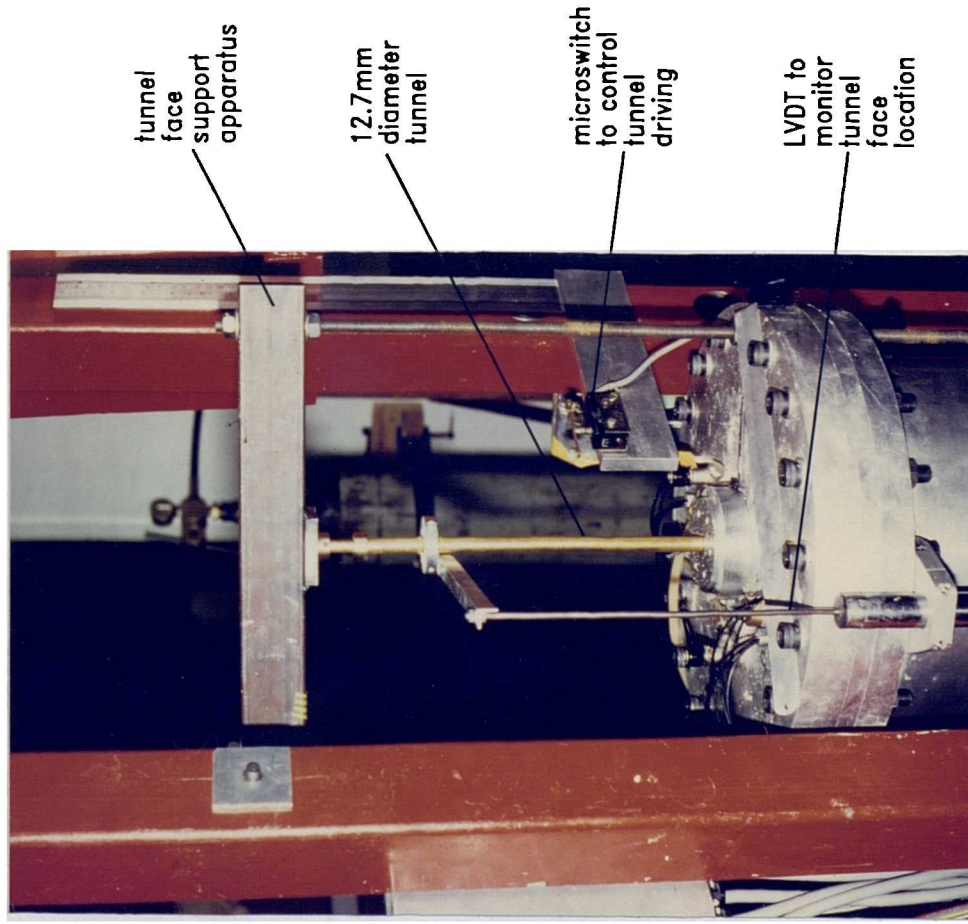


Figure 2.11 Sample reconsolidation prior to testing

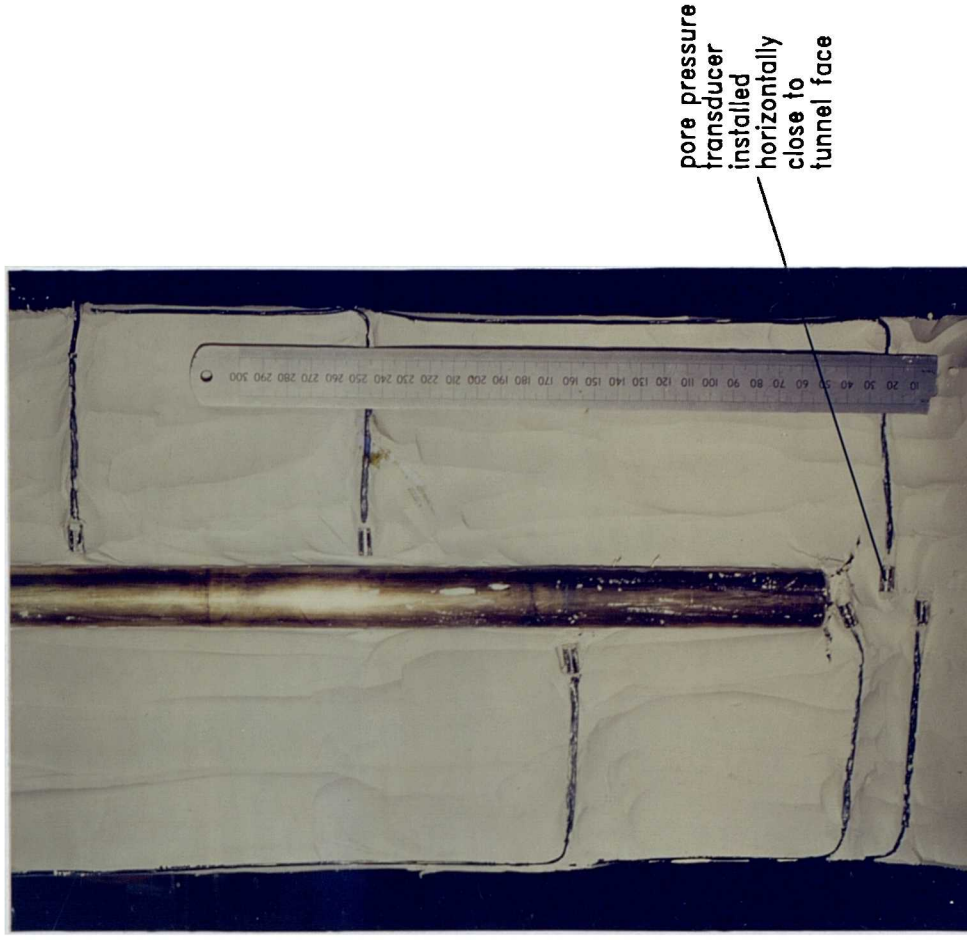


Figure 2.12 Section through sample after testing

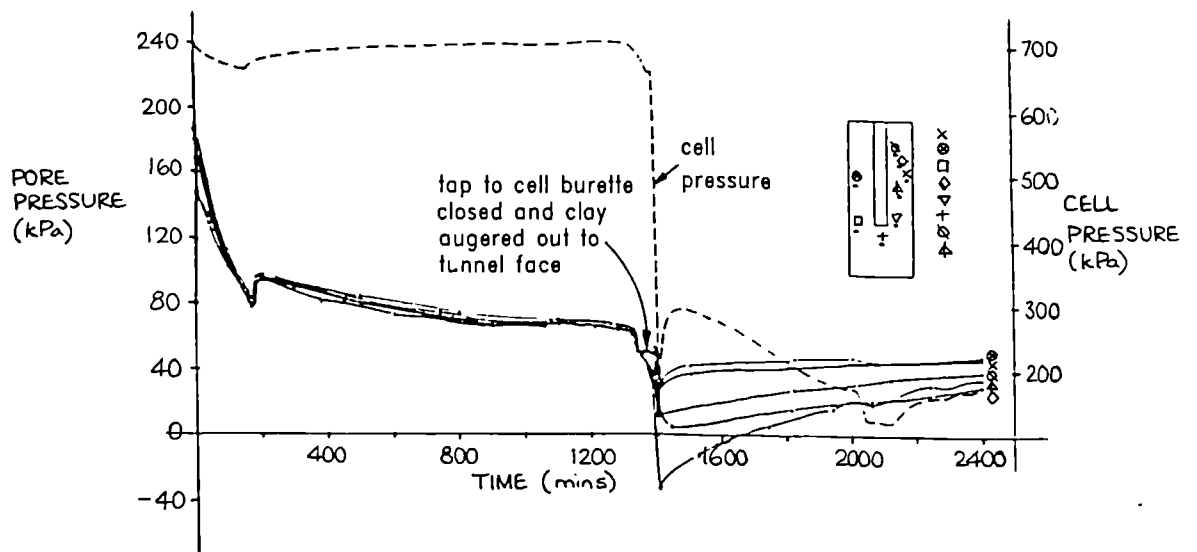


Figure 3.1(a) Pore pressure response during stage 3 of test no. 2

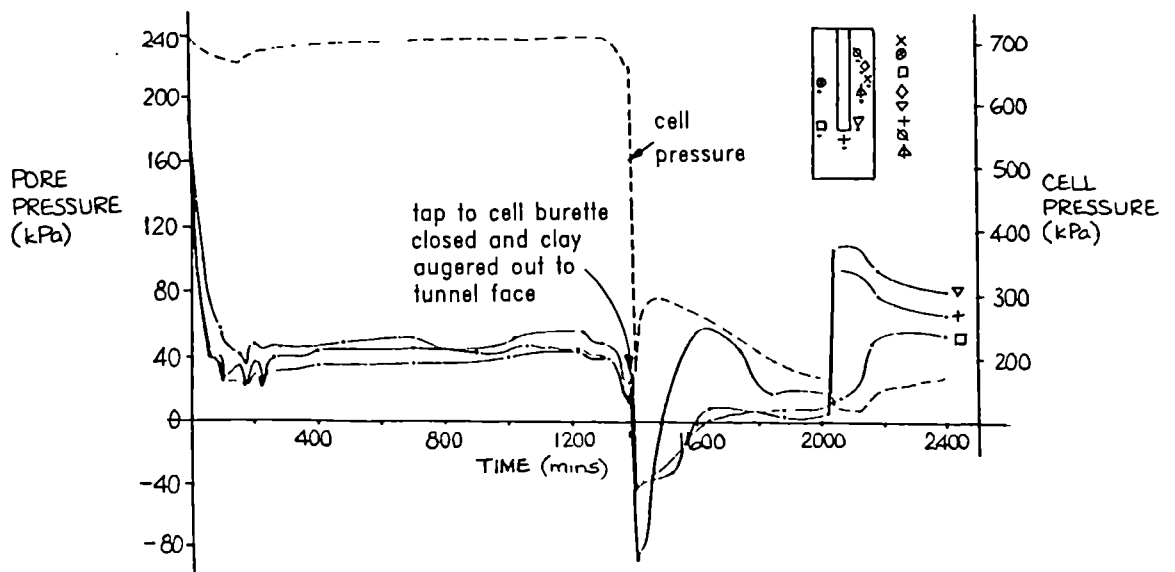


Figure 3.1(b) Pore pressure response during stage 3 of test no. 2

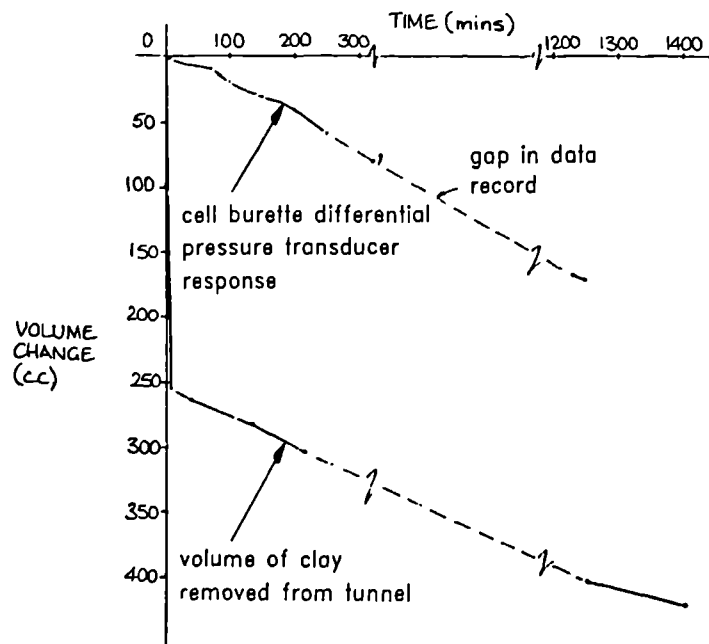


Figure 3.2(a) Change in volume (squeeze) of sample during stage 1 of test no. 1

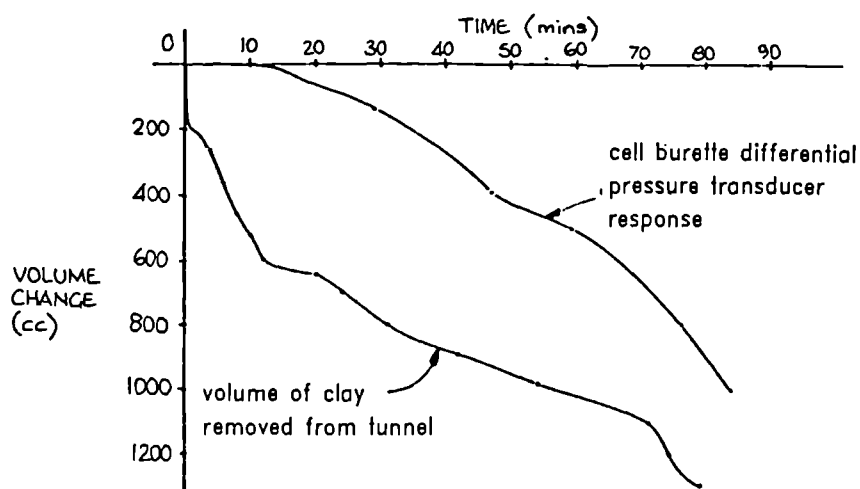


Figure 3.2(b) Change in volume (squeeze) of sample during stage 2 of test no. 1

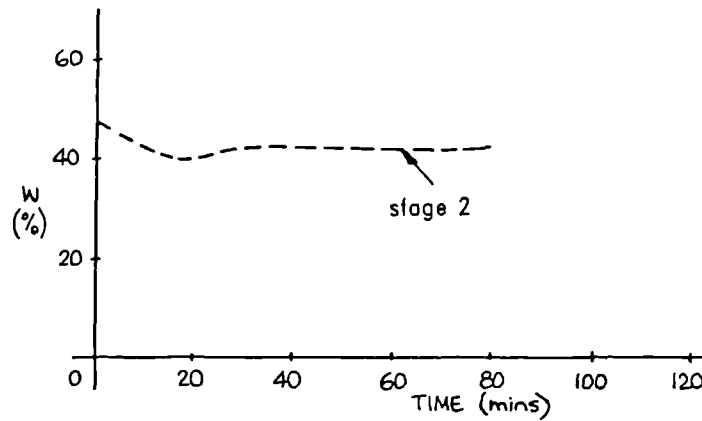
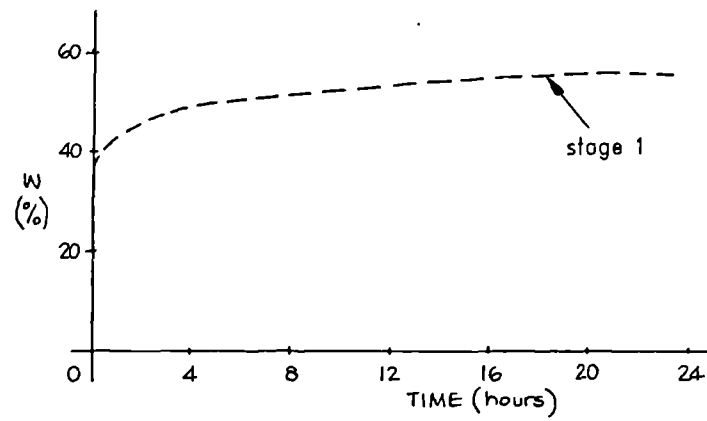


Figure 3.3(a) Water contents of clay augered out of tunnel during stages 1 and 2 of test no. 1

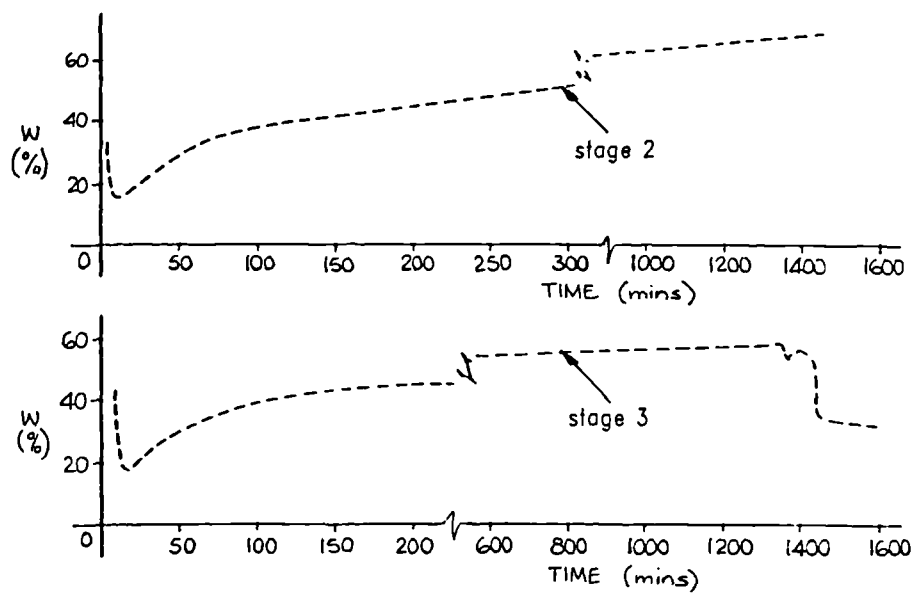


Figure 3.3(b) Water contents of clay augered out of tunnel during stages 2 and 3 of test no. 2

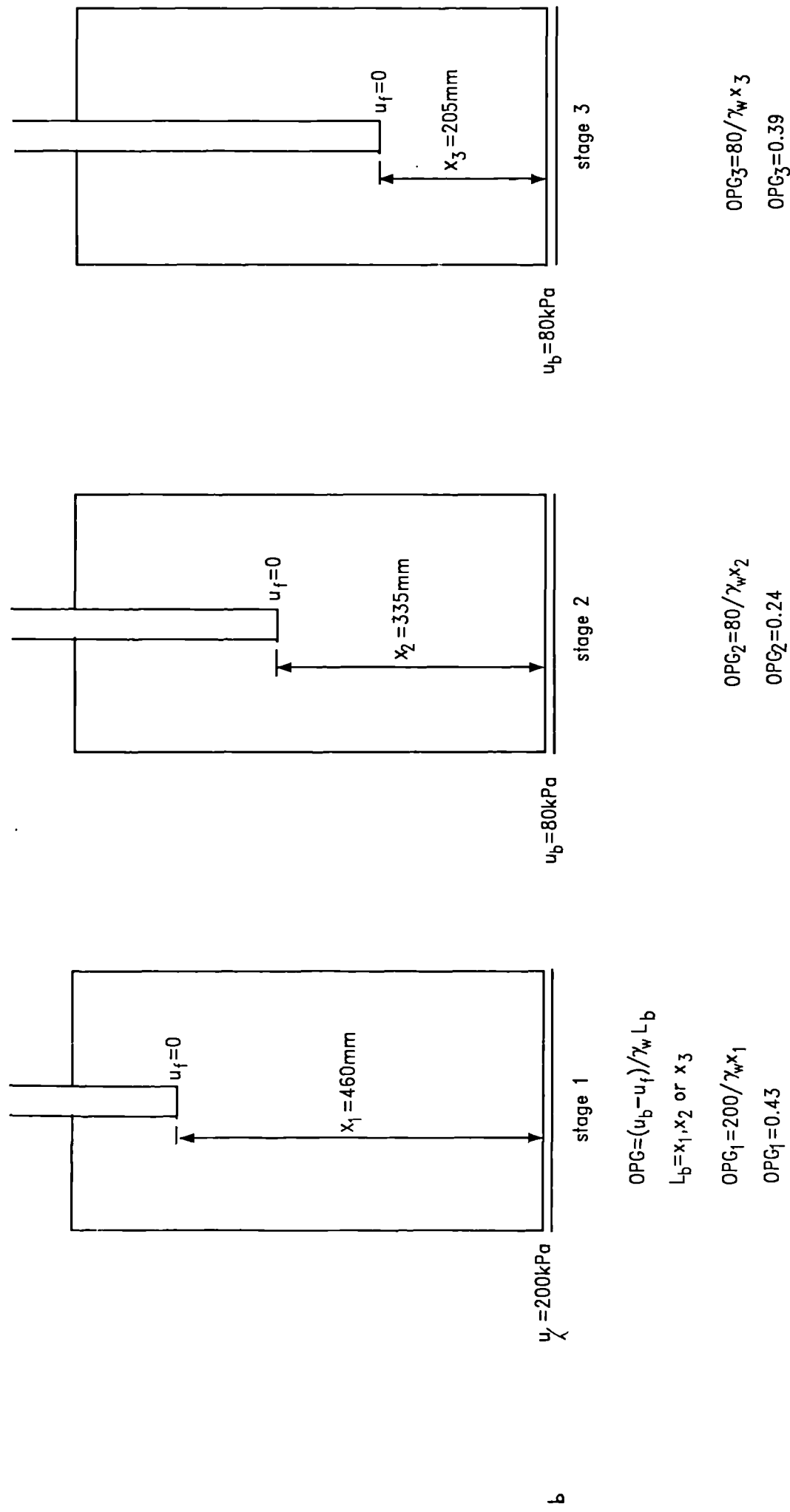


Figure 3.4 Definition of overall pressure gradient (OPG) and values used in the model tunnel tests of Series I

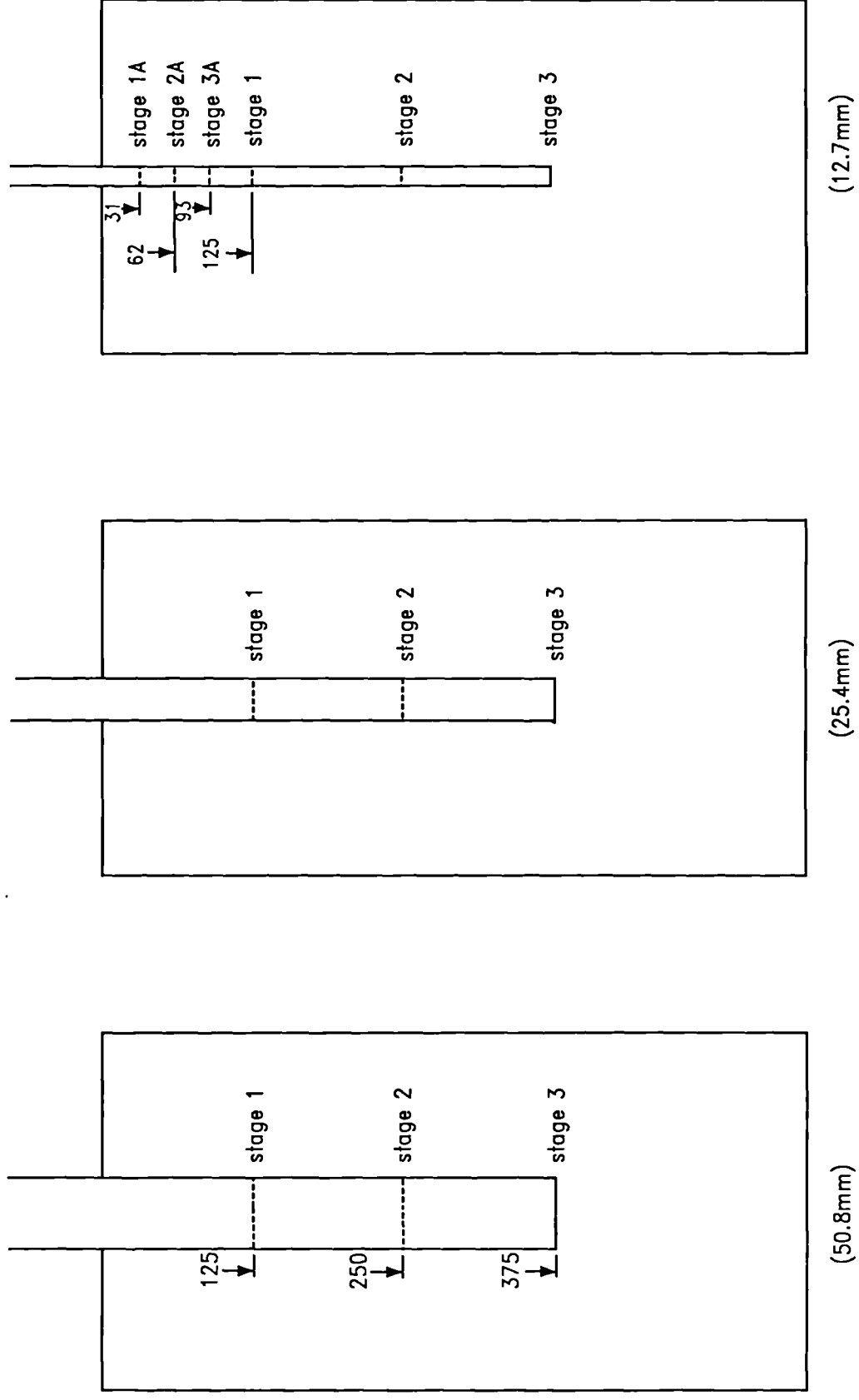


Figure 3.5(a) Locations of the model tunnel face for the various stages of the Series I tests and the tests in sample no. 13

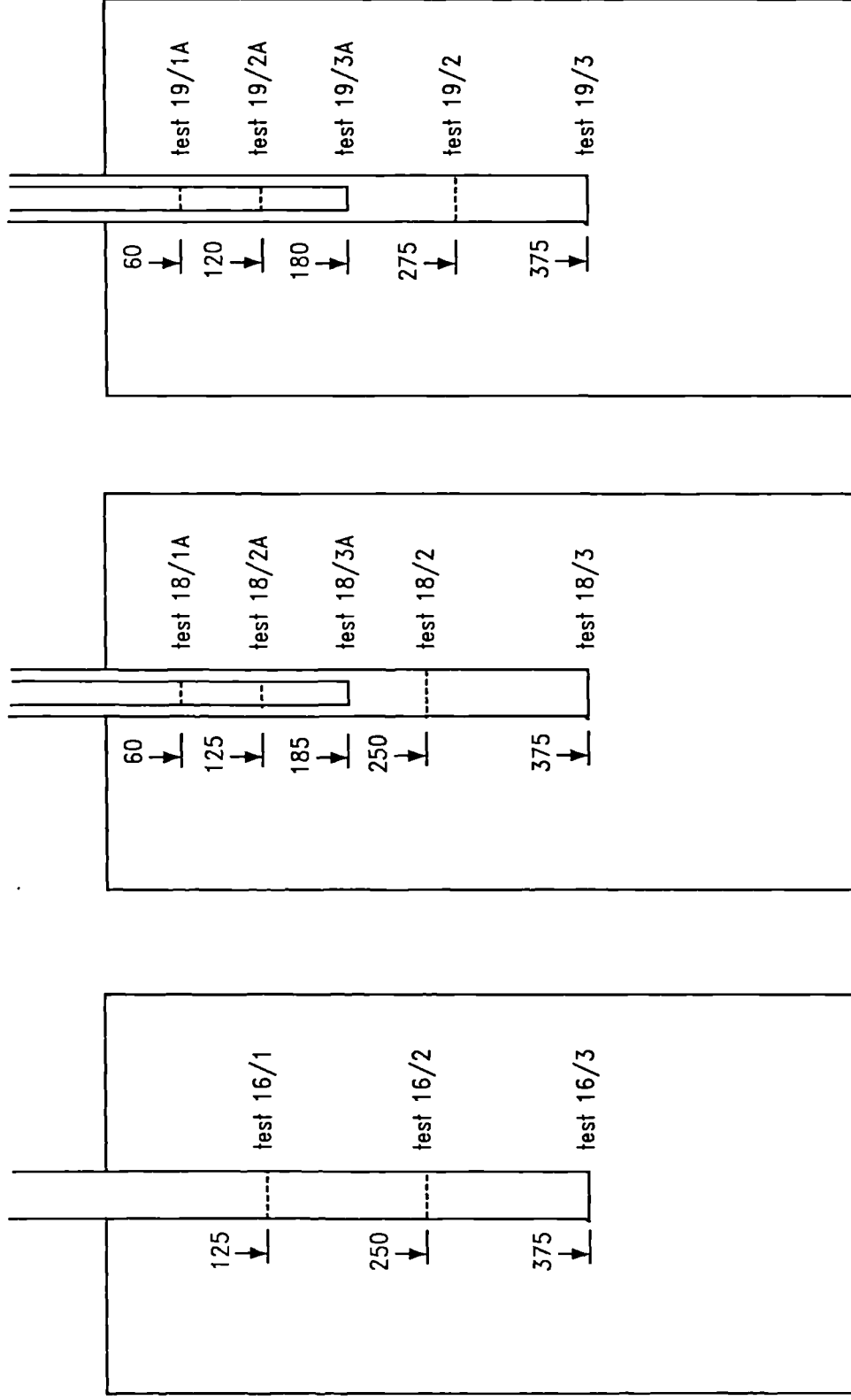


Figure 3.5(b) Locations of the model tunnel face for tests from Series 2

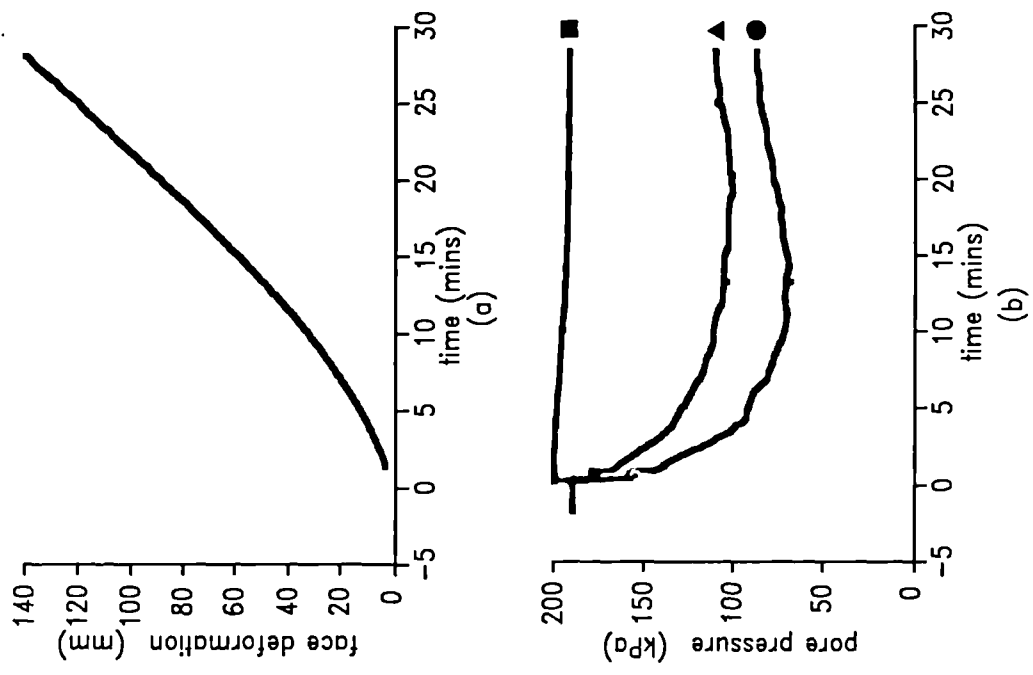


Figure 3.6 Deformation and pore pressure response
Test 14/1 (12.7mm) $p'=770\text{kPa}$ $u=199\text{kPa}$

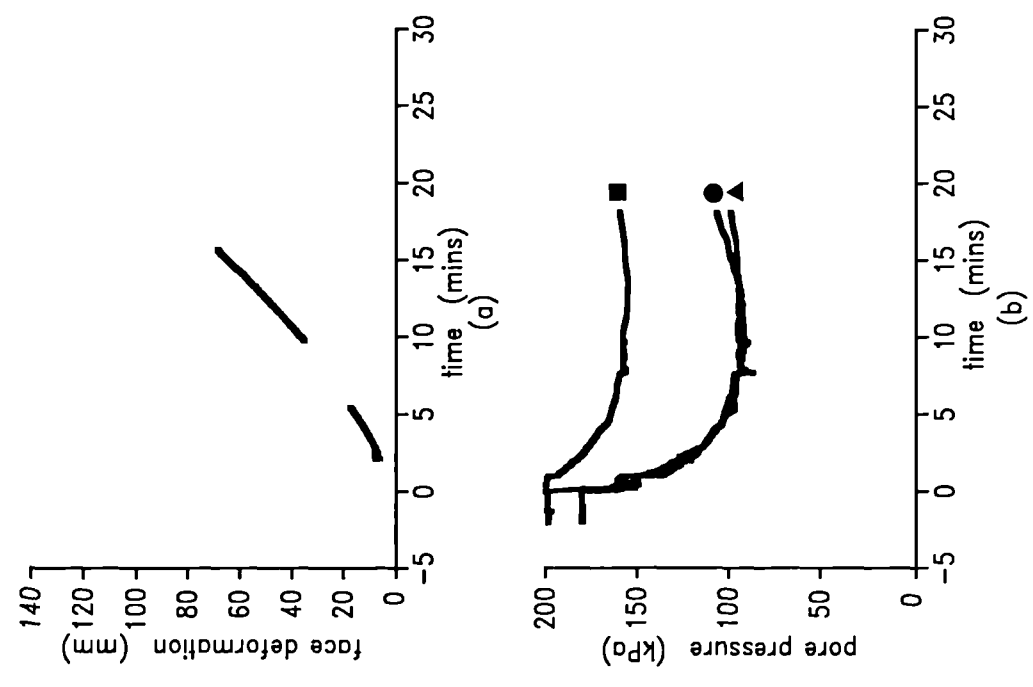


Figure 3.7 Deformation and pore pressure response
Test 12/1A (12.7mm) $p'=767\text{kPa}$ $u=198\text{kPa}$

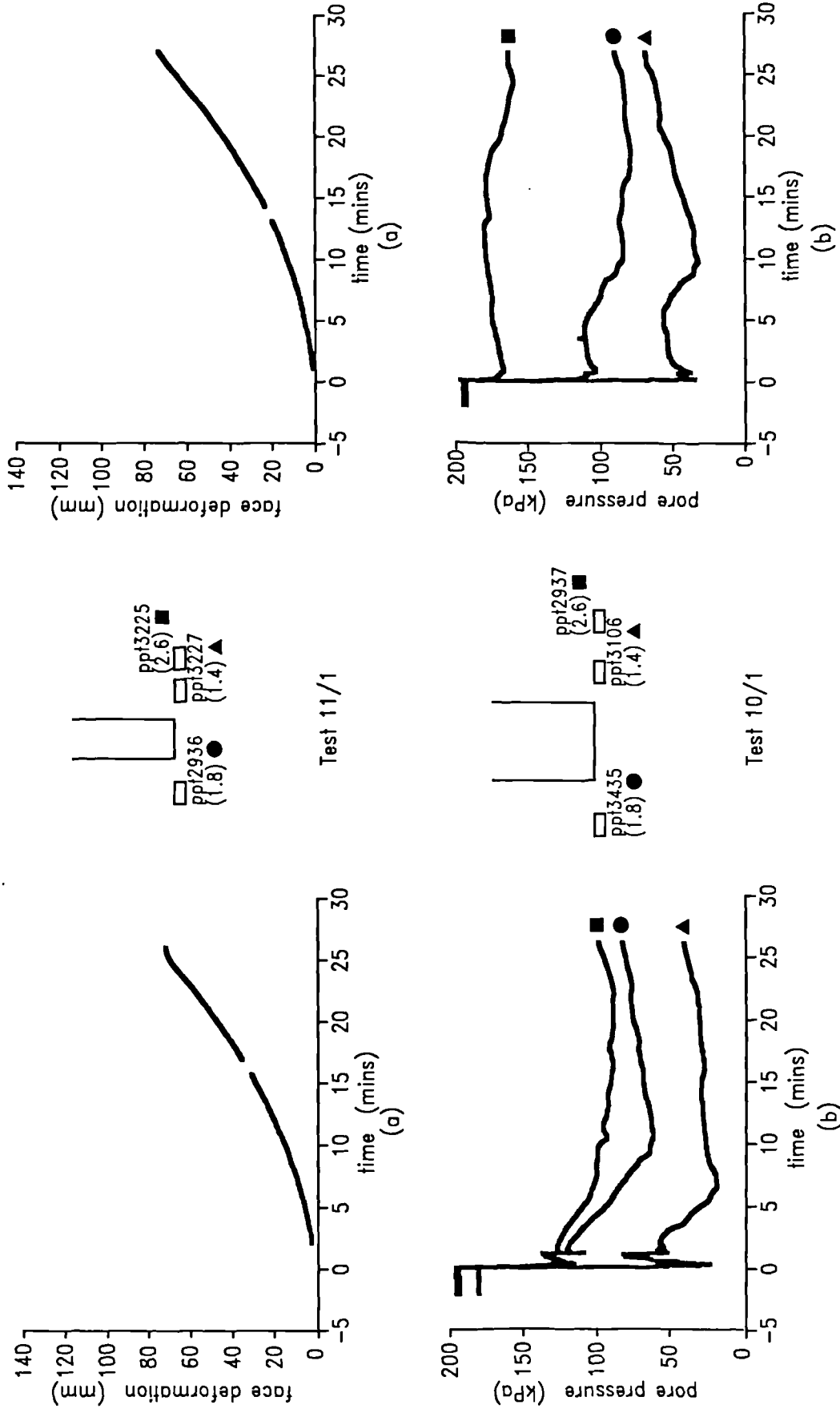


Figure 3.8 Deformation and pore pressure response
Test 11/1 (25.4mm) $p'=771\text{kPa}$ $u=193\text{kPa}$

Figure 3.9 Deformation and pore pressure response
Test 10/1 (50.8mm) $p'=766\text{kPa}$ $u=195\text{kPa}$

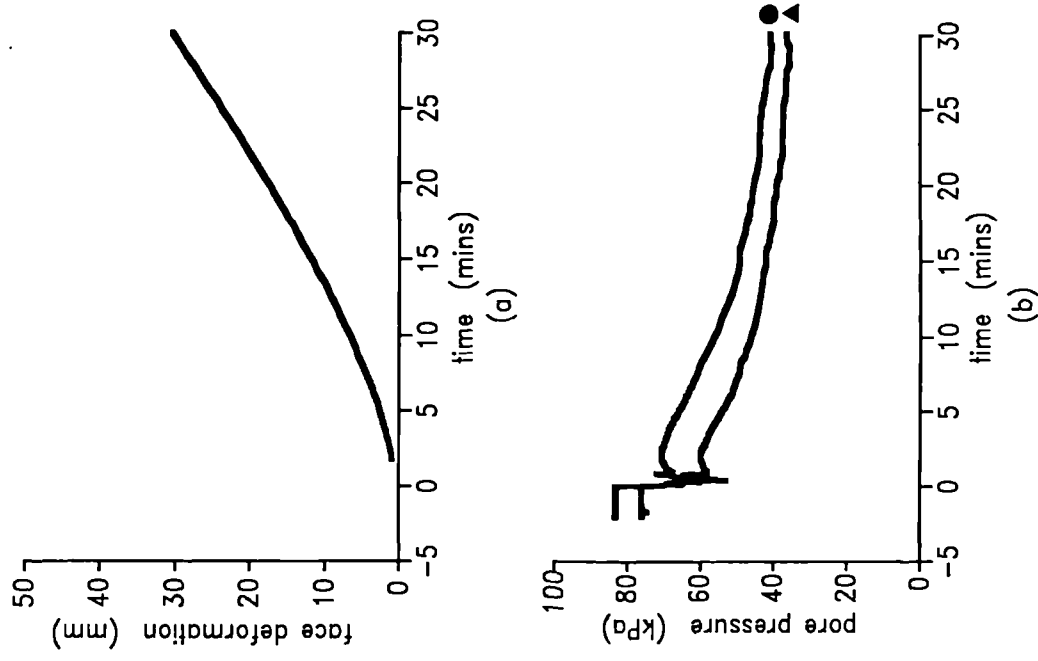


Figure 3.10 Deformation and pore pressure response
Test 12/2A (12.7mm) $p' = 799 \text{ kPa}$ $u = 80 \text{ kPa}$

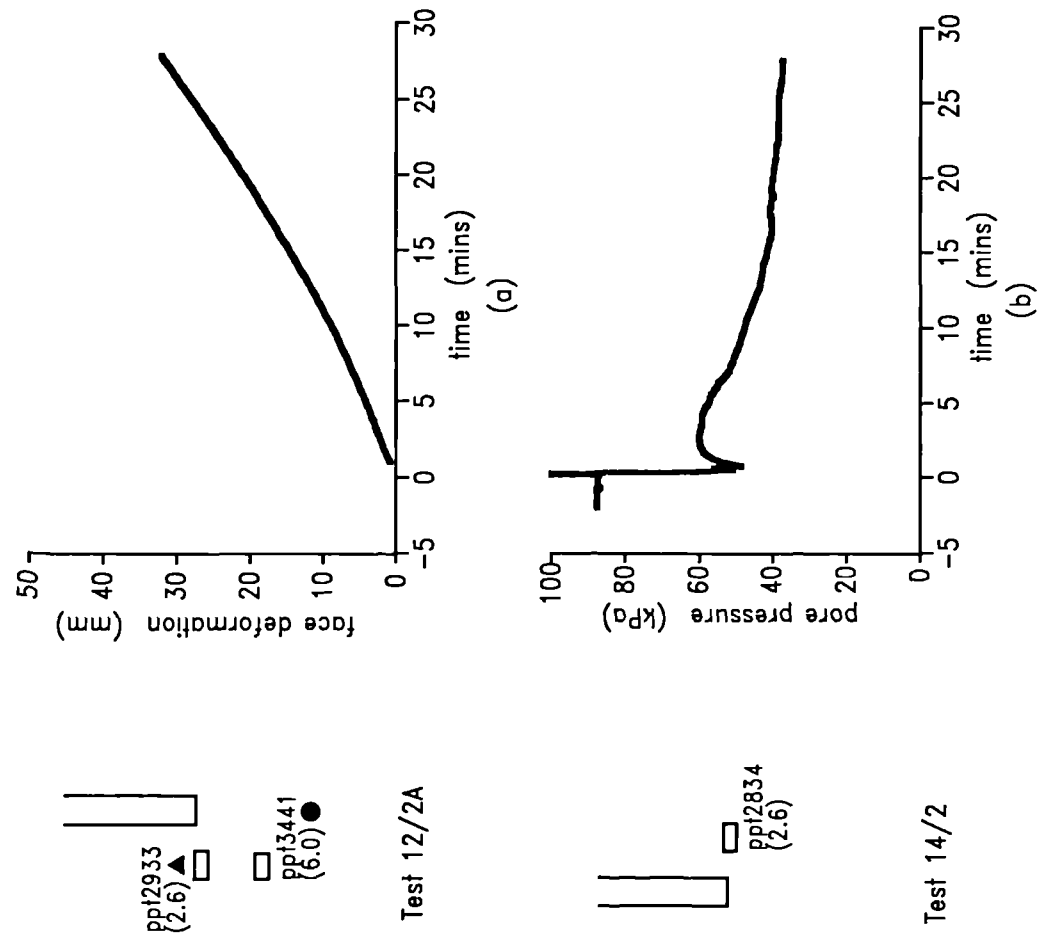


Figure 3.11 Deformation and pore pressure response
Test 14/2 (12.7mm) $p' = 779 \text{ kPa}$ $u = 80 \text{ kPa}$

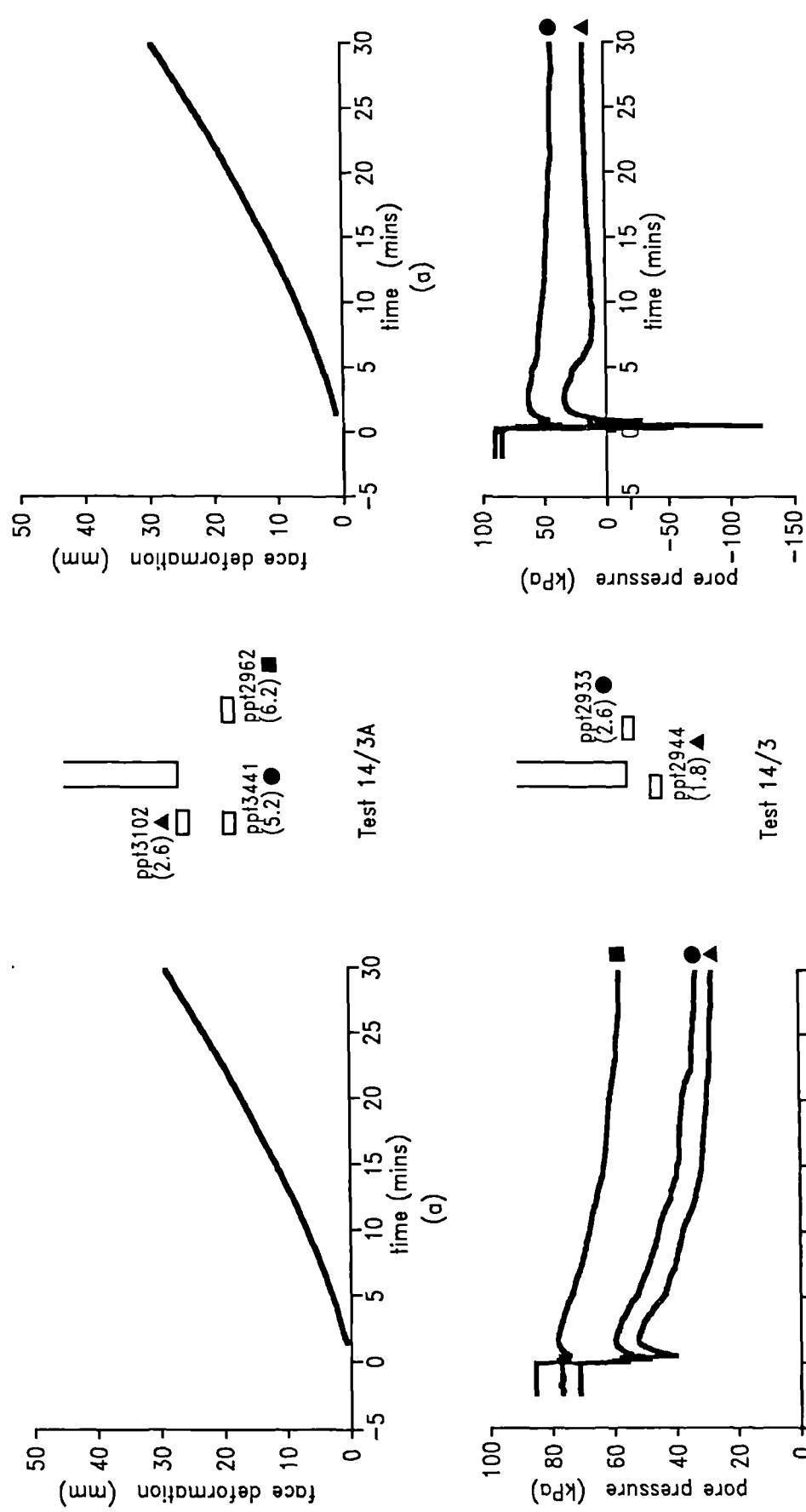


Figure 3.12 Deformation and pore pressure response
Test 14/3A (12.7mm) $p'=784\text{kPa}$ $u=78\text{kPa}$

Figure 3.13 Deformation and pore pressure response
Test 14/3 (12.7mm) $p'=782\text{kPa}$ $u=87\text{kPa}$

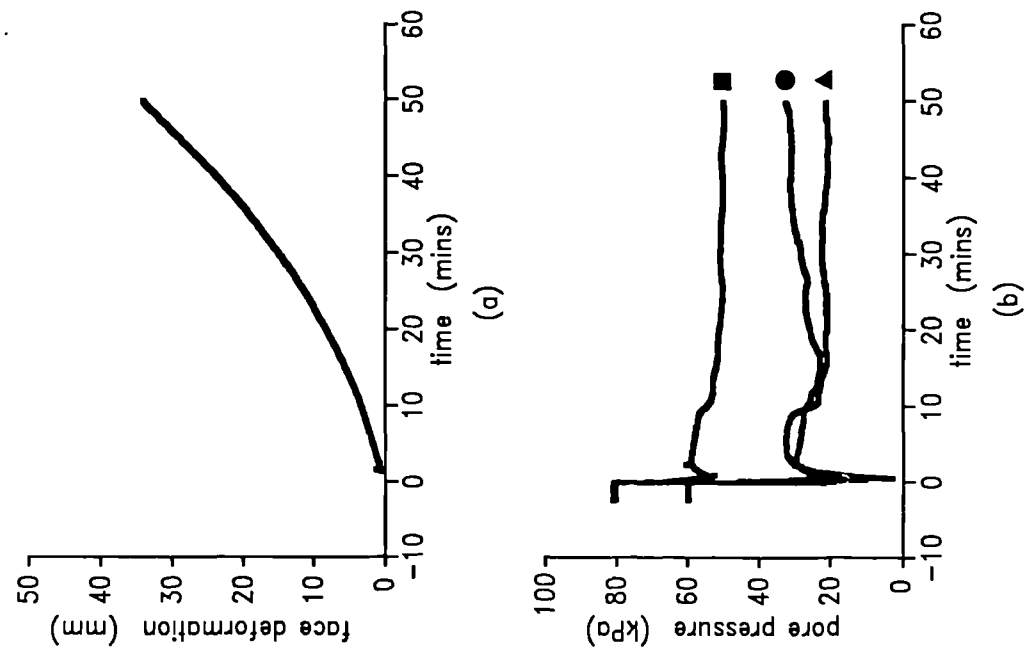


Figure 3.14 Deformation and pore pressure response
Test 11/2 (25.4mm) $p'=809\text{kPa}$ $u=74\text{kPa}$

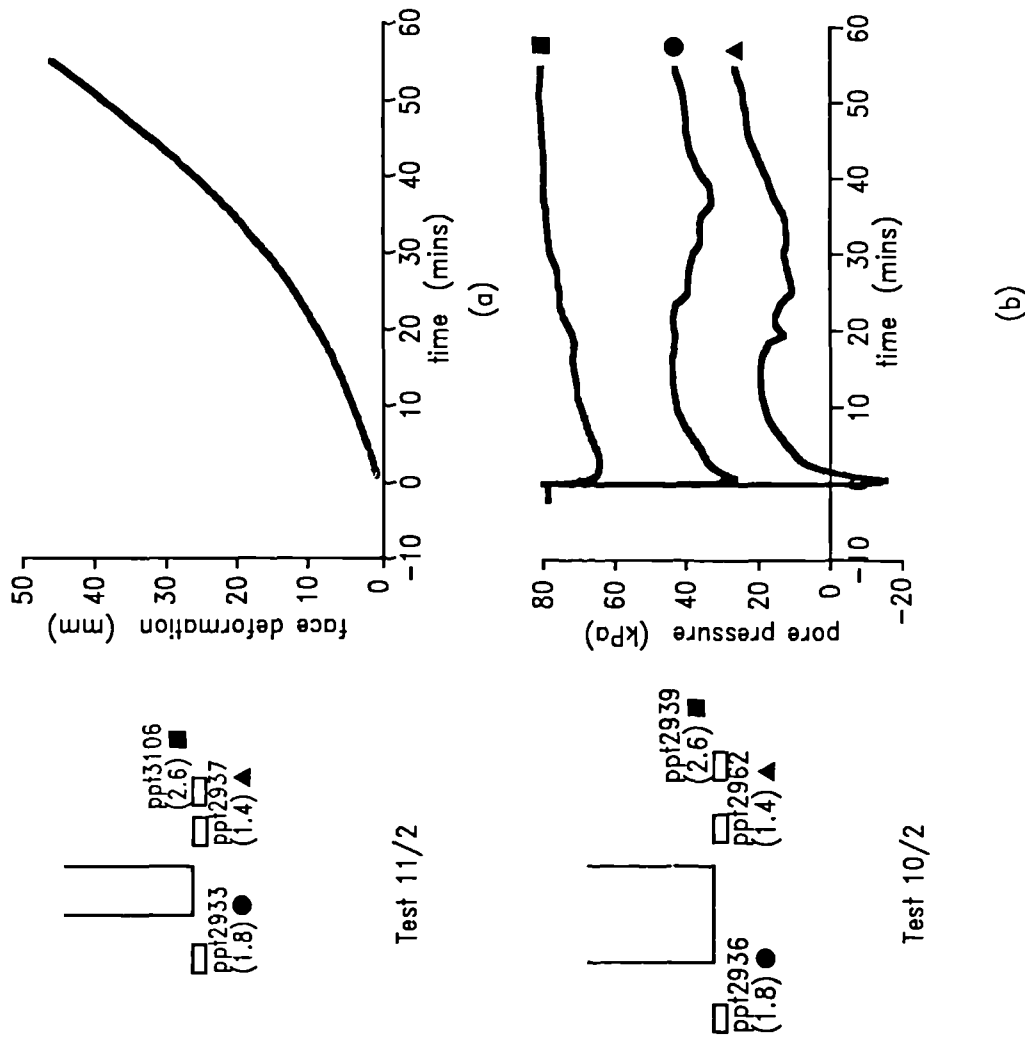


Figure 3.15 Deformation and pore pressure response
Test 10/2 (50.8mm) $p'=815\text{kPa}$ $u=76\text{kPa}$

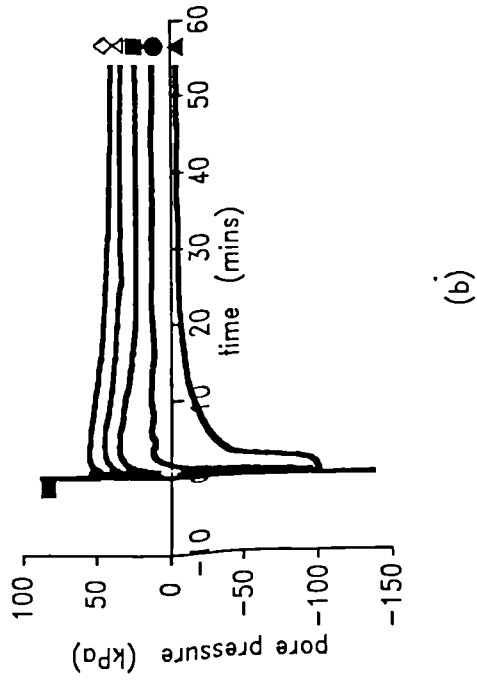
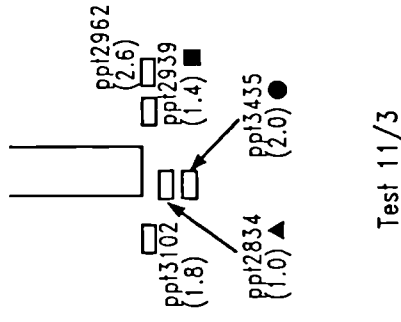
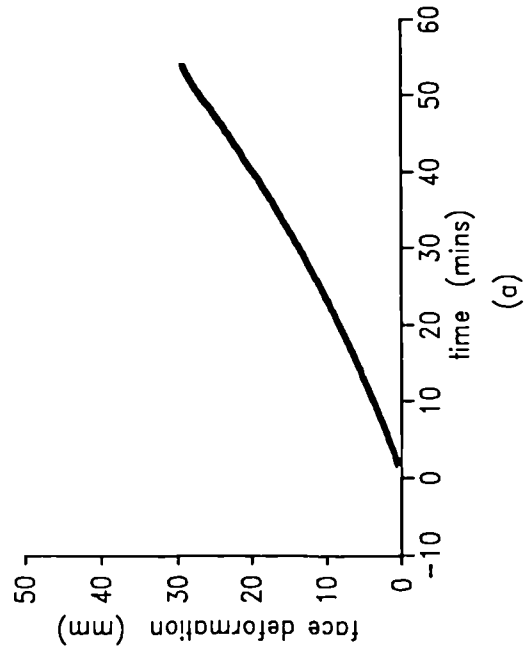


Figure 3.16 Deformation and pore pressure response
Test 11/3 (25.4mm) $p' = 783 \text{ kPa}$ $u = 78 \text{ kPa}$

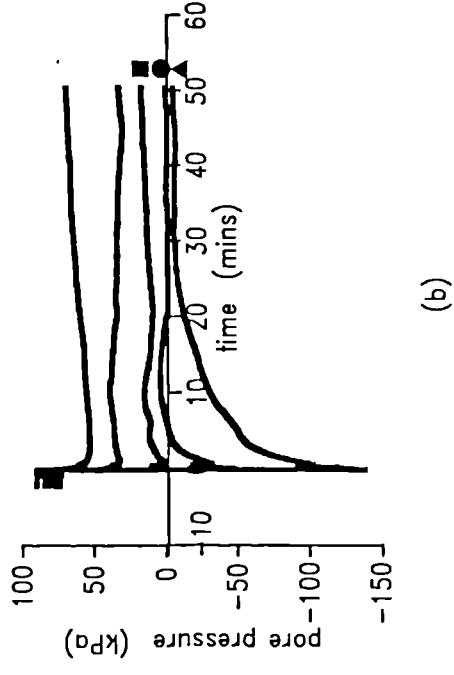
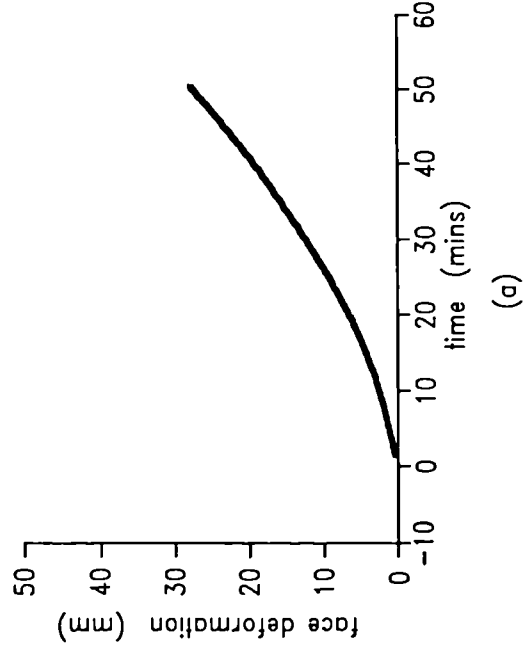
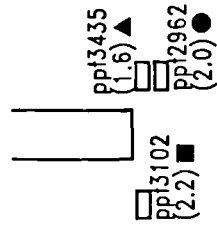
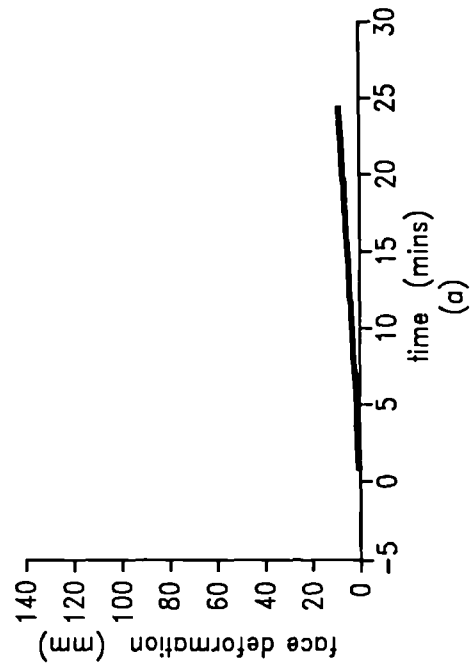
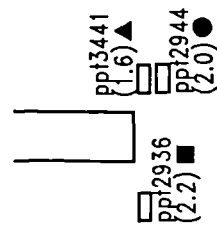
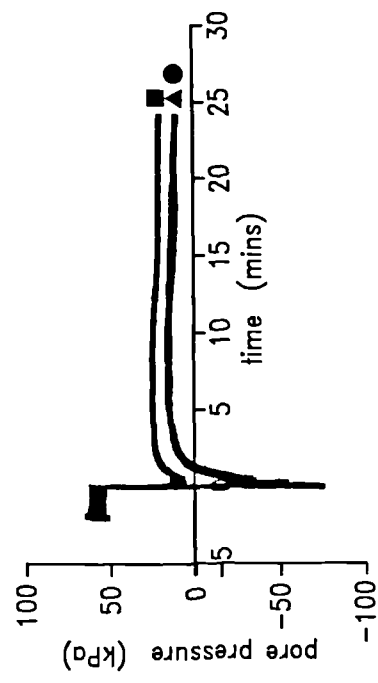


Figure 3.17 Deformation and pore pressure response
Test 10/3 (50.8mm) $p' = 784 \text{ kPa}$ $u = 80 \text{ kPa}$



Test 16/2

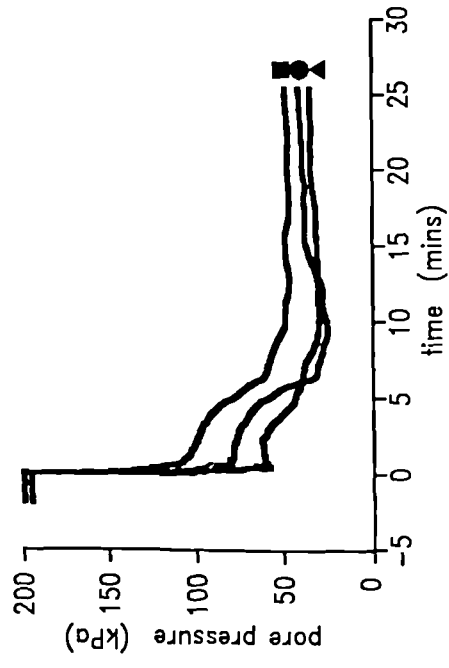
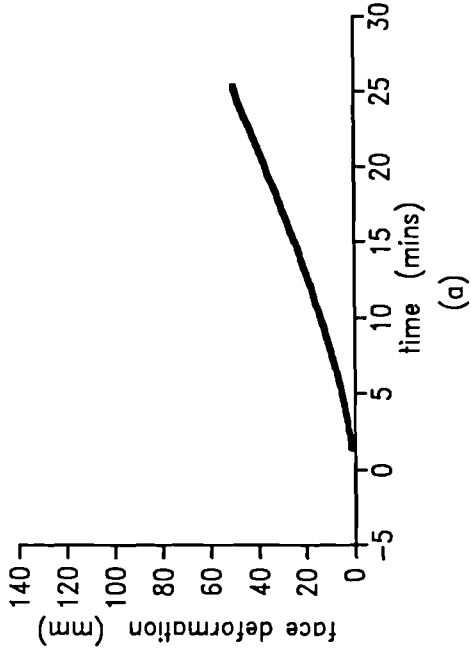
(a)



Test 16/1

(b)

Figure 3.18 Deformation and pore pressure response
 Test 16/2 (25.4mm) $p'=759\text{kPa}$ $u=56\text{kPa}$



(b)

Figure 3.19 Deformation and pore pressure response
 Test 16/1 (25.4mm) $p'=556\text{kPa}$ $u=200\text{kPa}$

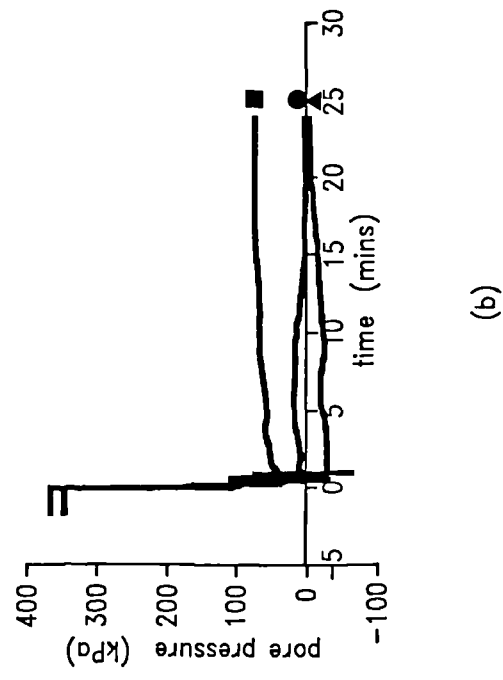
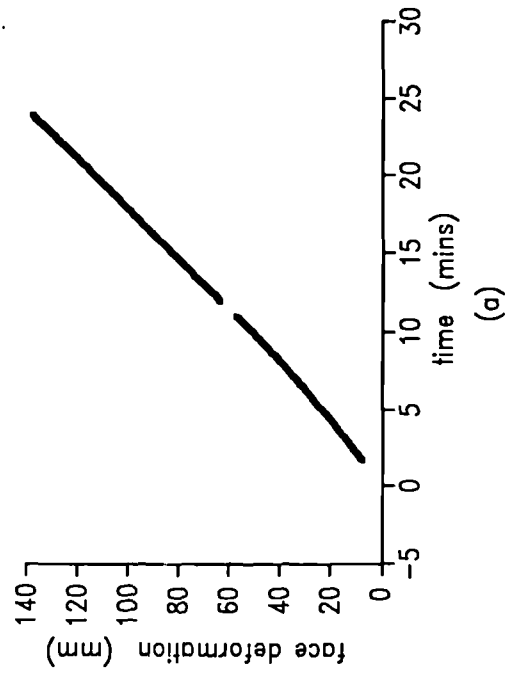


Figure 3.20 Deformation and pore pressure response
Test 16/3 (25.4mm) $p'=266\text{kPa}$ $u=350\text{kPa}$

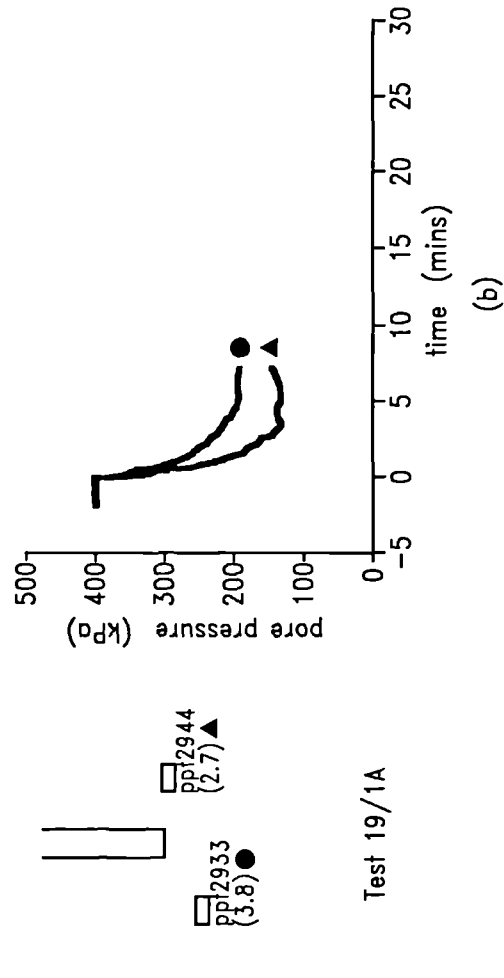
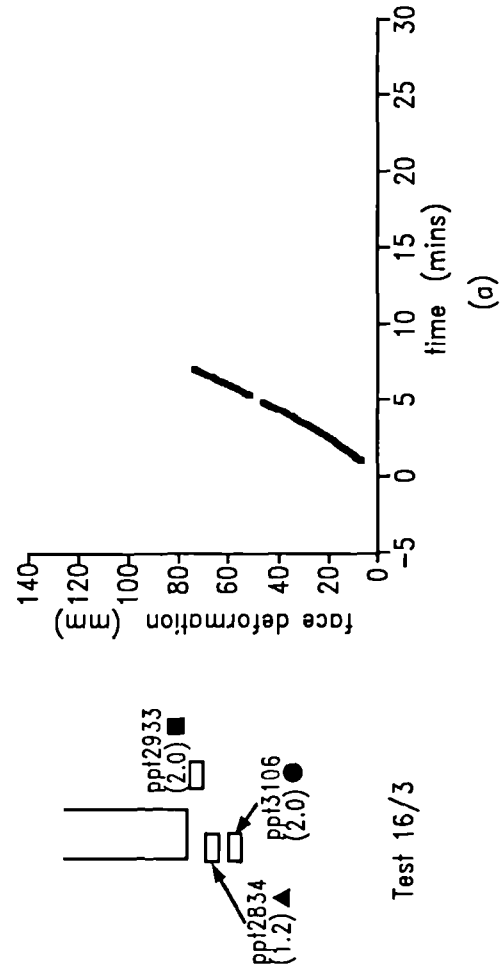


Figure 3.21 Deformation and pore pressure response
Test 19/1A (12.7mm) $p'=438\text{kPa}$ $u=401\text{kPa}$

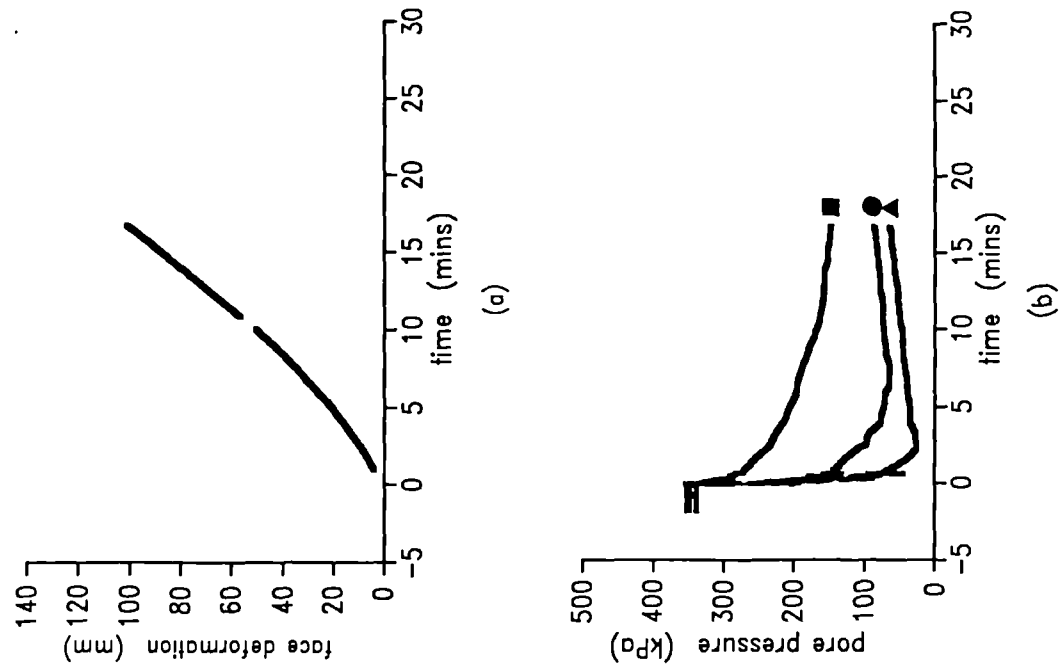


Figure 3.22 Deformation and pore pressure response
Test 17/1 (25.4mm) $p'=550\text{kPa}$ $u=350\text{kPa}$

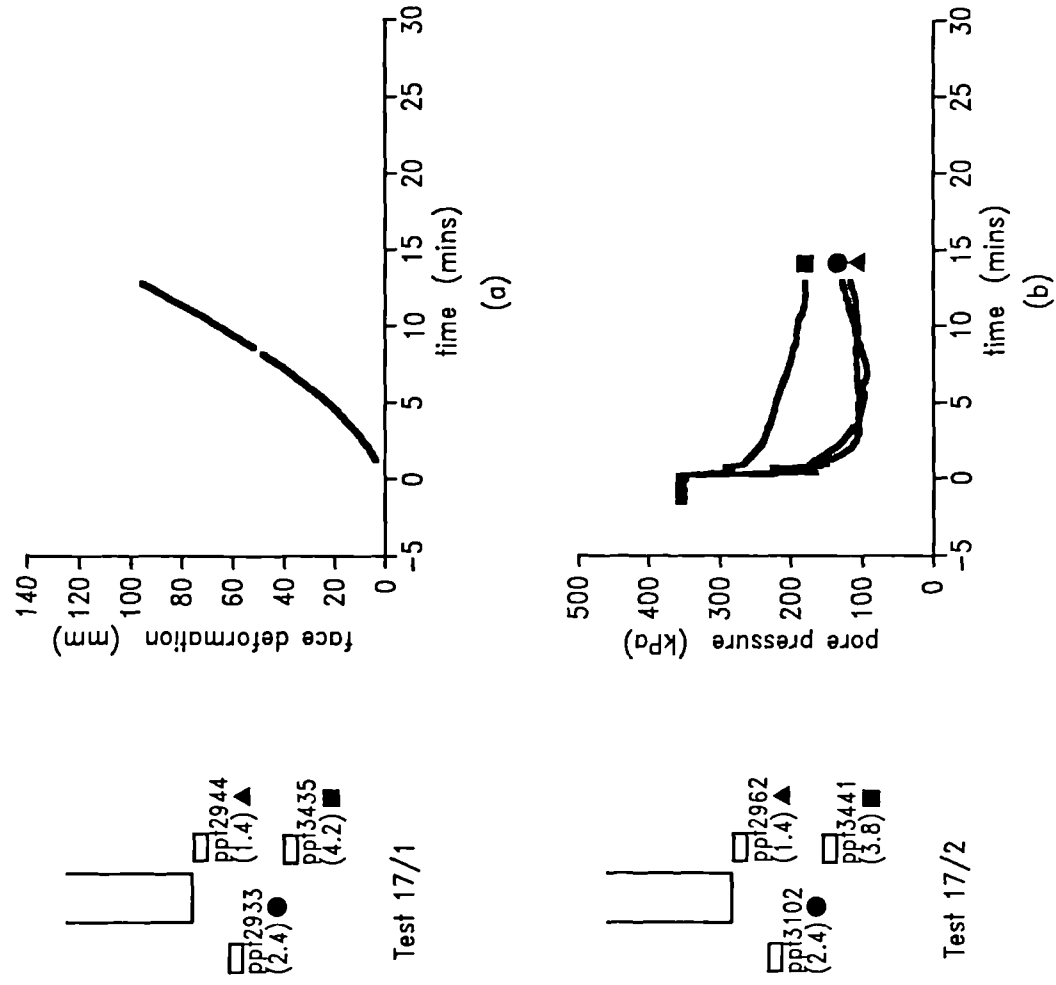


Figure 3.23 Deformation and pore pressure response
Test 17/2 (25.4mm) $p'=771\text{kPa}$ $u=352\text{kPa}$

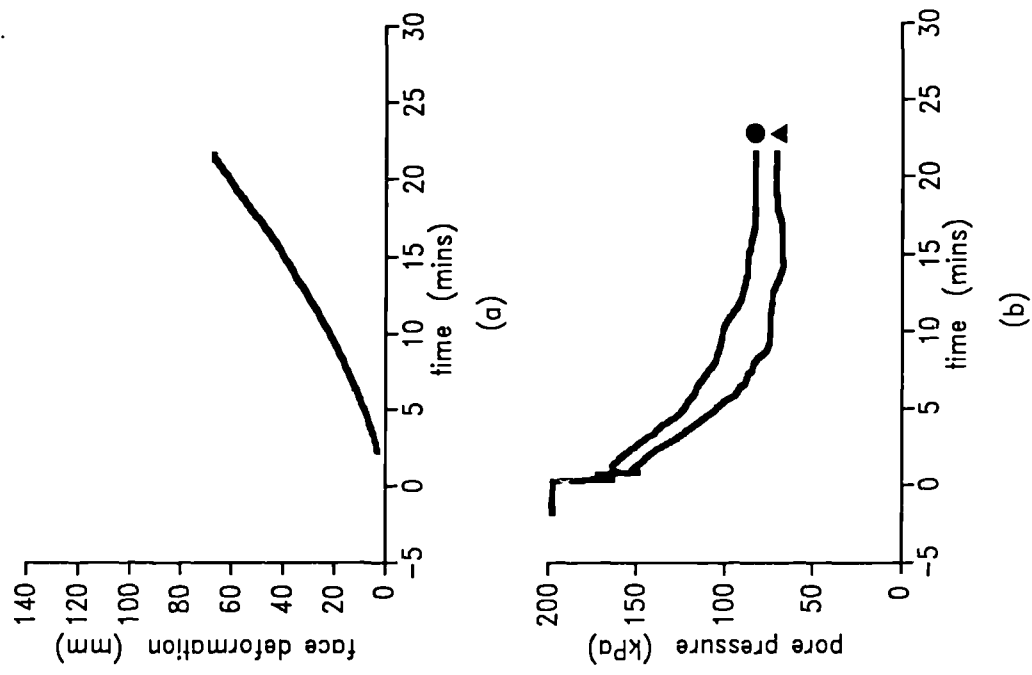


Figure 3.24 Deformation and pore pressure response
Test 18/1A (12.7mm) $p'=454\text{kPa}$ $u=203\text{kPa}$

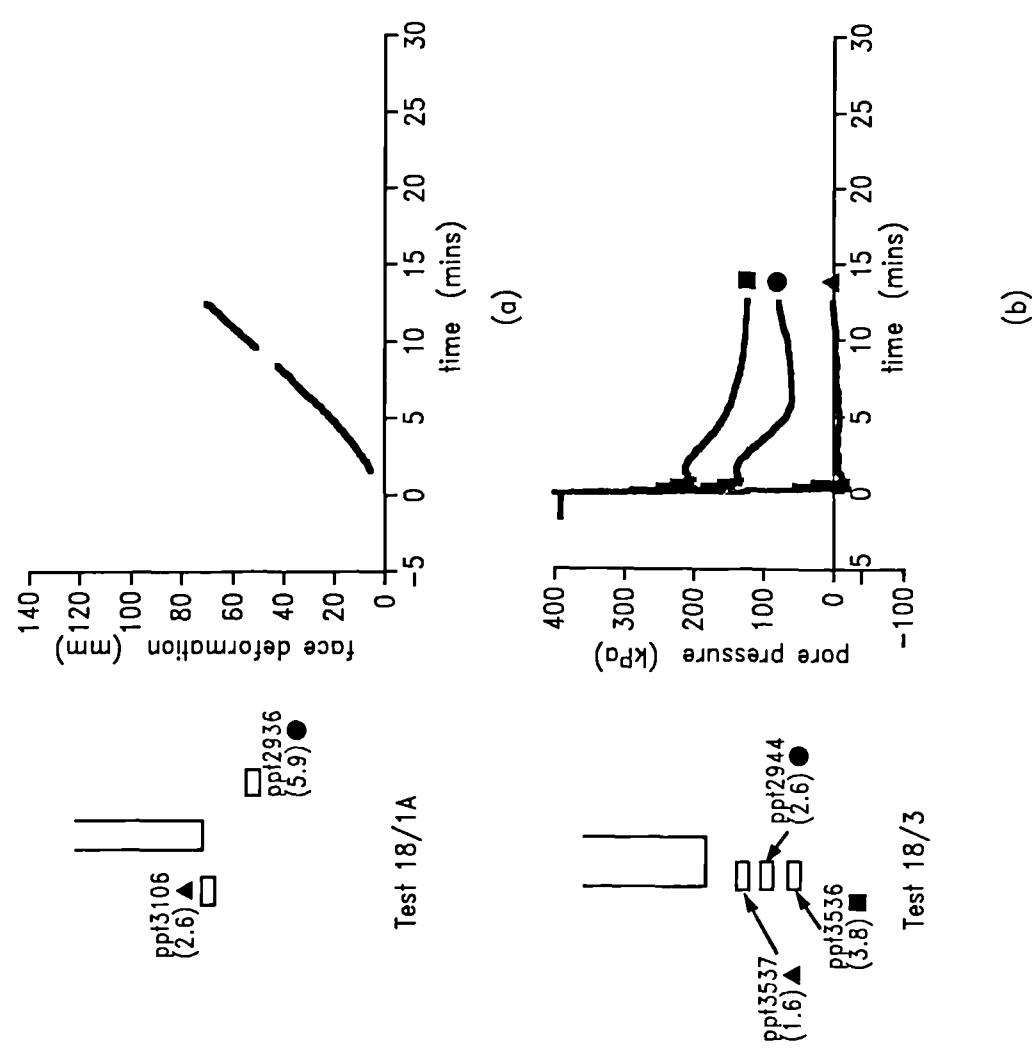


Figure 3.25 Deformation and pore pressure response
Test 18/3 (25.4mm) $p'=435\text{kPa}$ $u=398\text{kPa}$

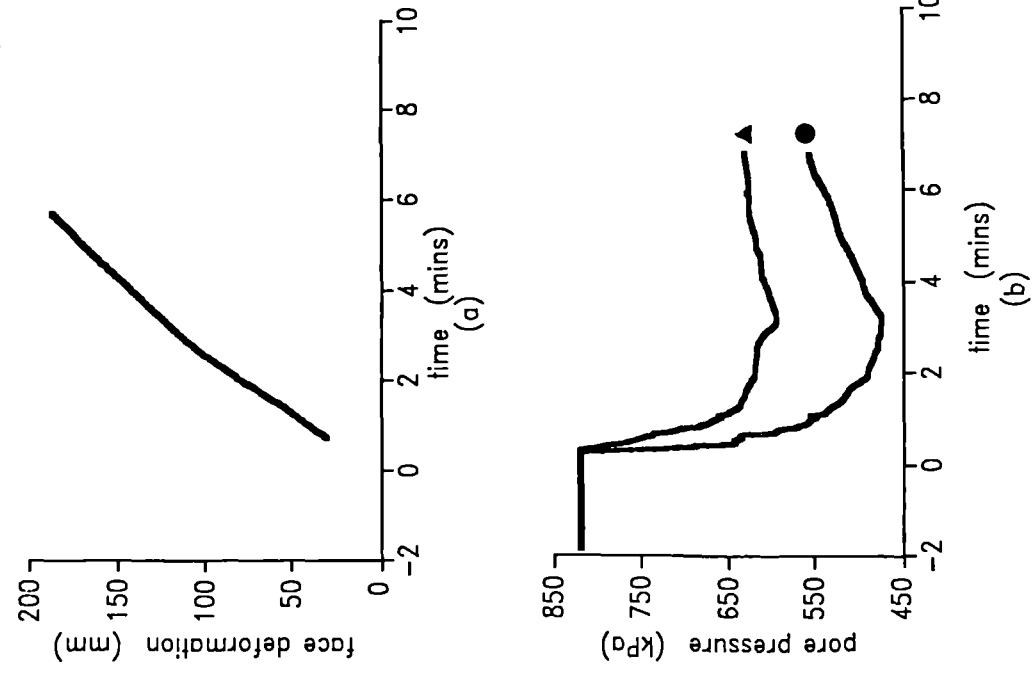


Figure 3.26 Deformation and pore pressure response
Test 19/3A (12.7mm) $p'=804\text{kPa}$ $u=820\text{kPa}$

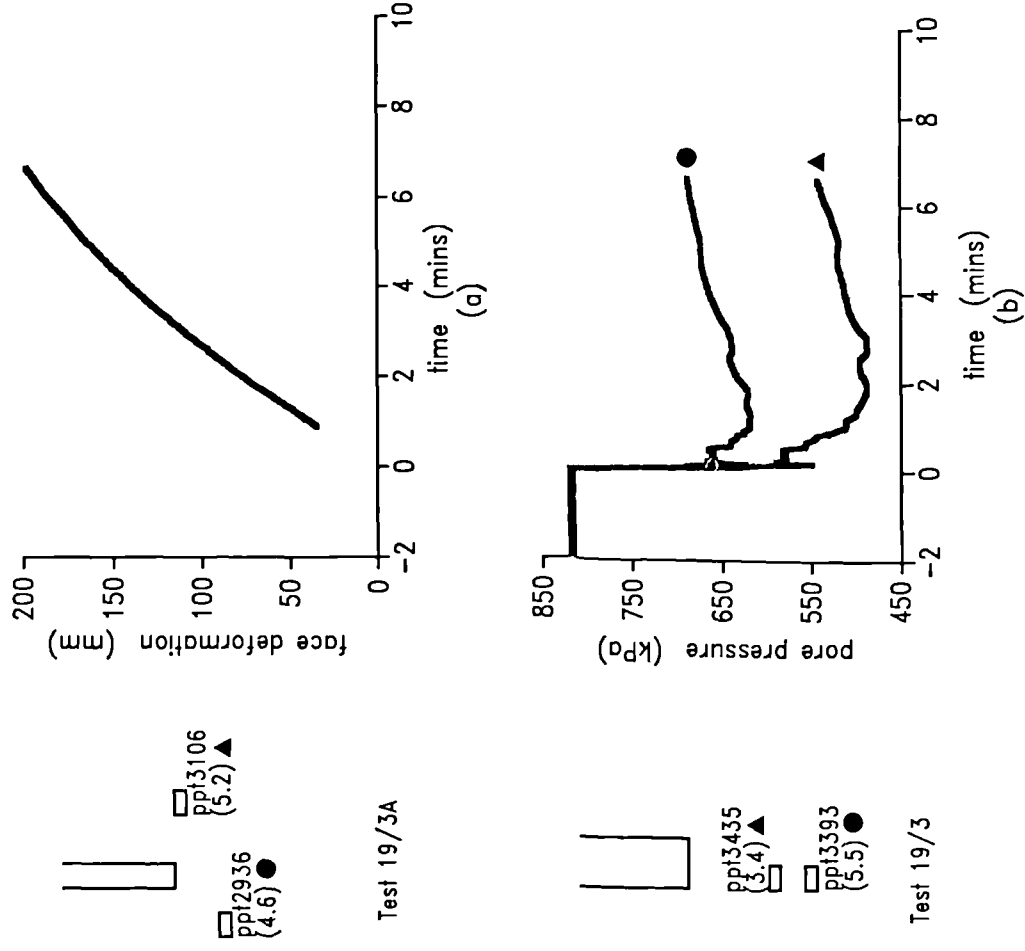


Figure 3.27 Deformation and pore pressure response
Test 19/3 (25.4mm) $p'=800\text{kPa}$ $u=820\text{kPa}$

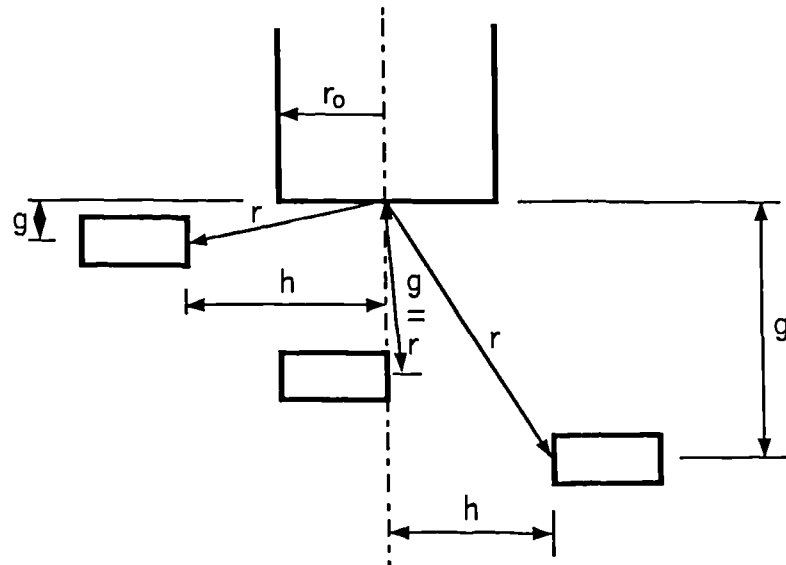


Figure 3.28 Variation in the g and h components of the distance r from the pore pressure transducer to the centre of the tunnel face

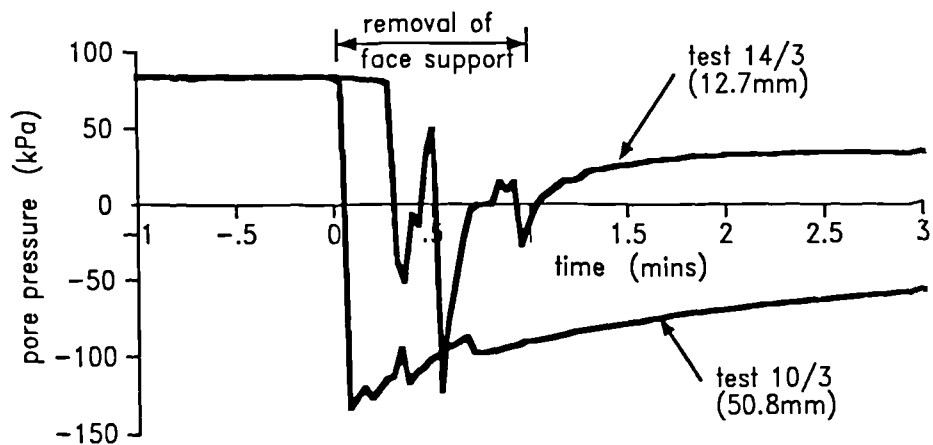


Figure 3.29(a) Comparison of the experimental pore pressure response at r/r_0 of 1.8 (along the central axis) to the removal of the face support

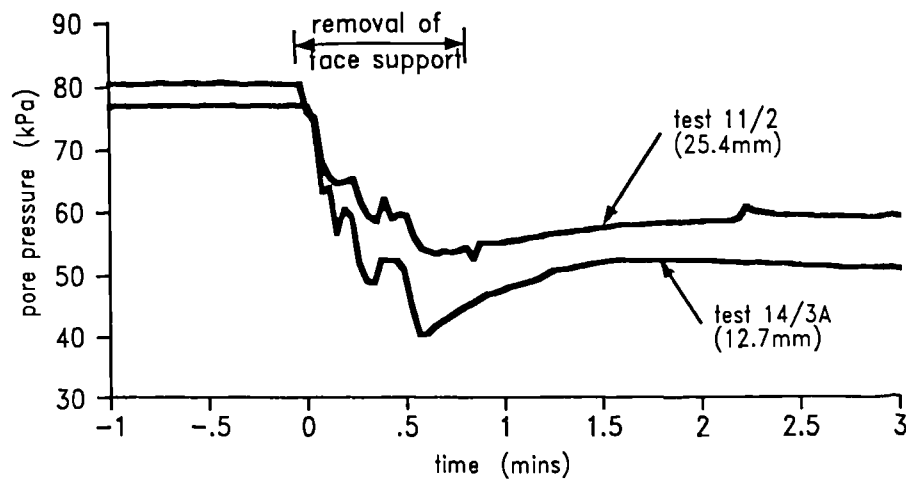


Figure 3.29(b) Comparison of the experimental pore pressure response at r/r_0 of 2.6 (perpendicular to the central axis) to the removal of the face support

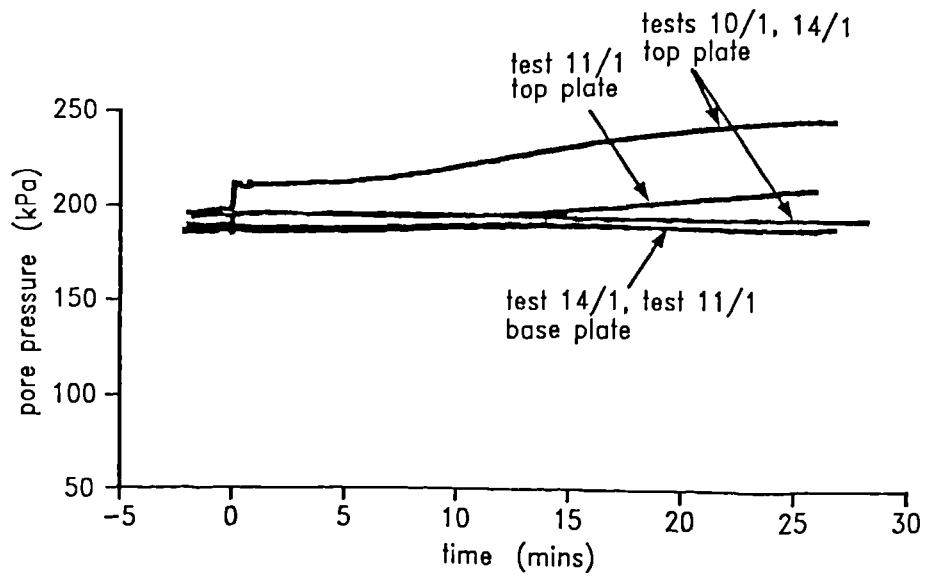


Figure 3.30(a) Pore pressure response recorded by transducers at the top and base of the sample

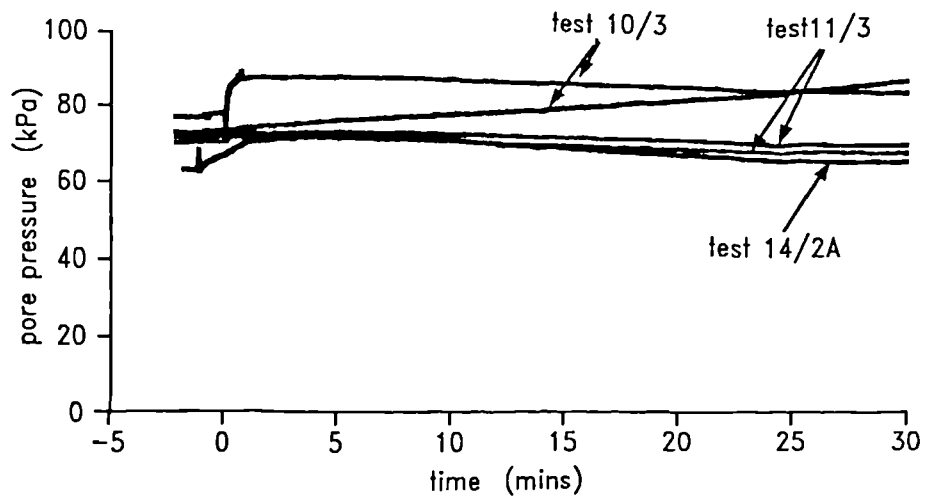


Figure 3.30(b) Pore pressure response recorded by transducers at top and base of sample

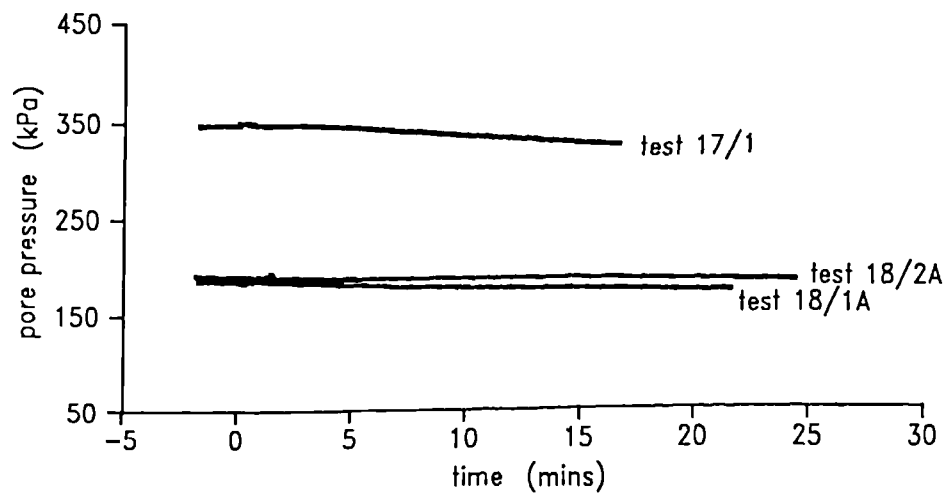


Figure 3.30(c) Pore pressure response recorded by transducers at top of sample

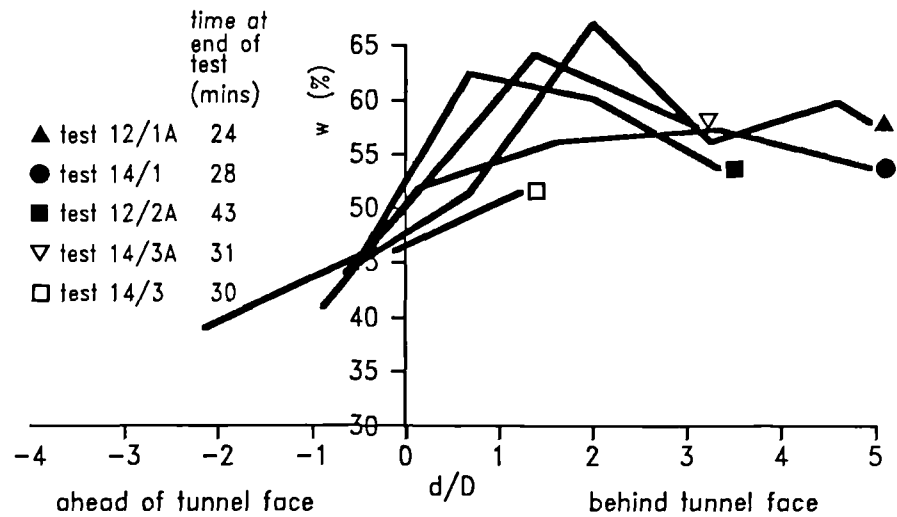


Figure 3.31 Measured water contents of samples of clay removed from the model at the end of a test demonstrating the influence of time

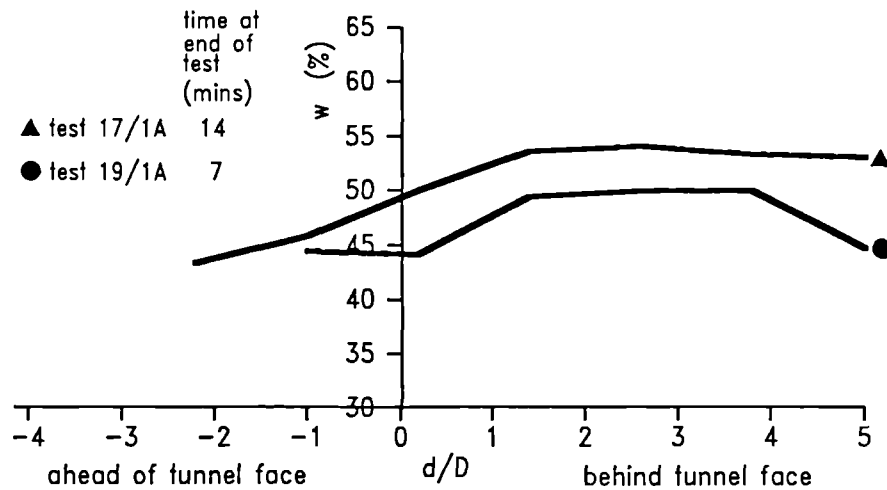


Figure 3.32 Measured water contents of samples of clay removed from the model at the end of a test demonstrating the influence of time

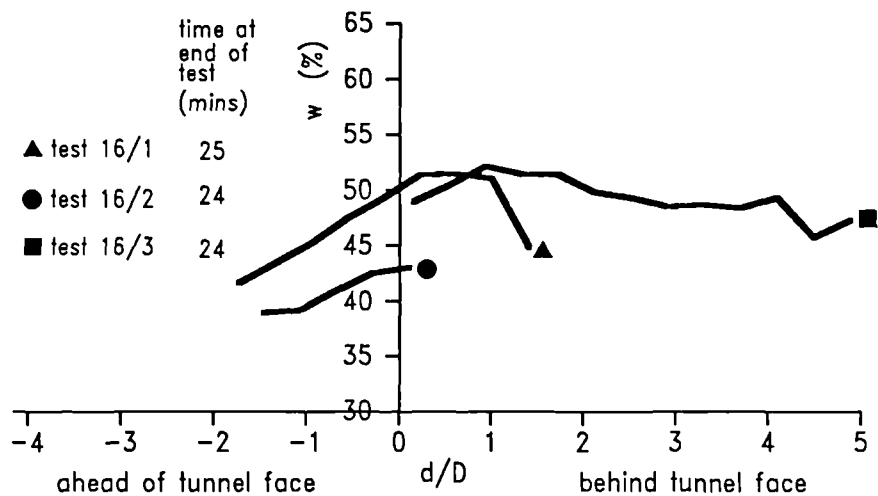


Figure 3.33 Measured water contents of samples of clay removed from the model at the end of a test demonstrating the influence of initial pore pressure

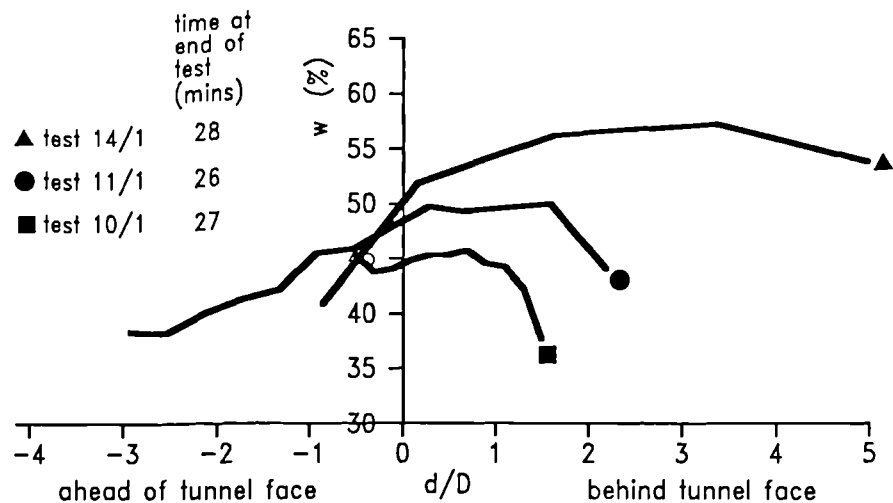


Figure 3.34 Measured water contents of samples of clay removed from the model at the end of a test demonstrating the influence of tunnel diameter

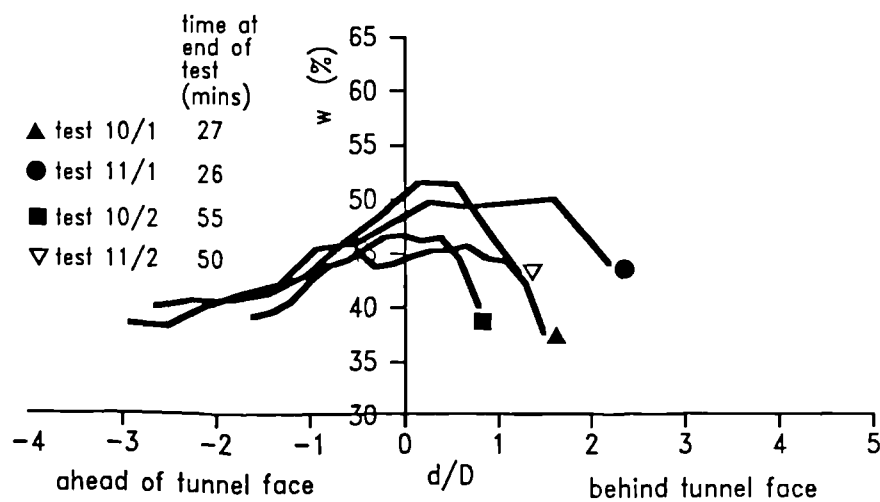


Figure 3.35 Measured water contents of samples of clay removed from the model at the end of a test demonstrating the influence of tunnel diameter

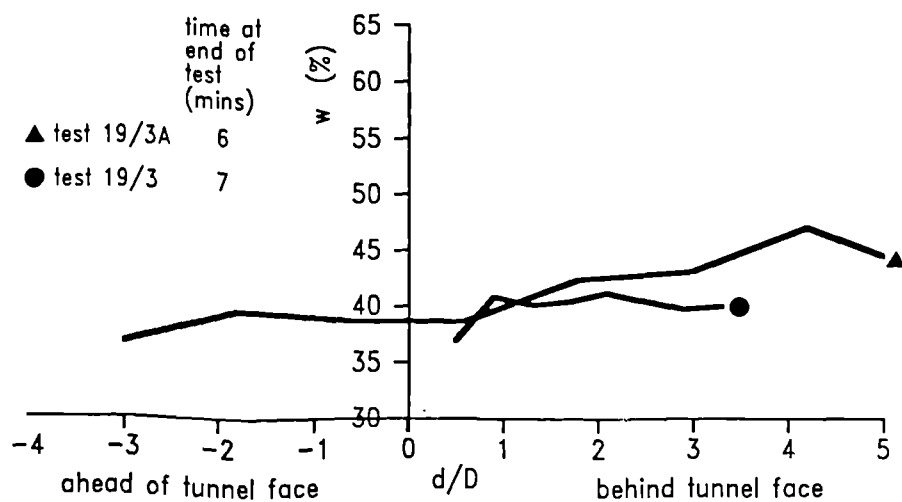
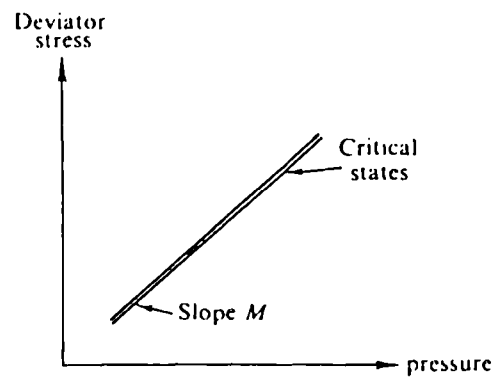
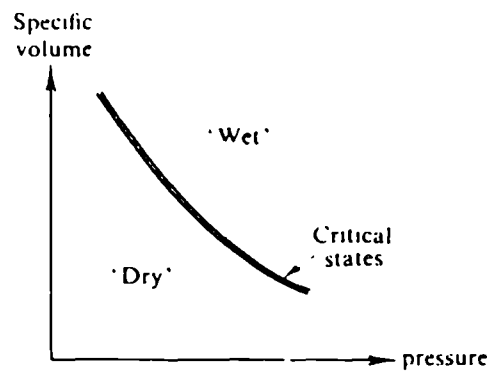


Figure 3.36 Measured water contents of samples of clay removed from the model at the end of tests performed at high load factor



(a)



(b)

Figure 4.1 Critical states (after Schofield and Wroth, 1968)

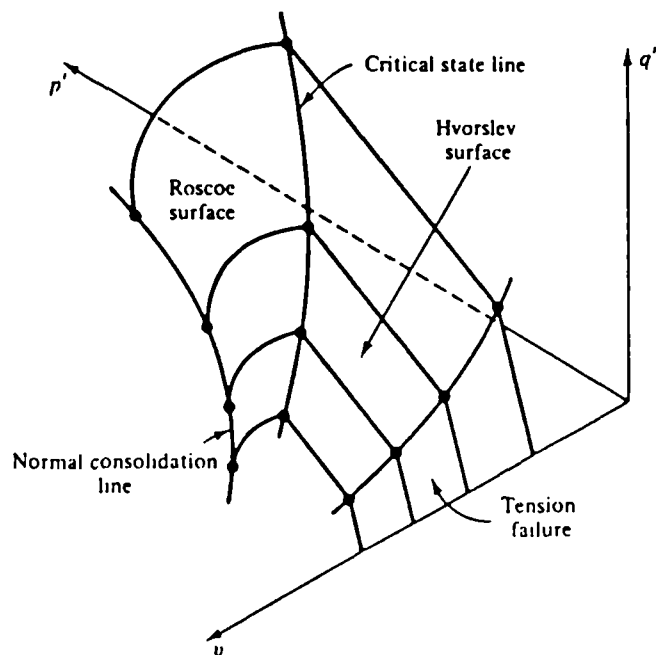


Figure 4.2 State boundary surface (after Atkinson and Bransby, 1978)

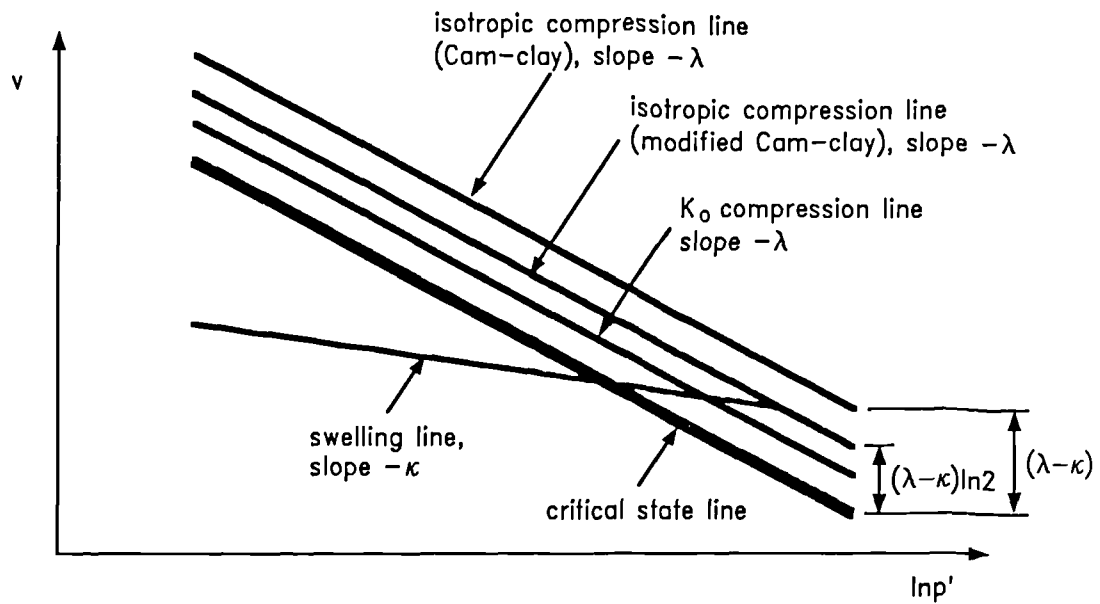


Figure 4.3 Projection of yield curves onto the $q=0$ plane in $v : \ln p'$ space

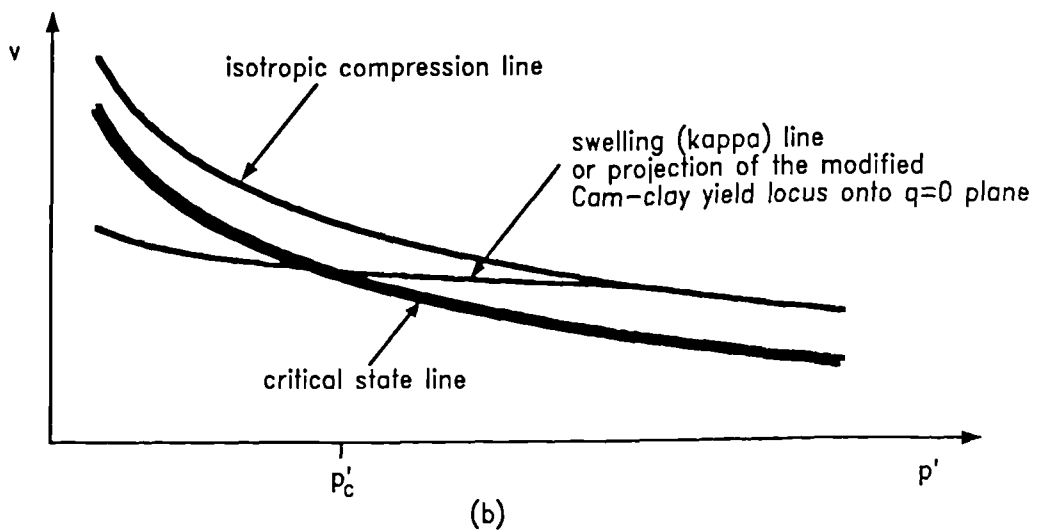
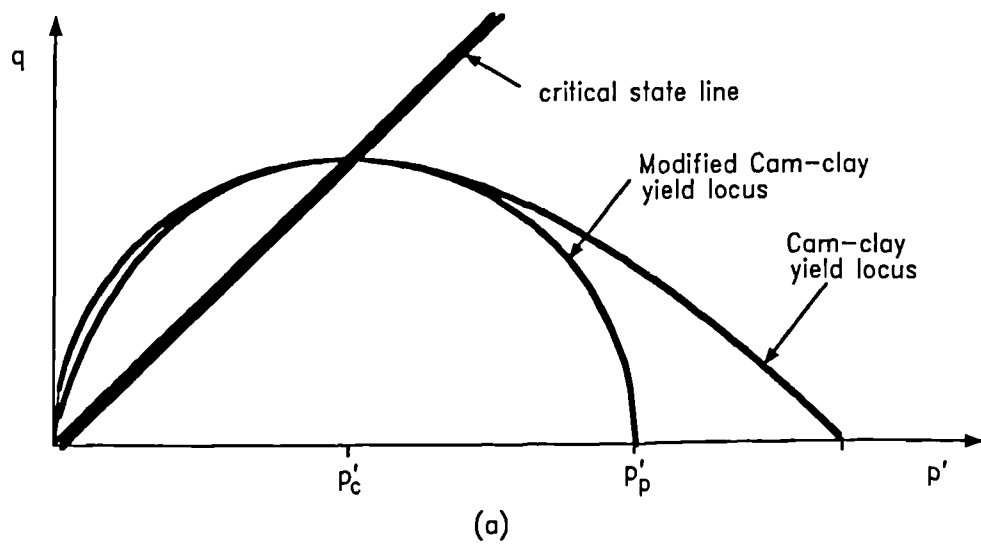


Figure 4.4 Projections of the Cam-clay and modified Cam-clay yield curves

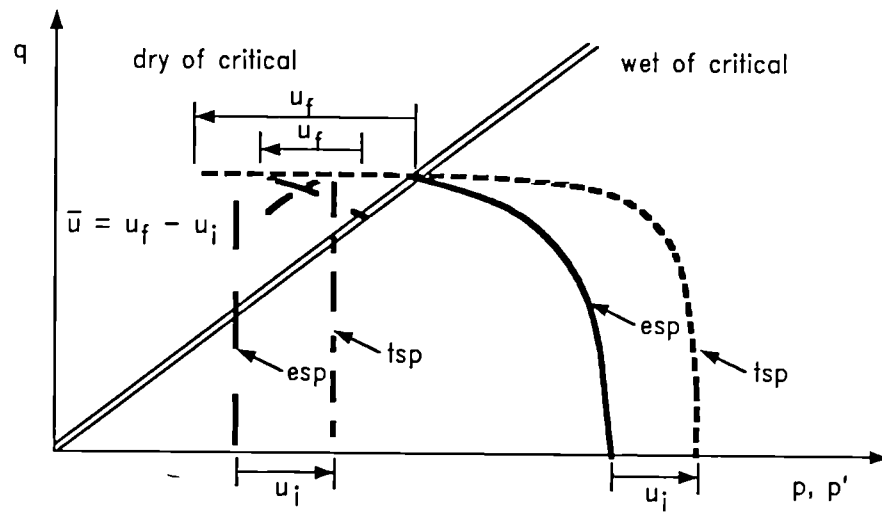


Figure 4.5(a) Typical undrained stress paths to failure for the Cam-clay soil model

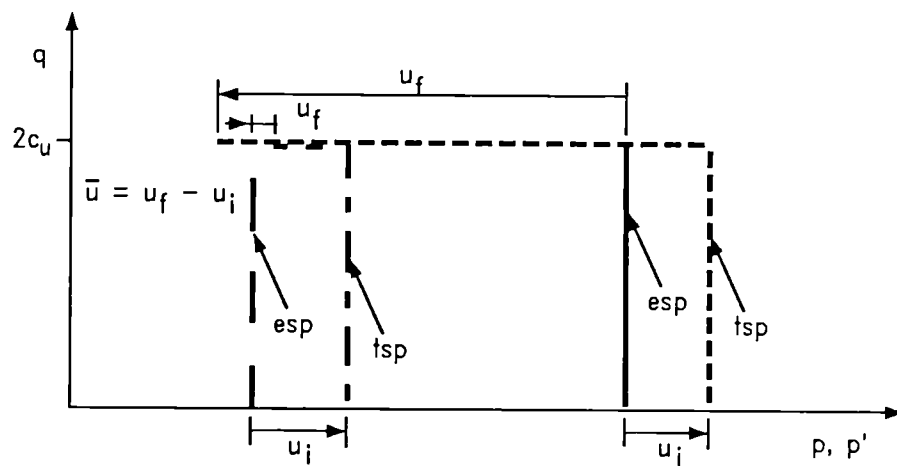


Figure 4.5(b) Typical stress paths to failure for an elastic-perfectly plastic model (Tresca criterion)

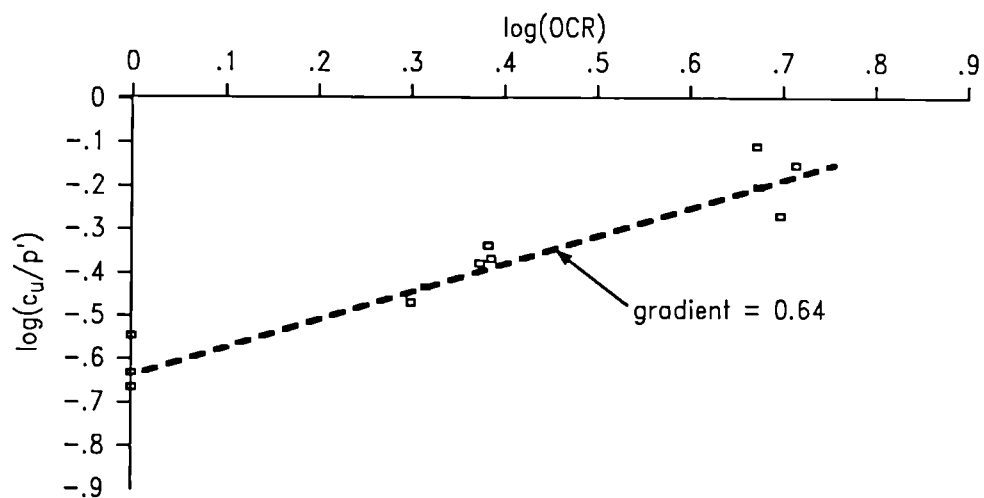


Figure 4.6 Variation of undrained shear strength with overconsolidation ratio in triaxial compression tests

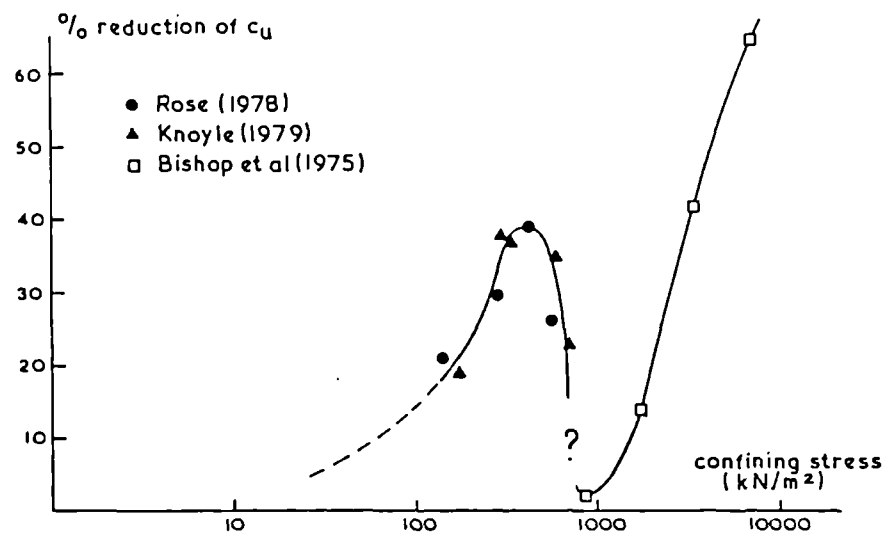


Figure 4.7 Influence of reducing confining stress to zero on the undrained shear strength of kaolin (samples consolidated isotropically to confining stress) (after Mair, 1979)

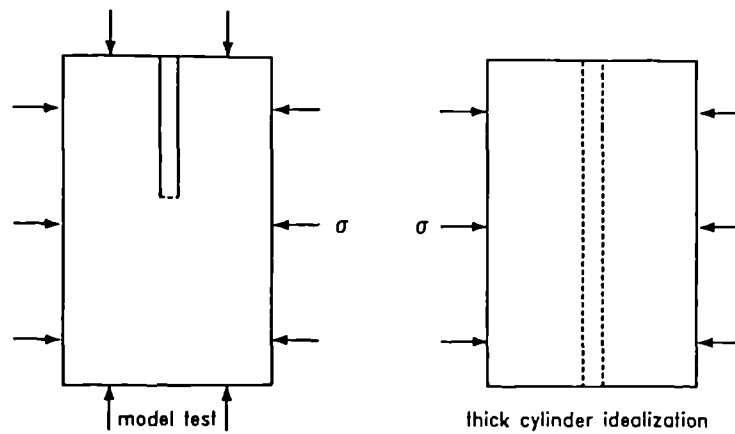


Figure 5.1(a) Comparison of model test conditions with the thick cylinder

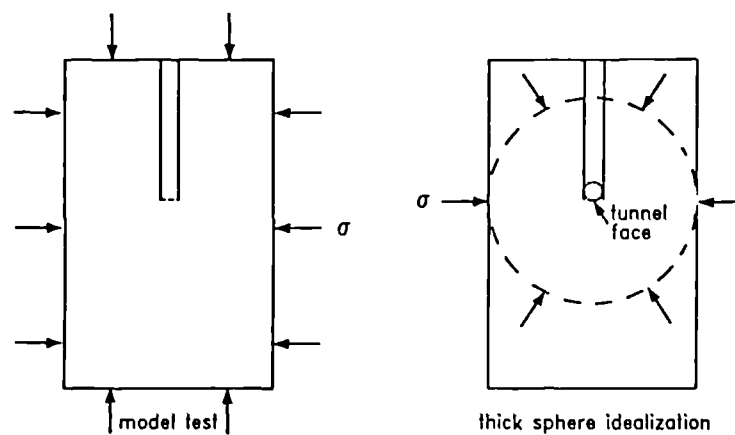


Figure 5.1(b) Comparison of model test conditions with the thick sphere

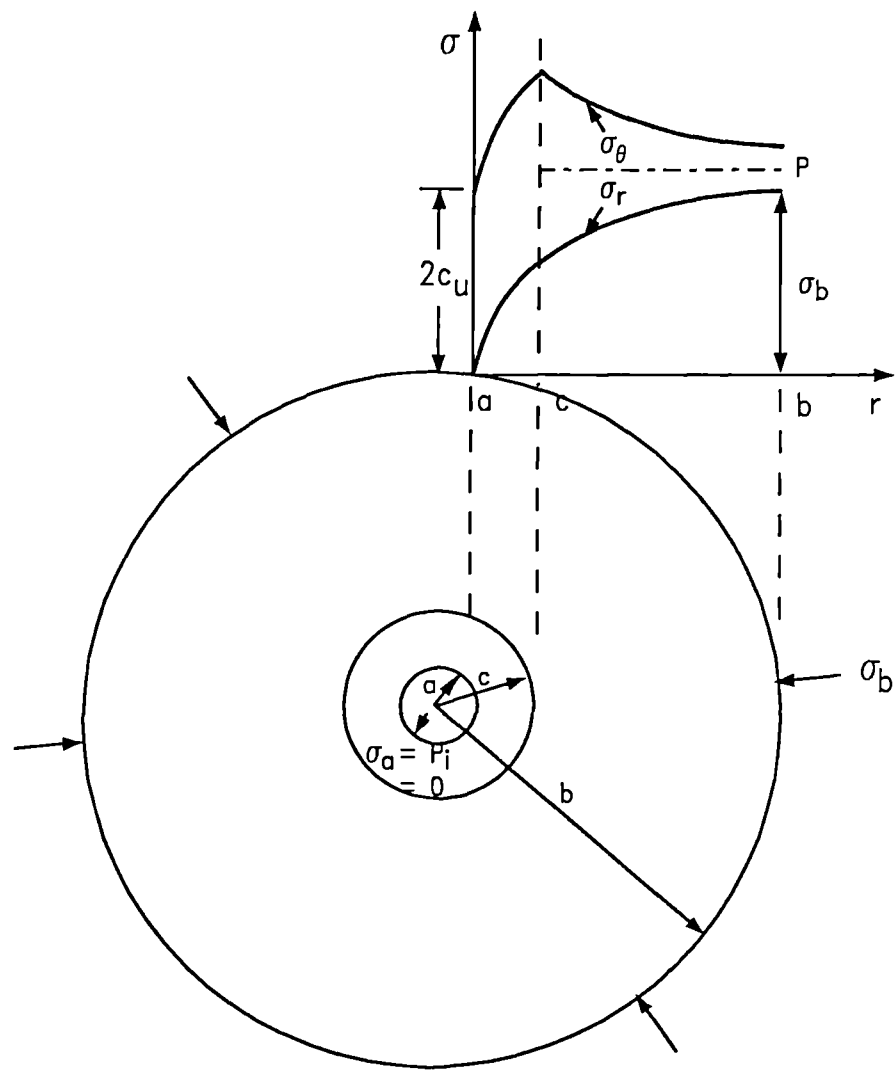


Figure 5.2 Idealized stress distribution for a thick cylinder

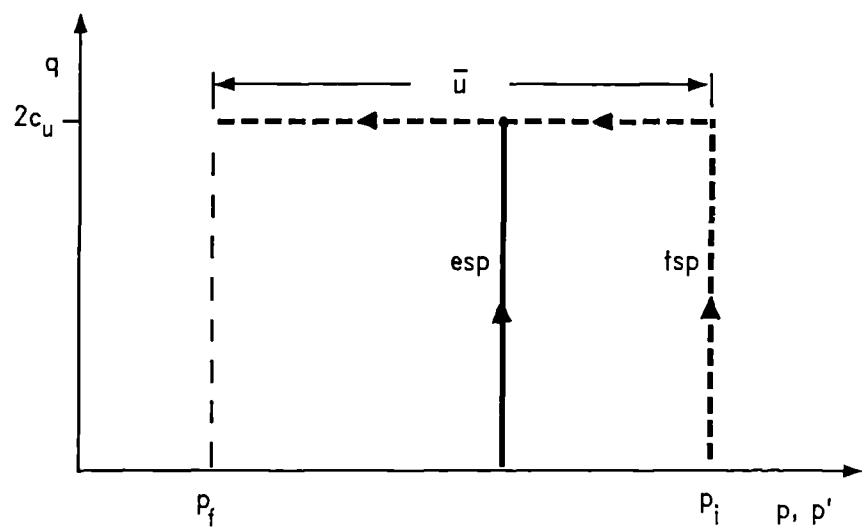


Figure 5.3 Total and effective stress paths for the Tresca yield criterion

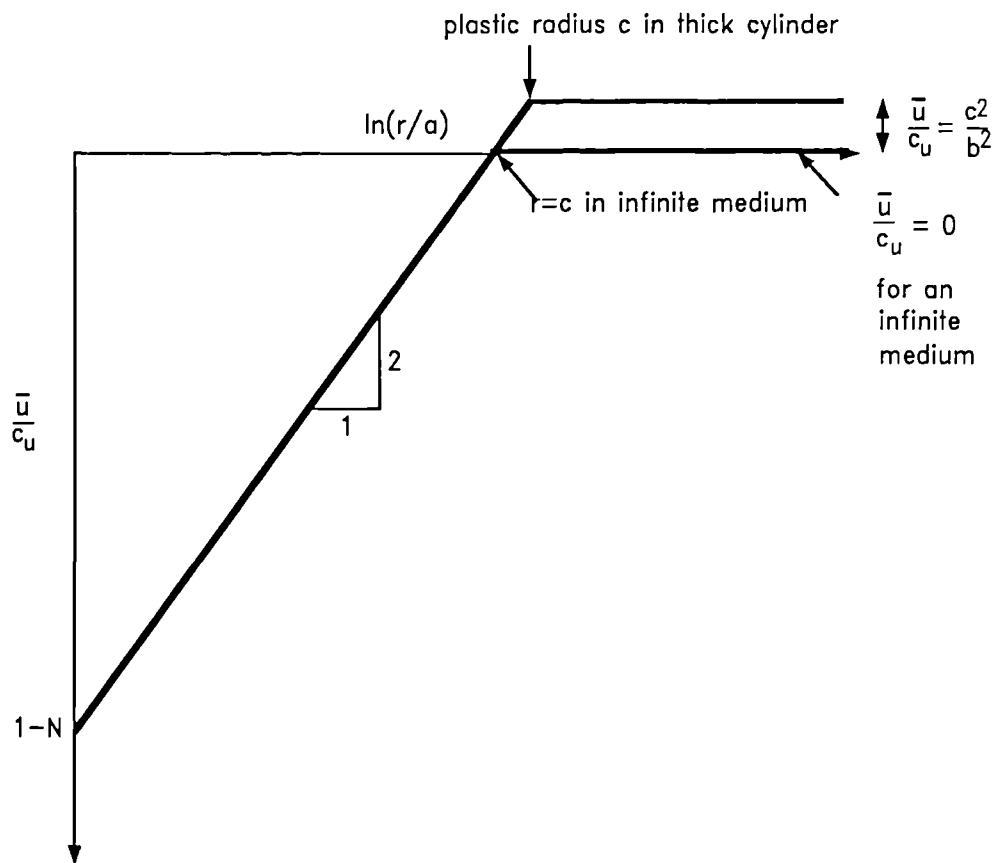


Figure 5.4 Idealized pore pressure distribution for a thick cylinder

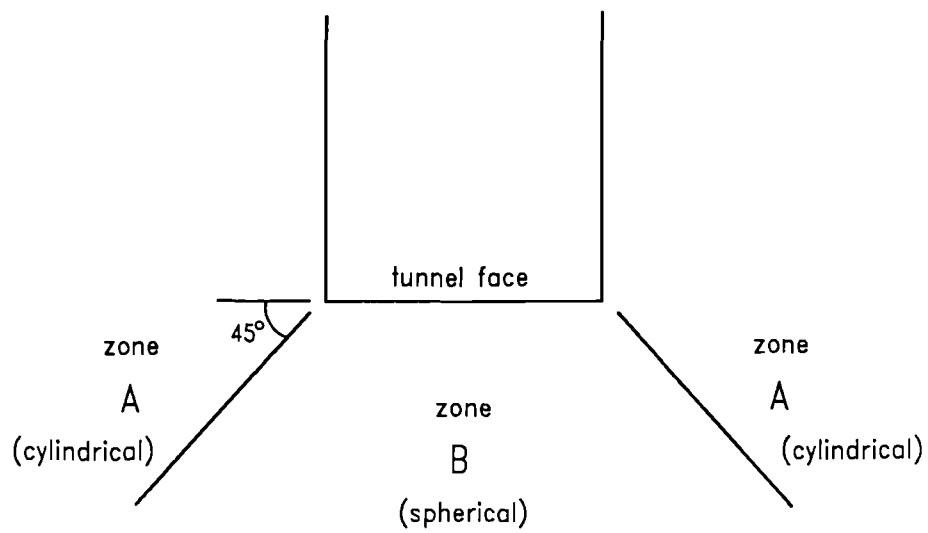


Figure 5.5 Zones of approximately cylindrical or spherical conditions

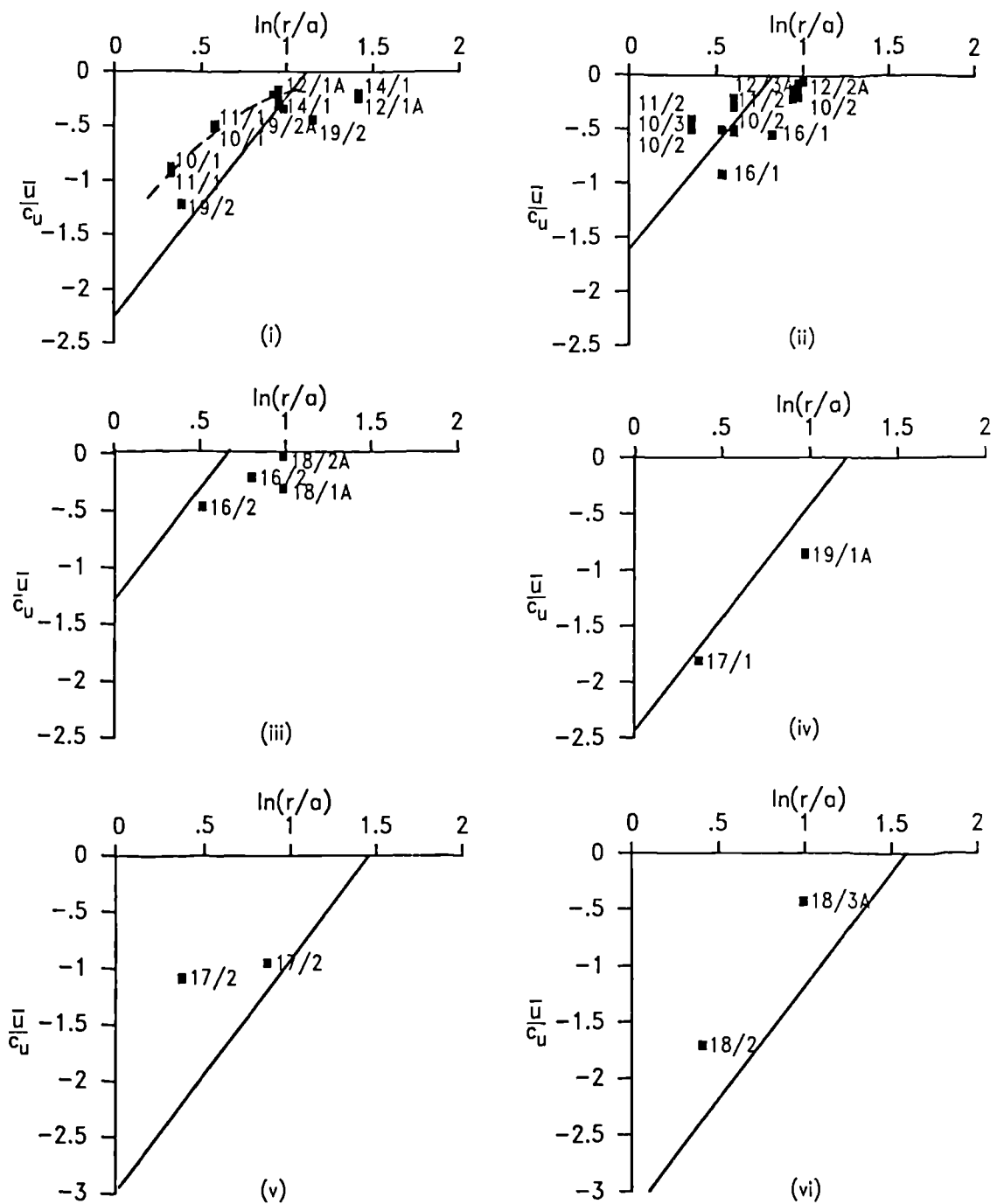


Figure 5.6(a) Experimental pore pressure response from zone A compared with theoretical distributions based on the thick cylinder solution using N^*

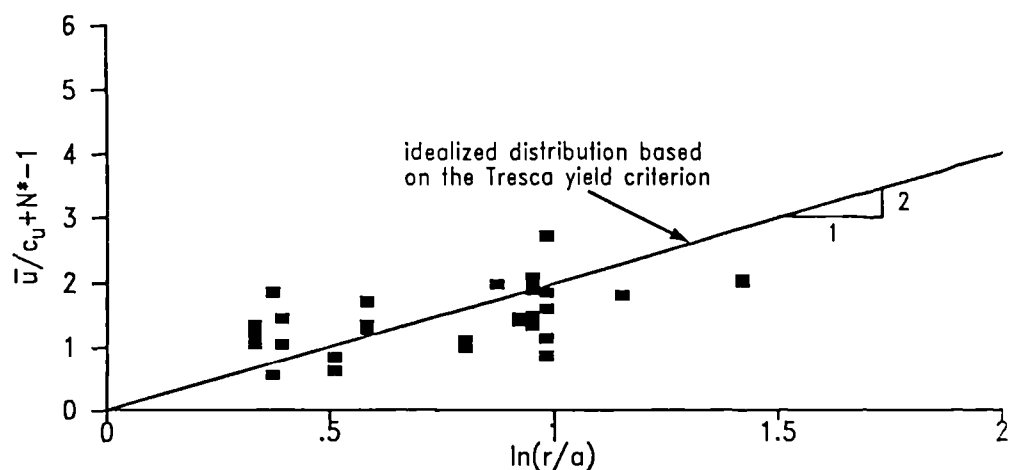


Figure 5.6(b) Experimental pore pressure responses in zone A plotted non-dimensionally using the modified stability ratio N^*

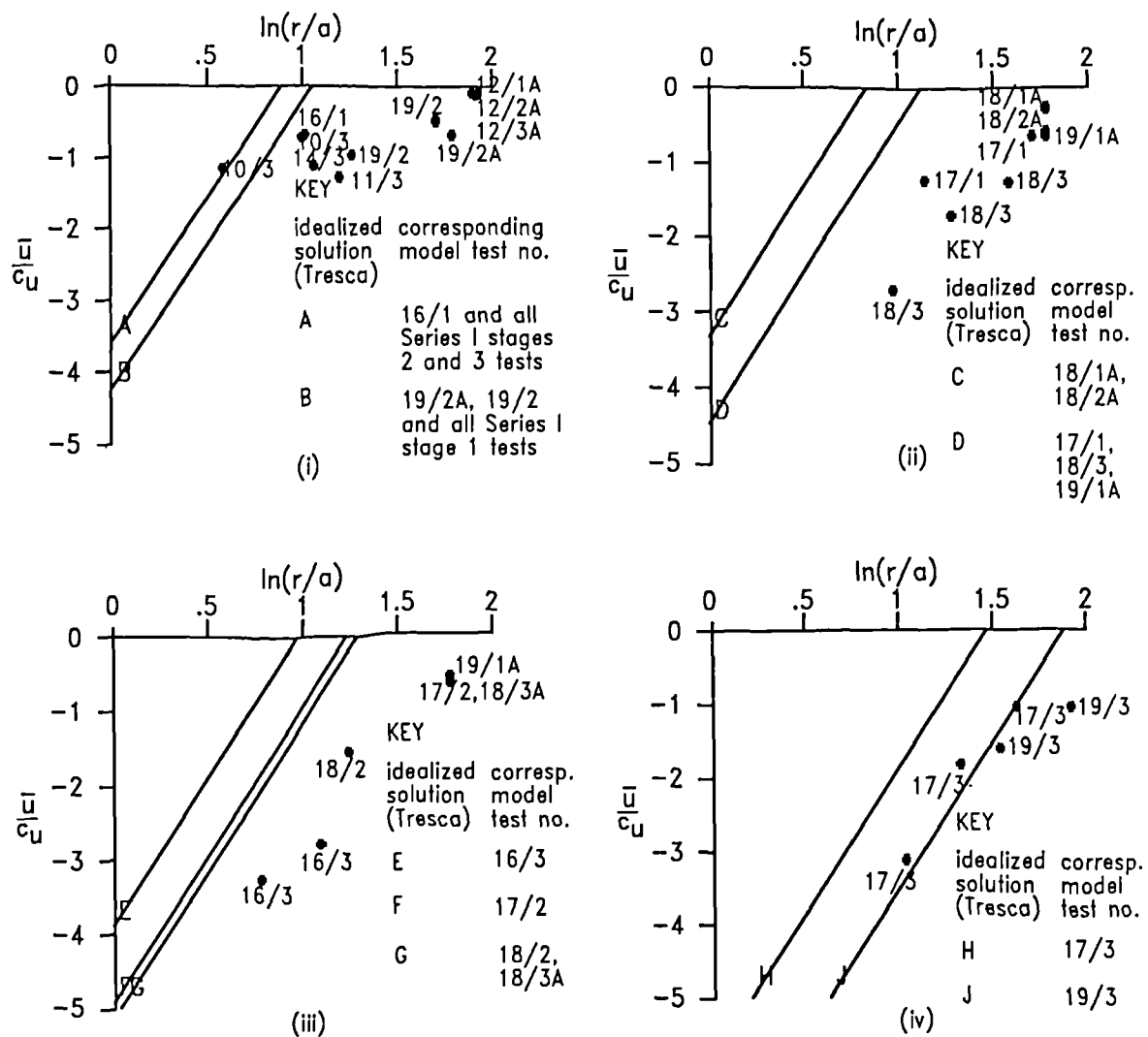


Figure 5.7(a) Experimental pore pressure response from zone B compared with the theoretical distributions based on the thick sphere solution

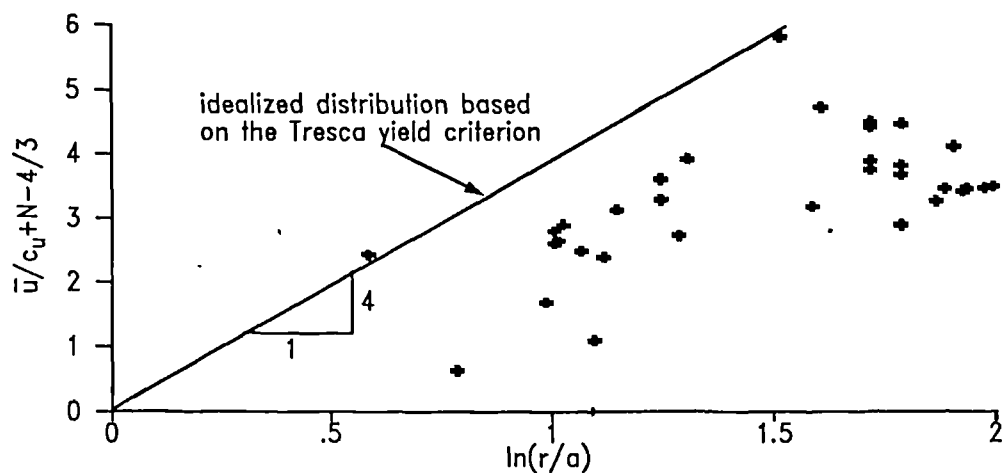


Figure 5.7(b) Experimental pore pressure response in zone B plotted with the non-dimensional idealized spherical pore pressure distribution

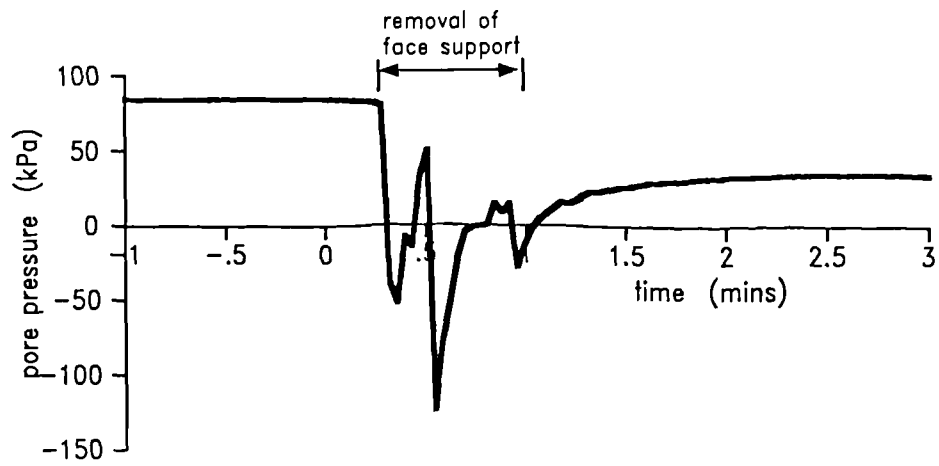


Figure 5.8(a) Response of a pore pressure transducer ahead of the tunnel face to the removal of the face support in test 14/3

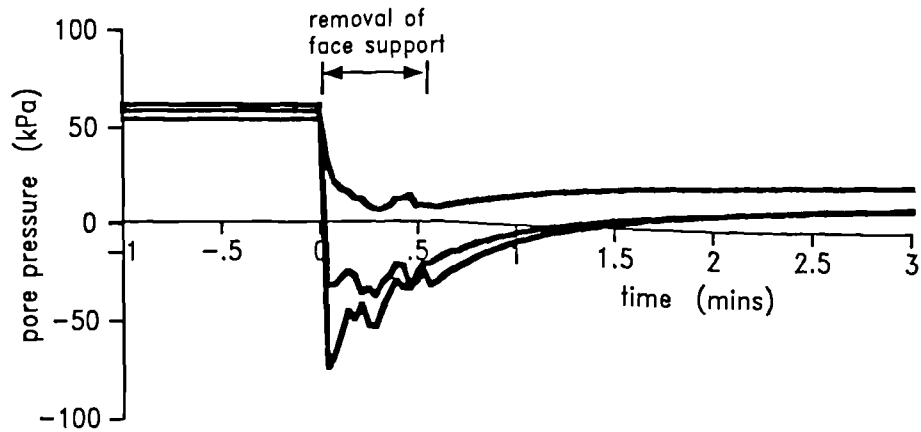


Figure 5.8(b) Response of pore pressure transducers some radial distance from the central axis to the removal of the face support in test 16/2

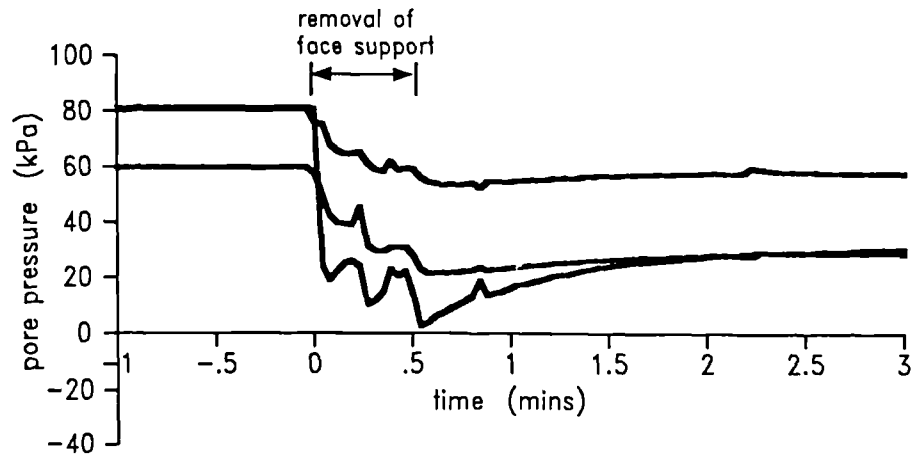


Figure 5.8(c) Response of pore pressure transducers some radial distance from the central axis to the removal of the face support in test 11/2

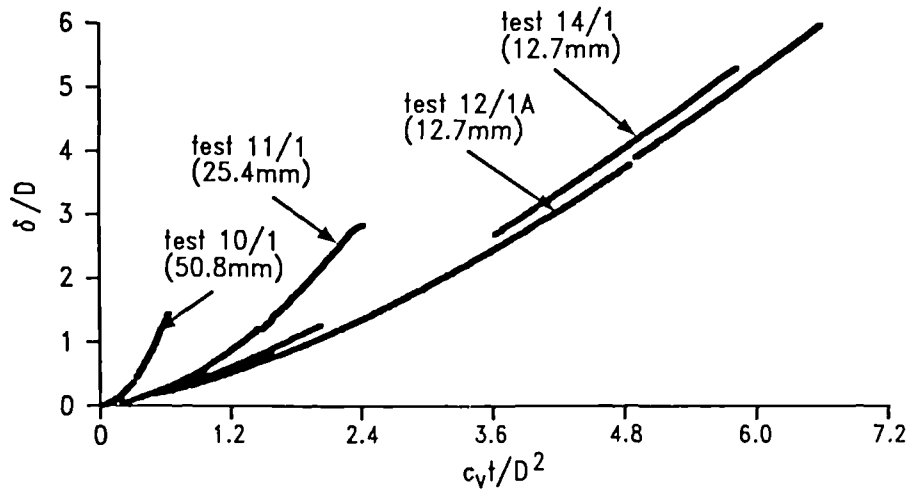


Figure 5.9 Comparison of Series I stage 1 face deformation data plotted in non-dimensional groups to demonstrate the influence of tunnel diameter

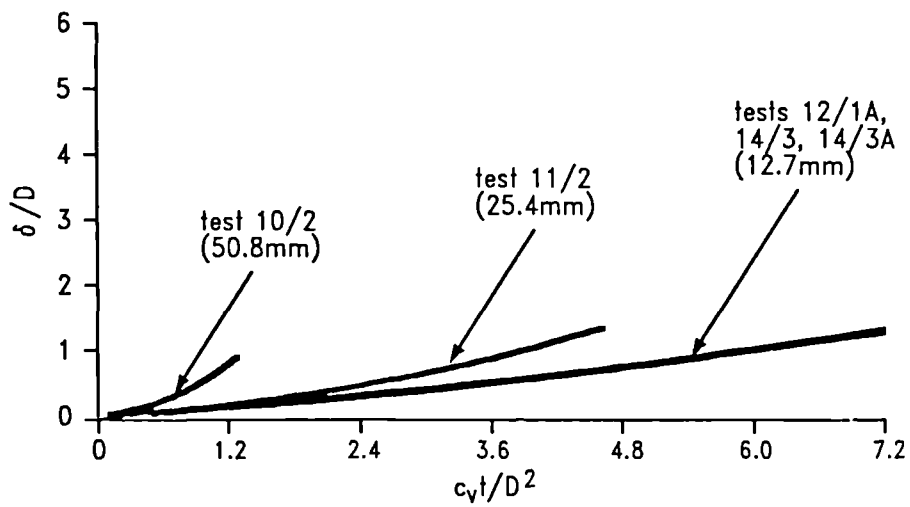


Figure 5.10 Comparison of Series I stage 2 and 3 face deformation data plotted in non-dimensional groups to demonstrate the influence of tunnel diameter

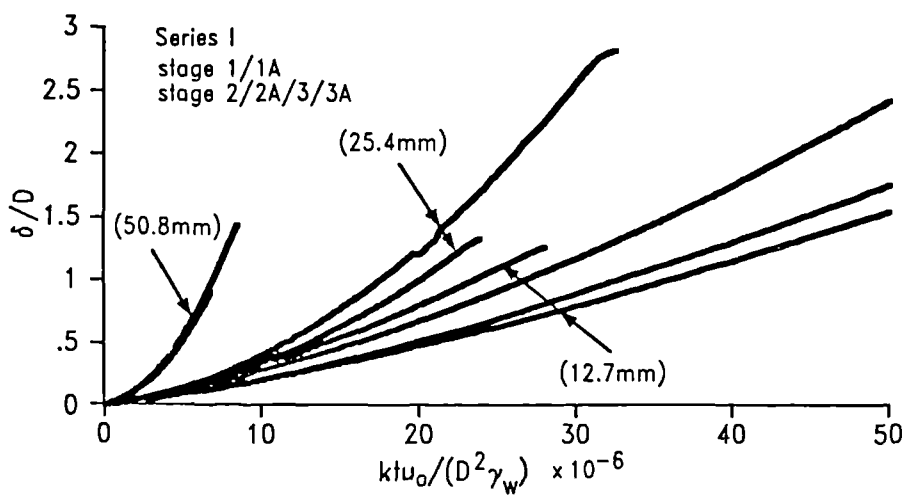


Figure 5.11 Influence of the inclusion of initial pore pressure in the non-dimensional time factor on Series I data (all stages)

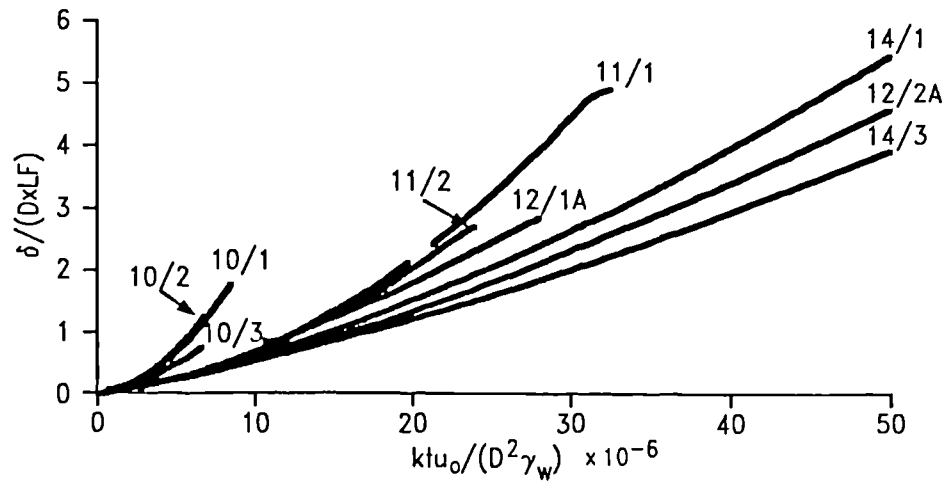


Figure 5.12 The influence of the inclusion of load factor in a non-dimensional group on the deformation data from Series I tests

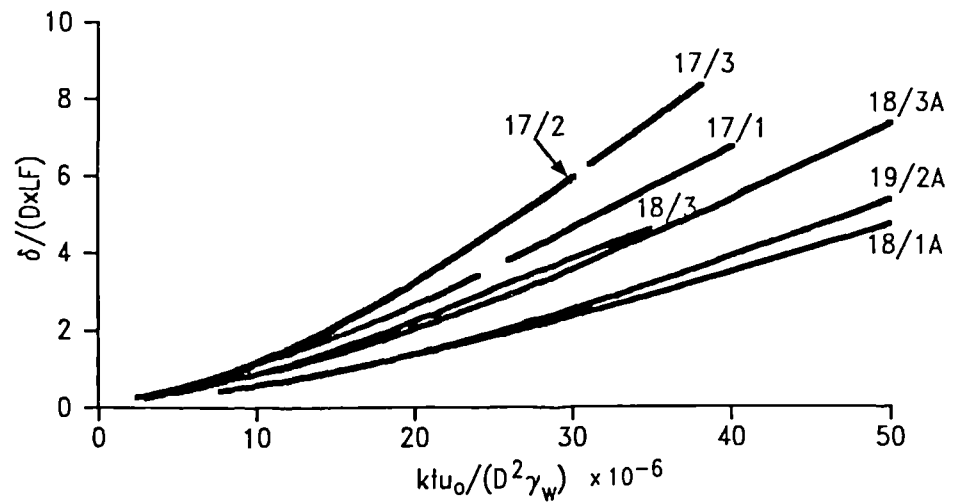


Figure 5.13 The influence of the inclusion of load factor in a non-dimensional group on the deformation data from Series II tests

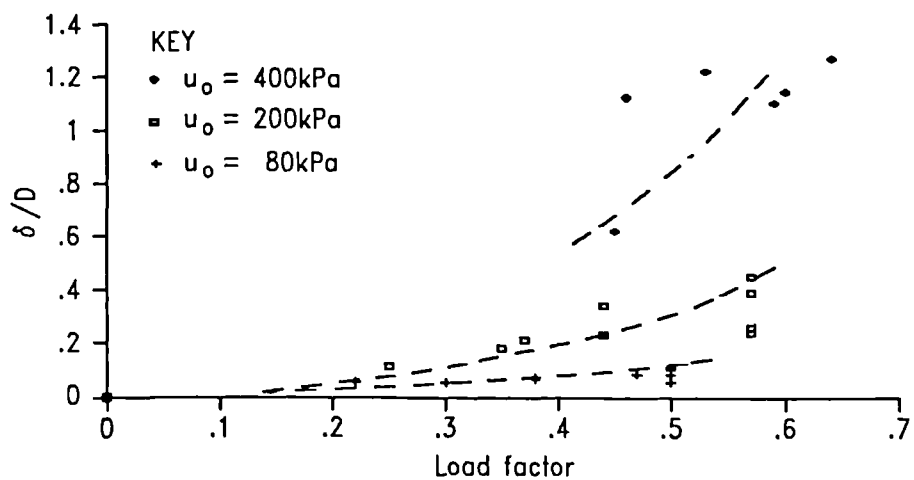


Figure 5.14 Experimental tunnel face deformations at a constant t/D^2 and various pore pressures

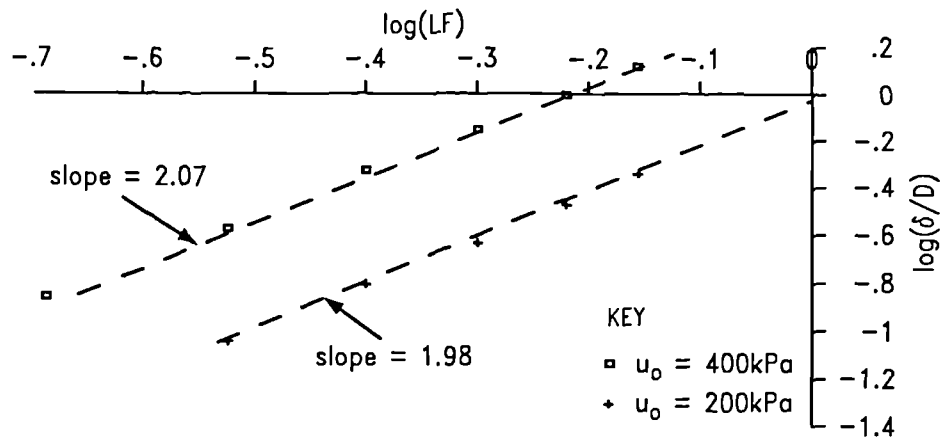


Figure 5.15 Experimental deformation data at a constant t/D^2 plotted in logarithmic space to determine variation with load factor

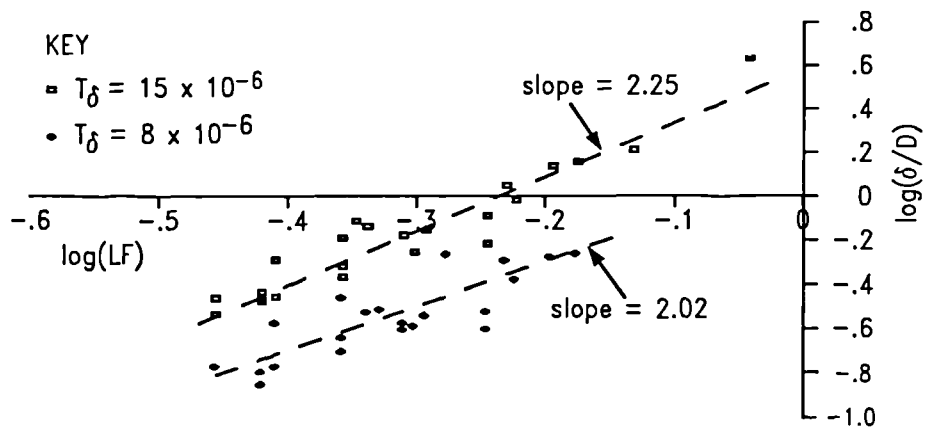


Figure 5.16 Experimental deformation data at a constant $ktu_0/(D^2\gamma_w)$ plotted in logarithmic space to determine variation with load factor

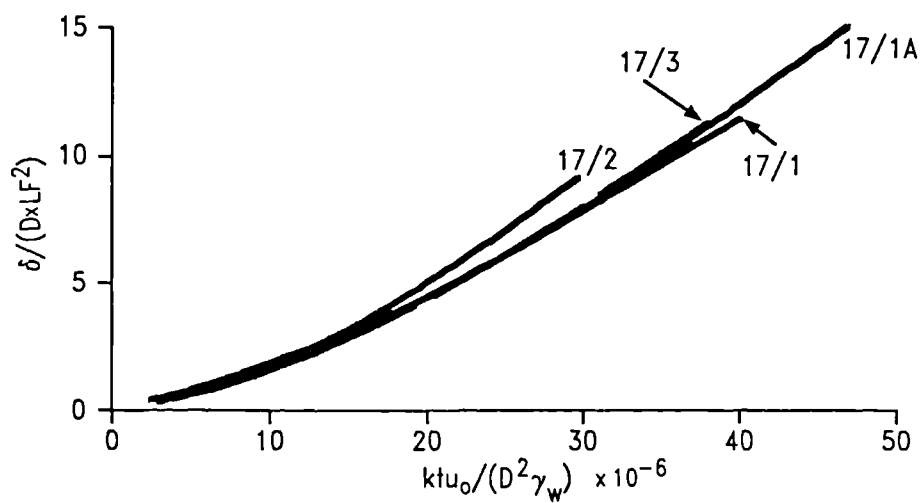


Figure 5.17 Deformation data from tests in sample no. 17 with a load factor range of 0.45 to 0.74 plotted in non-dimensional groups

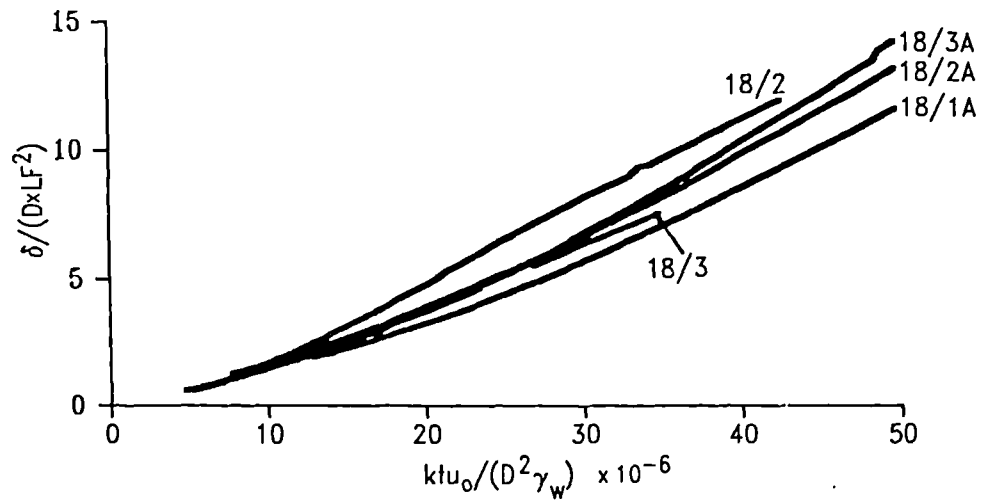


Figure 5.18 Deformation data from tests in sample no. 18 with a load factor range of 0.35 to 0.67 plotted in non-dimensional groups

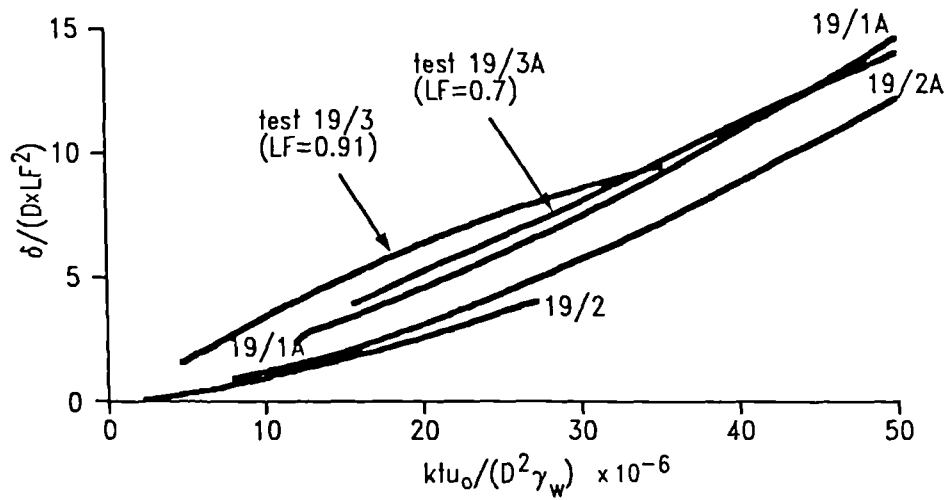


Figure 5.19 Deformation data from tests in sample no. 19 with a load factor range of 0.44 to 0.91 plotted in non-dimensional groups

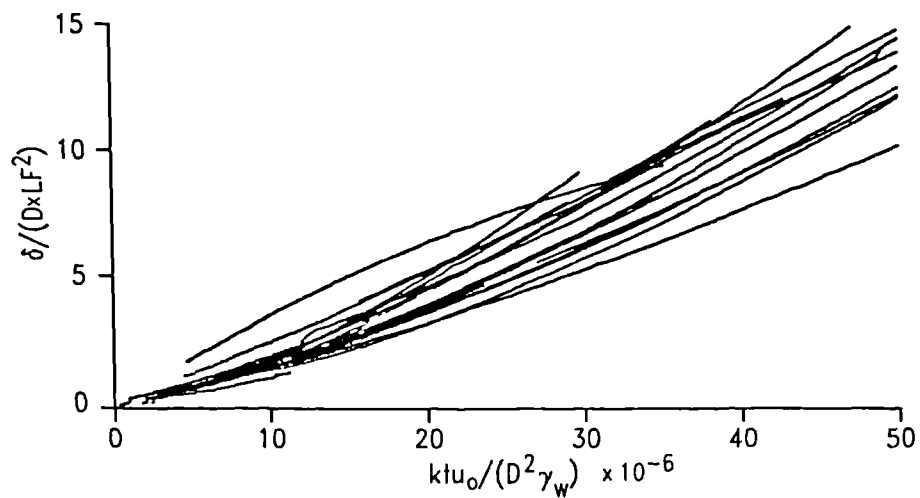


Figure 5.20 Comparison of deformation data from Series I and II excluding tests using the 50.8mm diameter tunnel

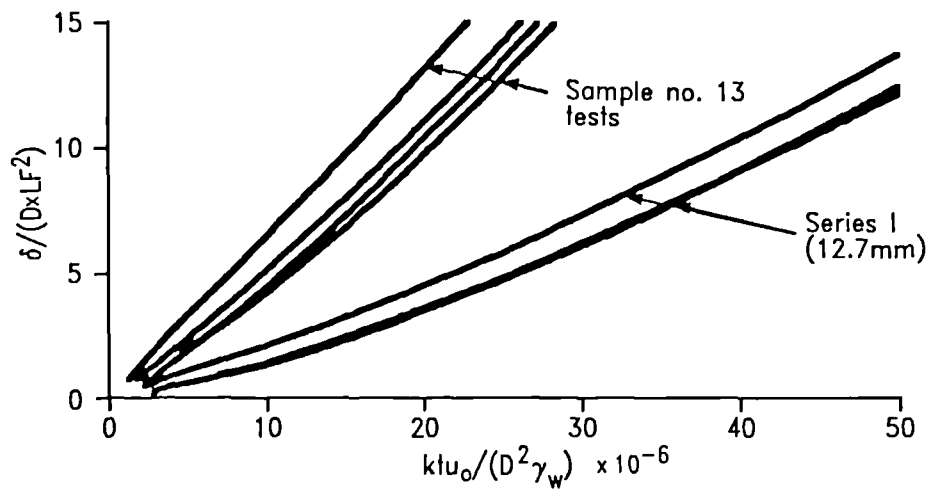


Figure 5.21 Comparison of deformation data (uncorrected for loss of strength) from tests in sample no. 13 with Series I tests

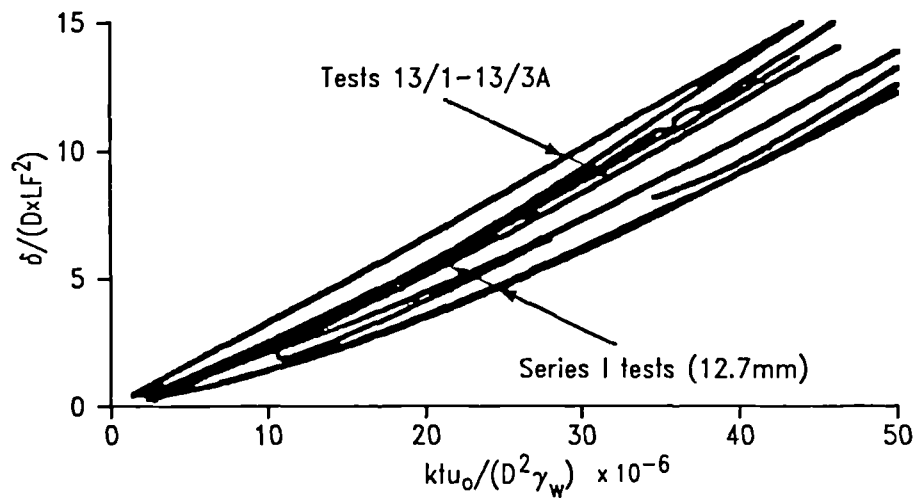


Figure 5.22 Comparison of tests in sample no. 13 with equivalent Series I tests using the 12.7mm diameter tunnel

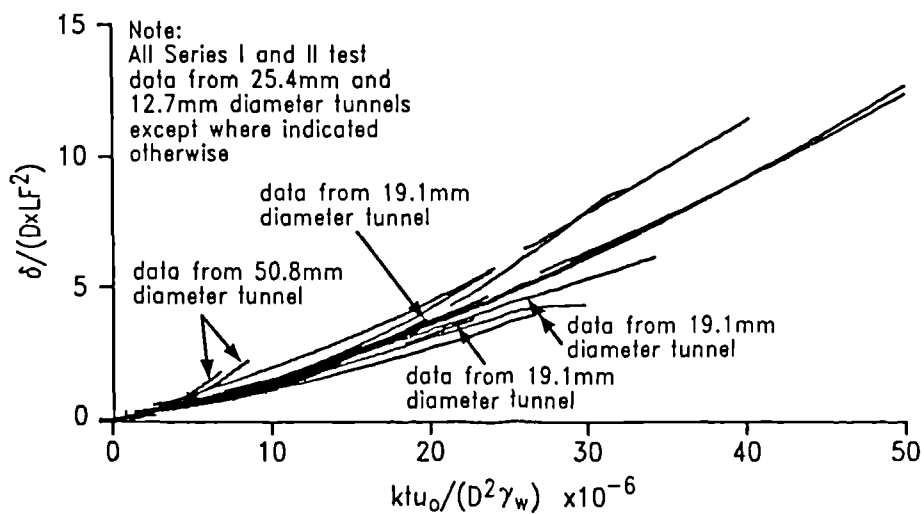


Figure 5.23 Comparison of data from the 19.1mm diameter tests with a number of the Series I and II tests

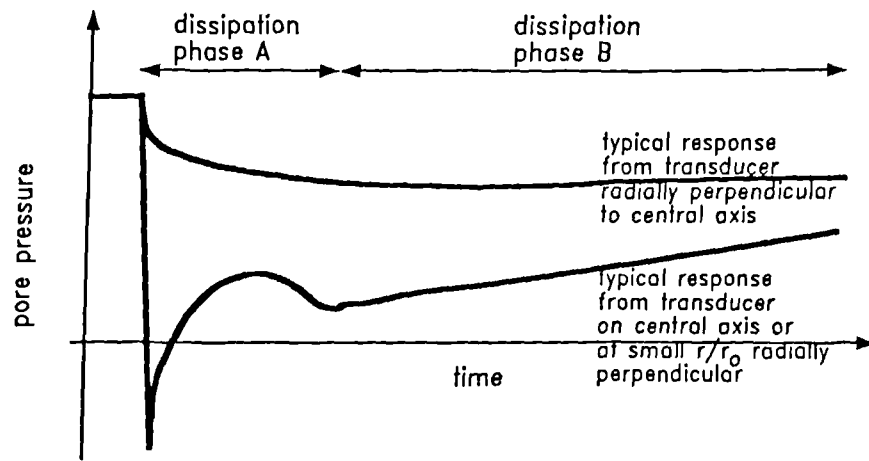


Figure 5.24 Two phases of pore pressure behaviour during the model tunnel tests

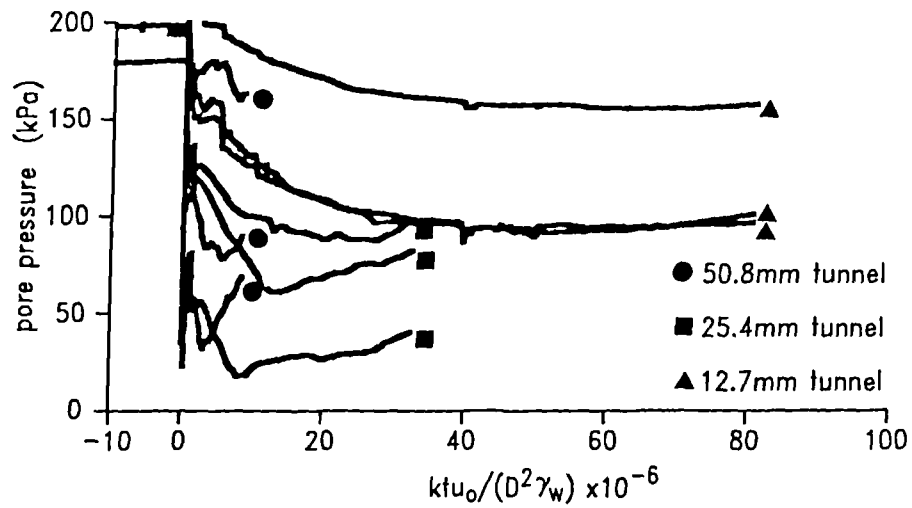


Figure 5.25 Pore pressure data from Series I stage 1 tests plotted against the non-dimensional time factor developed in the analysis of tunnel face deformations

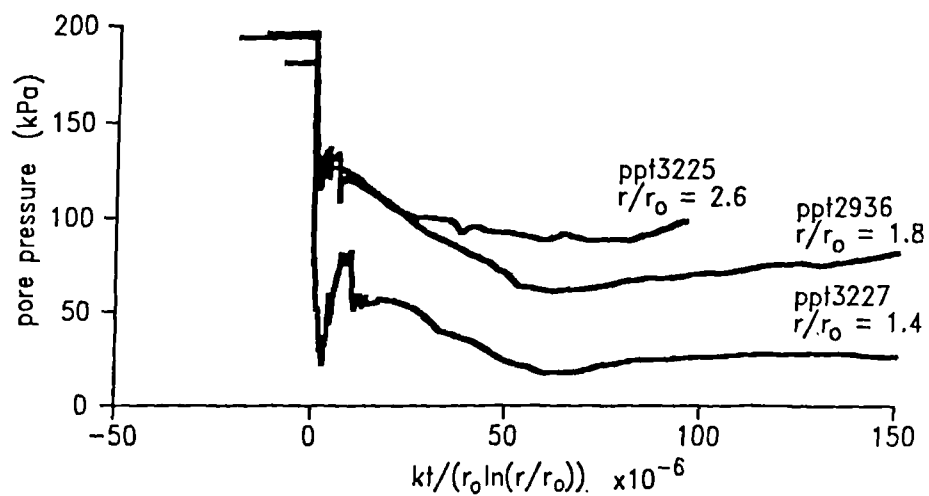


Figure 5.26(a) Pore pressure data at different r/r_o values in test 11/1

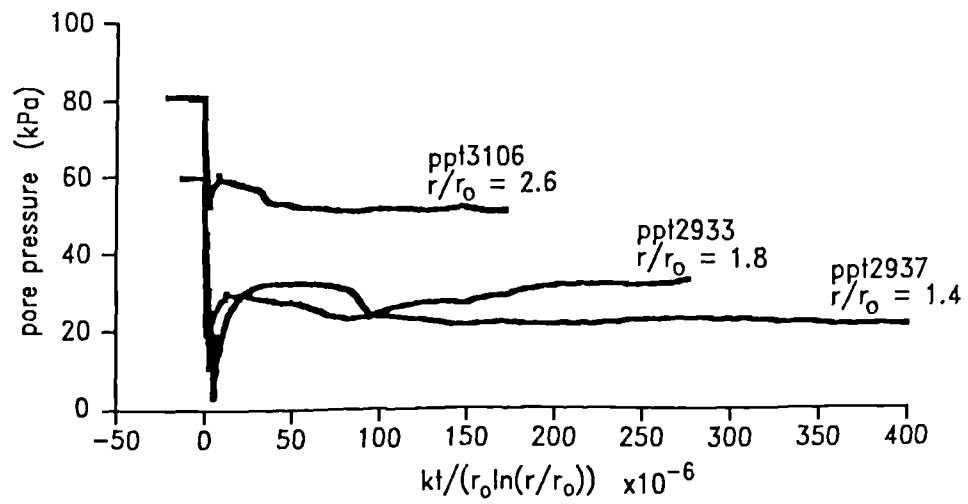


Figure 5.26(b) Pore pressure data at different r/r_0 values in test 11/2

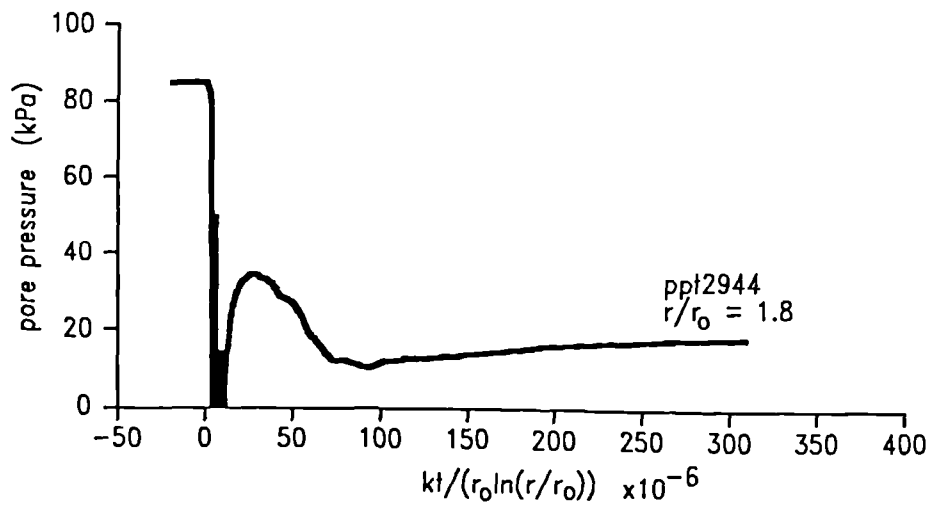


Figure 5.26(c) Pore pressure data from a transducer ahead of the tunnel face in test 14/3

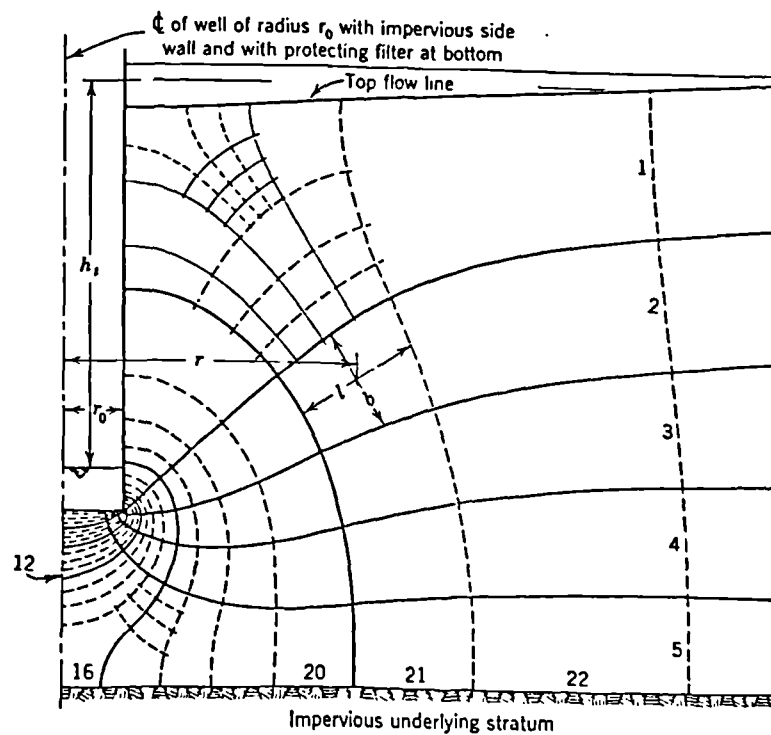


Figure 5.27(a) Seepage flow net for conditions of axisymmetry (after Taylor, 1948)

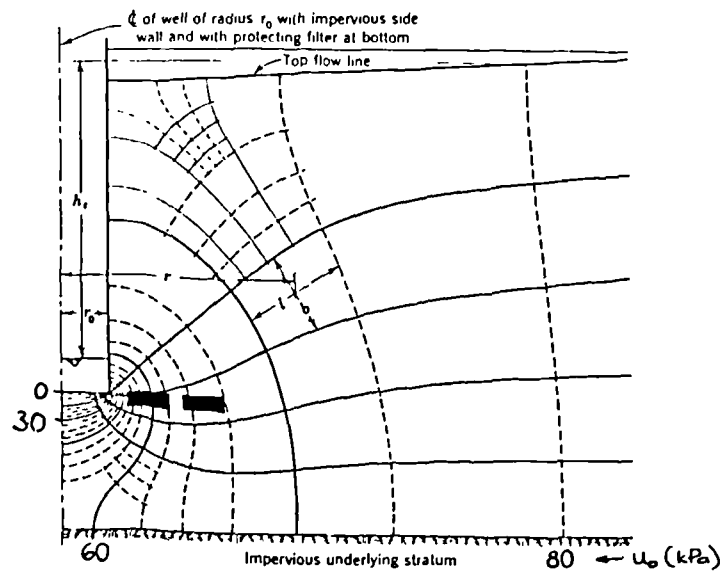


Figure 5.27(b) Comparison of pore pressures predicted for radial seepage and the phase B pore pressure measured in test 11/2

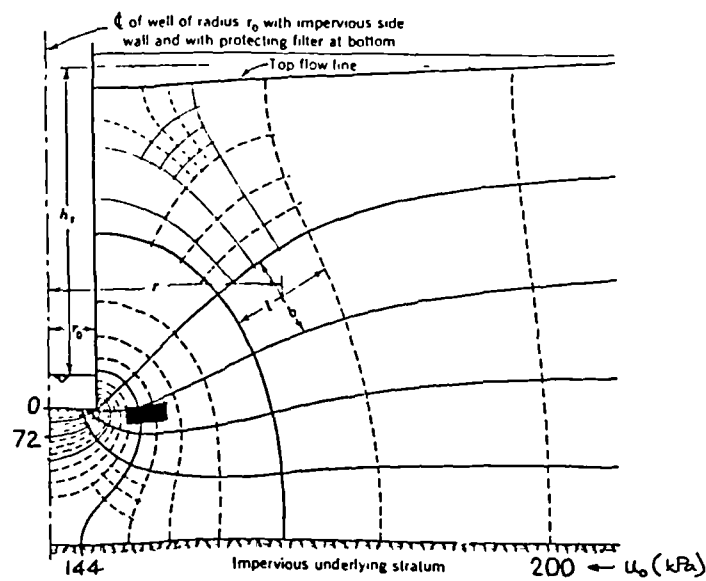


Figure 5.27(c) Comparison of pore pressures predicted for radial seepage and the phase B pore pressure measured in test 16/1

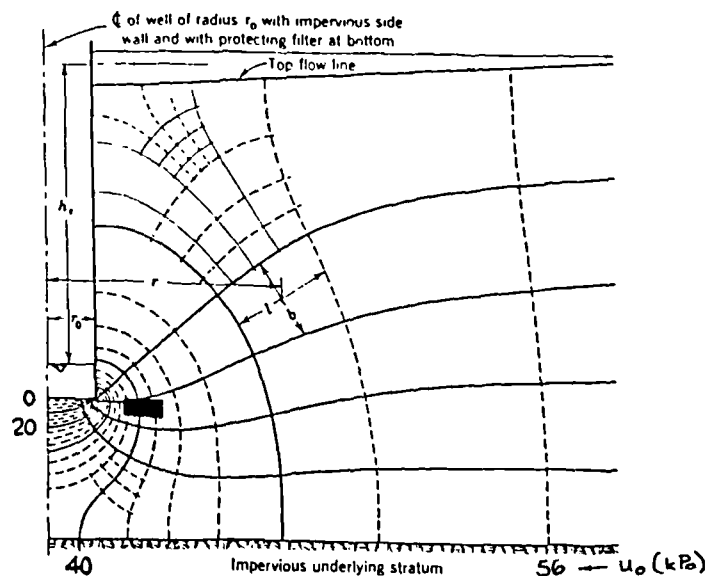


Figure 5.27(d) Comparison of pore pressures predicted for radial seepage and the phase B pore pressure measured in test 16/2

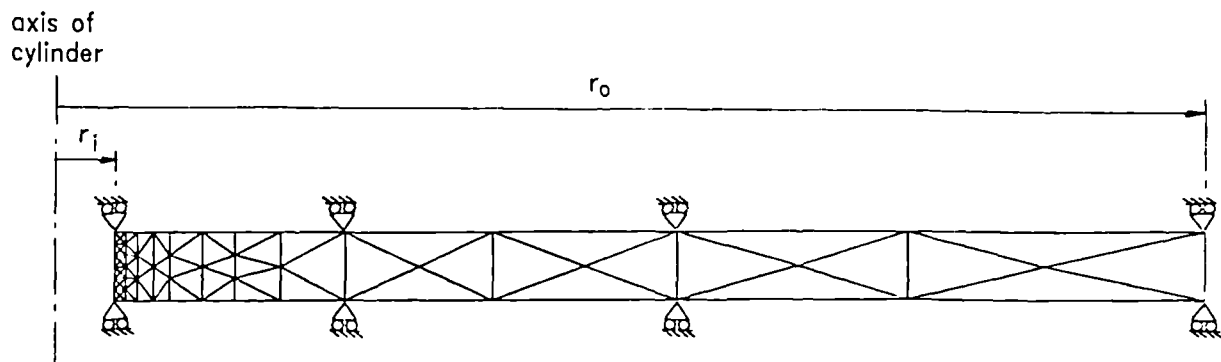


Figure 6.1(a) Finite element mesh for the thick cylinder analyses

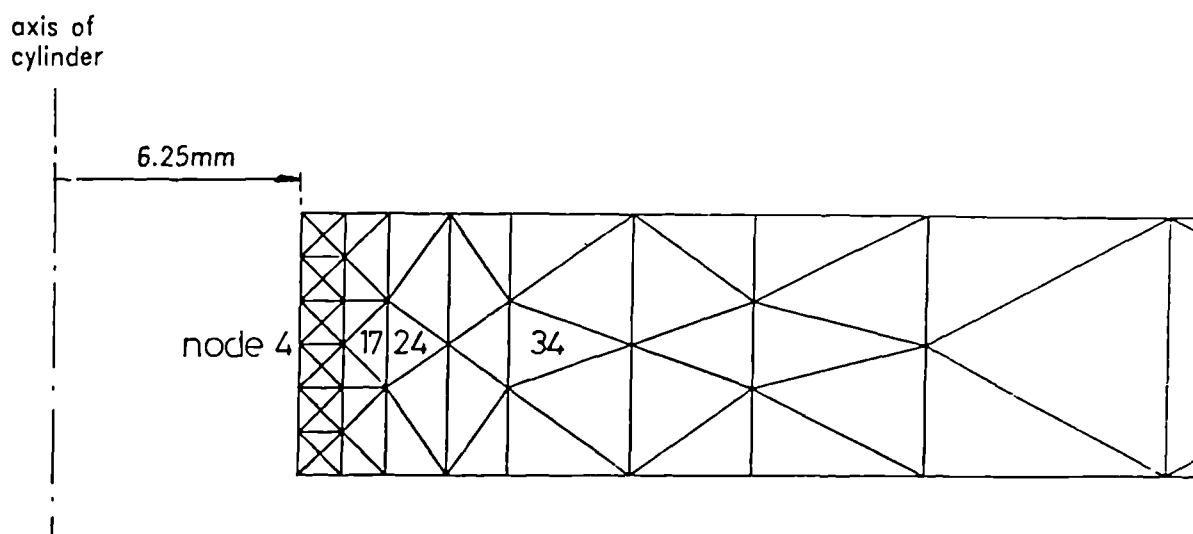


Figure 6.1(b) Detail of node and elements referred to in text close to the inner boundary of the thick cylinder

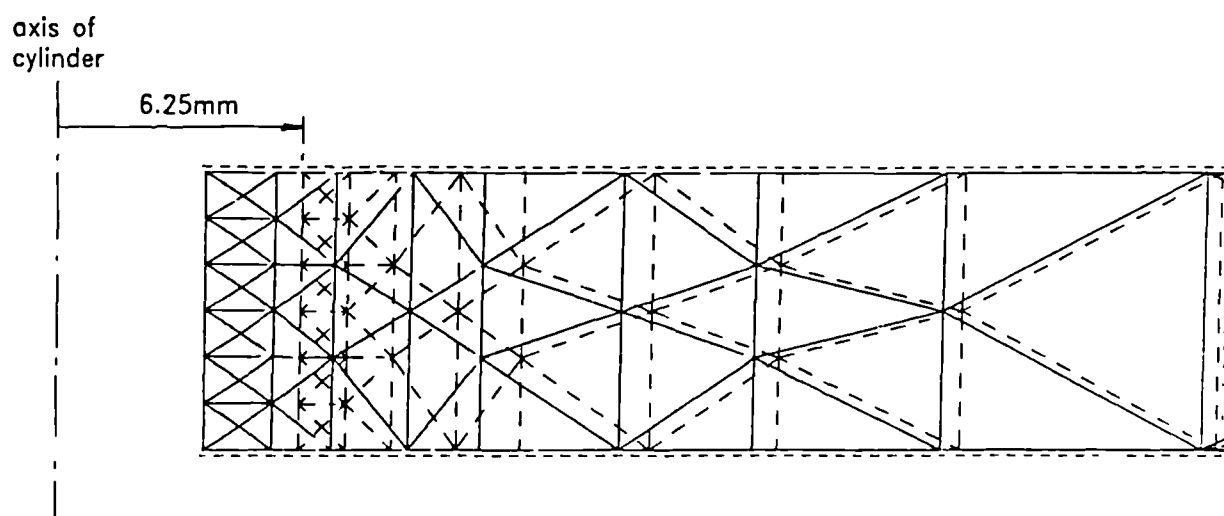


Figure 6.2(a) Deformed mesh at the end of analysis TCU1

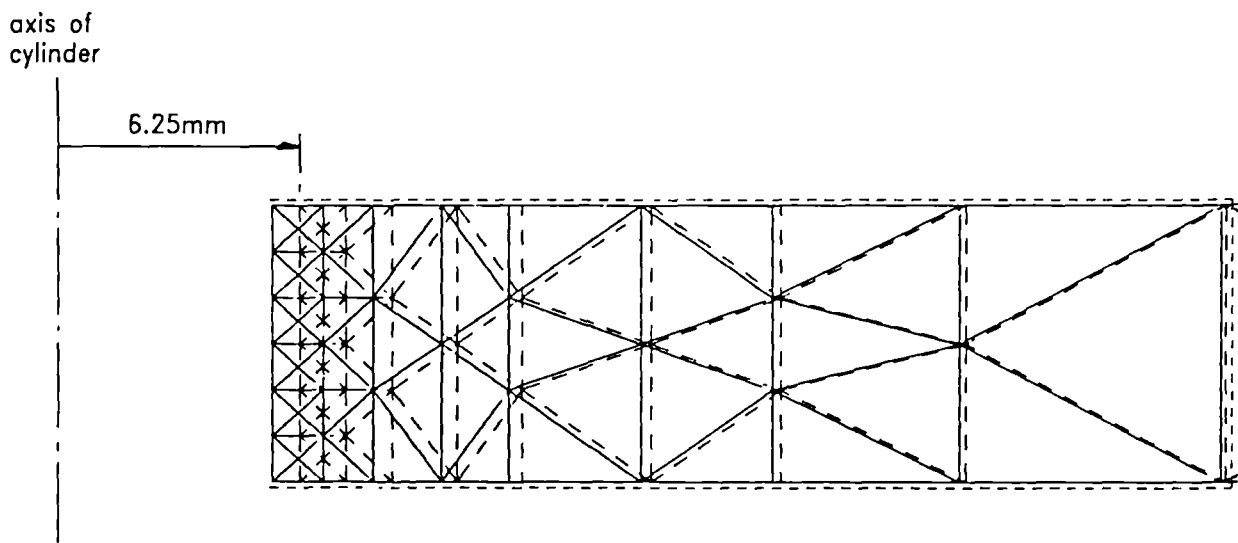


Figure 6.2(b) Deformed mesh at the end of analysis TCU2

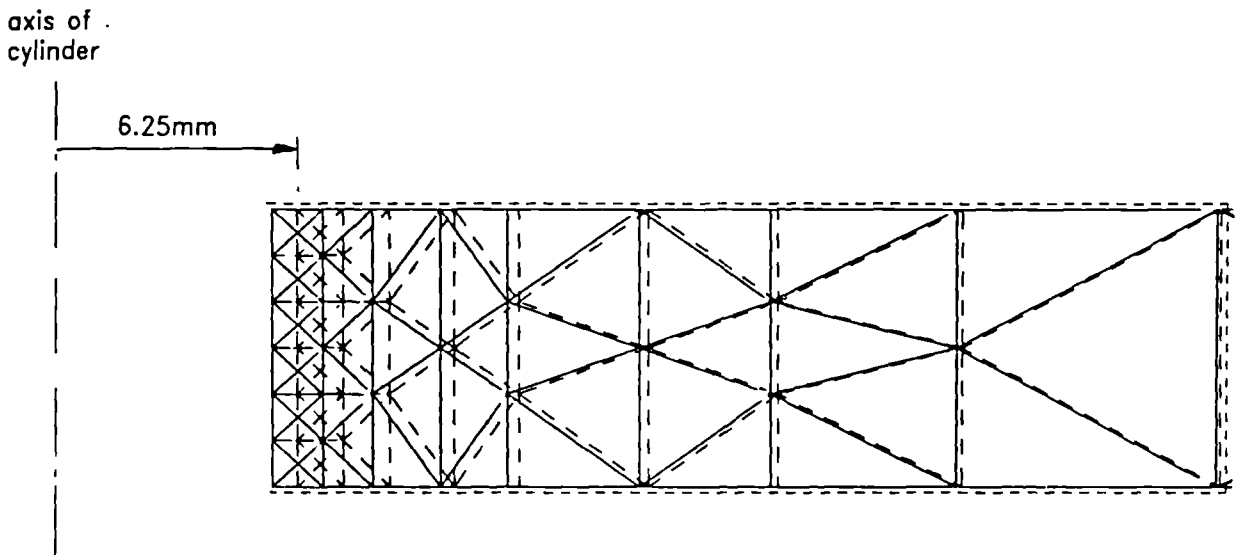


Figure 6.2(c) Deformed mesh at the end of analysis TCU3

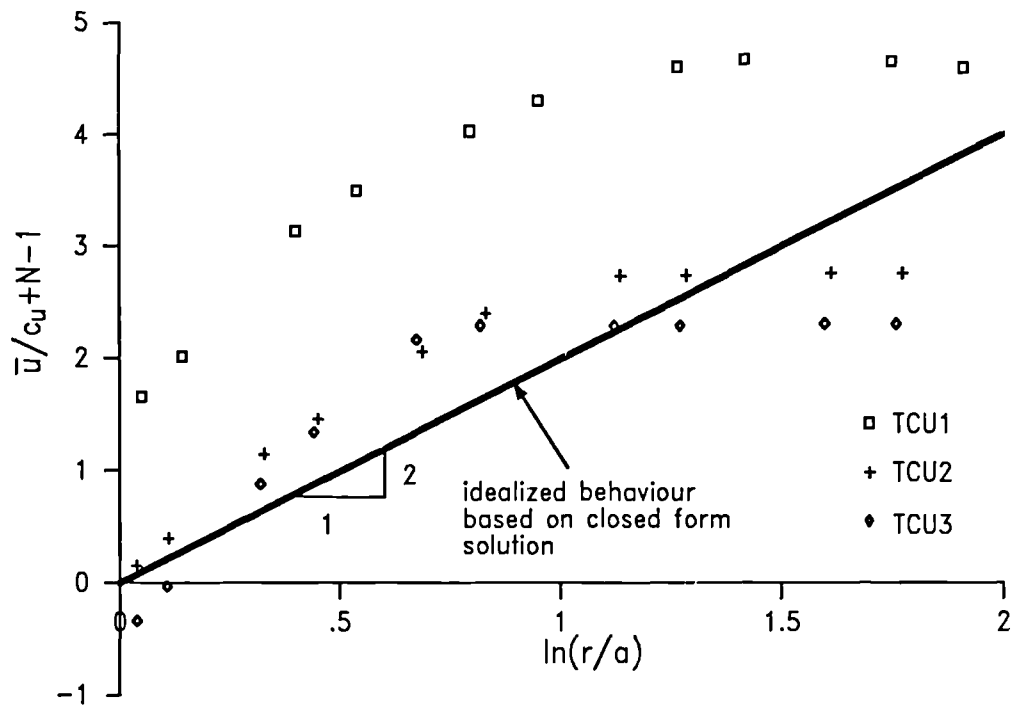


Figure 6.3(a) Predicted pore pressure changes at the end of undrained removal of support pressure at the inner radius of the thick cylinder from analyses using K_w of about $100K'$

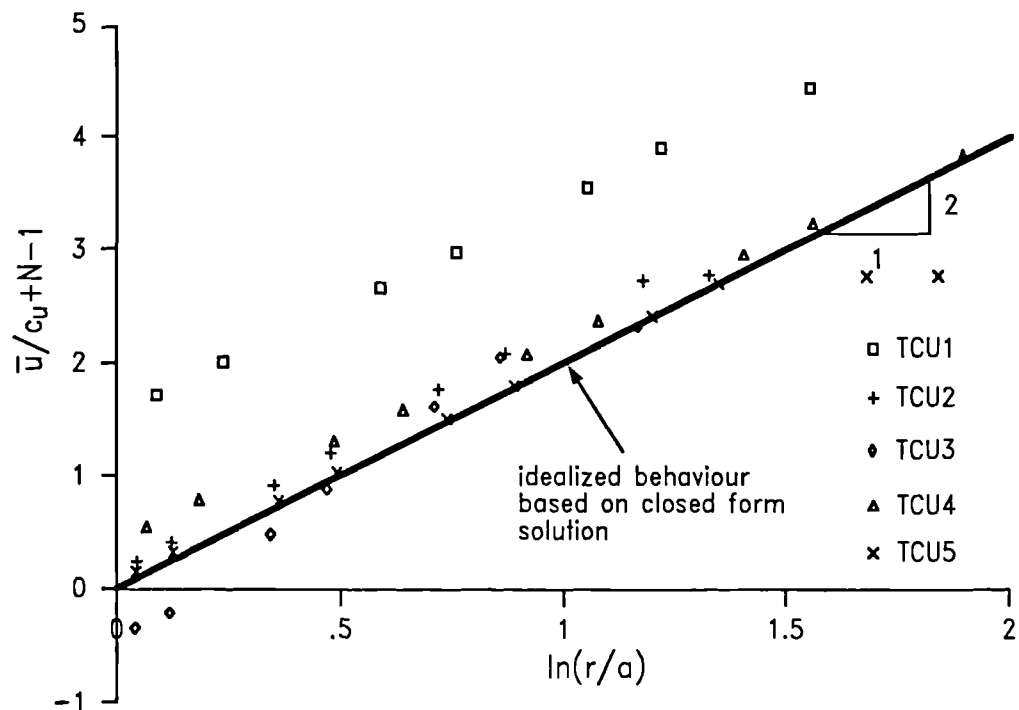


Figure 6.3(b) Predicted pore pressure changes at the end of undrained removal of support pressure at the inner radius of the thick cylinder from analyses using K_w of about $10K'$

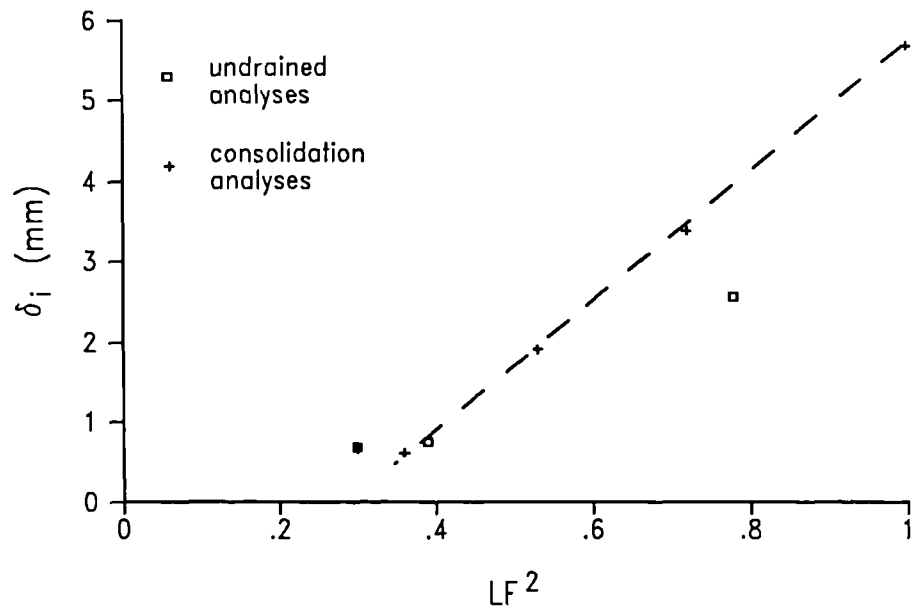


Figure 6.4 Initial deformation of the inner boundary at the end of the removal of support pressure as function of load factor

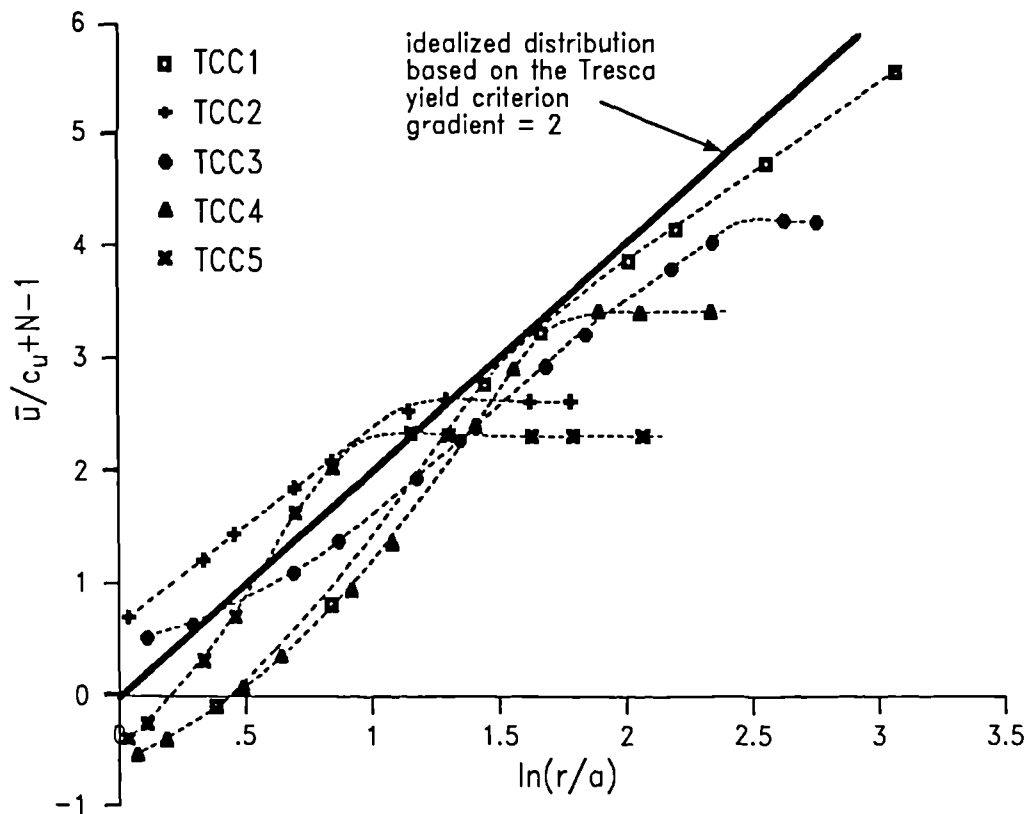


Figure 6.5 Comparison of predicted pore pressure changes at the end of the removal of support pressure at the inner radius in the thick cylinder consolidation analyses

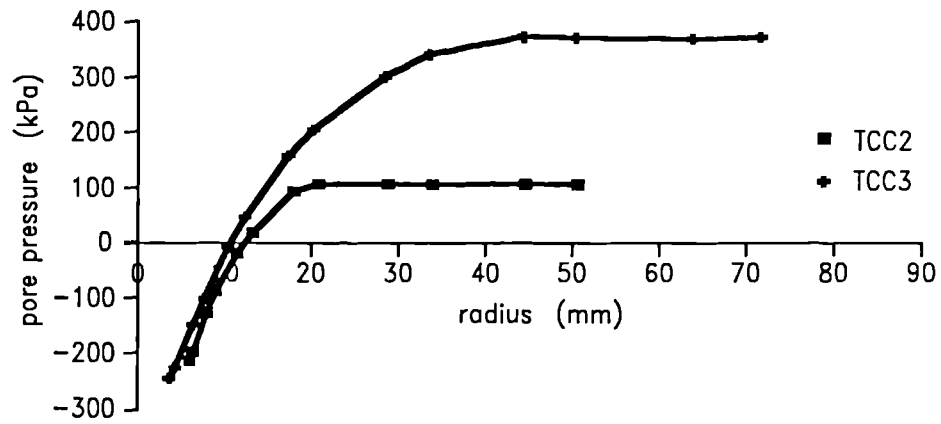


Figure 6.6(a) Pore pressure distribution at the end of removal of face support pressure $t=0.3$ seconds

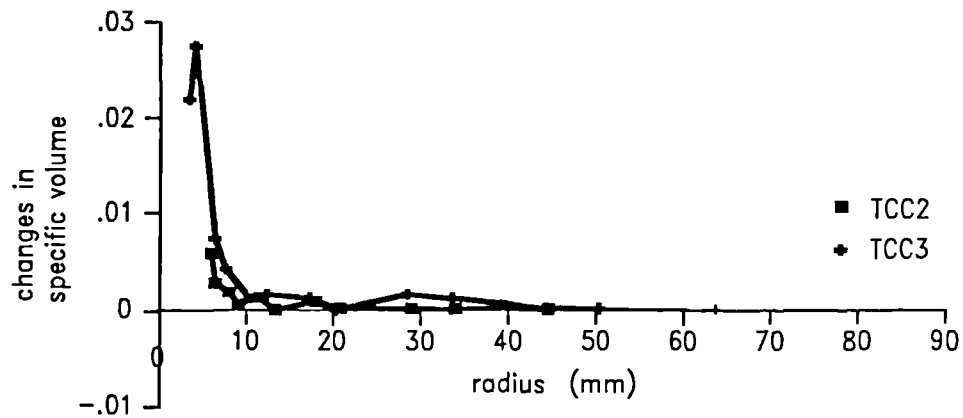


Figure 6.6(b) Changes in specific volume at the end of removal of face support pressure $t=0.3$ seconds

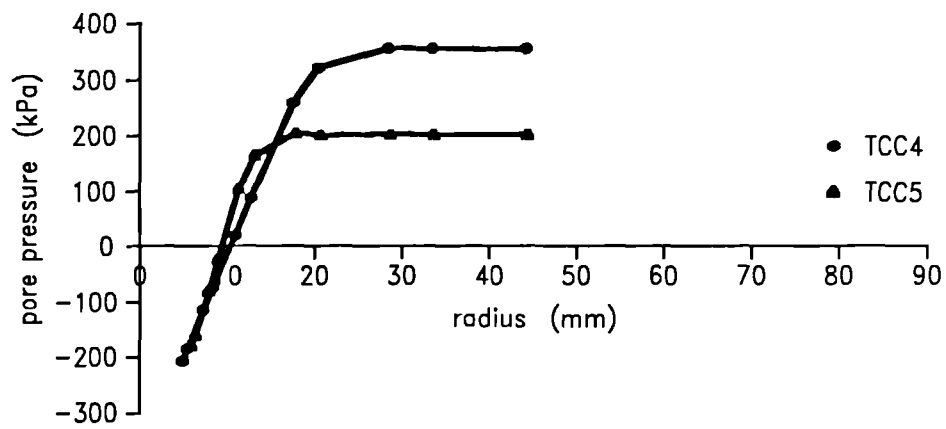


Figure 6.7(a) Pore pressure distribution at the end of removal of face support pressure $t=0.3$ seconds

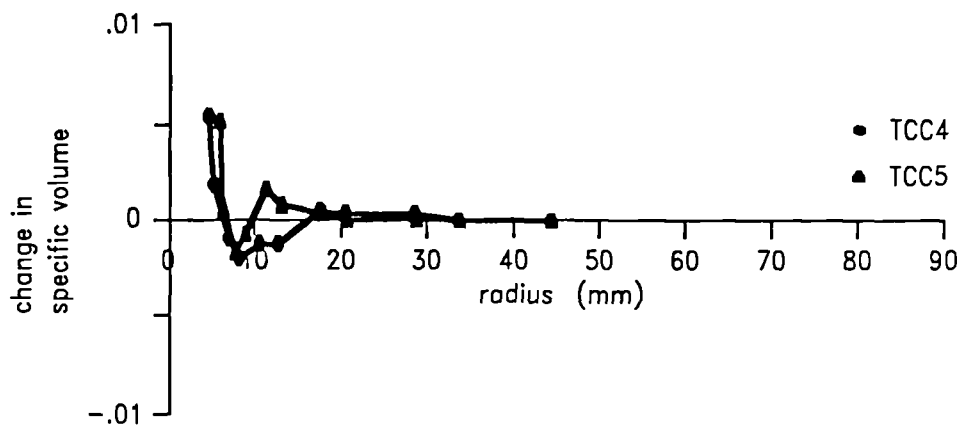


Figure 6.7(b) Changes in specific volume at the end of removal of face support pressure $t=0.3$ seconds

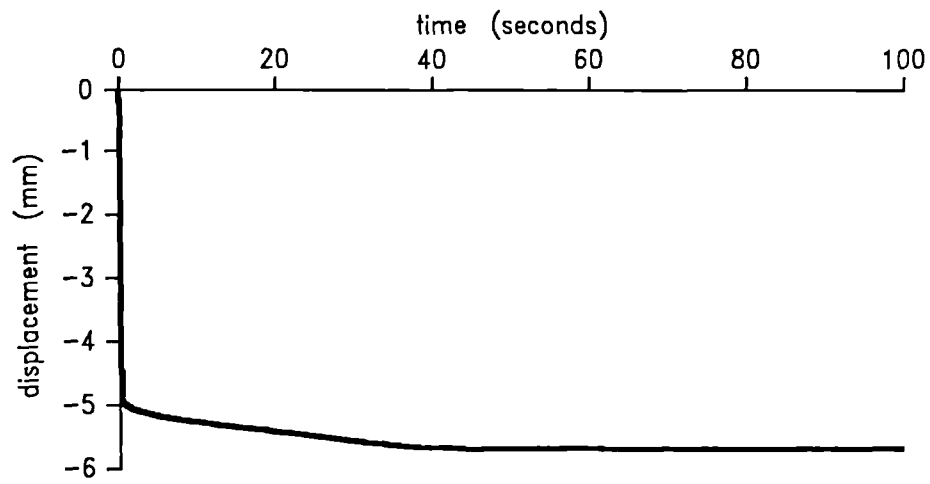


Figure 6.8 Predicted deformation at node 4 on the inner boundary from thick cylinder consolidation analysis TCC1

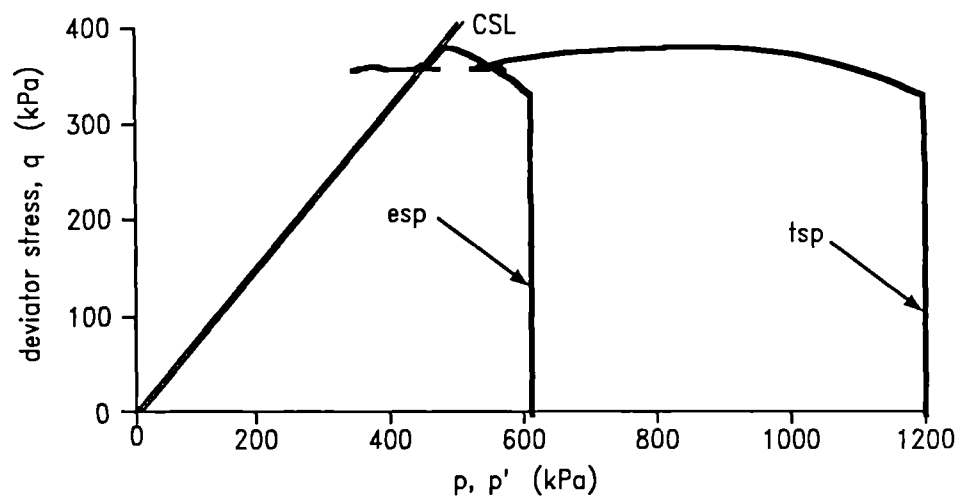


Figure 6.9 Total and effective stress paths predicted for element 17 in thick cylinder consolidation analysis TCC1

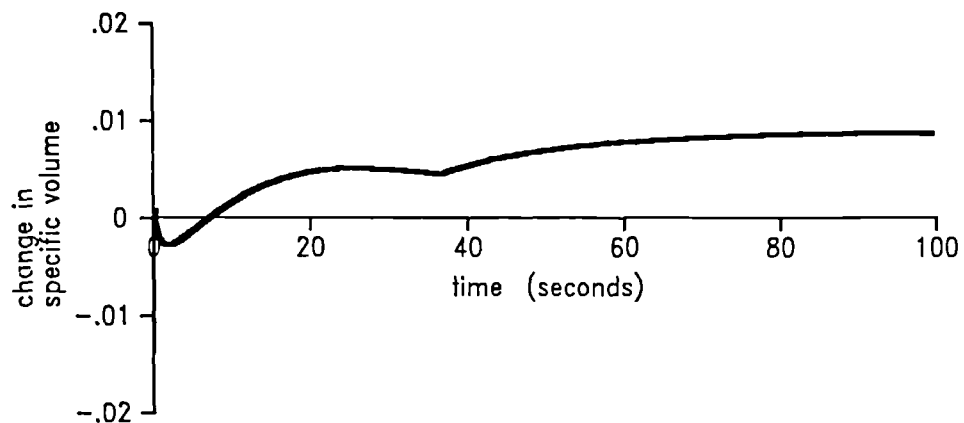


Figure 6.10 Predicted specific volume change for element 17 from thick cylinder consolidation analysis TCC1

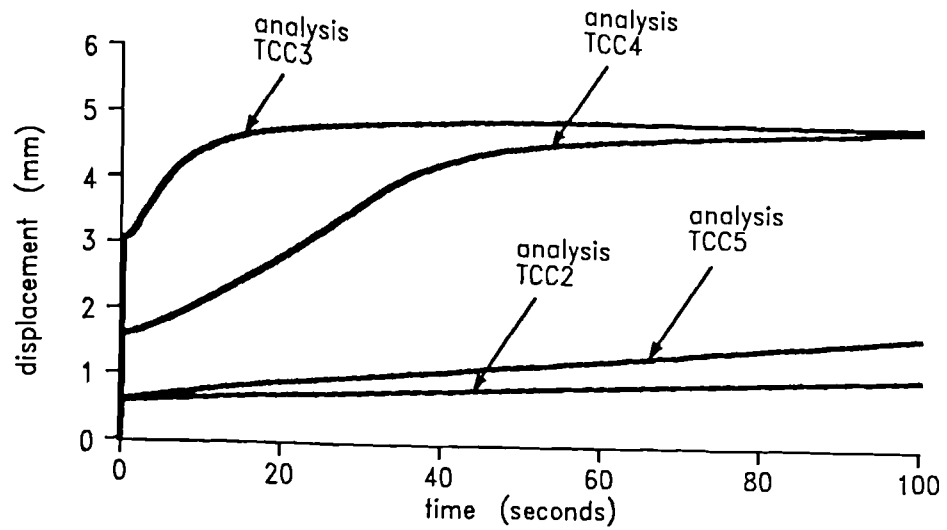


Figure 6.11(a) Deformation at inner boundary (node 4) during thick cylinder consolidation analyses

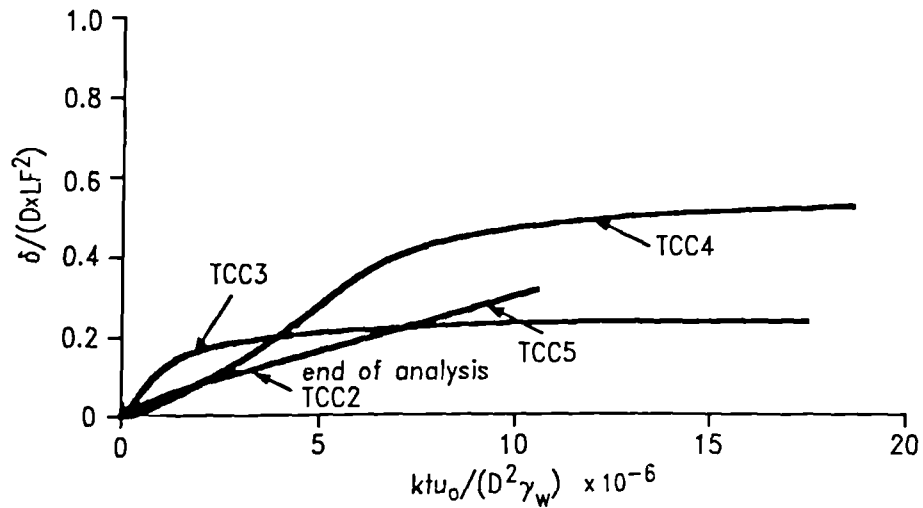


Figure 6.11(b) Deformation at node 4 on the inner boundary plotted in non-dimensional groups

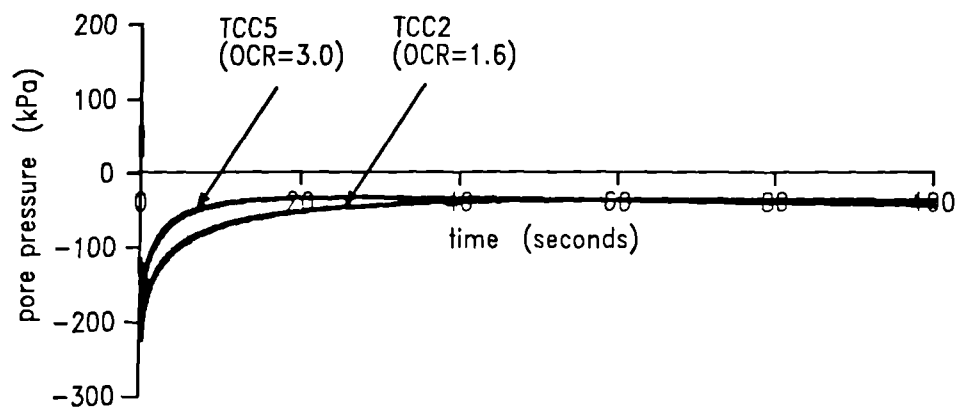


Figure 6.12 Predicted pore pressure response at node 4 on the inner radius of the thick cylinder from analyses with different initial OCR values

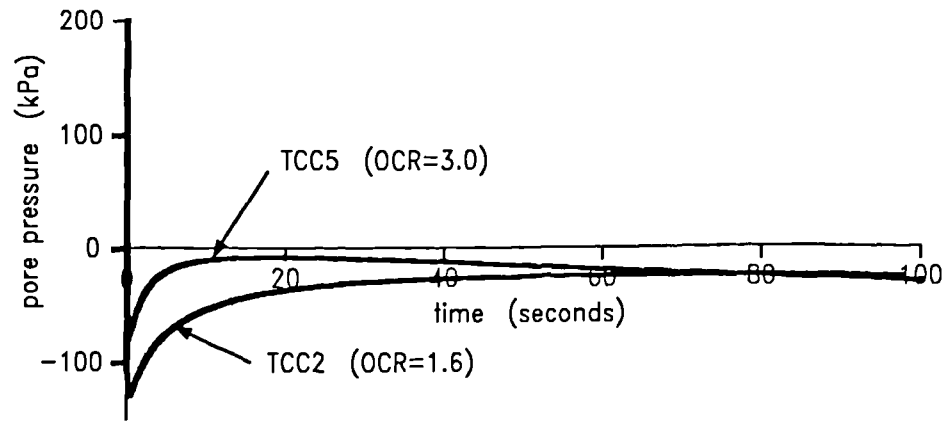


Figure 6.13 Predicted pore pressure response at element 17 from analyses with different initial OCR values

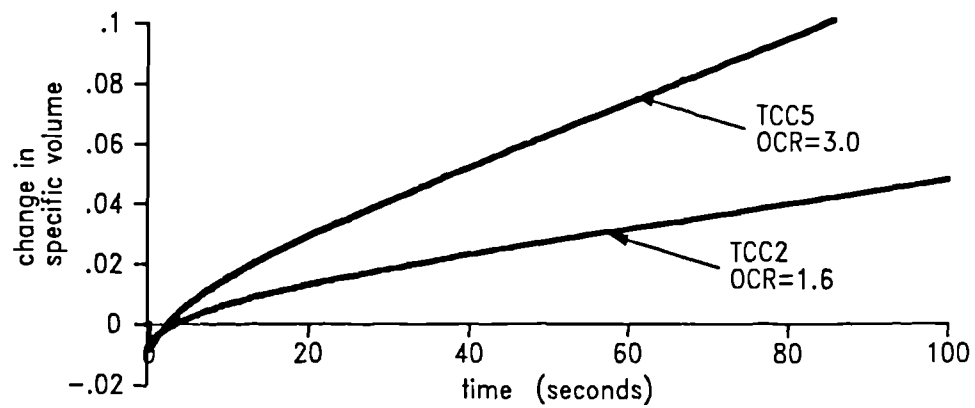


Figure 6.14 Comparison of specific volume changes at element 17 from analyses with different initial OCR values

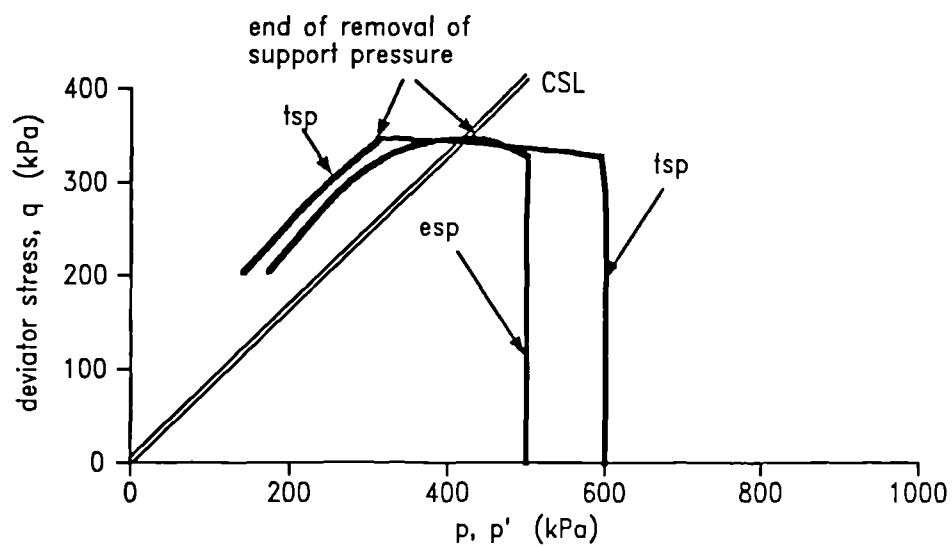


Figure 6.15(a) Total and effective stress paths predicted at element 17 in analysis TCC2

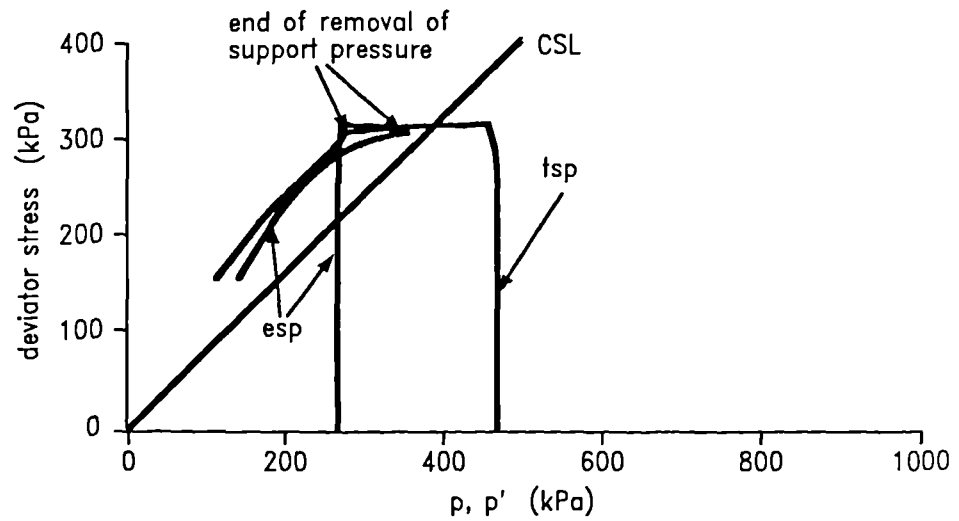


Figure 6.15(b) Total and effective stress paths predicted at element 17 in analysis TCC5

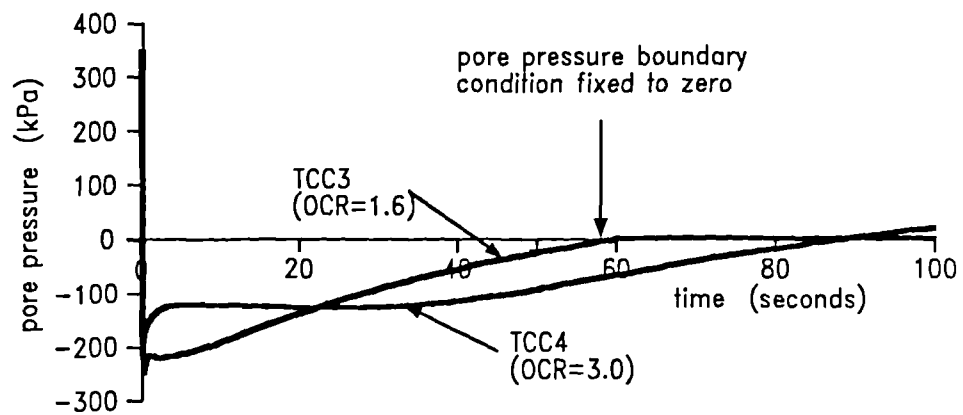


Figure 6.16 Predicted pore pressure response at node 4 on the inner radius of the thick cylinder from analyses with different initial OCR values

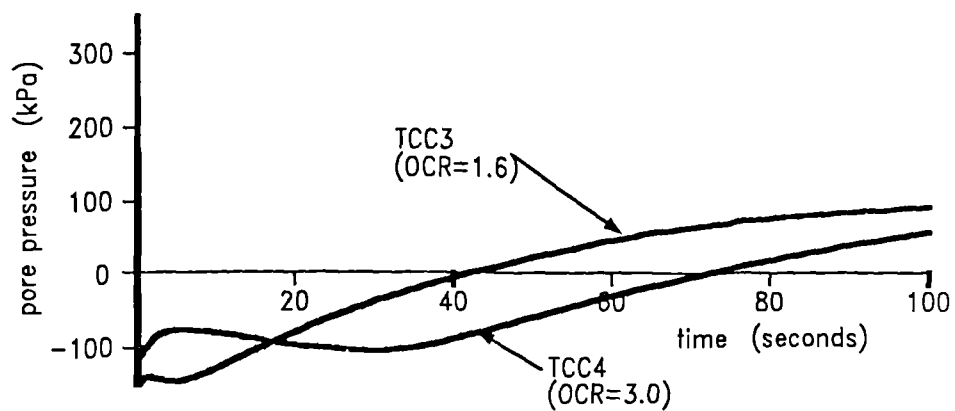


Figure 6.17 Predicted pore pressure response at element 17 from analyses with different initial OCR values

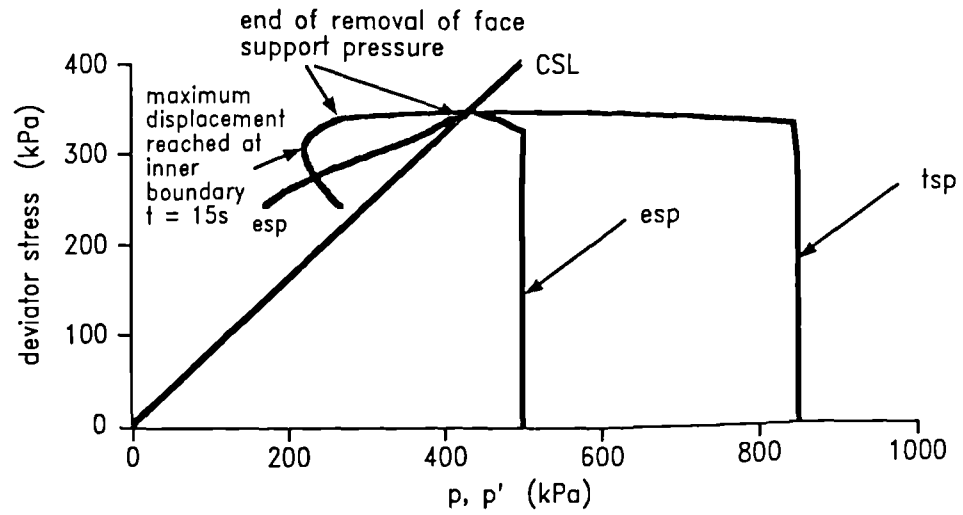


Figure 6.18(a) Total and effective stress paths predicted for element 17 in analysis TCC3

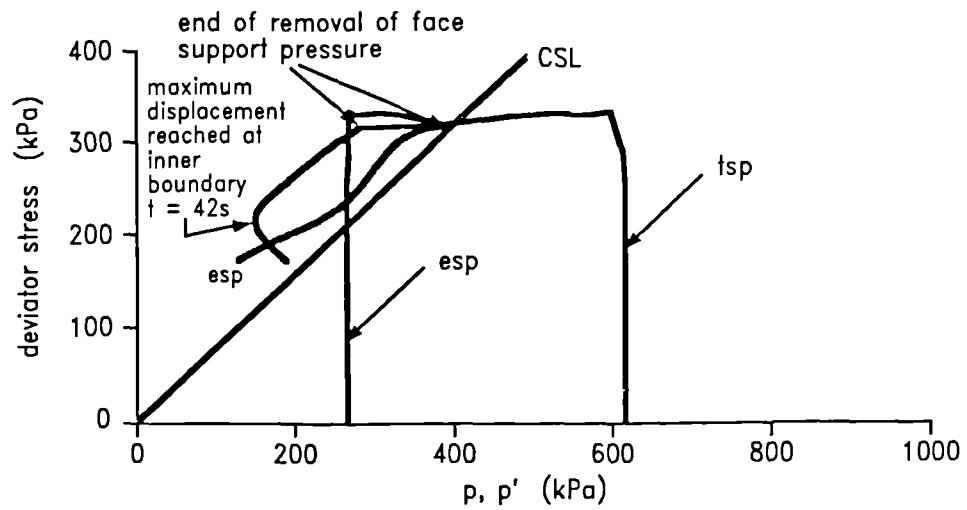


Figure 6.18(b) Total and effective stress paths predicted for element 17 in analysis TCC4

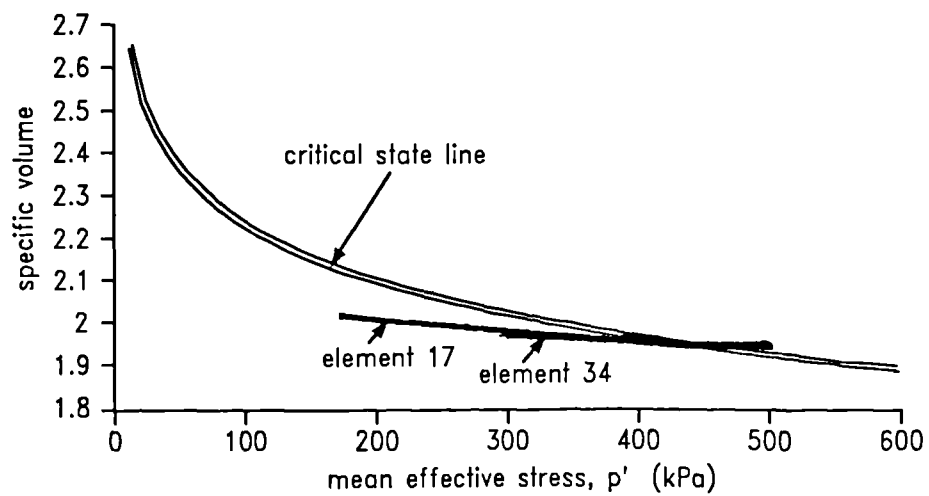


Figure 6.19 Specific volume changes at elements 17 and 34 in analysis TCC3 showing dry of critical behaviour

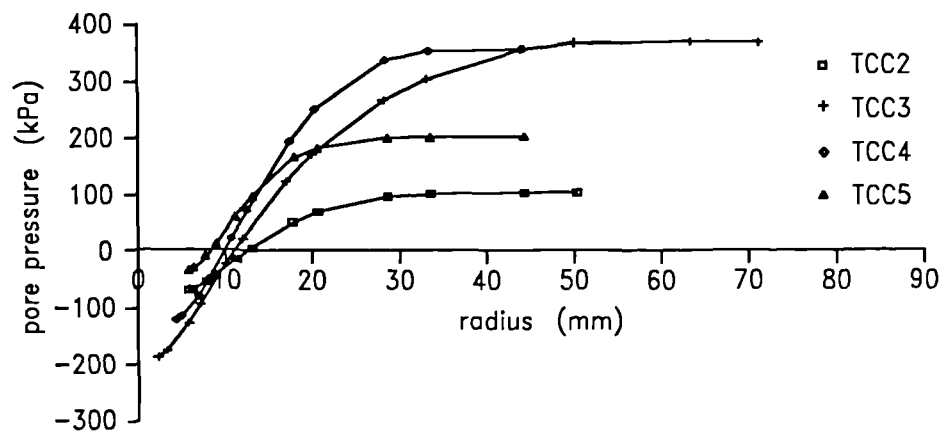


Figure 6.20(a) Pore pressure distribution at $t=10$ seconds

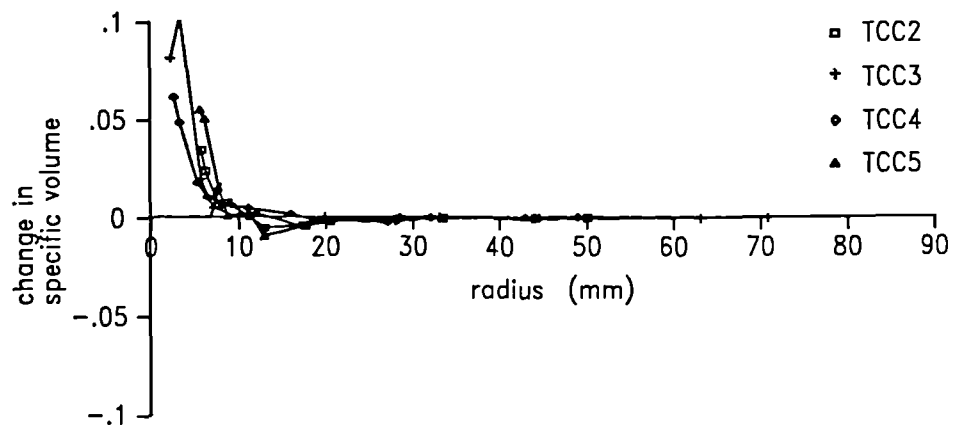


Figure 6.20(b) Specific volume changes at $t=10$ seconds

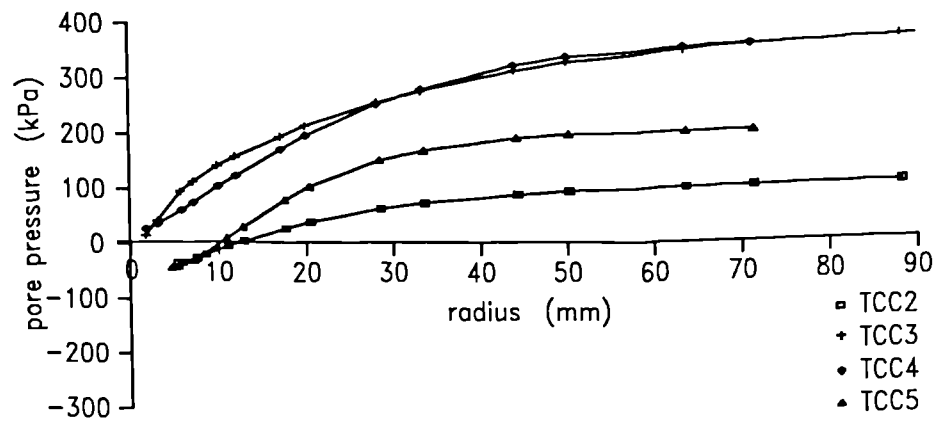


Figure 6.20(c) Pore pressure distribution at $t=100$ seconds

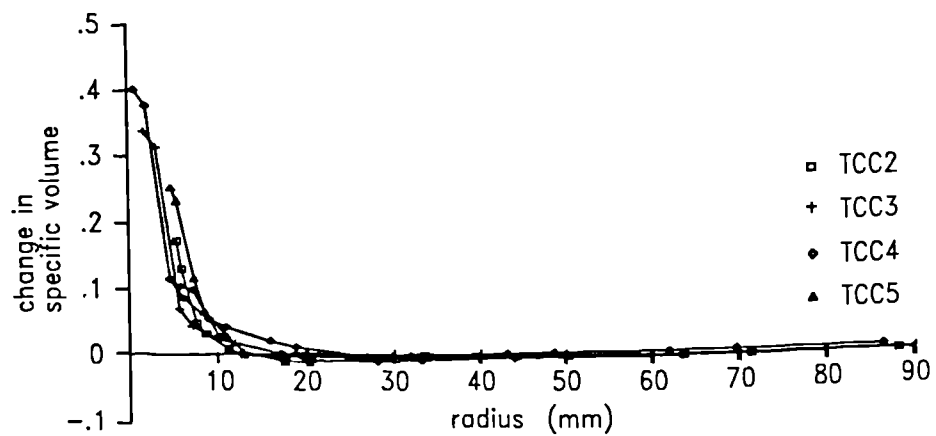


Figure 6.20(d) Specific volume changes at $t=100$ seconds

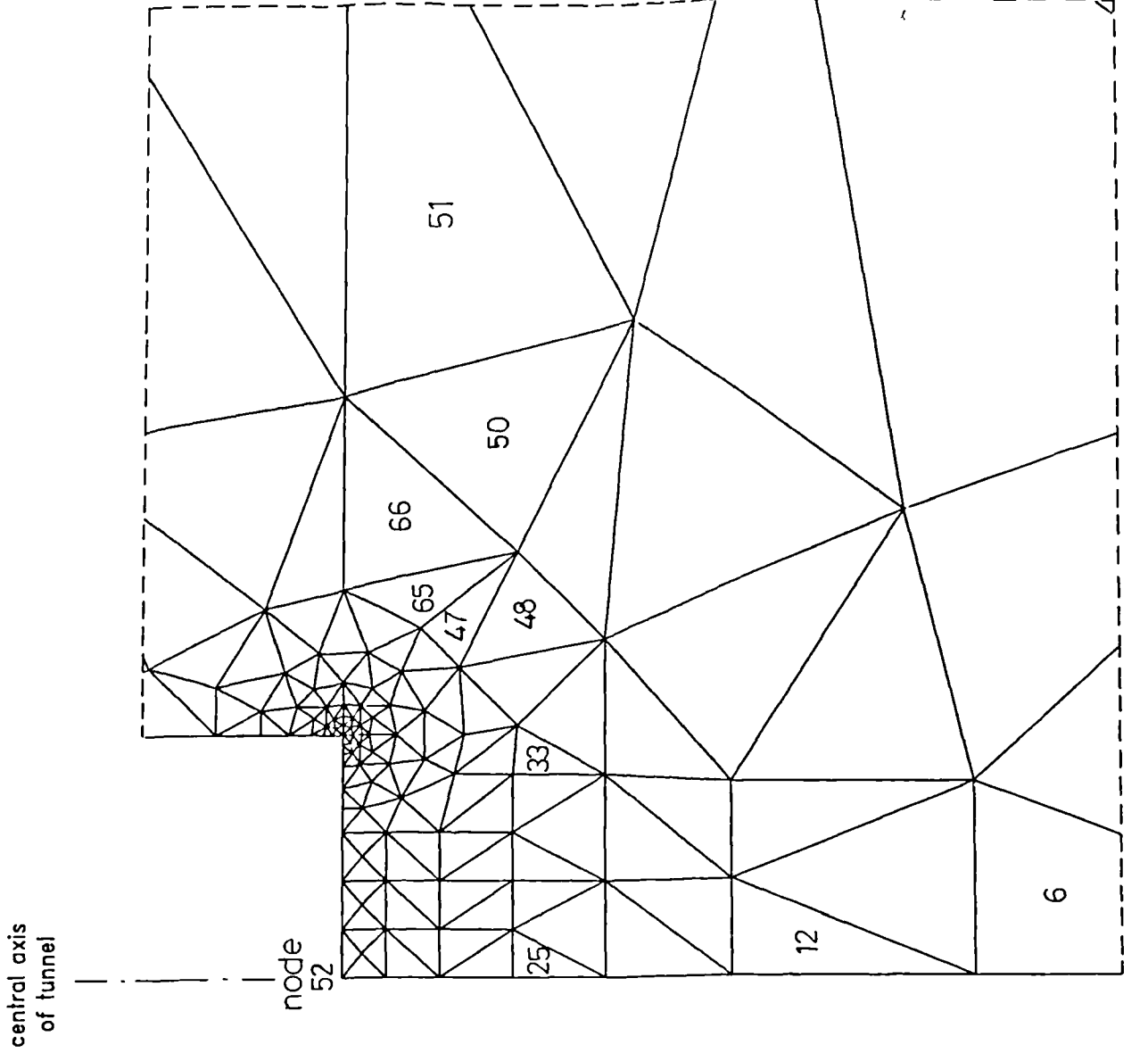


Figure 7.1(a) Mesh used in 50mm diameter tunnel analyses

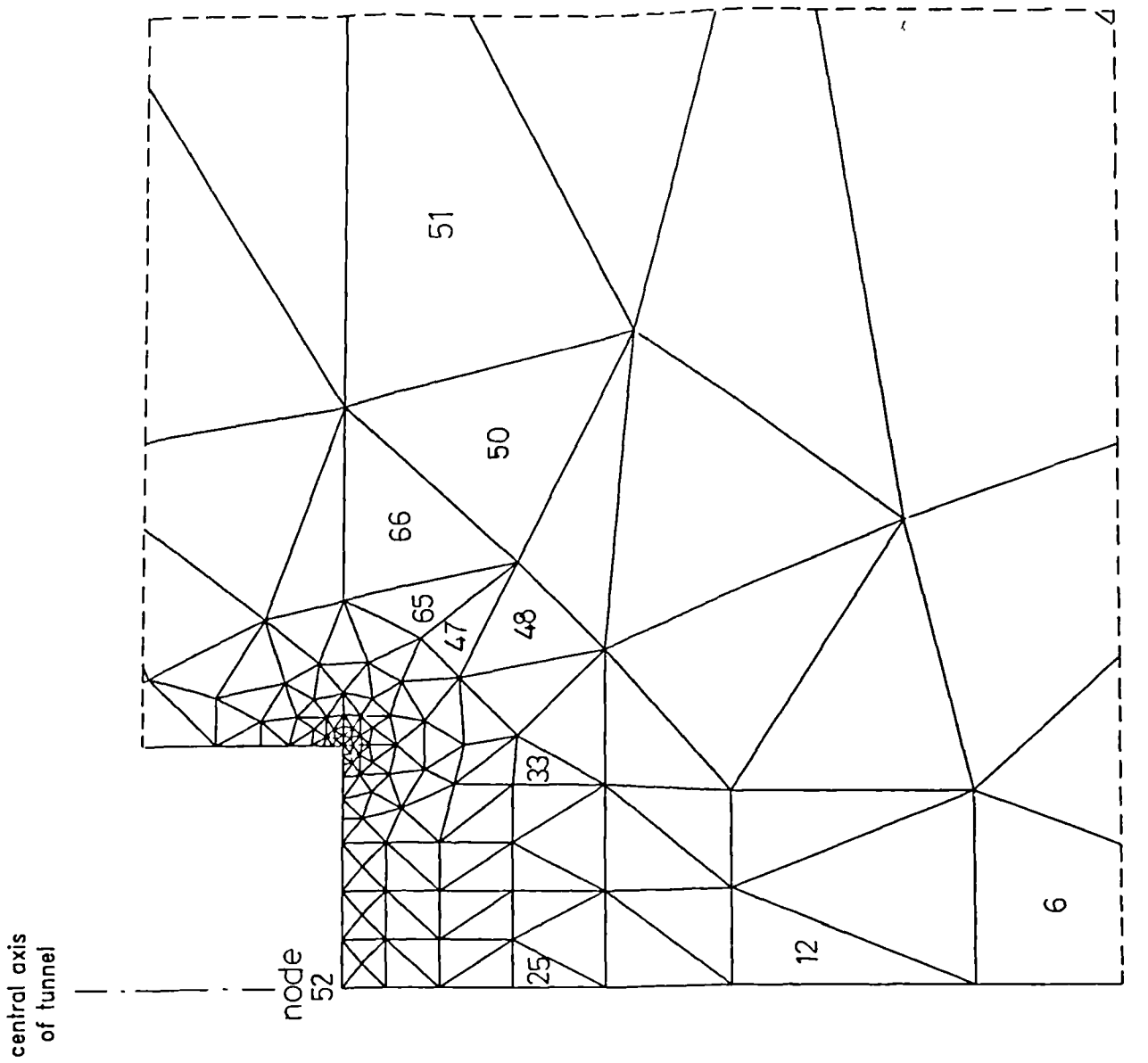


Figure 7.1(b) Detail of element layout close to tunnel face

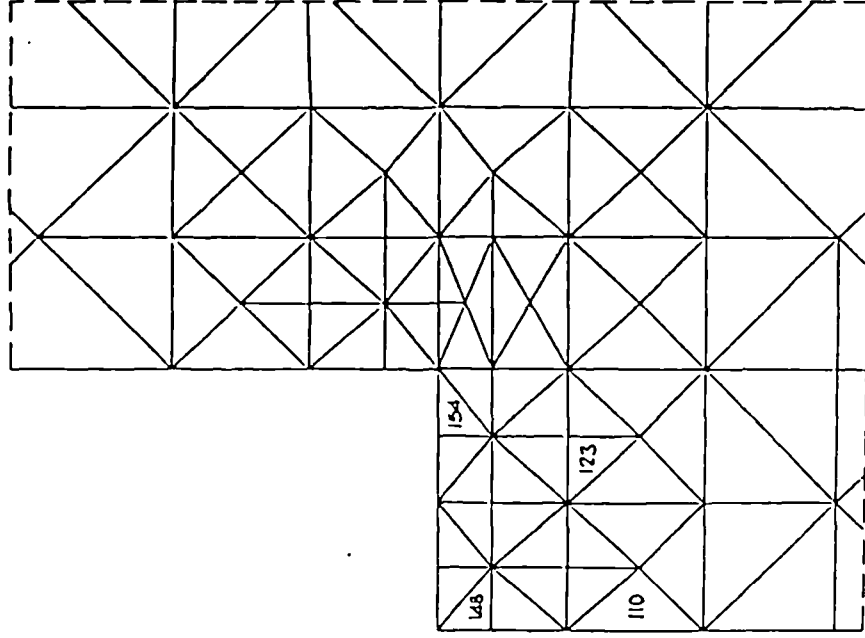


Figure 7.2(a) Mesh used in preliminary model tunnel test analyses

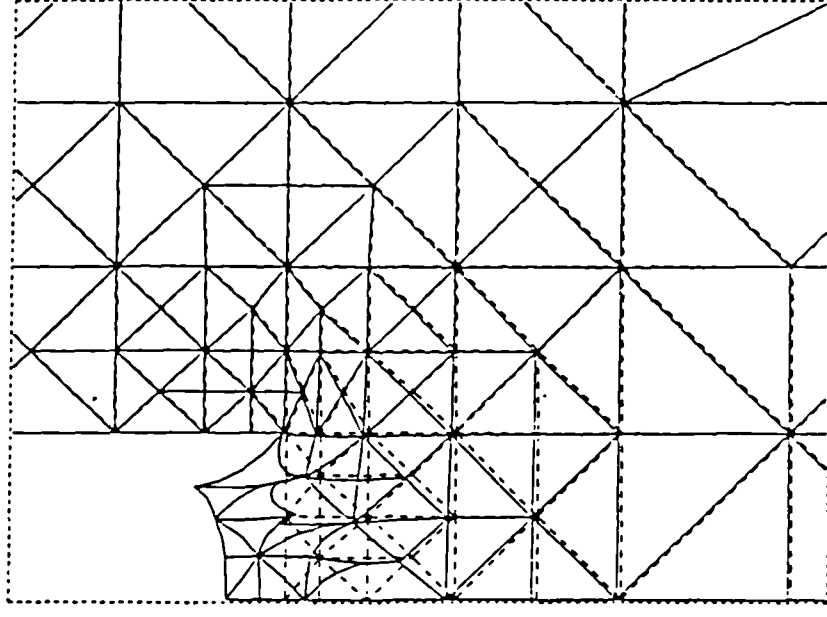


Figure 7.2(b) Deformation predicted at tunnel face from analyses using preliminary mesh

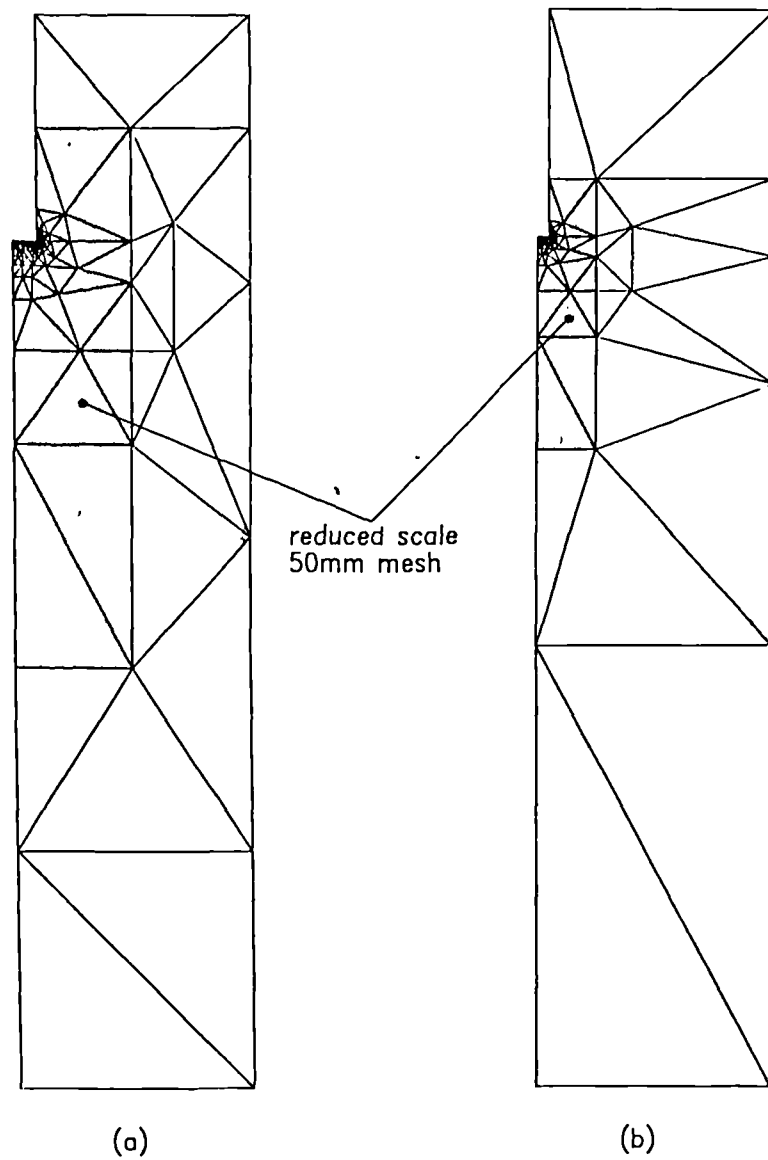


Figure 7.3 Meshes used in 25mm and 12.5mm diameter tunnel analyses, incorporating a reduced scale 50mm diameter tunnel mesh

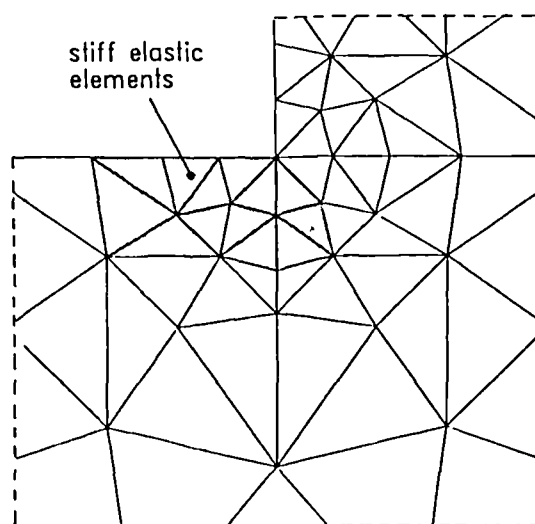
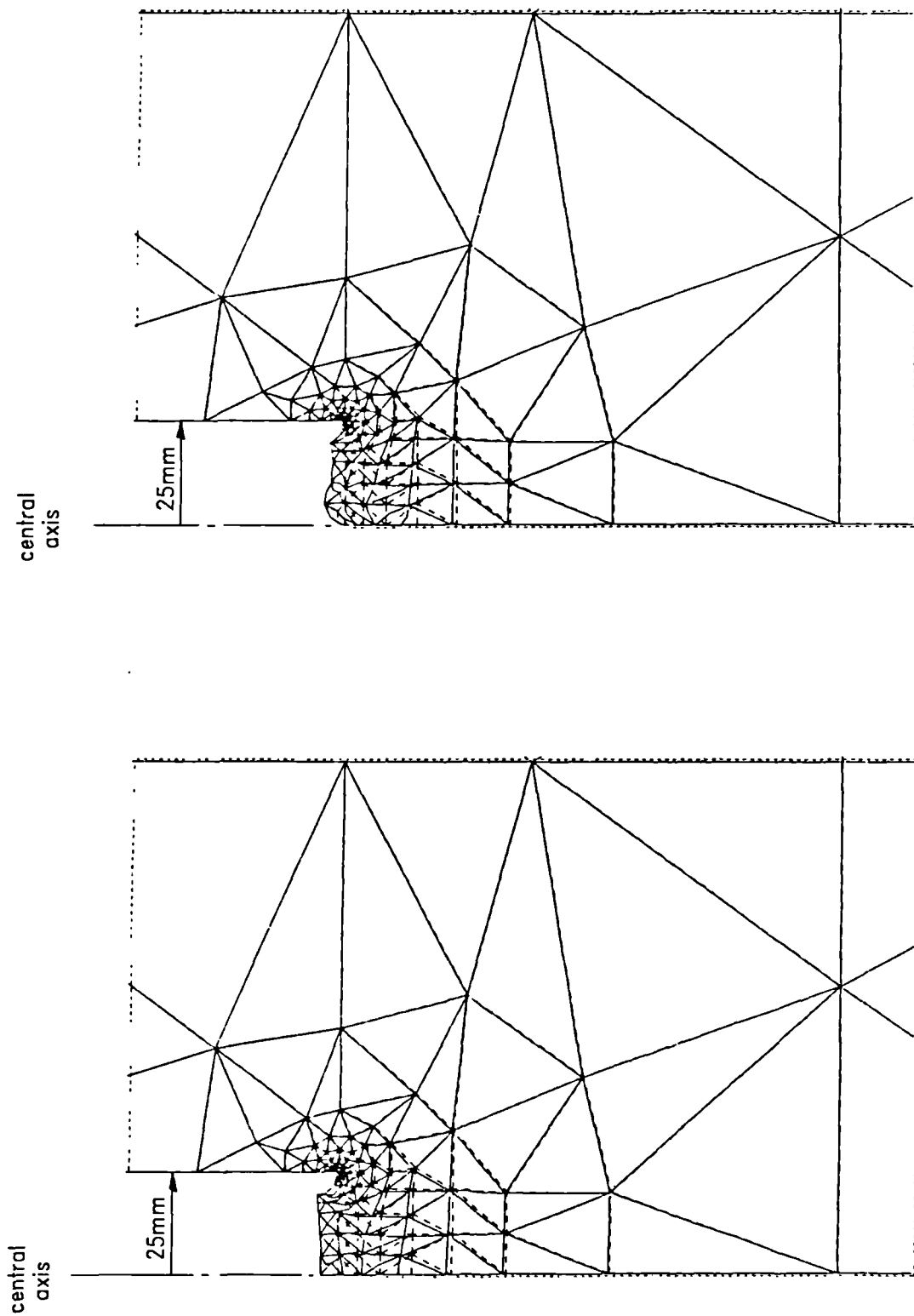


Figure 7.4 Elements affected by numerical difficulties in the modified Cam-clay analyses



(a) SI25

(b) SI13

Figure 7.5 Deformed meshes showing non-uniform distortions in analyses SI25 and SI13

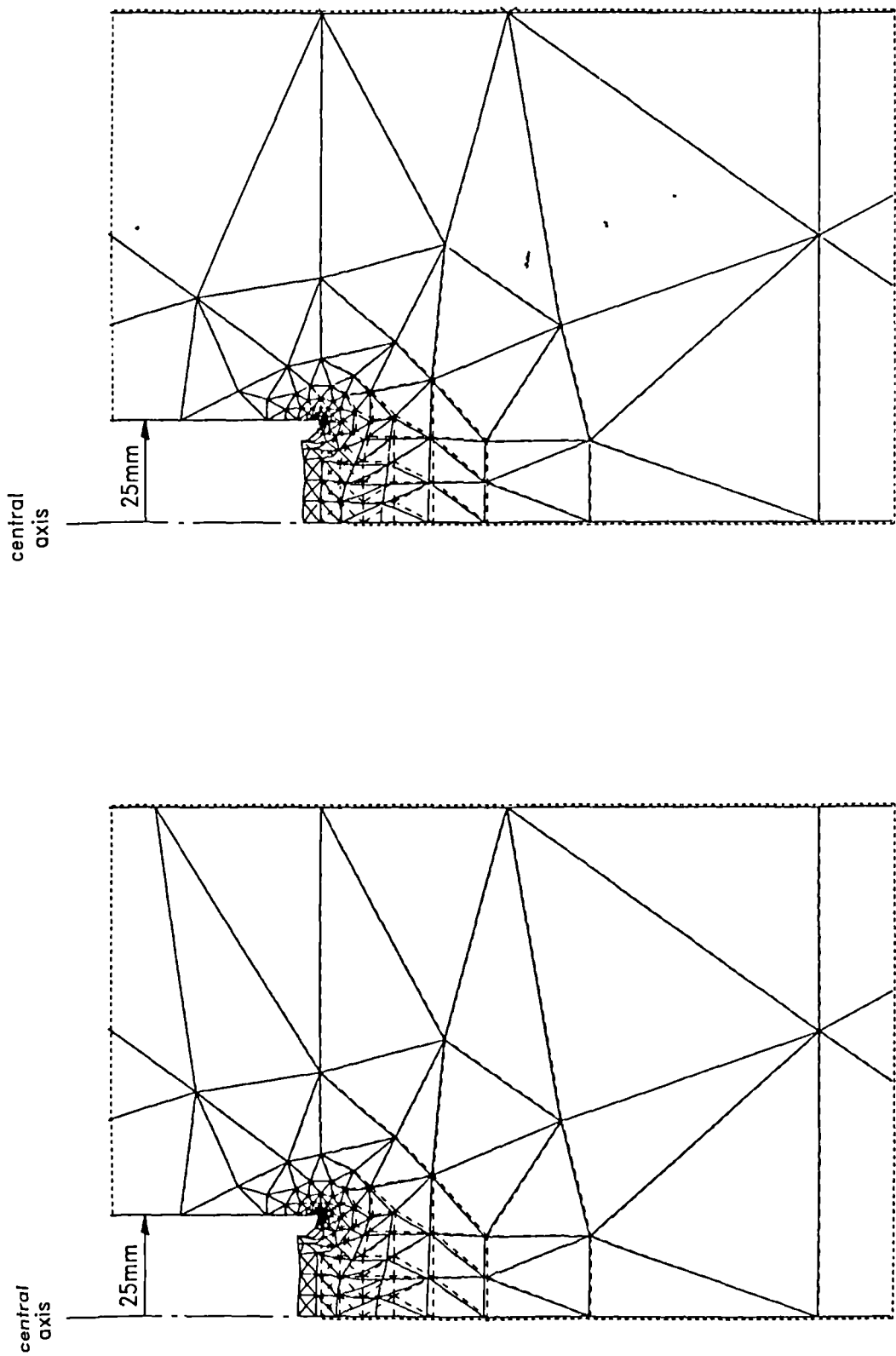


Figure 7.6 Deformed meshes and element states near the end of analyses investigating the influence of tunnel diameter

$$ktu_o/(D^2\gamma_w) = 4.4 \times 10^{-6}$$

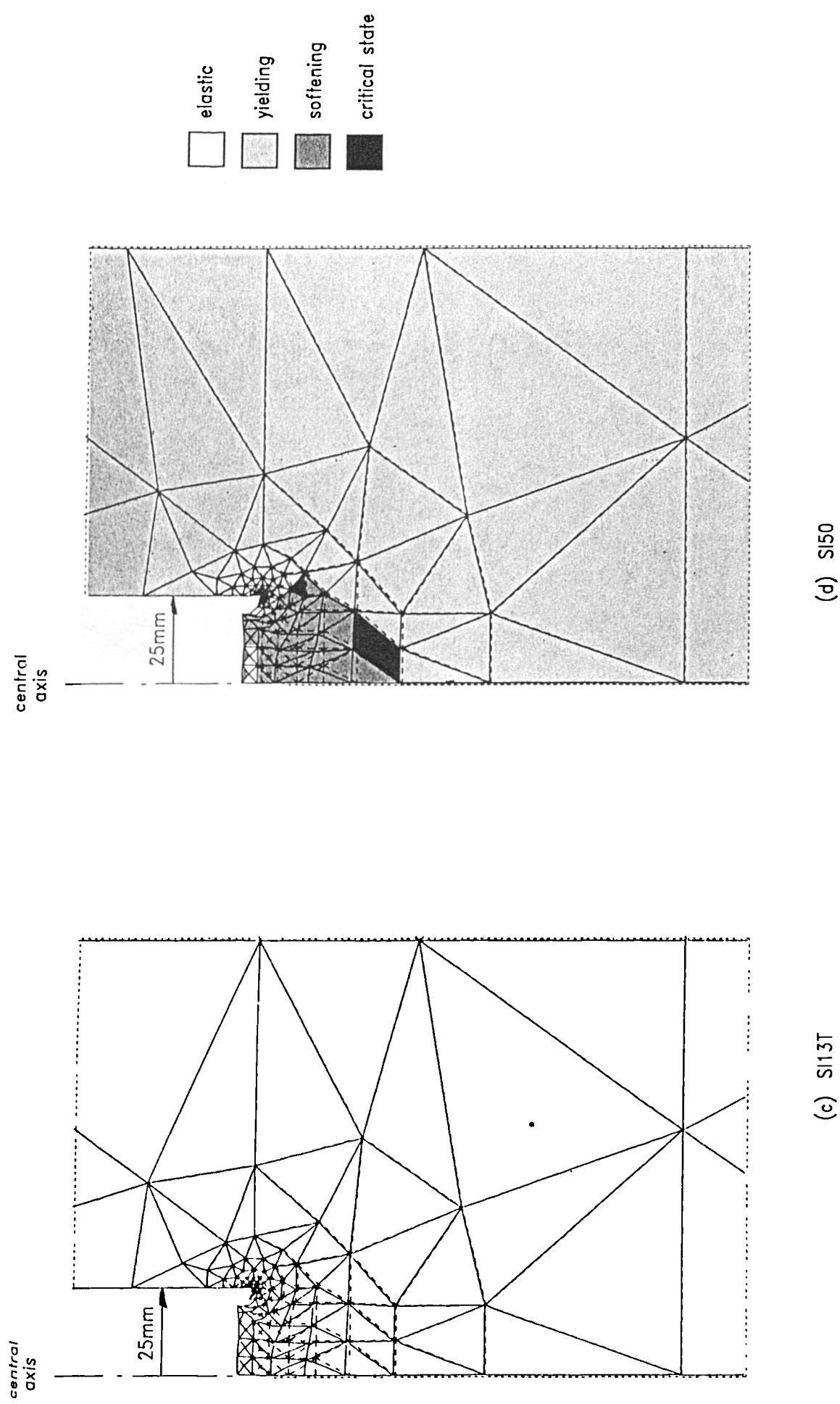


Figure 7.6 Deformed meshes and element states near the end of analyses investigating the influence of tunnel diameter

$$ktu_o/(D^2\gamma_w) = 4.4 \times 10^{-6}$$

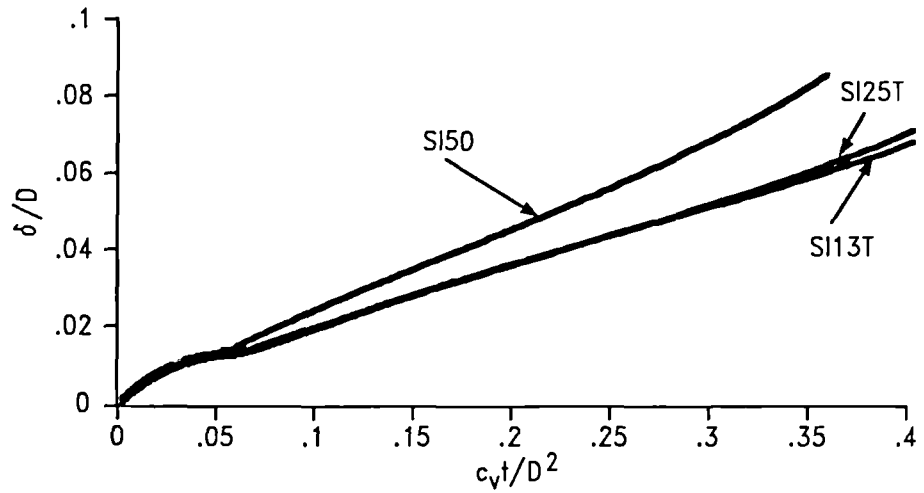


Figure 7.7 Deformation at the tunnel face from analyses of different tunnel diameters with identical initial stress states

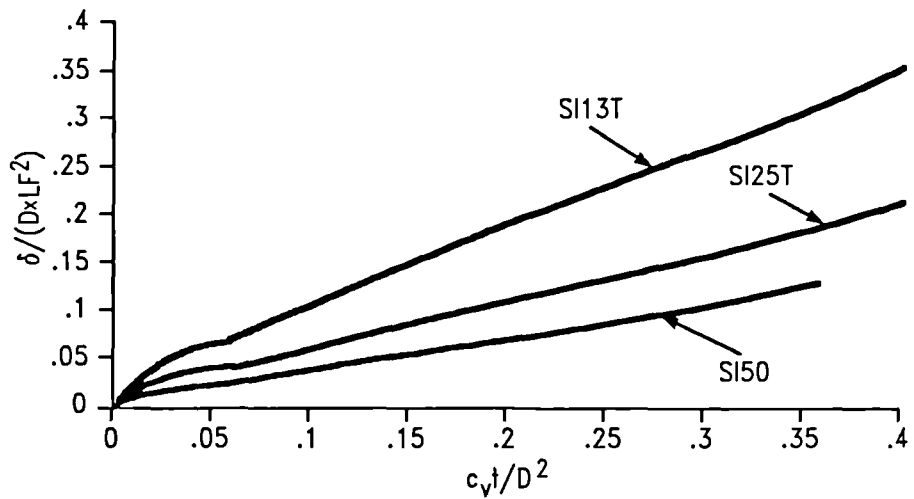


Figure 7.8 Influence of load factor on predicted tunnel face deformation for different tunnel diameters

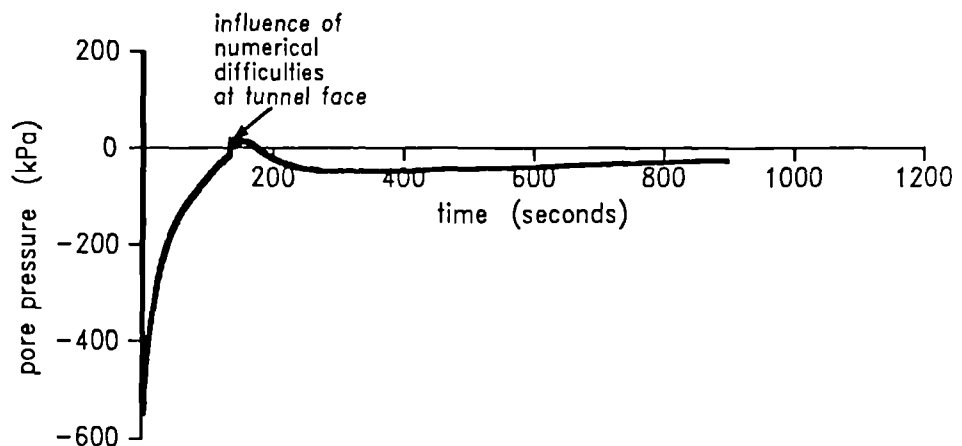


Figure 7.9 Predicted pore pressure behaviour at node 52 in analysis SI50

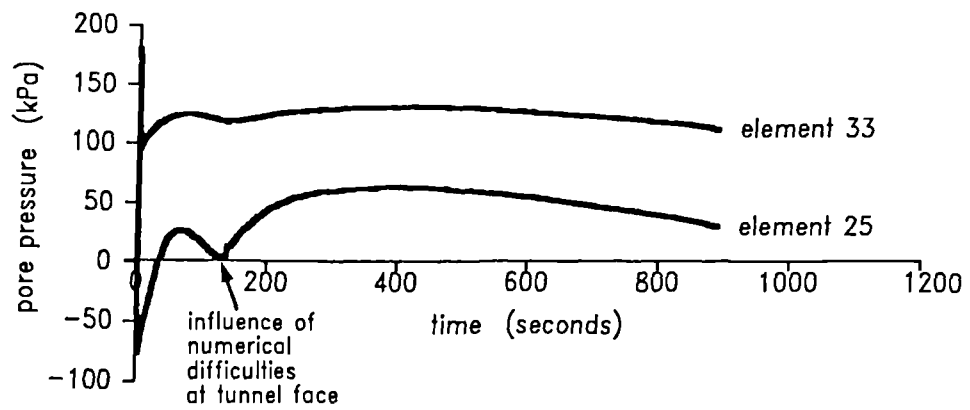


Figure 7.10 Pore pressure response with time ahead of the tunnel face in finite element analysis SI50

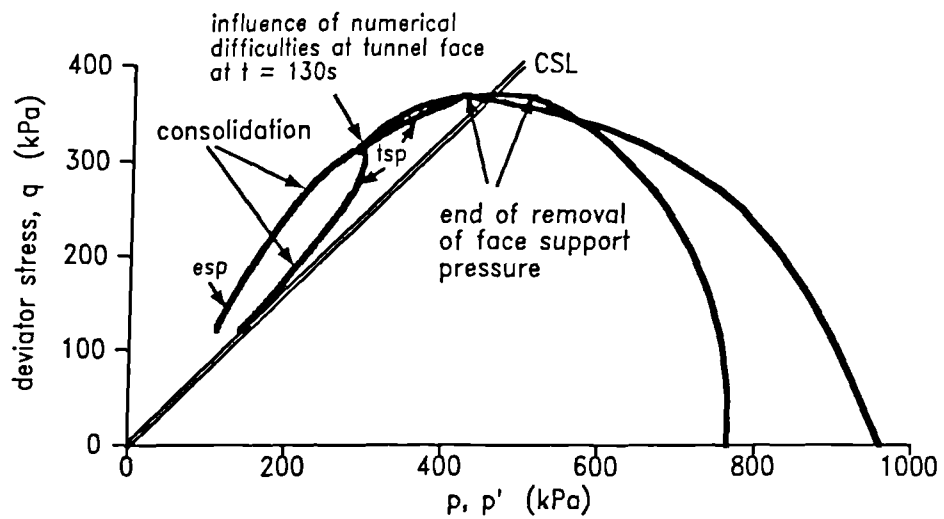


Figure 7.11 Total and effective stress paths predicted for element 25 in analysis SI50

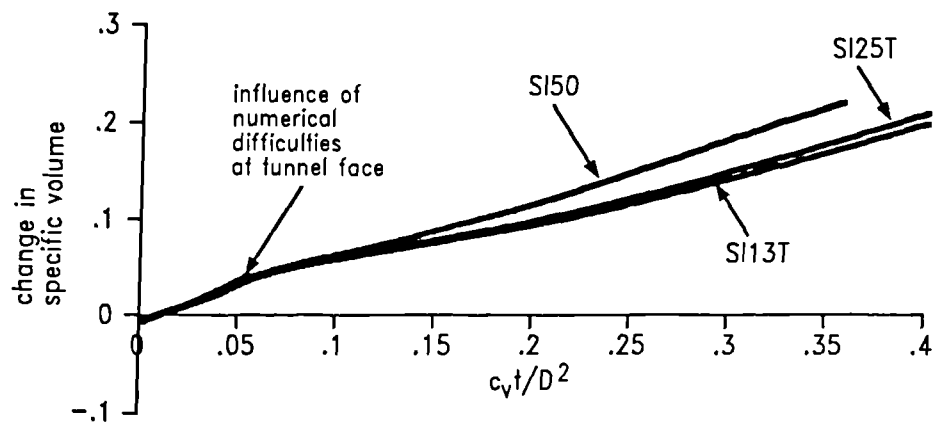


Figure 7.12 Comparison of specific volume changes predicted for element 25 from analyses of different tunnel diameters

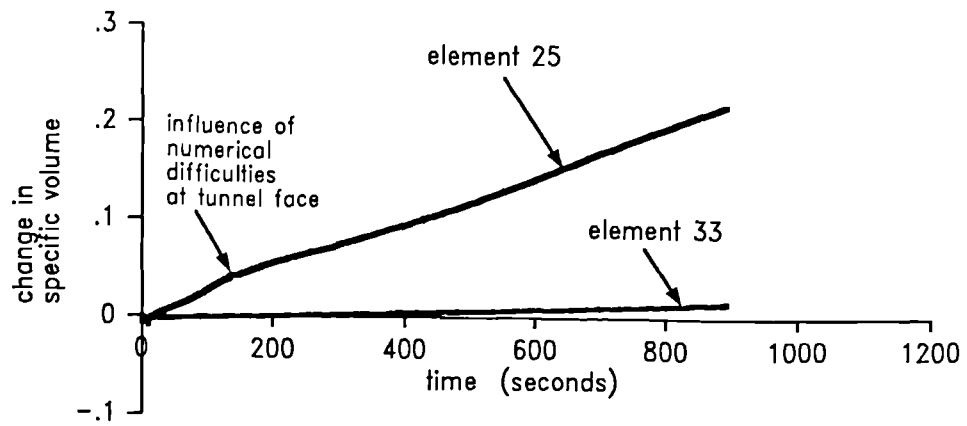


Figure 7.13 Predicted specific volume changes for elements 25 and 33 in analysis SI50

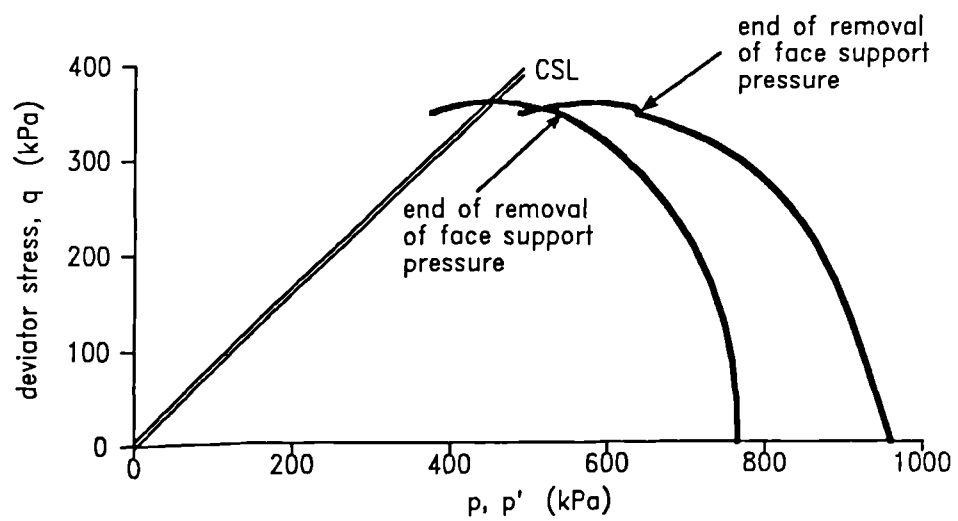


Figure 7.14 Total and effective stress paths predicted for element 33 in analysis SI50

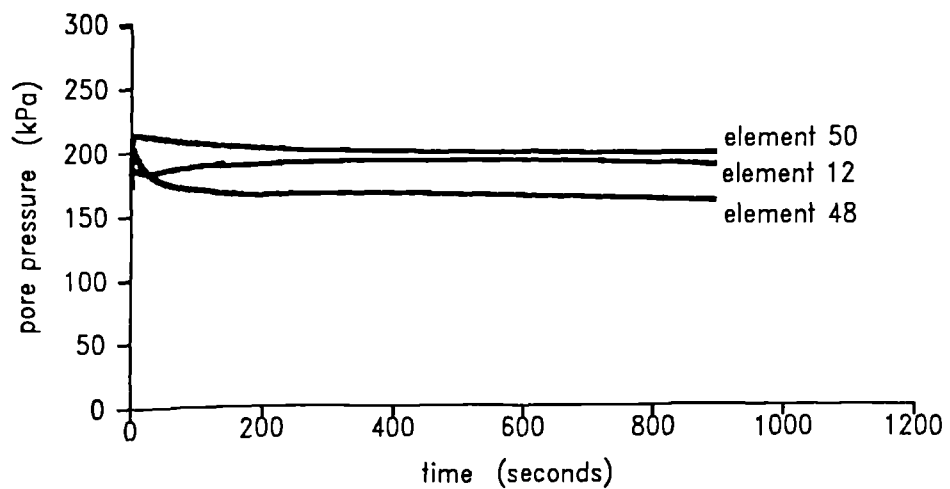


Figure 7.15 Pore pressure response with time from finite element analysis SI50

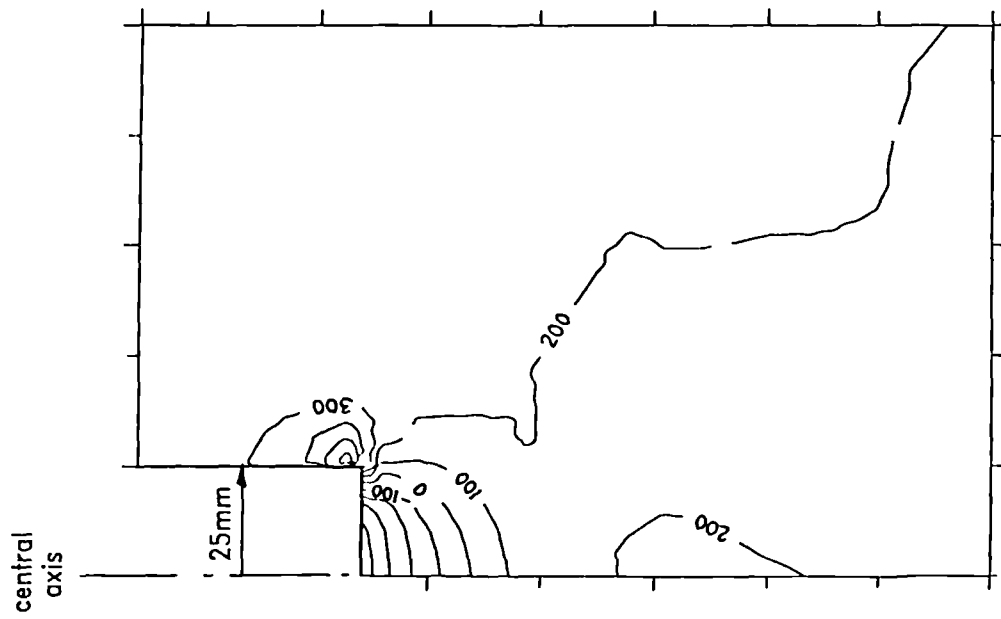


Figure 7.16(a) Pore pressure distribution at the end of removal of face support pressure in SI50

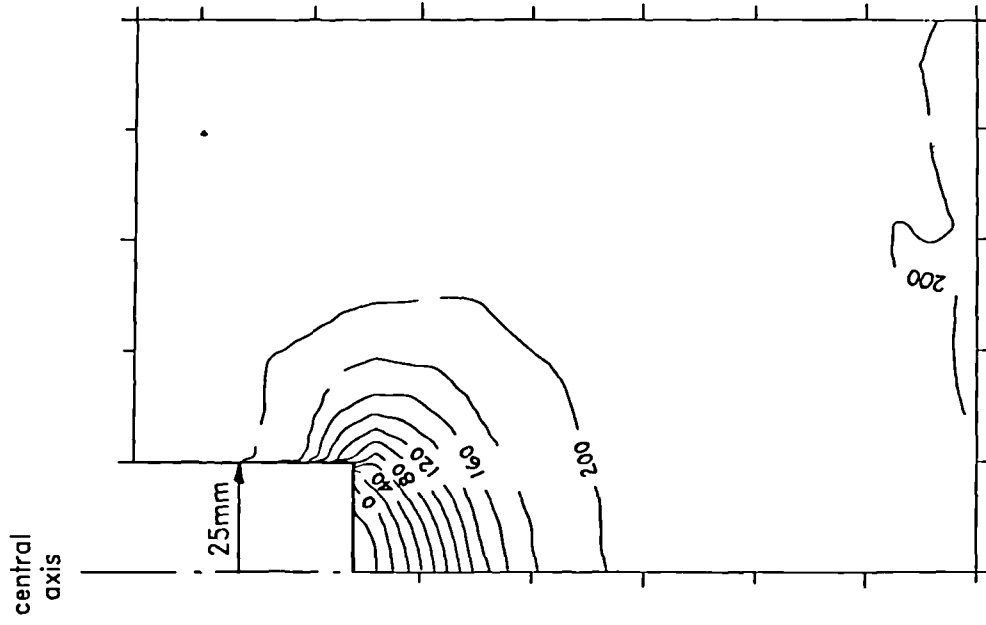


Figure 7.16(b) Pore pressure distribution during SI50
 $ktu_0/(D^2 \gamma_w) = 2.4 \times 10^{-6}$

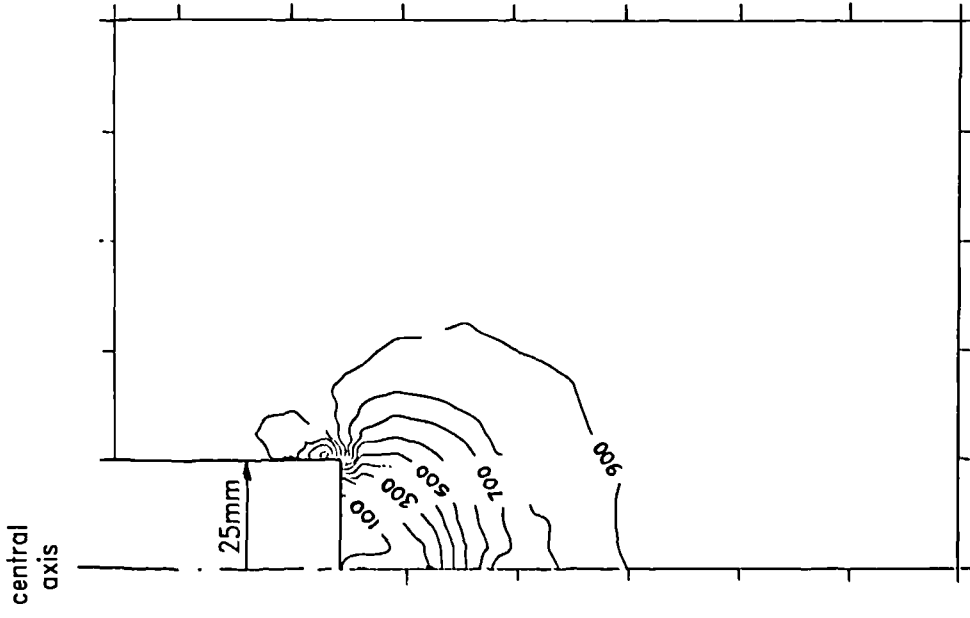


Figure 7.17(a) Total stress, p , distribution in analysis SI50 investigating the influence of diameter



Figure 7.17(b) Total stress, p , distribution in analysis SI25T investigating the influence of diameter

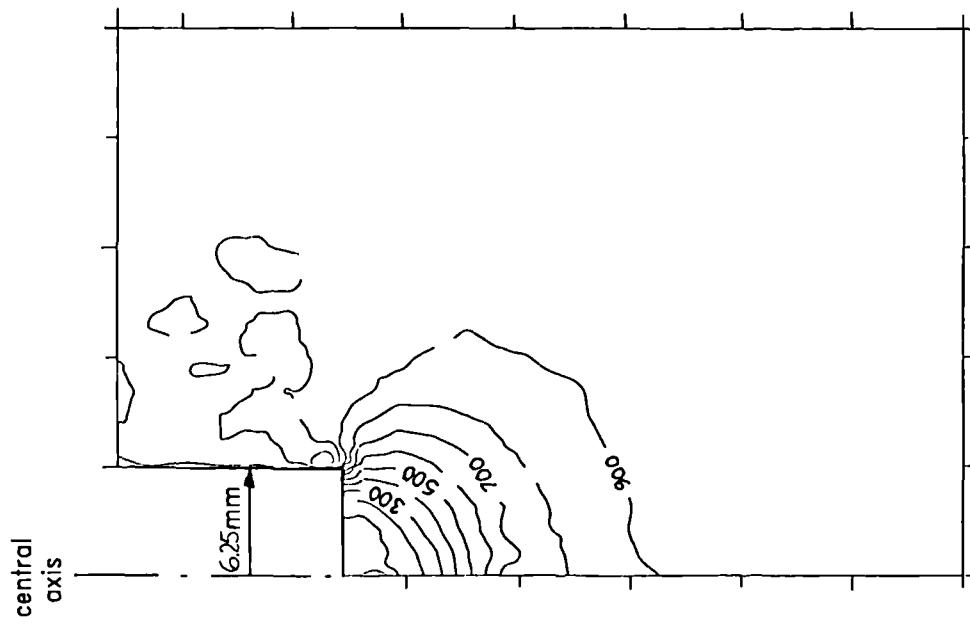


Figure 7.17(c) Total stress, p , distribution in analysis SI13T investigating the influence of diameter

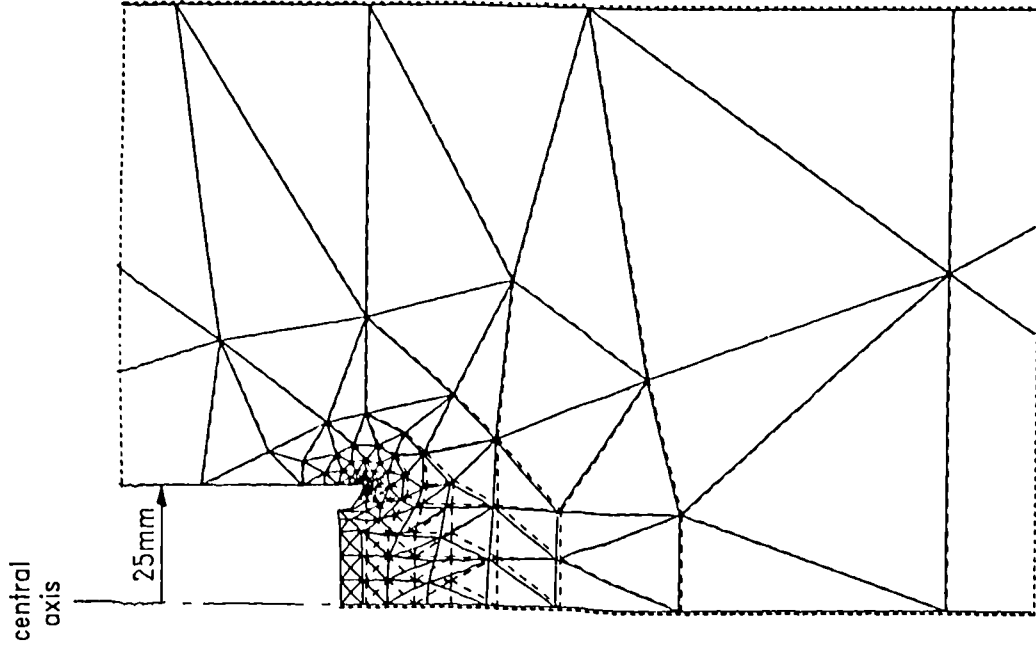


Figure 7.18(o) Deformed mesh during KAP05
 $ktu_o/(D^2\gamma_w) = 4.4 \times 10^{-6}$

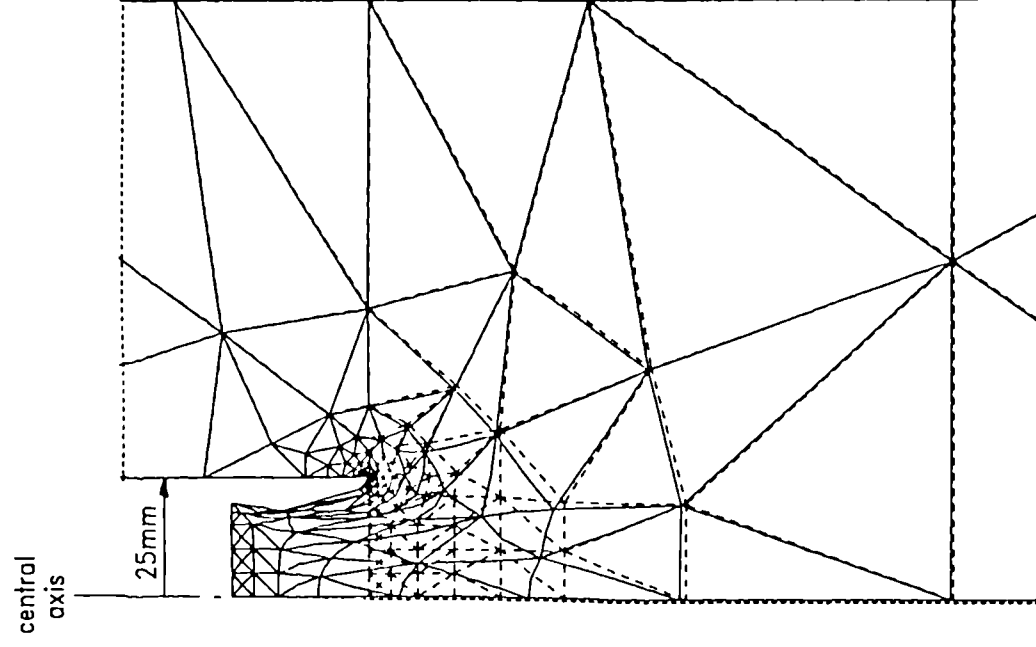


Figure 7.18(b) Deformed mesh at the end of KAP05
 $ktu_o/(D^2\gamma_w) = 15.1 \times 10^{-6}$

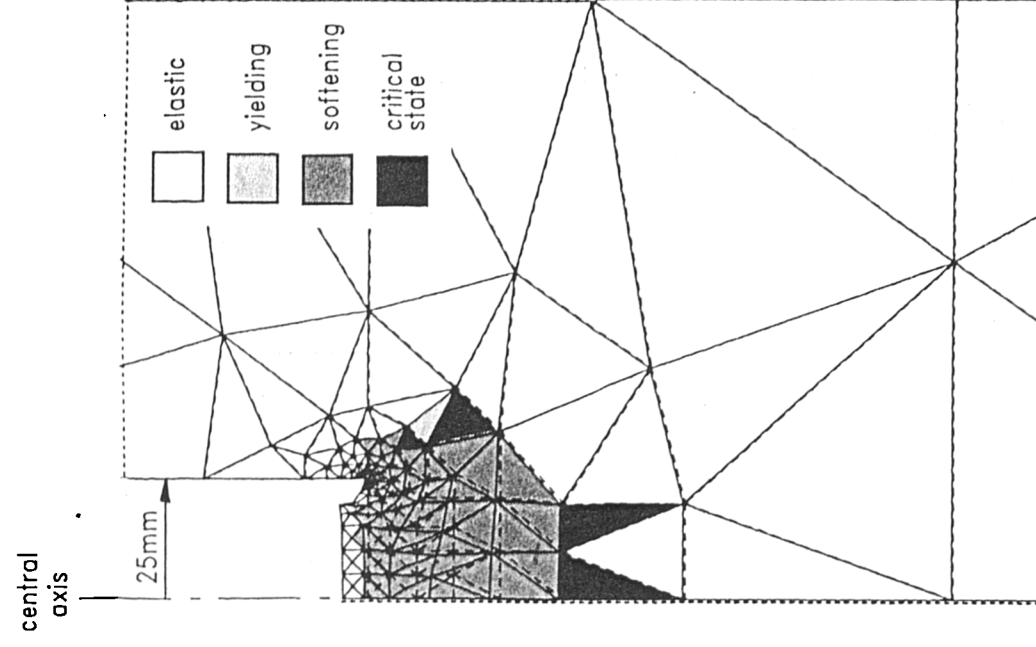


Figure 7.18(c) Element states during KAP05
 $ktu_o/(D^2\gamma_w) = 4.4 \times 10^{-6}$

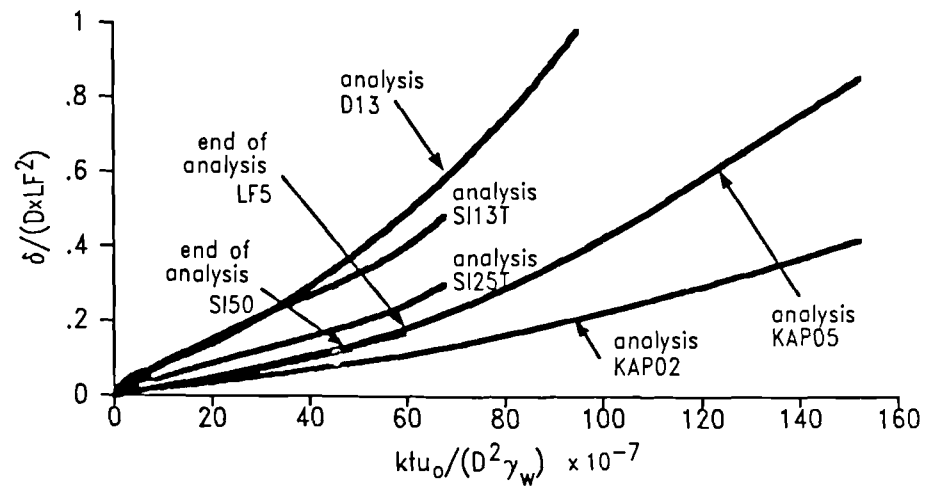


Figure 7.19 Comparison of tunnel face deformation using non-dimensional groups developed from experimental observations

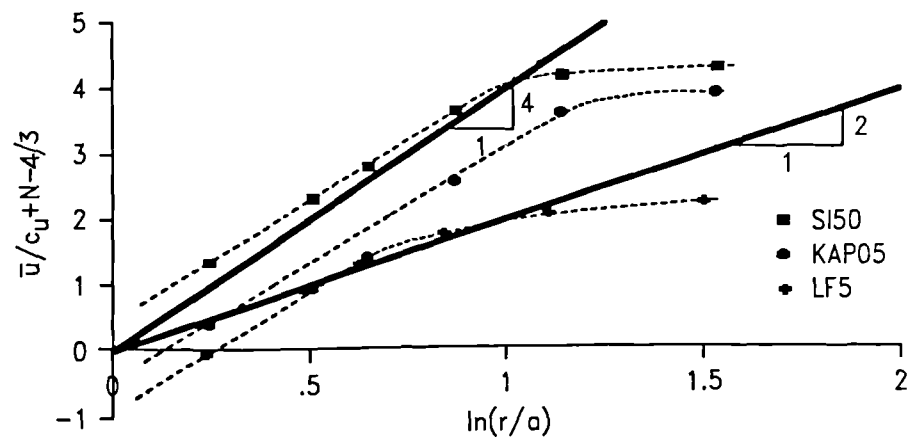


Figure 7.20 Pore pressure reductions ahead of the tunnel face plotted in non-dimensional groups

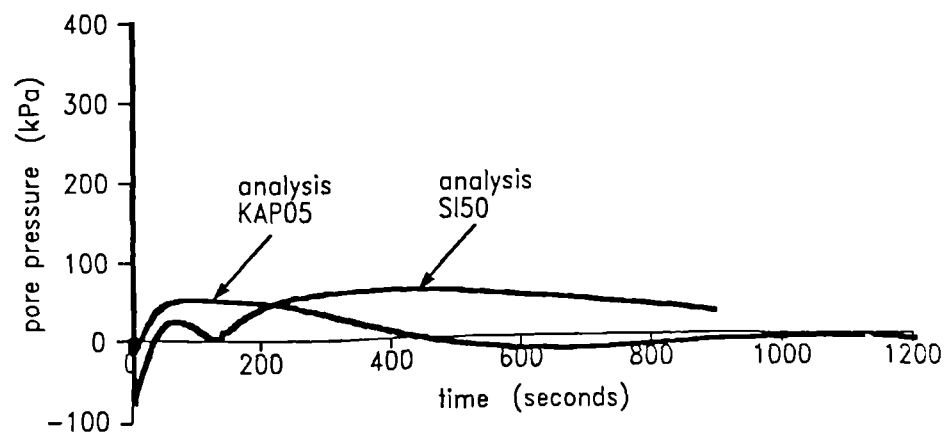


Figure 7.21 Comparison of pore pressure predictions for element 25 in finite element analyses SI50 and KAP05

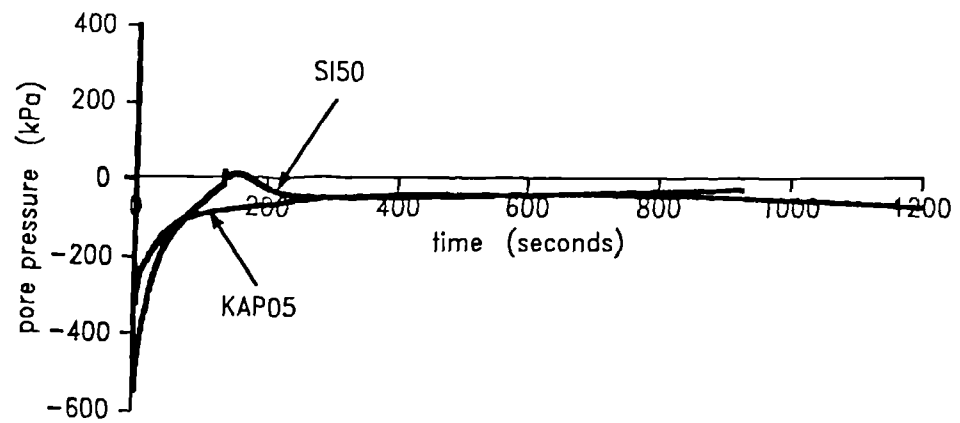


Figure 7.22 Comparison of pore pressure predictions for node 52 at the tunnel face in analyses SI50 and KAP05

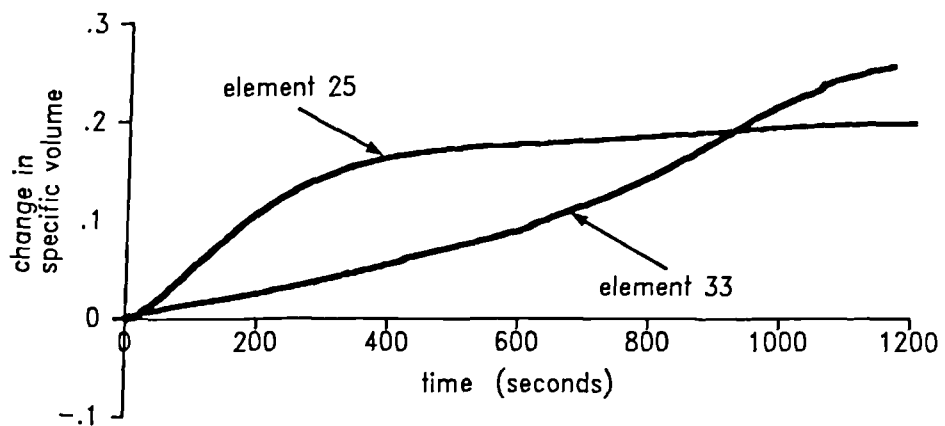


Figure 7.23 Comparison of specific volume changes predicted for elements 25 and 33 in analysis KAP05

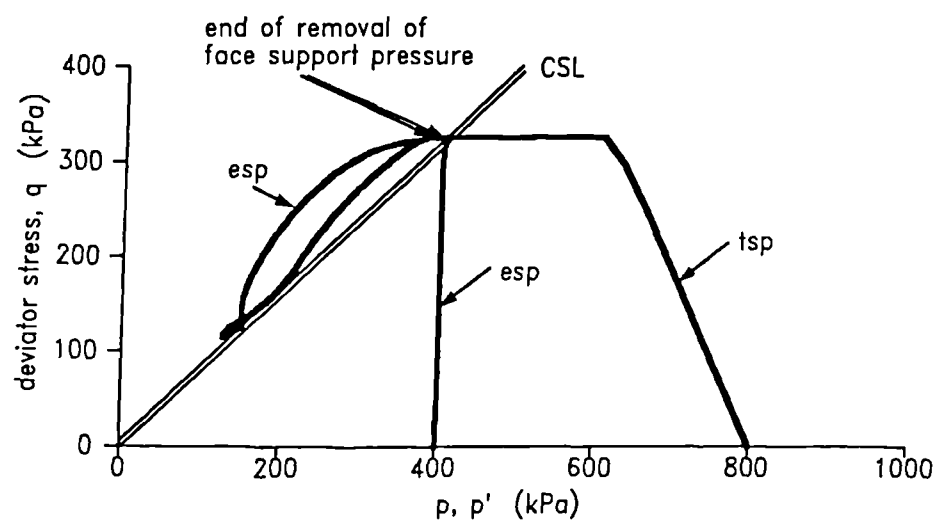


Figure 7.24 Total and effective stress paths predicted for element 25 in analysis KAP05

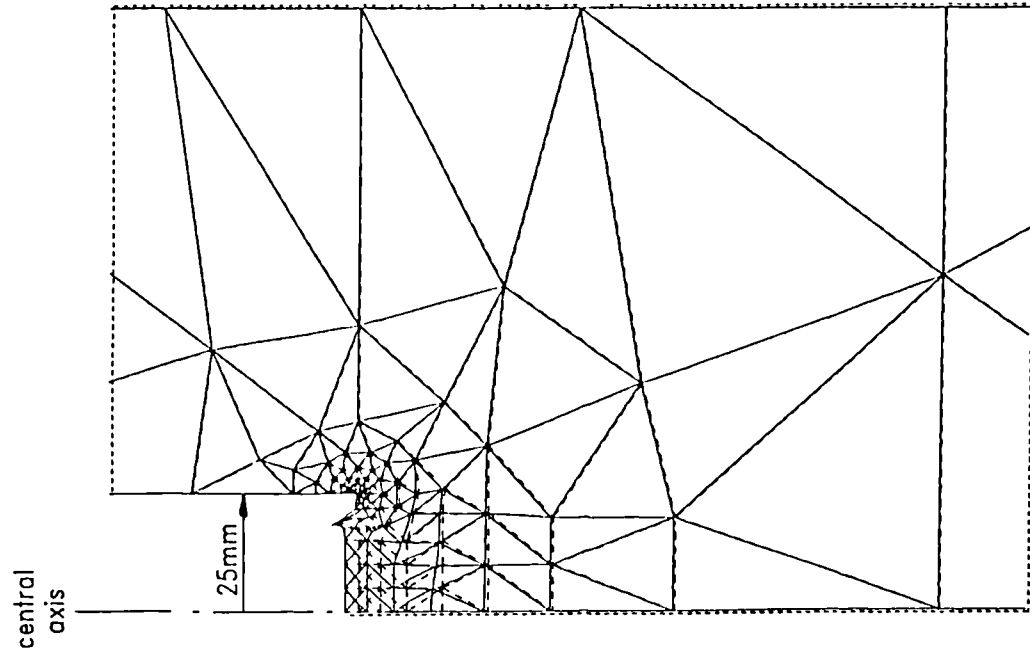


Figure 7.25(a) Deformed mesh from analysis LF5
 $ktu_o/(D^2\gamma_w) = 4.4 \times 10^{-6}$

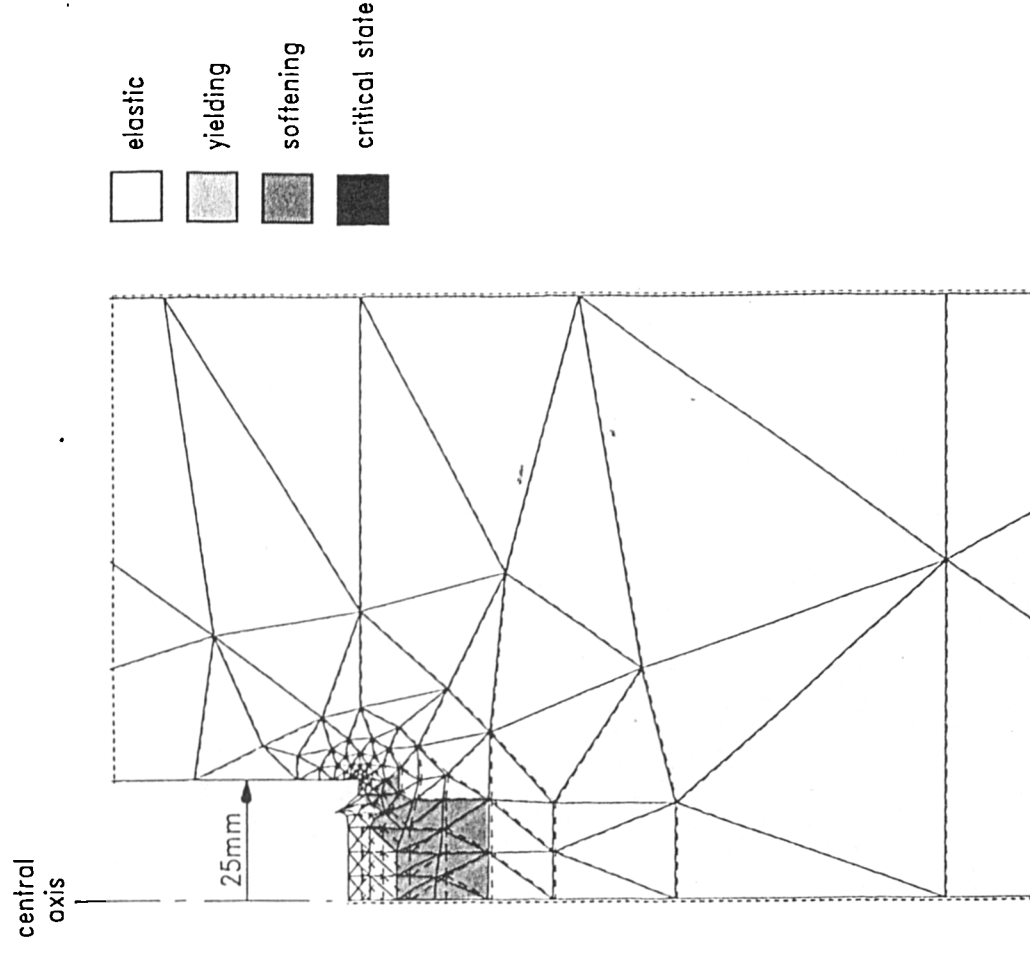


Figure 7.25(b) Element states during analysis LF5
 $ktu_o/(D^2\gamma_w) = 4.4 \times 10^{-6}$

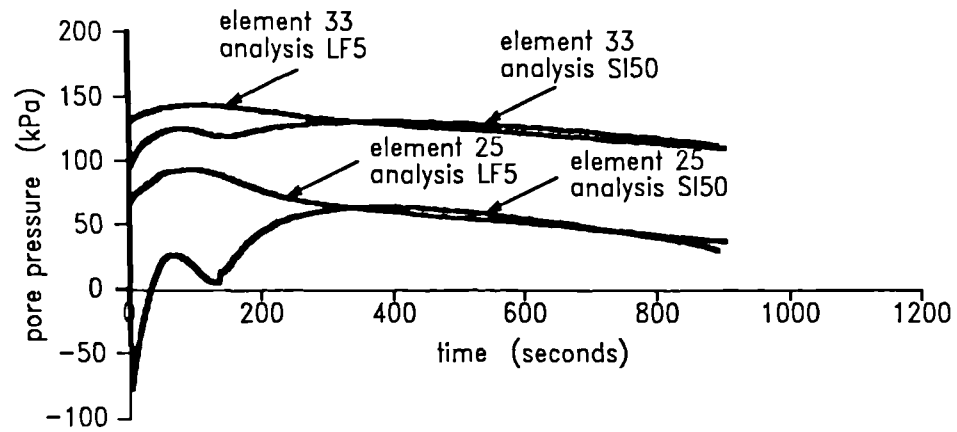


Figure 7.26 Comparison of predicted pore pressure behaviour for elements 25 and 33 in analyses LF5 and SI50

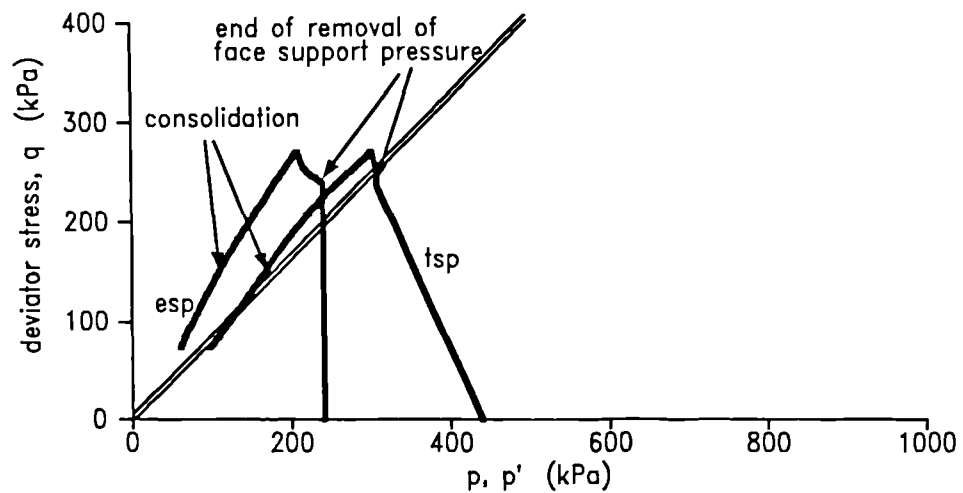


Figure 7.27 Total and effective stress paths predicted for element 25 in analysis LF5

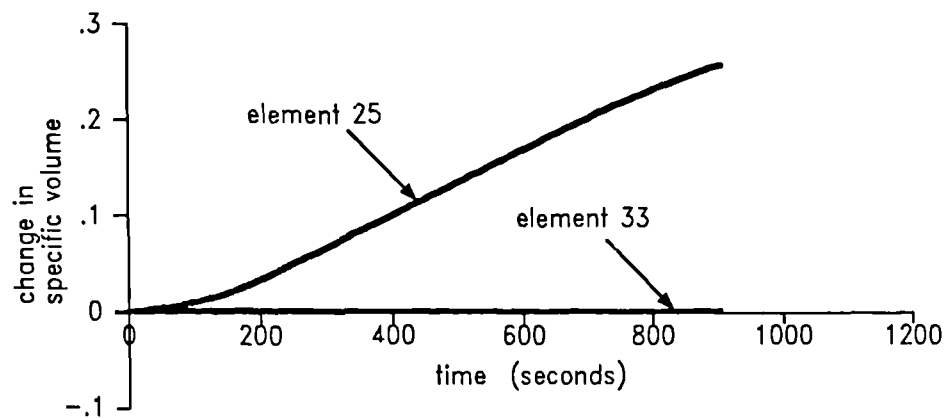


Figure 7.28 Comparison of specific volume changes at elements 25 and 33 in analysis LF5

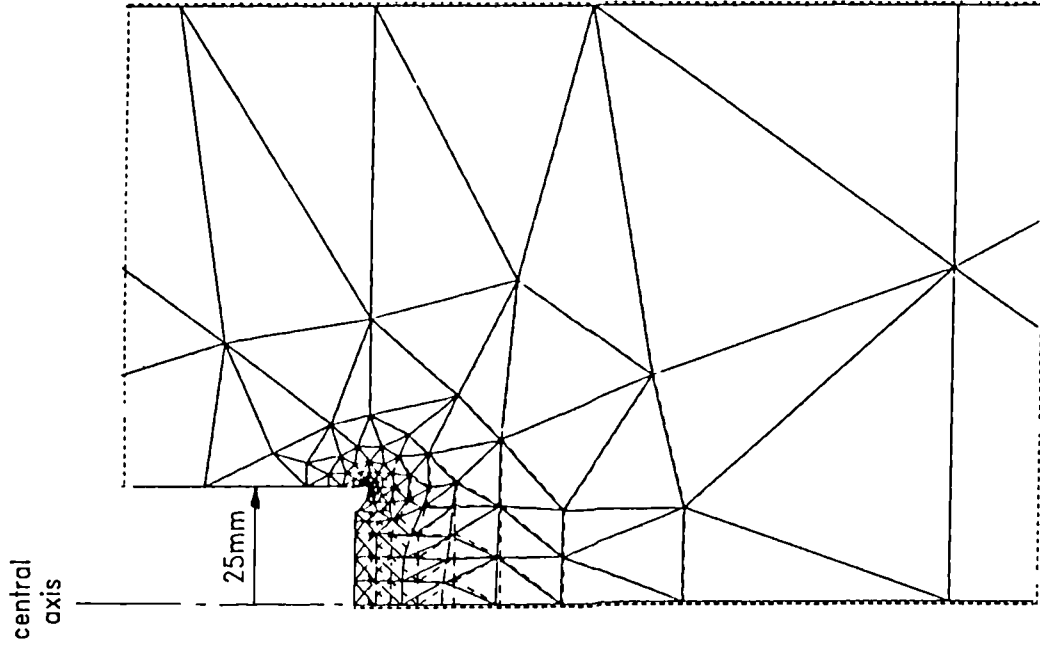


Figure 7.29(a) Deformed mesh from analysis KAP02
 $ktu_o/(D^2\gamma_w) = 4.4 \times 10^{-6}$

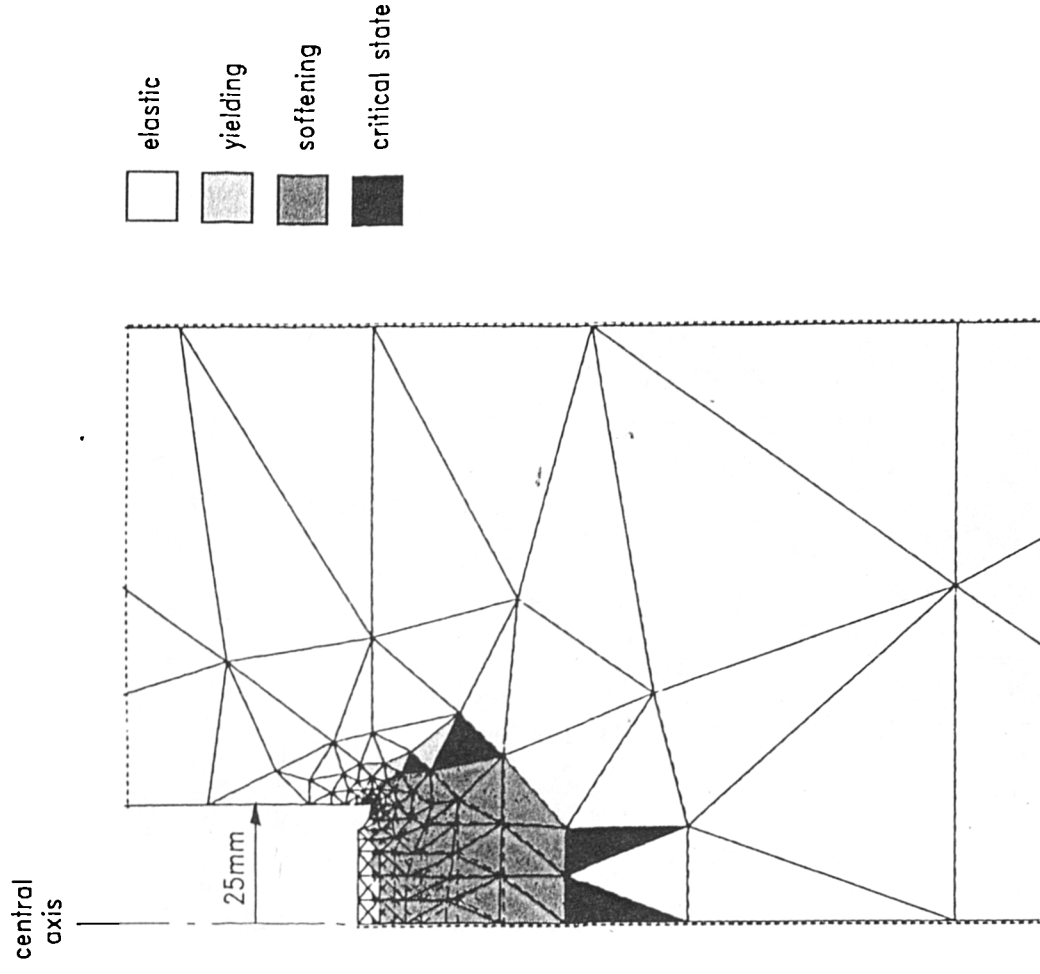


Figure 7.29(b) Element states during analysis KAP02
 $ktu_o/(D^2\gamma_w) = 4.4 \times 10^{-6}$

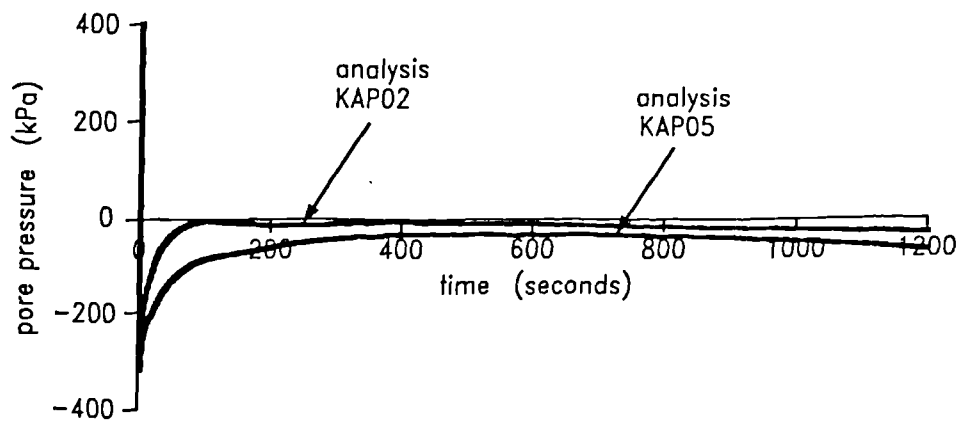


Figure 7.30 Comparison of pore pressure predictions for node 52 at the tunnel face in analyses KAP05 and KAP02

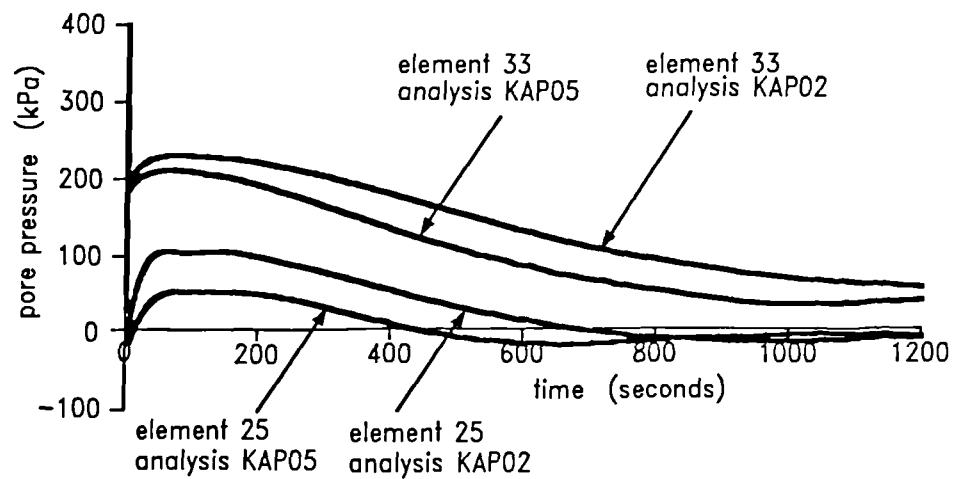


Figure 7.31 Comparison of predicted pore pressure change with variation in κ in analyses KAP05 and KAP02

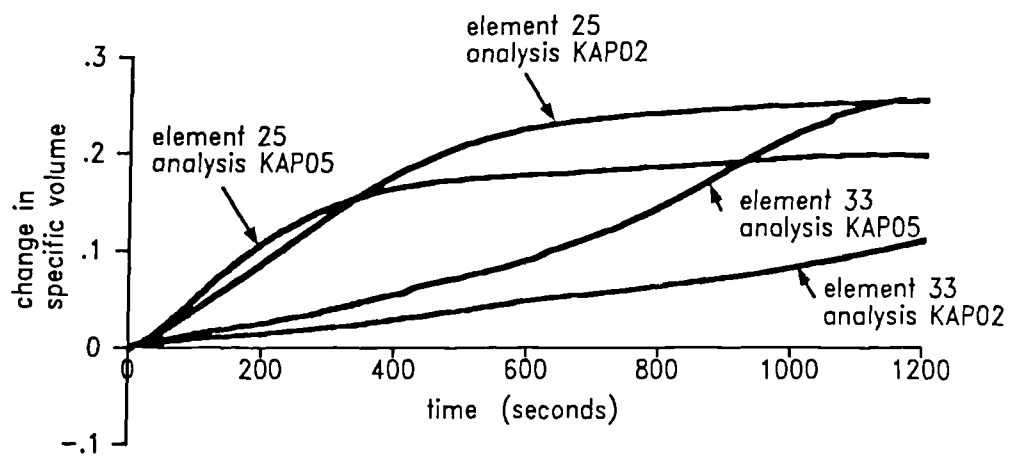


Figure 7.32 Comparison of predicted specific volume changes for variation in κ in analyses KAP05 and KAP02

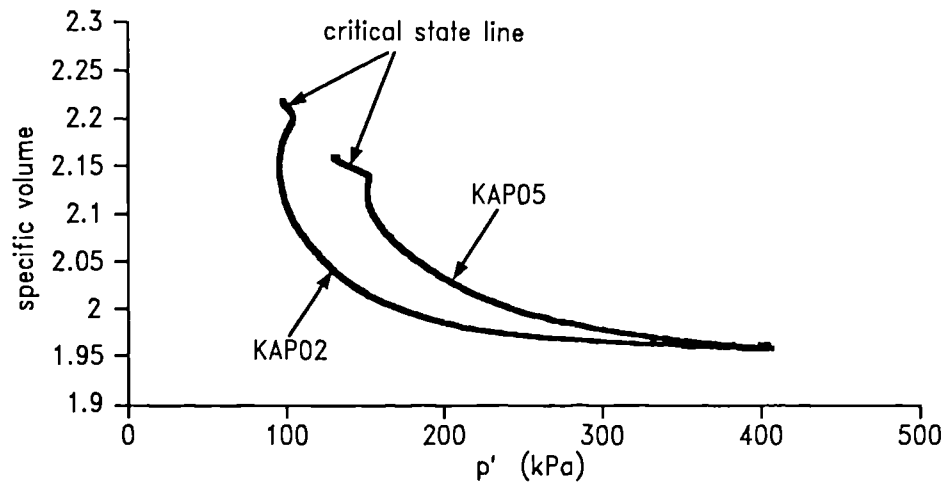


Figure 7.33 Influence of κ on the specific volume of element 25 in analyses KAP05 and KAP02

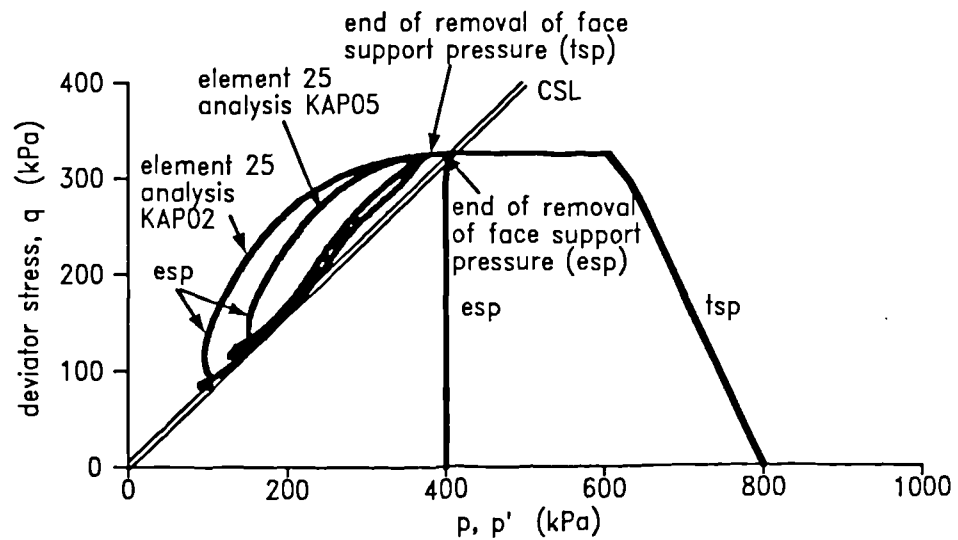


Figure 7.34 Total and effective stress paths for different κ values in finite element analyses

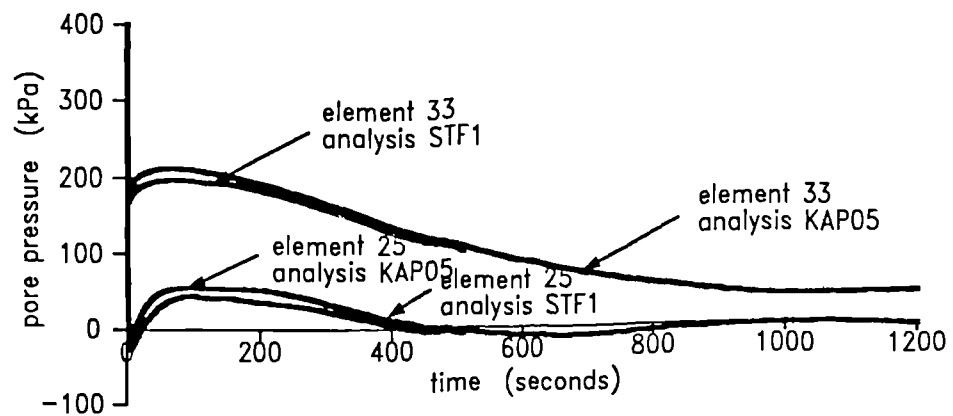


Figure 7.35 Comparison of pore pressure changes to illustrate the influence of the stiff elastic elements

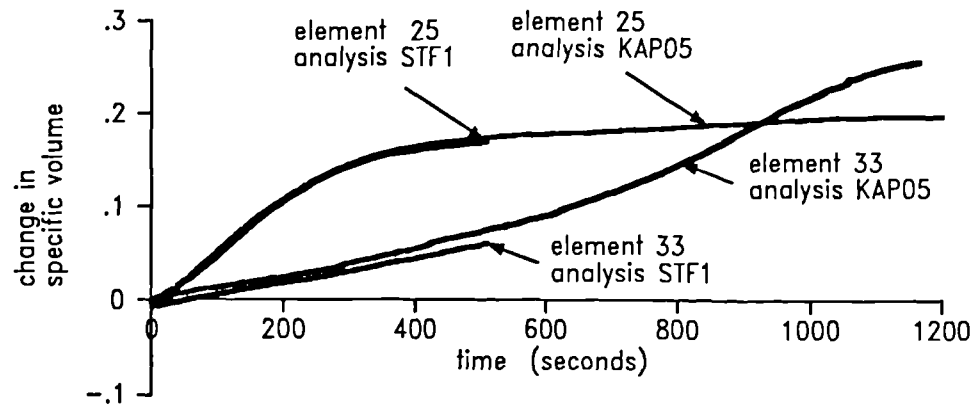


Figure 7.36 Comparison of specific volume changes to illustrate the influence of the stiff elastic elements

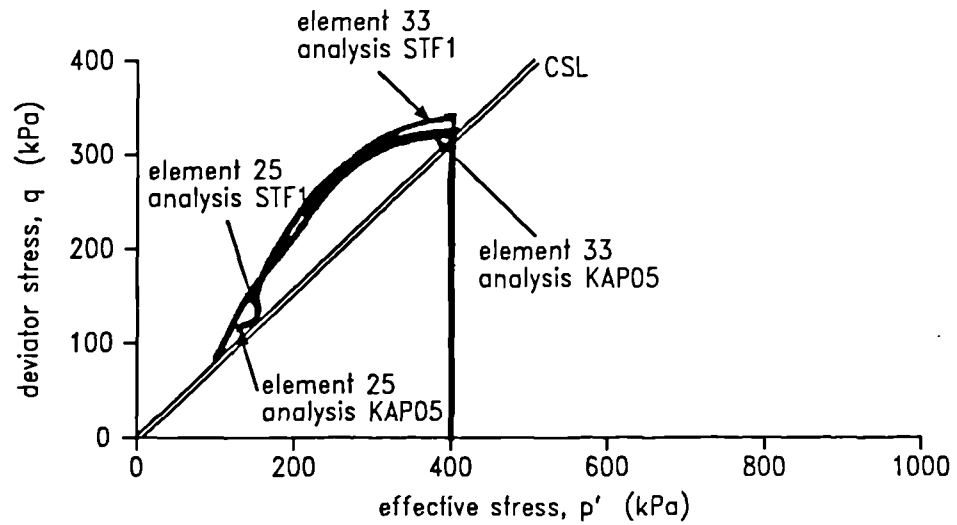


Figure 7.37 Comparison of effective stress paths to illustrate the influence of the stiff elastic elements

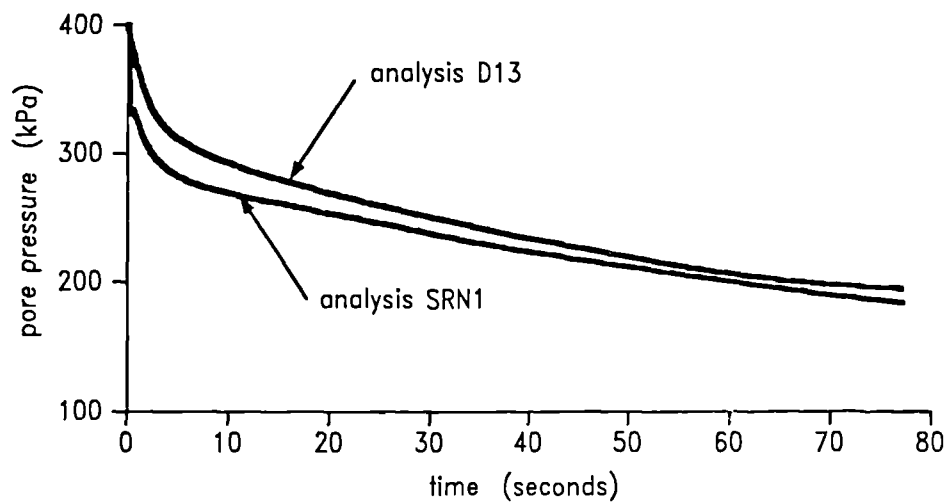


Figure 7.38(a) Comparison of predicted pore pressure behaviour at element 65 in front of a typical transducer location (element 66)

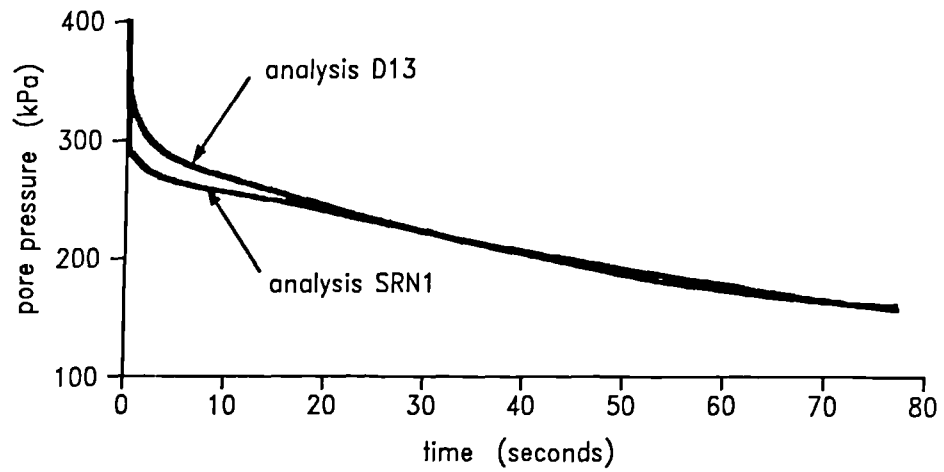


Figure 7.38(b) Comparison of predicted pore pressure behaviour at element 47 in front of a typical transducer location (element 66)

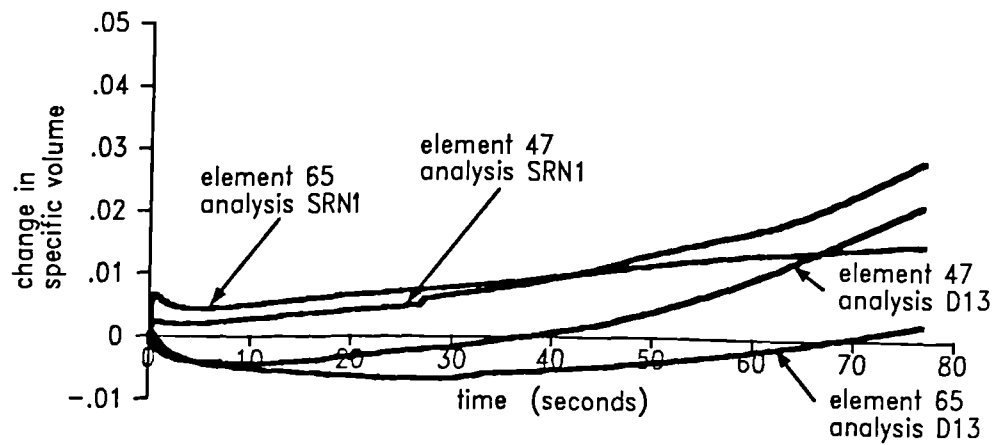


Figure 7.39 Comparison of specific volume changes at elements in front of a typical transducer location (element 66)

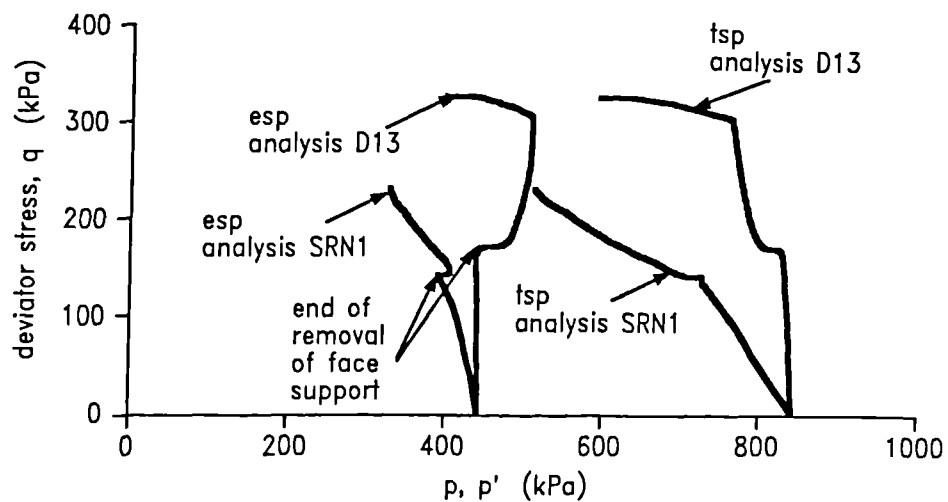


Figure 7.40 Comparison of the total and effective stress paths predicted at element 65

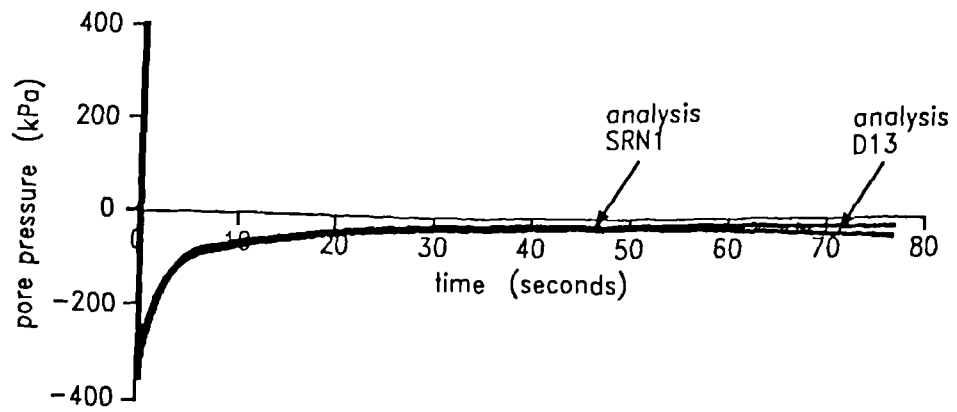


Figure 7.41 Comparison of pore pressures predicted for node 52 at the tunnel face with and without a stiff ring

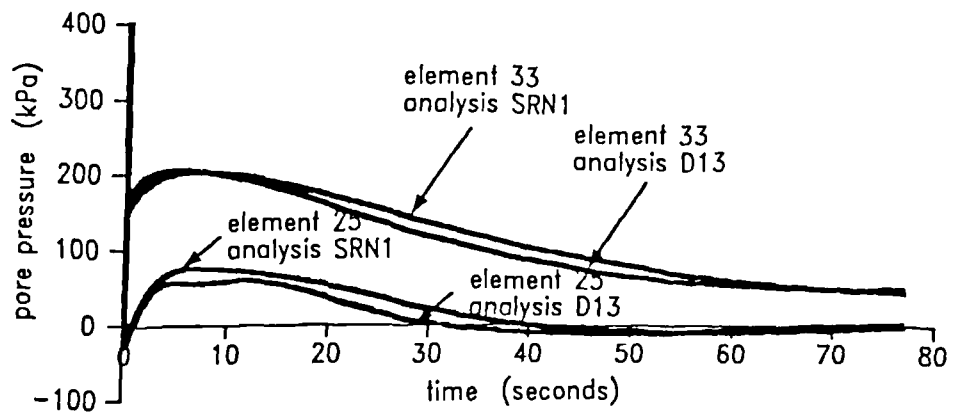


Figure 7.42 Comparison of pore pressure response to illustrate the effect of modelling pore pressure transducers as a stiff ring

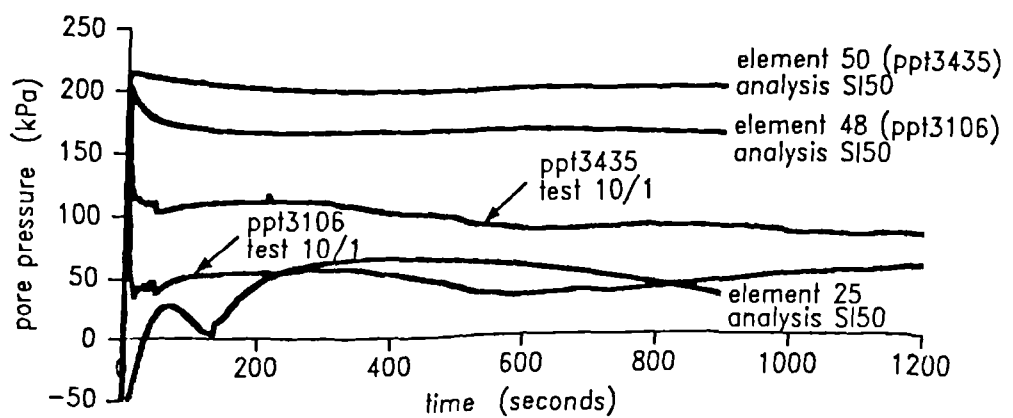


Figure 7.43 Comparison of predicted and experimental pore pressure behaviour close to the tunnel face

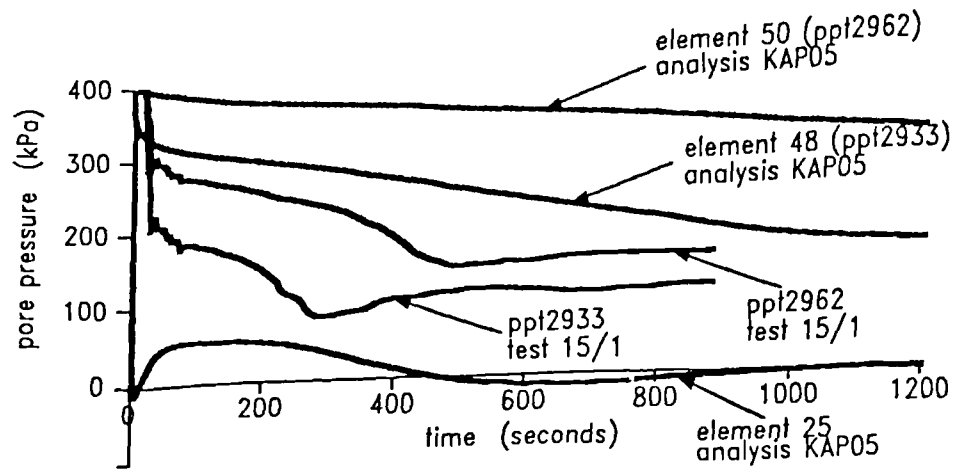


Figure 7.44 Comparison of predicted and experimental pore pressure responses at r/r_o of about 1.6 and 2.2 perpendicular to the central axis

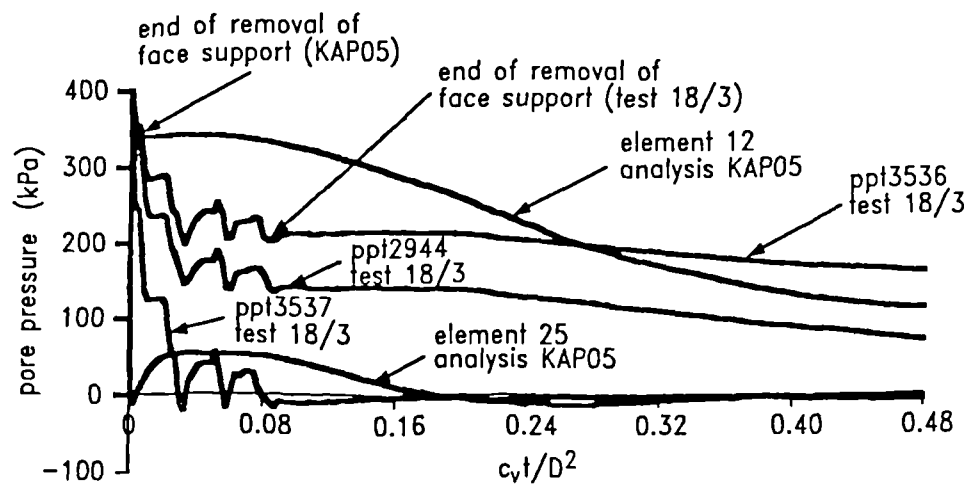


Figure 7.45 Comparison of predicted and experimental pore pressure responses ahead of the tunnel face

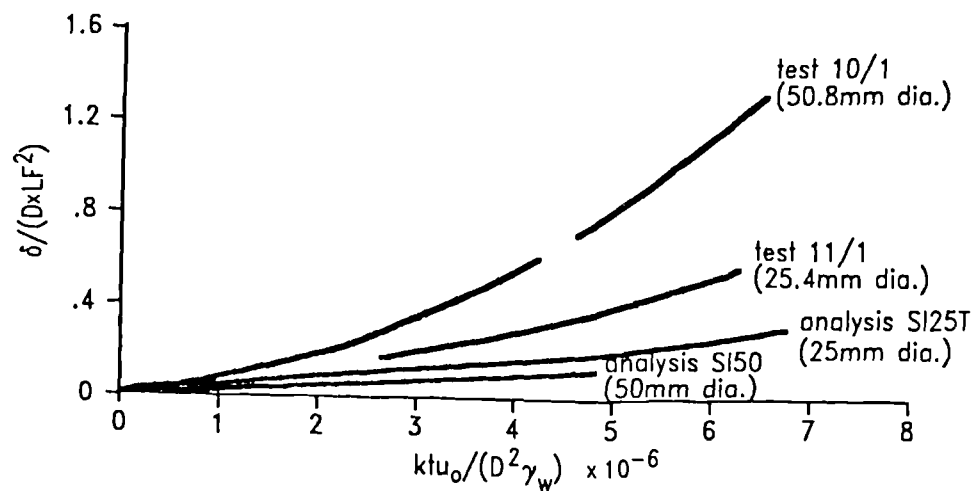


Figure 7.46 Experimental and predicted deformation of the tunnel face in terms of dimensionless groups

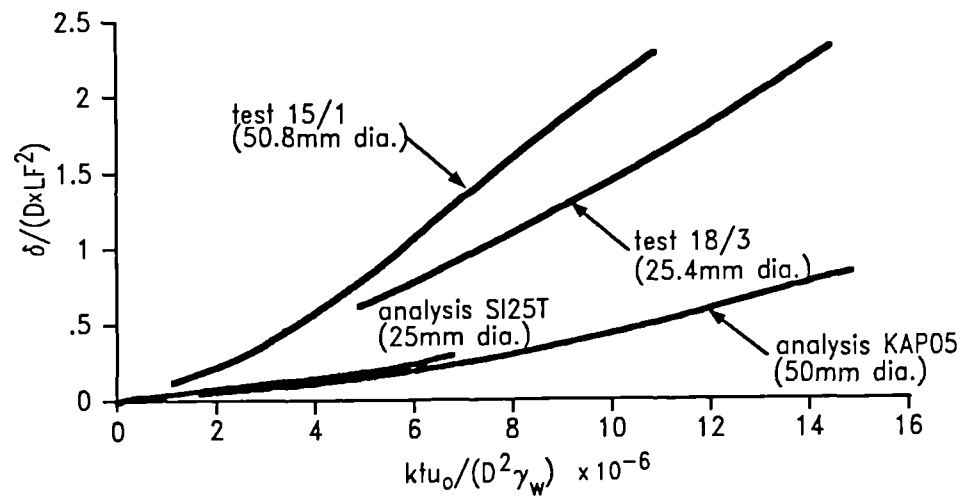


Figure 7.47 Experimental and predicted deformation of the tunnel face in terms of dimensionless groups